Inertial Fragmentation Processes Associated with Ocean Wave Breaking

Kaitao Tang

Reuben College
University of Oxford

A thesis submitted for the degree of
Doctor of Philosophy

Hilary 2025

Abstract

Ocean sprays are liquid droplets ejected from the sea surface, which enhance mass, momentum and energy transfer at the air-sea interface. Depending on their sizes, ocean sprays interact with their environment and influence the global climate system differently. They are produced from breaking ocean waves through a few dominant mechanisms, including film and jet drops associated with bursting surface bubbles, spume drops sheared from wave crests under high winds, and splash drops due to the collapse of corrugated wave fronts. Here, we use the open-source numerical solver Basilisk to investigate the latter two spray generation mechanisms, which remain poorly understood due to difficulties in the detailed analysis of breaking waves. Due to the extremely high computational cost of resolving all spray production events during wave breaking, we instead investigate two canonical fragmentation configurations as toy models for ocean spray generation, namely the bag breakup of droplets in airflows and the transverse collision of liquid rims.

For droplet aerobreakup, we utilise a recently proposed Manifold Death (MD) algorithm to artificially perforate thin liquid films in a controlled manner, establishing numerical grid convergence of the statistics of large fragments for the first time. We then analyse different fragmentation mechanisms leading to bag film rupture and discuss their contribution to fragment statistics. We further implement the Synthetic Turbulence Generation Method to investigate the influence of air-phase turbulence on the early-time evolution of bag morphology, where the decrease in droplet aspect ratio, late-time tilting of the bag and formation of small-scale surface corrugations are systematically measured and analysed.

As for rim collision, we identify ligament merging as the dominant underlying mechanism causing the increase of the size of splash drops over time, and establish a quasi-steady theoretical framework capable of predicting the long-term fragment size and velocity distributions. Gravity arrests the ligament merging process by pulling back the liquid lamella arising from rim coalescence. The size and velocity distributions of the splash drops compare favourably with available wave-breaking data, and we propose a novel theoretical model accounting for the time evolution in the rim fragment size distribution. We further propose sea spray generation functions corresponding to splash drops produced from realistic sea states. Our discovery of fragmenting large splash drops challenges the previous speculation that wave splashing is an inefficient sea spray generation mechanism, thus bearing far-reaching implications for modelling efforts in air-sea interaction. Overall, the numerical results and physical insights obtained here serve as a stepping stone towards fully understanding ocean spray formation with the aid of two-phase direct numerical simulations.

Inertial Fragmentation Processes Associated with Ocean Wave Breaking

Kaitao Tang

Reuben College

University of Oxford

A thesis submitted for the degree of

Doctor of Philosophy

Hilary 2025

Acknowledgements

Firstly, I would like to thank my DPhil supervisor Prof. Wouter Mostert, the Virgilio who so far has guided nearly the entirety of my journey through the *Commedia* of computational fluid dynamics. Ever since our first encounter in the Engineering Quad at Princeton in 2019, he has been particularly supportive of and trusting in my research efforts, even at times when I was dismayed by setbacks along the way. Moreover, his physical insights and rigorous research style have been indispensable in shaping my own perspectives and approaches to scientific problems as an early-career researcher. Special thanks also go to my second supervisor Prof. Thomas Adcock, who has also been supportive of my research and offered valuable advice throughout my DPhil, alongside his encyclopedic knowledge of ocean wave flows and his typical British sense of humour, which may occasionally require additional effort to fully grasp. I am grateful to Profs. Alfonso Castrejón-Pita and R. Jason Hearst, whose suggestions have helped improve various aspects of this work; and to Profs. Chris Macminn and Stéphane Zaleski for carefully reviewing my thesis and acting as my *Viva Voce* examiners. Credits also go to colleagues at the Oxford Environmental Fluid Mechanics Group, who have provided a good chunk of anecdotes, laughter, and at times subtle embarrassment to digest over these years.

This research would not have taken place without the Research Studentship (No. 1411916) I received from the Department of Engineering Science, University of Oxford, and computational resources required through the UK Turbulence Consortium (EP/R029326/1). I also acknowledge the use of the University of Oxford Advanced Research Computing (ARC) facility.

I would also like to thank my friends Haotian (Walden) Wu, Junyu (Loveday) Liu, Yinxuan Huang, Si Si Ng, En Chang, Muxin Yan, and Donglin (Jacob) Zheng, both at Oxford and beyond. Their invaluable perspectives and support during this unique phase of my life have transcended the epistemological boundaries of modern-day academic disciplines, and can never be enclosed by the few words here. "*Simul ergo cum in unum congregamur / Ne nos mente dividamur, caveamus*" ("Ubi Caritas").

Lastly, I am especially indebted to my fiancée Lingjie (Sara) Ding. You have always been there as my best friend *coram Deo* since our undergraduate times, and have brought so much joy and reassurance to my final year of DPhil which would have otherwise been particularly challenging to go through due to all the uncertainties it

presents. "*Overseas from coast to coast / To find a place I love the most / Where the fields are green / See you once again, my love*" (Westlife, "My Love"). I would also like to thank my parents for the care and support they have shared with me until today, especially their understanding that I would like to pursue an academic career far away from the world they have known.

Abstract

Ocean sprays are liquid droplets ejected from the sea surface, which enhance mass, momentum and energy transfer at the air-sea interface. Depending on their sizes, ocean sprays interact with their environment and influence the global climate system differently. They are produced from breaking ocean waves through a few dominant mechanisms, including film and jet drops associated with bursting surface bubbles, spume drops sheared from wave crests under high winds, and splash drops due to the collapse of corrugated wave fronts. Here, we use the open-source numerical solver Basilisk to investigate the latter two spray generation mechanisms, which remain poorly understood due to difficulties in the detailed analysis of breaking waves. Due to the extremely high computational cost of resolving all spray production events during wave breaking, we instead investigate two canonical fragmentation configurations as toy models for ocean spray generation, namely the bag breakup of droplets in airflows and the transverse collision of liquid rims.

For droplet aerobreakup, we utilise a recently proposed Manifold Death (MD) algorithm to artificially perforate thin liquid films in a controlled manner, establishing numerical grid convergence of the statistics of large fragments for the first time. We then analyse different fragmentation mechanisms leading to bag film rupture and discuss their contribution to fragment statistics. We further implement the Synthetic Turbulence Generation Method to investigate the influence of air-phase turbulence on the early-time evolution of bag morphology, where the decrease in droplet aspect ratio, late-time tilting of the bag and formation of small-scale surface corrugations are systematically measured and analysed.

As for rim collision, we identify ligament merging as the dominant underlying mechanism causing the increase of the size of splash drops over time, and establish a quasi-steady theoretical framework capable of predicting the long-term fragment size and velocity distributions. Gravity arrests the ligament merging process by pulling back the liquid lamella arising from rim coalescence. The size and velocity distributions of the splash drops compare favourably with available wave-breaking data, and we propose a novel theoretical model accounting for the time evolution in the rim fragment size distribution. We further propose sea spray generation functions corresponding to splash drops produced from realistic sea states. Our discovery of fragmenting large splash drops challenges the previous speculation that wave splashing is an inefficient sea

spray generation mechanism, thus bearing far-reaching implications for modelling efforts in air-sea interaction. Overall, the numerical results and physical insights obtained here serve as a stepping stone towards fully understanding ocean spray formation with the aid of two-phase direct numerical simulations.

Contents

List of Figures

List of Tables

List of Abbreviations

1-D, 2-D . . . One- or two-dimensional, referring in this thesis to spatial dimensions.

AMR . . . . . Adaptive Mesh Refinement Scheme.

ABL . . . . . Atmospheric Boundary Layer.

DNS . . . . . Direct Numerical Simulation.

FFT . . . . . Fast Fourier Transform.

HIT . . . . . Homogeneous Isotropic Turbulence.

KH . . . . . Kelvin-Helmholz.

LES . . . . . Large Eddy Simulation.

MD . . . . . Manifold Death.

NS . . . . . Navier-Stokes.

ODE . . . . . Ordinary Differential Equation.

PDE . . . . . Partial Differential Equation.

pdf . . . . . Probability Density Function.

PSD . . . . . Power Density Spectrum.

rms . . . . . Root Mean Squared.

RT . . . . . Rayleigh-Taylor.

RP . . . . . Rayleigh-Plateau.

SSGF . . . . . Sea-Spray Generation Function.

TC . . . . . Taylor-Culick.

TKE . . . . . Turbulent Kinetic Energy.

VOF . . . . . Volume of Fluid.

1 Introduction

Knowledge of the motion and properties of the ocean, which dominates the surface of our Earth, remains of paramount significance to human activities even as the Space Age unfolds [1]. Apart from providing nutrition and means of transport for human beings, the ocean plays a key role in regulating the climate by partially mitigating the effects of increasing levels of atmospheric greenhouse gases and rising global temperature [2], a topic of pressing concern for the current post-industrial world.

In the last few decades, human society has become increasingly aware of the climate as a coupled system where the ocean and atmosphere interact across a wide range of time and length scales, as witnessed by a consistent converging trend of two previously standalone disciplines: atmospheric science and oceanography [1, 3]. This is especially true for the marine atmospheric boundary layer (ABL) populated by multiscale fluid dynamical processes where both the liquid and the gas phases are involved, the understanding of which is crucial to weather forecasting and coastal engineering [4]. Among these physical processes, deep-ocean wave breaking limits the build-up of wave heights under wind forcing, while also greatly facilitating the exchange of mass, momentum and energy between the two phases due to a transition from laminar to turbulent flow states [5].

To date, many aspects of wave breaking remain shrouded in mystery, where even a universal criterion for predicting its onset poses a significant challenge to the community

[5–7]. One specific consequence of wave-breaking that motivated the present work is the production of ocean sprays via liquid fragmentation [8], often accompanied by the converse process of air entrainment and dissolution [9]. Small spray drops are often transported over long distances within the ABL before evaporating, thereby supplementing the atmosphere with water vapour and salt crystals, and affecting its radiative balance and cloud formation. On the other hand, large spray drops preferentially stay close to the ocean surface and may serve to reduce air-sea drag coefficients, leading to the intensification of tropical cyclones [10]. Studies of ocean spray formation are therefore of great significance, as they provide us with the knowledge of the initial size and velocity of the sprays, which is crucial for predicting their subsequent dynamic behaviour using, for example, rigid particle approximations [10].

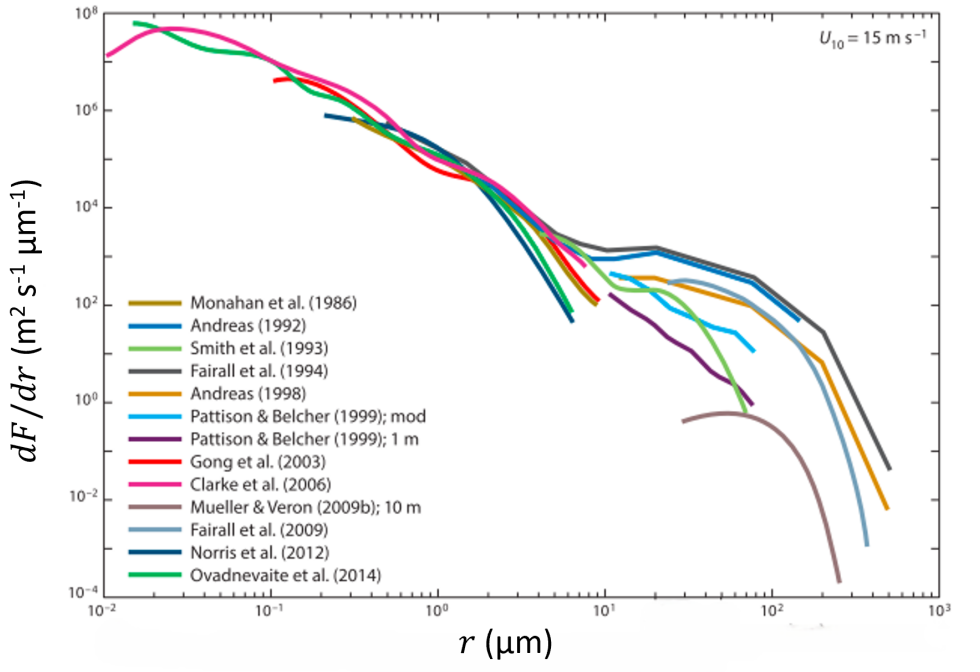

Figure 1.1: Evolution of currently available sea spray generation functions dF/dr (F being the local generation rate of spray drops) with increasing droplet radius r, obtained at a 10-m equivalent wind speed $U_{10} = 15\,\mathrm{m}\cdot\mathrm{s}^{-1}$. Adapted from Ref. [10] with permission.

Nonetheless, our current understanding of the generation mechanisms of ocean sprays, especially those of large spray drops, remains unsatisfactory. This is reflected in the large range of scatter in the currently available sea spray generation functions (SSGF) shown in fig. 1.1, which is defined as the number of spray drops generated per unit ocean

surface area, per unit time and per unit radius increment. SSGFs are indispensable for the calculation of sensible and latent heat fluxes associated with ocean spray drops in atmospheric models [11]. Due to difficulty in direct measurements, they are typically inferred via assuming universal function forms coupled with available laboratory data [12] or based on limited knowledge of the underlying spray generation mechanisms [13, 14]. Both approaches produce SSGFs with multiple empirical coefficients, and they oversimplify the spray generation process under realistic ocean conditions where different spray generation mechanisms are simultaneously present and coupled with one another. The difficulties surrounding the study of ocean spray formation are centred around the lack of any typical fragment sizes in liquid breakup phenomena [8]. Indeed, this puts stringent demands on the spatial and temporal resolutions of measurements at the liquid-gas interface in field and experimental studies of spray formation. While recent development of computational power enables numerical investigations of atomisation phenomena via two-phase direct numerical simulations, studies of ocean spray generation remain challenging due to insufficient grid resolution and spurious breakup events [15].

It has also been noted that a wide range of physical mechanisms can produce ocean sprays, each resulting in different fragment characteristics. As can be observed in fig. 1.2, the first class of such fragmentation mechanisms involves bubble bursting at the ocean surface, where droplets can be ejected either due to the rupture of bubble cap films or the pinch-off at the tip of liquid jets after the collapse of bubble cavities. Alternatively, spume drops may be directly torn off from overturning wave crests under high-wind conditions. Additionally, splash drops are produced after a plunging wavefront collapses onto the ocean surface, as the wave bulk merges with the irregularly shaped splash-up immediately ahead. Among these three classes of fragmentation mechanisms, film and jet drops associated with surface bubbles are the most widely studied, whereas considerably less attention is paid to the latter two mechanisms, most likely because they tend to produce large spray drops with radii greater than 10 microns, which are thought to fall back rapidly to the ocean and vanish [5, 10]. Very little is known about wave splashing, which is thought to be much less efficient compared with other spray generation mechanisms. However, discrimination among

different spume generation mechanisms is a prerequisite for the future development of physically informed parameterisations of ocean spray generation [10], which necessitates the investigation of the latter two spray production mechanisms.

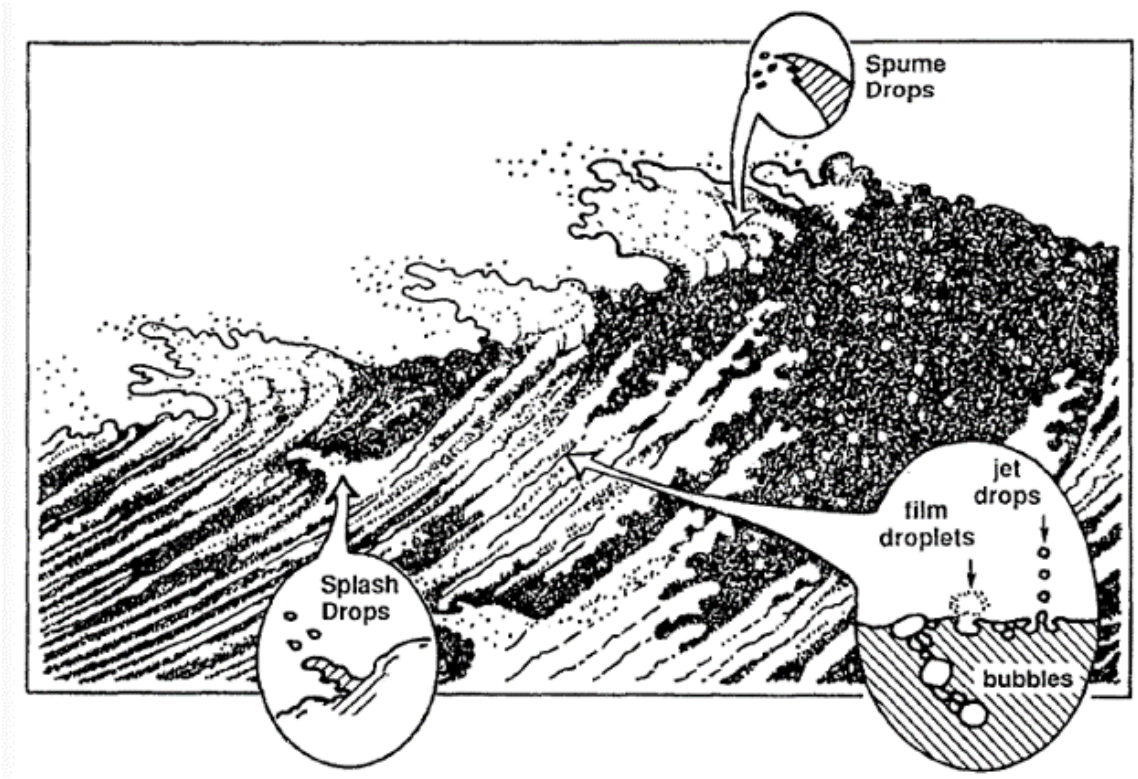

Figure 1.2: Sketch showing the major mechanisms responsible for the generation of ocean sprays: film and jet drops ejected from bursting surface bubbles entrained by overturning waves, spume drops torn from wavecrests under high wind conditions, and splash drops produced from the inertial collision between different parts of a breaking wave. Reproduced from Ref. [16] with permission.

In the current thesis, we investigate the formation of spume and splash drops within the context of ocean wave breaking. As fully resolved direct numerical simulation of spray formation during wave breaking incorporating turbulent wind forcing remains prohibitively expensive [17], here we study two simplified prototype flow configurations, namely those of the aerobreakup of a spherical droplet (§4-5) and the transverse collision of two cylindrical liquid rims (§6-7). This allows us to focus on detailed fragmentation dynamics without complications from other stages of wave breaking. Additionally, our results are applicable to other relevant fields of scientific and engineering applications

where droplet aerobreakup and impact processes are present, including liquid propellant combustion [18] and pathogen transmission [19].

1.1 Thesis outline

All the work presented in this thesis was completed by the writer under the supervision of Prof. Mostert and co-supervision of Prof. Adcock. Where numerical schemes have been borrowed from others this has been fully acknowledged. All the writing was initially drafted by the writer with input from the supervision team.

This integrated thesis comprises a series of publications. By the time of thesis submission, the contents of §4-6 have been published in two peer-reviewed journals (§4 and §6 in *Journal of Fluid Mechanics* and §5 in *Physical Review Fluids*). Those of §7 are still under ongoing preparation. The outline for the remainder of this thesis is shown below.

Chapter 2 - Literature Review: This chapter is divided into two parts, where the state of research for each of the two prototype flow configurations at the commencement of this project is overviewed, namely the bag breakup of droplets and the collision of liquid cylinders. The non-dimensional groups and the corresponding parameter spaces for both problems are also specified.

Chapter 3 - Methodology: Here we present the theoretical and numerical frameworks employed in the following chapters. We first introduce the nonlinear, incompressible and variable-density Navier-Stokes equations, which govern the fluid motion for both the aerobreakup and the rim splashing problem. We then provide an overview of the open-source numerical solver Basilisk, which is utilised to simulate both problems. The Manifold Death (MD) algorithm for artificial thin film perforation proposed by Chirco *et al.* [20] and the synthetic turbulence generation method developed by Xie and Castro [21], which are crucial to the aerobreakup studies, are discussed afterwards.

Chapter 4 - Droplet bag breakup in laminar airflows: We investigate the droplet bag breakup phenomena in uniform airflows. We first examine the viscous effect on the early-time drop deformation, comparing with theory and experiment. Next, we

adapt the MD algorithm to the problem, with which we demonstrate grid convergence of fragment statistics. The fragment behaviour and bag film disintegration mechanisms including ligament breakup, node detachment and rim destabilisation are then analysed. We also study viscous effects on the bag breakup process and fragment statistics, where a non-monotonic dependency of the average diameter of bag film fragments on the droplet Ohnesorge number Oh is found. We note that our choice of the critical thickness parameter L_{sig} is limited by numerical constraints and thus yields critical bag film perforation thicknesses larger than experimentally observed.

Chapter 5 - Droplet bag formation in turbulent airflows: Here we investigate droplet aerobreakup in turbulent airflows. We implement Xie and Castro's synthetic turbulence generation method [21], and compare characteristics of the air-phase turbulence with available theoretical and numerical results. Within our parameter space, ambient turbulence causes a droplet centre-of-mass acceleration largely independent of the specific turbulence configuration. At late times, the droplet becomes tilted and corrugated under strong turbulence intensity, for which we discuss possible physical mechanisms associated with turbulence intermittency. Lastly, the influences of liquid-gas viscosity ratio are examined and the implications of air-phase turbulence on the later bag film breakup process are discussed.

Chapter 6 - Splashing of cylindrical rims without gravity: Here we present direct numerical simulations of the collision between two cylindrical liquid rims. Interfacial perturbations with a truncated white noise frequency profile are introduced to the rims before their collision. We first derive analytical solutions predicting the unsteady interfacial and velocity profiles of the expanding splash sheet, and develop scaling laws for the evolution of the lamella rim under capillary deceleration. We then analyse the formation and growth of transverse ligaments ejected from the lamella rims, which originate from the initial corrugated geometry of the perturbed rim surface. Novel scaling models are proposed for predicting the decay of the ligament number density due to the ongoing ligament merging phenomenon, which agree well with the numerical results. The role of the splashing mechanism in breaking waves is discussed further and necessary next steps in the problem are identified.

Chapter 7 - Splashing of cylindrical rims with finite gravity: Here we further develop our theoretical framework in §6 to incorporate early-time transient effects under gravity, which is found to induce a superimposed free-fall motion without directly affecting the evolution of rim thickness or the ligament merging dynamics. The size and velocity distributions of the splash drops are in excellent agreement with available wave-breaking data, and we develop a novel theoretical model accounting for the time evolution in the droplet size distribution. Utilising this size distribution model for rim splash drops, we propose a sea spray generation function corresponding to the secondary wave splashing phenomena which compares favourably with currently available data from the literature.

Chapter 8 - Conclusions: This chapter summarises the key contributions of this thesis and discusses prospects of future work.

2
Literature Review

As is specified in §1, in this thesis we model the production of spume and splash drops using two simple flow configurations, namely those of droplet bag breakup and transverse collision of liquid rims. Here, we provide a thorough literature review for the current understanding of each of these two flow configurations, and clarify their connections with the original wave breaking context.

2.1 Droplet bag breakup

While it has been speculated that large spume drops torn off by wind stress are mostly responsible for the spray-induced momentum and enthalpy fluxes at the air-sea interface, large uncertainties remain with their statistics due to poor knowledge of their production mechanisms. It was only recently found by Troitskaya *et al.* [22] that the fragmentation of small-scale sea surface perturbations arising from the nonlinear Kelvin-Helmholtz (KH) instability is the dominant mechanism of sea spume generation under extreme wind conditions, producing large droplets with typical sizes of $10^2 \sim 10^3\,\mu$m [14, 22–24]. As can be observed in fig. 2.1, breakup events of this type start with a small-scale elevation of the water surface, which then undergoes nonlinear evolution into a 'micro sail', further inflating into a bag featuring a liquid film bordered by a thicker rim. Finally, the bag film blows up producing hundreds of spray droplets, followed by the breakup of

the bordering rim [23]. Despite complicating factors including irregular shapes of the canopy bag and the nonuniform distribution of bag thickness [22], the evolution patterns of the perturbation structure after the formation of the 'micro sail' closely resemble that of droplet bag breakup. The latter also features a late-time expansion into thin films surrounded by a thick rim, both of which eventually break up to form fragments.

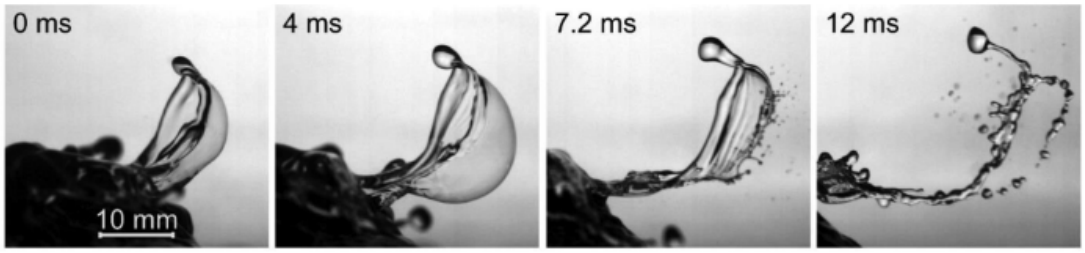

Figure 2.1: Experimental photographs showing bag formation from the initial perturbation (up to $t = 4$ms) and its subsequent breakup ($t > 4$ms) at the air-water interface, with a equivalent 10-m wind speed $U_{10} = 25\,\mathrm{m\,s^{-1}}$. Adapted from Ref. [22] with permission.

2.1.1 Dimensional analysis

The configuration of droplet aerobreakup is generally set up as follows. An initially quiescent droplet with density ρ_l, viscosity μ_l, diameter d_0 and surface tension σ is placed in an ambient gas flow with density ρ_a, viscosity μ_a and uniform incoming velocity U_0 [25]. Based on the aforementioned physical properties, four non-dimensional controlling parameters can be proposed using Buckingham's Pi Theorem (see e.g. Table 1 in Ref. [26]):

$$We \equiv \frac{\rho_g U_0^2 d_0}{\sigma}, \quad Oh \equiv \frac{\mu_l}{\sqrt{\rho_l d_0 \sigma}}, \quad \rho^* \equiv \frac{\rho_l}{\rho_g}, \quad \mu^* \equiv \frac{\mu_l}{\mu_g}. \tag{2.1}$$

Among these, We and Oh are respectively the Weber and Ohnesorge numbers quantifying the ratio of inertial to capillary and viscous to capillary forces. ρ^* and μ^* are respectively the density and viscosity ratios of the liquid and gas phases. Alternatively, the Reynolds number $Re \equiv \rho_g U_0 d_0/\mu_a$ is sometimes used in place of Oh.

2.1.2 The bag-breakup regime

Within literature, various secondary atomisation regimes have been identified where the droplet shows different deformation and breakup patterns. The transition thresholds

between these regimes have traditionally been delineated using the Weber number We and Ohnesorge number Oh (see e.g. Figure 2.2) [27–29], although some recent works have shown that the density ratio ρ^* may also play an important role, particularly within the context of combustion sprays under high ambient pressure [29–31]. Oh influences the transition thresholds only when exceeding a critical value of 0.1 [32]; and as We increases, vibrational, bag, multi-mode (bag-stamen), sheet-thinning and catastrophic breakup regimes are observed [26, 33]. Alternatively, based on the governing hydrodynamic instability involved in the process, the aforementioned four breakup regimes are sometimes re-grouped into two major categories: Rayleigh-Taylor piercing (RTP), where a flattened drop is penetrated by one or more unstable Rayleigh-Taylor (RT) waves; and shear-induced entrainment (SIE), where tiny films and filaments are gradually peeled off from the drop periphery due to the Kelvin-Helmholtz (KH) instability [34]. However, despite the extensive amount of related work, the underlying physical mechanisms determining the aerobreakup regime transition are still largely unclear, and the empirical transition correlations proposed so far are often in conflict [27, 34]. This is because secondary atomisation is a complex problem involving large spans of time and length scales, and further complicated by the presence of wake and freestream turbulence [31]. Notably, there is a consensus that the critical Weber number at which bag breakup initiates is $We_c = 11 \pm 2$ when $Oh < 0.1$ [25, 27, 35].

Bag breakup is of specific interest among the identified droplet breakup regimes, as it bears a strong resemblance to certain breakup modes of round liquid jets [36, 37], and dominates the previously mentioned fragmentation of small-scale sea-surface perturbations under extreme wind conditions [14, 23] and bioaerosol generation during violent respiratory activities like coughing and sneezing [38]. Therefore, knowledge of the physical mechanism and fragment statistics associated with the bag-breakup regime can greatly improve the understanding of physical mechanisms underlying diverse fields of application well beyond single drop dynamics.

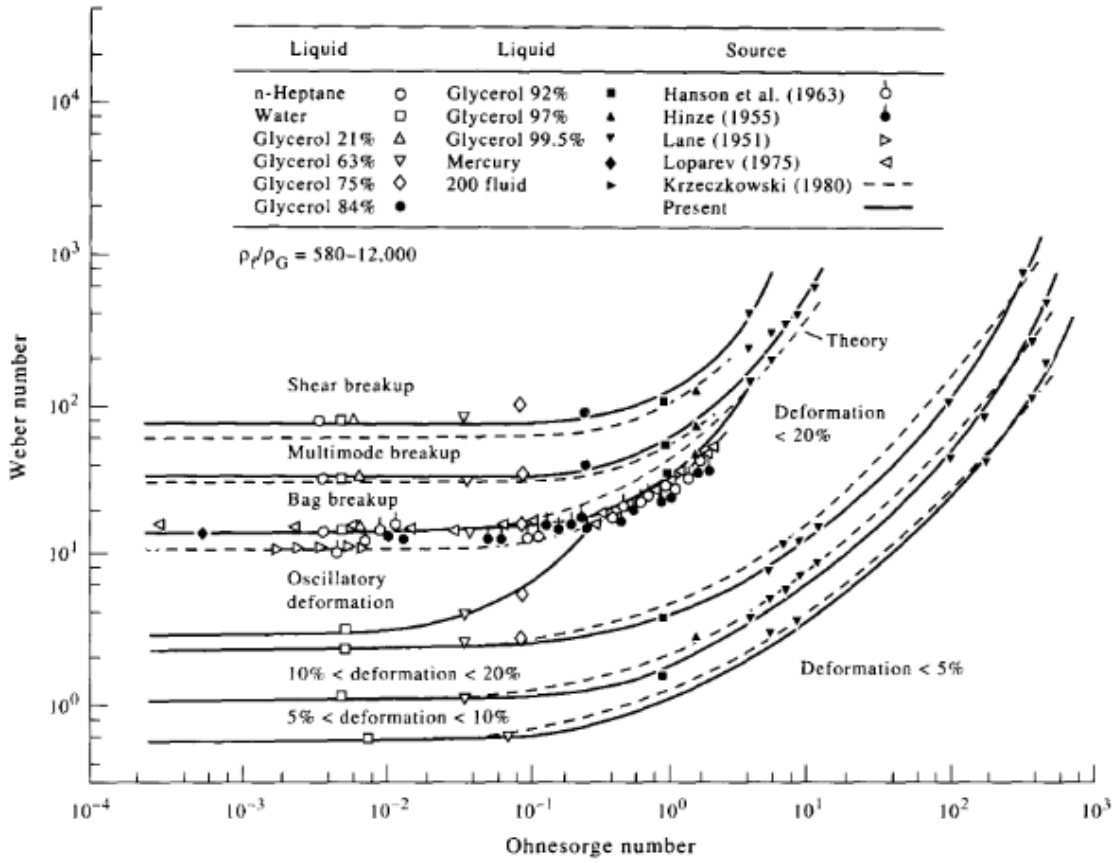

Figure 2.2: Regime diagram for droplet breakup measured from a shocktube with incident shock Mach number $1.08 \leq M \leq 1.31$. For the droplet, $1.15 \leq \rho^* \leq 12000$, $0.0005 \leq Oh \leq 600$, $0.004 \leq We \leq 700$, and $0.03 \leq Re \leq 16000$. Solid and dashed lines indicate empirical correlations demarcating different breakup regimes, whereas scattered dots correspond to individual experimental measurements. As We increases beyond 10, the breakup regime transfers from oscillatory deformation to bag, multimode and shear-induced breakup; whereas small Oh values below 0.1 do not affect the drop breakup behaviour. Reproduced from Ref. [32] with permission.

Droplet deformation

Figure 2.3 shows the morphological evolution of a drop undergoing bag breakup. The initially stationary and spherical droplet is first compressed in the streamwise direction and elongated spanwise, evolving into an oblate disc-like shape while accelerating downstream. For this phase of drop deformation, Ranger and Nicholls [40] proposed a characteristic timescale $t^* \equiv \sqrt{\rho_l/\rho_a}d_0/U_0$, which may be derived from the balance between the air- and liquid-phase stagnation pressure at the windward face of the drop [41]. The deforming drop generally reaches a minimum *global* streamwise thickness around $t = t^*$, which is defined as the end of the first phase of drop deformation [42].

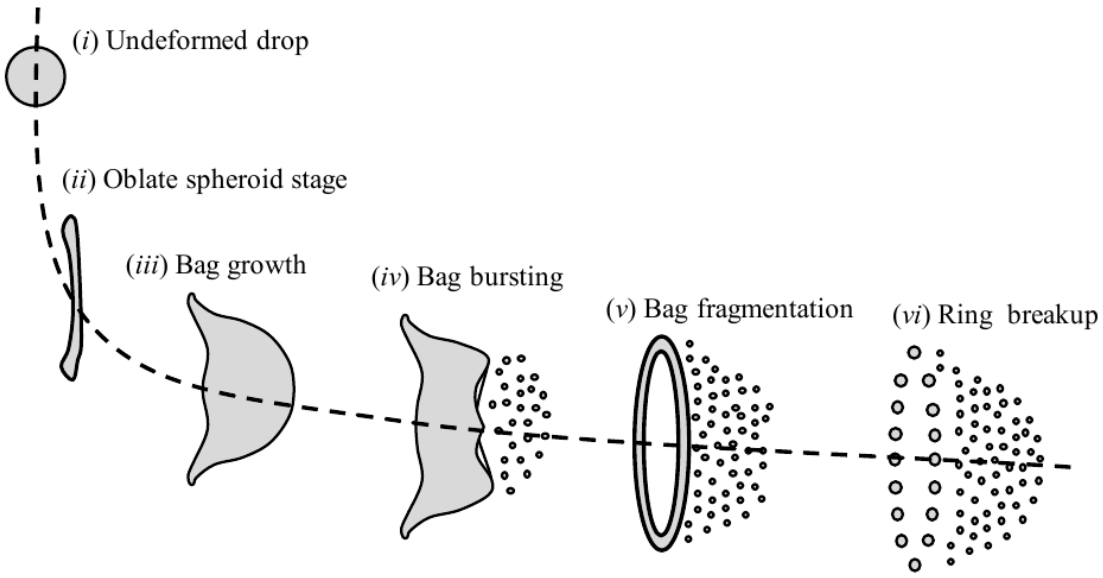

Figure 2.3: Sketch showing different stages of drop deformation during a typical bag-breakup event, reproduced from Ref. [39].

As the droplet becomes fully flattened, it is thicker near the periphery and thinner towards the centre. In the second deformation phase, the disc centre is blown downstream and inflates into a hollow bag attached to a toroidal rim. The prevalent theoretical model ascribes this phenomenon to the influence of the RT instability, which occurs when a corrugated interface separating fluids with different densities is accelerated [43]. It is assumed that the non-uniform local disc thickness provides initial corrugations on the windward surface, which are then susceptible to the RT instability as here the inertial force due to drop acceleration points from the liquid to the gas phase. Based on this assumption, the transition from oscillatory deformation to bag breakup and from bag breakup to multi-mode breakup regimes may be explained using the wavenumber $N_{\mathrm{RT}} \equiv d_{\mathrm{cro}}/\lambda_{\mathrm{max}}$, which is the ratio between the cross-sectional diameter d_{cro} of the flattened droplet and the wavelength of the most unstable RT wave λ_{max} [25, 27, 44], as shown in fig. 2.4. For a semi-infinite plane of inviscid fluid with density ρ_l, bounded by a corrugated interface with surface tension σ and acceleration a_l, the most unstable RT wavelength is given by [45]

$$\lambda_{\mathrm{max}} = 2\pi\sqrt{\frac{3\sigma}{\rho_l a_l}}. \tag{2.2}$$

For a deforming droplet with initial diameter d_0 and cross-sectional diameter d_{cro}, its acceleration a_l can be expressed in terms of its instantaneous drag coefficient C_D as follows,

$$a_l \equiv \frac{F_l}{m_l} = \frac{\pi/8\, C_D \rho_g U_0^2 d_{\text{cro}}^2}{\rho_l d_0^3/6} = \frac{3C_D}{4\rho^*}\frac{d_{\text{cro}}^2}{d_0^3}U_0^2, \tag{2.3}$$

which combined with Eq. 2.2 yields [46],

$$N_{\text{RT}} \equiv \frac{d_{\text{cro}}}{\lambda_{\max}} = \frac{1}{4\pi}\left(\frac{d_{\text{cro}}}{d_0}\right)^2\sqrt{C_D We}. \tag{2.4}$$

Further assumptions are needed to estimate the cross-sectional diameter d_{cro} and the drag coefficient of the drop C_D. For example, Zhao *et al.* [44] adopts the following empirical correlation between d_{cro} and We proposed by Hsiang and Faeth [47],

$$\frac{d_{\text{cro}}}{d_0} = 1 + 0.19\sqrt{We}, \tag{2.5}$$

and the following prescription for C_D proposed by Liu *et al.* [48],

$$\frac{C_D}{C_s} = 1 + 2.632\left[1 - \left(\frac{d_0}{d_{\text{cro}}}\right)^2\right], \tag{2.6}$$

where $C_s \approx 0.4$ is the instantaneous drag coefficient of solid spheres within the droplet Re range of interest. The relationship between N_{RT} and We can then be established as [44],

$$N_{\text{RT}} = \frac{1}{4\pi}(1 + 0.19\sqrt{We})^2\sqrt{0.4We}\sqrt{\left(1 + 2.632\left[1 - \left(1 + 0.19\sqrt{We}\right)^{-2}\right]\right)}. \tag{2.7}$$

Bag, bag-stamen and multi-bag breakup occur when $1/\sqrt{3} \leq N_{\text{RT}} \leq 1$, $1 \leq N_{\text{RT}} \leq 2$ and $2 \leq N_{\text{RT}} \leq 3$, respectively; which agree reasonably well with available experimental and numerical results [44], especially at large density ratios ρ^* [31]. However, this hydrodynamic instability model has difficulty in accounting for the influence of viscous boundary layers at the liquid-gas interface [26], fluid dynamics prior to the formation of the flattened disc, and effects of finite disc thickness and peripheral rim [42].

Alternatively, some works propose the internal flow mechanism which focuses on the influence of liquid-phase flows within the droplet on its deformation patterns [25, 42, 49–51]. These works typically make the following assumptions to develop theoretical models predicting drop deformation:

1. The drop contours remain spheroidal during the first phase of deformation;

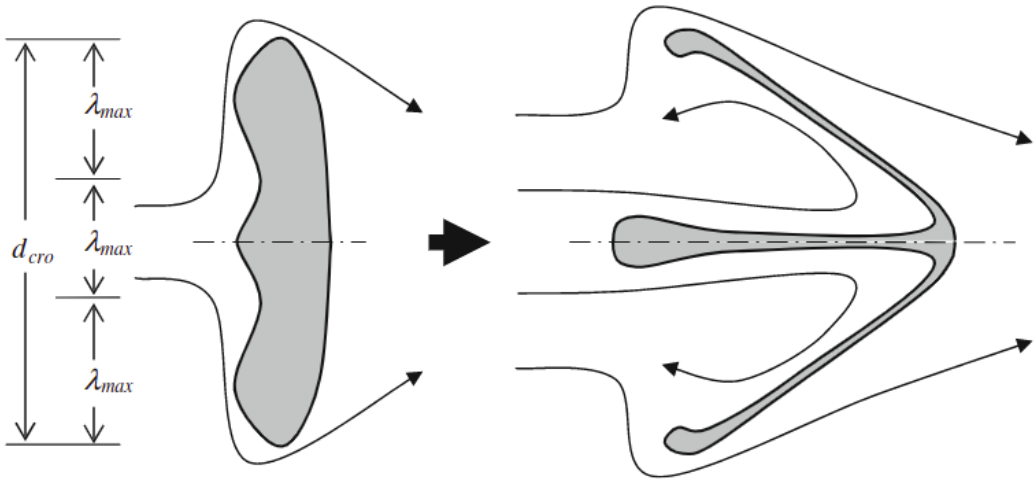

Figure 2.4: Sketch showing the development of RTI perturbations on the frontal surface of the droplet, whose growth causes the droplet to undergo multi-modal breakup. Reproduced from Ref. [25] with permission.

2. The internal flow within the droplet is axisymmetric, inviscid and purely radial;

3. The outer airflow near the windward drop surface is an inviscid stagnation-point flow.

An exception is the recent work of Obenauf *et al.* [50], which modelled the internal flow as a pair of deforming Hill vortices for the multi-bag breakup regime. However, as pointed out by Jackiw and Ashgriz [51], Hill vortices are only observed in droplets during free-fall [52] and have not been reported in aerobreakup events, most likely due to insufficient time for building up internal circulations.

Compared with the RT instability model used to demarcate different global breakup regimes, the internal flow model reveals more detailed information at the early deformation stage. For example, Jackiw and Ashgriz [42] were able to develop the following model describing a constant growth rate of the spanwise diameter R, which agrees well with their experimental observations:

$$\dot{R} = \frac{R_0}{32\tau}\left(a^2 - \frac{128}{We}\right), \tag{2.8}$$

where R_0 is the initial drop radius, $\tau \equiv \sqrt{\rho_l/\rho_g}d_0/U_0$ is the characteristic droplet deformation time [40], and $a \approx 6$ is the air-phase axial stretching rate close the droplet frontal stagnation point. Villermaux and Bossa [49] used the same approach to derive

the following exponential decay law of the streamwise drop thickness h, which also agrees in trend with simulation results reported by Kant *et al.* [38]:

$$h(t) \sim d_0 e^{-\frac{4t}{\tau}}. \tag{2.9}$$

However, this approach is less successful in offering a straightforward explanation of droplet breakup behaviour and involves considerable empiricism (e.g. Ref. [42] assumes $a \approx 6$, which is in fact varying over time). Furthermore, the assumption of inviscid airflow around the droplet fails to account for the complex interaction between the drop surface and separation vortices in the vicinity of the drop [29], which might be responsible for deviations from theoretical models like Eq. (2.8) and Eq. (2.9).

The second phase of drop deformation sees the bag blown out from the centre of the disc, thinning and approaching eventual breakup. While the RT instability model views this phenomenon as the result of RT wave growth on the drop surface and does not predict the bag growth rate, most likely due to the lack of available theories on the late-time development of RT instability, the internal flow model ascribes this to a competition of inertia between the heavier outer region of the disc constituting the bag rim and the lighter inner region forming the bag film [29], and there have been some efforts on predicting theoretically the growth of bag size β based on the balance of momentum at the tip of the bag [42, 49],

$$\ddot{\beta}(t) = \frac{p_0}{\rho_l h(t)}, \tag{2.10}$$

where p_0 is the stagnation air pressure within the bag, and h is the local bag thickness. It has been shown that the stagnation air pressure p_0 dominates other factors such as capillary and viscous effects [42, 53]. In this phase of deformation, the exponential decay law (2.9) is not directly applicable as the drop has significantly deviated from a spheroidal shape. For the sake of simplicity, a few works assume h to be uniform over the entire bag film [42, 49], and further apply conservation of mass for the bag and the rim separately for its calculation [41]. However, as discussed in [51], the fluid within the bag may deplete into the rim and thus violate the assumed mass conservation. Consequently, a comprehensive and physically based model for the thinning of bag films

remains to be developed, where works on film thickness evolution within the context of buoyant surface bubbles might be elucidating [54–56].

Bag rupture and rim dynamics

As the bag gradually expands and thins driven by the fore-aft air pressure difference, it becomes more and more susceptible to film rupture, which typically occurs at a few 'weak spots' near the bag centre where the film is thinnest, triggering expansion of holes on the surface of the bag and eventually causing it to burst into a large number of tiny fragments. Afterwards, the remnant toroidal rim also breaks up forming smaller amounts of larger fragments [25, 41, 42, 57], as shown in the schematic sketch in fig. 2.3 and the experimental photographs in fig. 2.5a.

While there is still intense debate on the exact physical mechanisms responsible for the initial film nucleation within the context of fragmentation phenomena, where various factors such as Marangoni effects [54] and chemical and temperature inhomogeneities [38, 58] might play a role, for the scenario where local acceleration occurs perpendicular to the film, it is argued that RT thickness modulations might arise across the film, eventually causing perforation when the modulation length scale becomes comparable to the film thickness h [38, 42, 49, 53]. As the small film thickness inhibits instability development, RT instability on thin films occurs at a critical wavelength value of [53]

$$k = \frac{\rho a_l h}{2\sigma}, \tag{2.11}$$

rather than the classical wavelength of the RT instability developing between two infinitely thick fluid layers (2.2). This instability features the following growth rate [42]

$$\omega = \sqrt{\frac{\rho a_l^2 h}{2\sigma}}, \tag{2.12}$$

which, combined with the bag tip acceleration value given by Eq. (2.10) and assumption of mass conservation, was used to predict the bag breakup time t^* by Jackiw and Ashgriz [42]. It is also observed by the same authors [51] that bag rupture initiates when the bag film thickness reduces to the level of $0.1 - 1\,\mu$m, regardless of the specific value of We.

Once holes are formed on the bag film, they will expand and collect liquid from the film into their bordering rims. Driven by surface tension, the retraction velocity

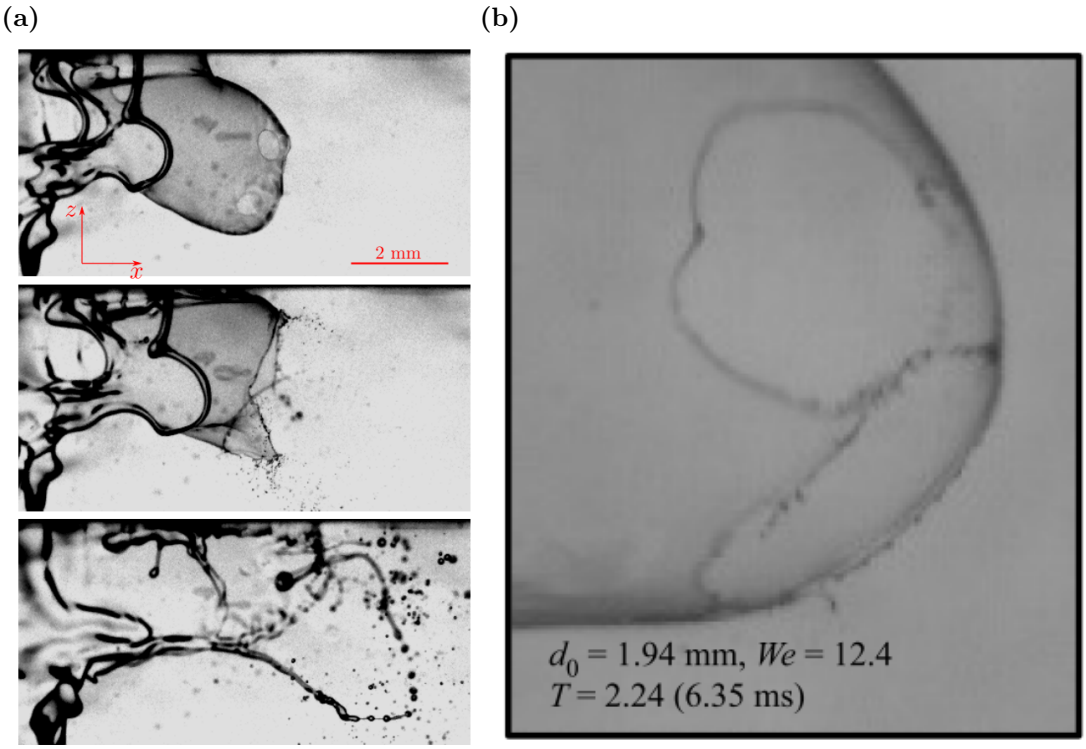

Figure 2.5: Experimental photographs showing the breakup of bags, reproduced from Ref. [38] (a) and Ref. [51] (b) with permission. For (a), the bag originates from a thin liquid film under strong wind forcing, where the film consists of glycerol solutions with viscosity μ_l ranging between 1 and 132 mPa s, while the freestream air-phase velocity is between 10 to 30 m/s. Neighbouring frames are 0.075 ms apart. The top frame shows the perforation of bag films at the location of 'weak spots', followed by the destabilisation of receding hole rims forming many small fragments in the middle frame. The bag rim breaks up to form larger fragments after the bag film is destroyed, as shown in the bottom frame. For (b), the bag is viewed from one side, and the droplet undergoing bag breakup features $We = 12.4$ and $Oh = 0.0027$. Two expanding holes are visible on the bag film, whose bordering rims continue to shed fragments while receding.

of the liquid rims approaches the following Taylor-Culick velocity after an initial transient regime [59],

$$v_{\mathrm{TC}} \equiv \sqrt{\frac{2\sigma}{\rho_l h}}, \tag{2.13}$$

which has been used extensively for indirect measurements of the bag film thickness h [41, 51]. The hole rims recede over a bag film with a finite radius of curvature R, which induces a centripetal acceleration $a_{\mathrm{rr}} = v_{\mathrm{TC}}^2/R$ perpendicular to the bag surface. This makes the rims susceptible to destabilisation, and might account for the fingering phenomena and detachment of tiny fragments as shown in fig. 2.5. There

are a few candidates of hydrodynamic instabilities that might be involved in receding rim destabilisation, for example the RT instability [54] or the Rayleigh-Plateau (RP) instability [51]. The recent experimental results of Jackiw and Ashgriz [51] support the RP instability mechanism, with an important hypothesis that the centripetal acceleration a_{rr} regulates the rim thickness b, in line with the universal Bond-number principle proposed by Wang and Bourouiba [60]:

$$Bo_{\mathrm{rim}} \equiv \frac{\rho_l b^2 a}{\sigma} = 1. \tag{2.14}$$

As there are usually multiple holes generated on the bag surface, the receding rims bordering them eventually collide with each other, as observed in fig. 2.5b [51], and form a web of interconnected liquid ligaments [61]. The collision of two neighbouring rims has been investigated systematically by Néel *et al.* [62] and Agbaglah [63], which will also be reviewed in the following section of this chapter.

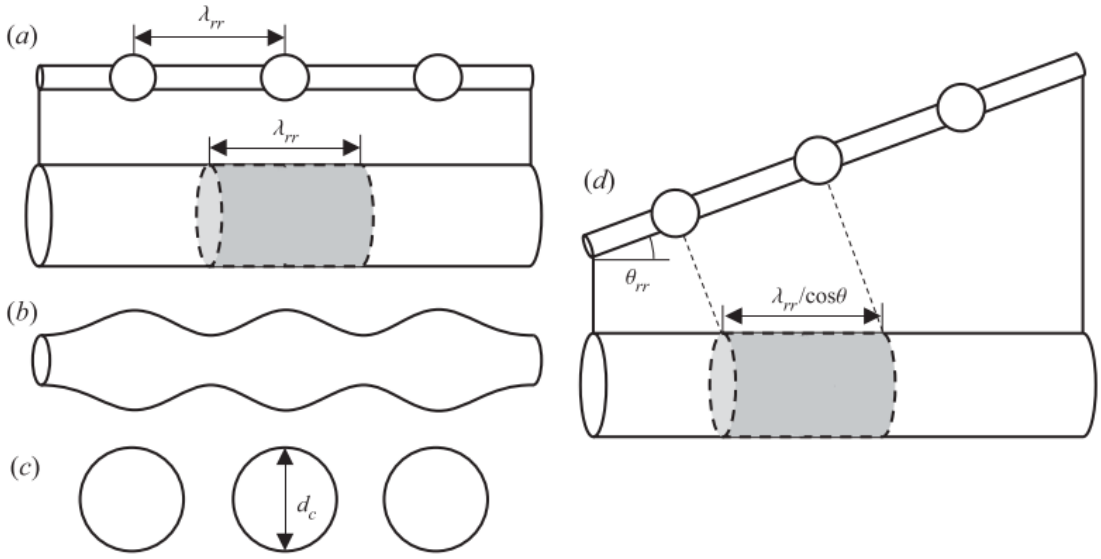

Figure 2.6: (a)-(c): Sketches showing the frontal collision between the receding hole rim and the bag rim. Before collision, the hole rim is perfectly aligned with the bag rim laden with ligaments separated by a distance λ_{rr} (a). The fused liquid rim formed from collision becomes strongly corrugated (b), and subsequently breaks up to form fragments with diameter d_c. (d): Sketch showing the oblique rim collision scenario, where the angle between the receding hole rim and the bag rim is $\theta_{rr} \neq 0$. Adapted from Ref. [51] with permission.

Eventually, the bag film fully disintegrates and the receding hole rims collide with the remnant bag rim, which remains largely intact during the hole expansion stage

due to the possible stabilising effects of the bag, except for the shedding of rim nodes reported in a few experimental studies [35, 44, 51]. The breakup of the remnant rim has traditionally been explained using the RP instability model [42], but this view is challenged by the recent work of Jackiw and Ashgriz [51] which suggests rim breakup is caused by a combination of the RP instability and the impact of the corrugated receding rim and main remnant rim as shown in fig. 2.6(a-c). This uneven impact, which might be further complicated by the nonzero alignment angle θ_{rr} between the two colliding rims as shown in fig. 2.6(d), induces a non-uniformly distributed mass and momentum transfer which causes the remnant rim to break up faster than the prediction of RP instability.

Fragment behaviour and statistics

As is discussed in §2.1.2, the major pathways of fragment generation include destabilisation and collision of receding hole rims, drop shedding from the toroidal rim, and breakup of the remnant rim after the bag completely disintegrates [51]. These mechanisms produce fragments of various shapes, sizes and speeds, which may then collide and merge with each other, or be transported further downstream by the ambient air flow, while undergoing significant interfacial oscillations as they relax towards a spherical shape. As the Weber numbers of the fragments $We_i \equiv \rho_a U^2 \bar{d}_i/\sigma$ (where $\bar{d}_i$ is the equivalent diameter of the fragments assuming a spherical shape) are much smaller than that of the main drop, it is highly unlikely that the fragments will undergo subsequent aerobreakup events.

With mechanisms discussed in §2.1.2 contributing to bag fragmentation at various time and length scales, it is difficult to propose a simple probability density function (pdf) model for fragment size or velocity that delineate each mode of contribution accurately. There have been a few experimental works reporting the size distribution of the drop fragments [38, 49, 65–67], but a consensus with regard to the form of the fragment size pdf has not been reached. Numerical results of aerobreakup fragment statistics remain scarce to date, primarily due to the difficulty in establishing grid convergence when using the Volume-of-Fluid (VOF) interface reconstruction method, with which thin films spontaneously break up as they reach the minimum grid size.

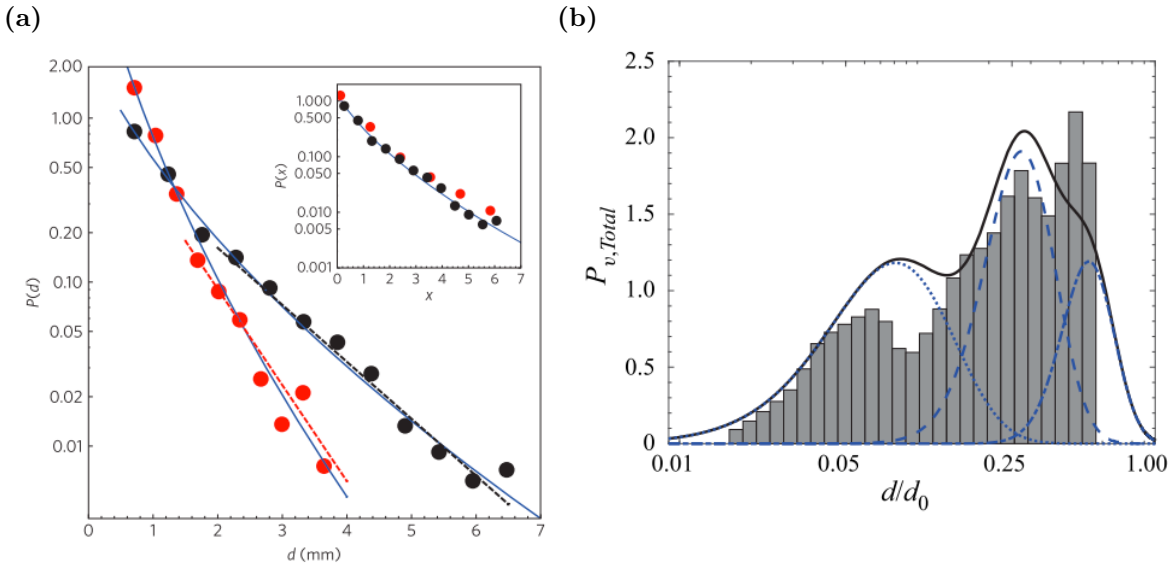

Figure 2.7: Distributions of the bag breakup fragments sizes (a) and volumes (b) as functions of the fragment diameter d, reproduced respectively from Refs. [49] (a) and [64] (b) with permission. The red and black dot in (a) correspond to fragments produced from free-falling water drops with initial diameter $d_0 = 6$mm and 12 mm, respectively. The inset shows that the size distributions can be described by the Marshall-Palmer exponential model $p(x = d/\bar{d}) \approx e^{-x}$ for $x > 1$. The fragment size distribution in (b) are obtained from a droplet undergoing aerobreakup with $d_0 = 3.09$ mm ($We = 12.9$), which is found to feature three distinctive peaks. The contributions from the breakup of the bag film, the bag rim and the rim nodes are shown in blue dotted, dashed and dash-dotted curves, respectively, corresponding to the three peaks in the fragment size distribution. The black solid curve indicates the overall distribution modelled by the summation of contributions from all three breakup modes.

Recently Chirco *et al.* proposed the Manifold Death (MD) algorithm which is capable of artificially perforating thin films as they approach a prescribed critical thickness, allowing for the establishment of grid convergence for fragment statistics [20].

Among the experimental works cited above, the earlier studies of Villermaux and Bossa [49] and Zhao *et al.* [65] find the overall distribution of bag-breakup fragment sizes to follow the Marshall-Palmer exponential distribution as shown in fig. 2.7a. However, Guildenbecher *et al.* [66], Radhakrishna *et al.* [67] and Ade *et al.* [64] show the fragment size distribution function to be multi-modal with distinct maxima, as shown in fig. 2.7b. It is worth noting that the recent works of Jackiw and Ashgriz [51] and Ade *et al.* [64] attempt to construct theoretically the size distribution of aerobreakup fragments by conducting a weighted summation of contributions from various breakup mechanisms discussed in §2.1.2. They reach good agreement with experimental results, albeit with

many empiricisms incorporated in the process. The velocity distribution of aerobreakup fragments sees much less discussion in the literature, with only Guildenbecher *et al.* [66] presenting the results shown in fig. 2.8, where the velocity of bag-breakup fragments shows a large range of scatter, particularly for the smallest fragments. This is ascribed to the influence of the intensified gas-phase turbulence in the wake of the bag [66].

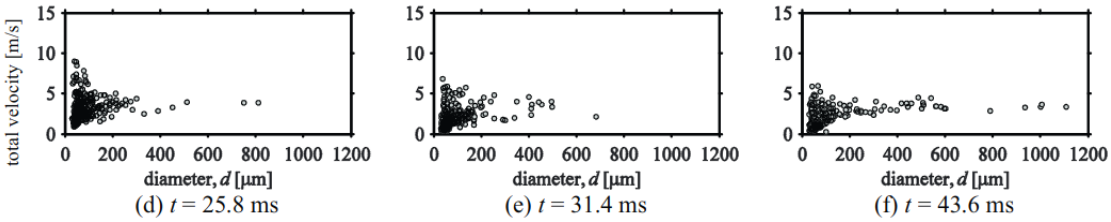

Figure 2.8: Scattered plots showing speeds of individual fragments as functions of their sizes at three different times, recorded for an ethanol droplet with $We = 13.8$ whose bag breakup phase starts at $t = 20$ms. The largest ranges of scatter are observed for the smallest bag breakup fragments. Reproduced from [66] with permission.

Generally speaking, size and velocity distribution data of droplet aerobreakup fragments are still scarce [65]. It is also noted that the influence of Oh on the fragment statistics still remains an open question, as most of the previous works study the aerobreakup phenomena at a given Oh value and do not provide a full picture. The recent work of Kant *et al.* [38] sheds some light on this aspect by showing an abrupt decrease in the mean fragment size D_{10} when the bag Ohnesorge number $Oh_{\text{bag}} \equiv \mu_l/\sqrt{\rho_l \sigma h}$ exceeds 1, although the underlying physical mechanism leading to such a decrease still awaits further investigation.

2.1.3 Effects of gas-phase turbulence

It is noted that most of the works investigating secondary atomisation phenomena feature uniform ambient airflows. However, in recent years there have been a few studies investigating the influence of air-phase turbulence on the drop breakup behaviour [68–71] that reveal more diverse dynamic behaviour and more closely resemble the breakup of sea surface perturbations in turbulent wind conditions [24]. The air-phase turbulence can be characterised by the integral length scale L_0 and velocity fluctuation u_{rms}. Correspondingly, two new controlling parameters arise apart from

those introduced in Eq. (2.1), namely the turbulent Weber number We_{turb} and the non-dimensionalised Hinze scale d_h/d_0,

$$We_{\text{turb}} \equiv \frac{2\rho_a \varepsilon^{2/3} d_0^{5/3}}{\sigma} = \frac{2\rho_a u_{\text{rms}}^2 d_0^{5/3}}{\sigma L_0^{2/3}}, \tag{2.15}$$

$$\frac{d_h}{d_0} \propto \left(\frac{\sigma}{\rho_a}\right)^{3/5} \varepsilon^{-2/5} = We^{-3/5} \left(\frac{u_{\text{rms}}}{U_0}\right)^{-6/5} \left(\frac{L_0}{d_0}\right)^{2/5}, \tag{2.16}$$

where ε is the turbulence dissipation rate per unit volume, which for homogeneous isotropic turbulence (HIT) equals u_{rms}^3/L_0. While the Hinze Scale d_h is an important size threshold in differentiating the turbulence-driven fragmentation behaviour of submerged bubbles [72, 73], its role in the aerobreakup problem where a mean flow exists remains unprobed.

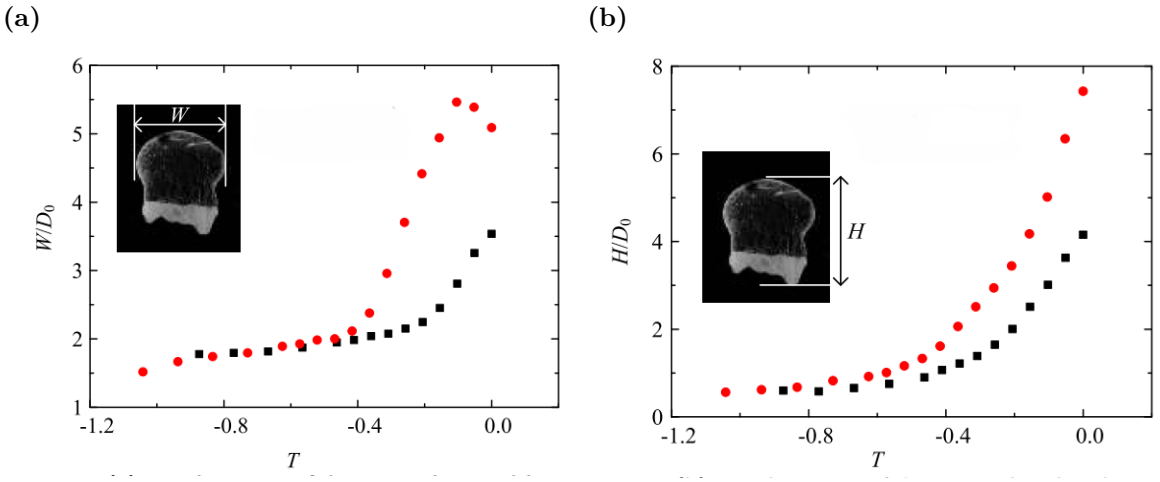

Figure 2.9: The evolution of the width W (a) and height H (b) of droplets undergoing bag breakup in turbulent airflows, adapted from Ref. [69] with permission. Here, turbulent aerobreakup is achieved by releasing droplets with an initial diameter $D_0 = 3.7$ mm into confined turbulent counterflows generated by blowing air through perforated plates with varying solidity. Here, $T \equiv t/\tau = 0$ corresponds to the time when the bag film is perforated. Red and black dots indicate ambient turbulence with intensities $u_{\text{rms}}/U_0 = 0.027$ and 0.237, respectively. The width and the height of the droplet bag are found to increase with ambient turbulence intensity.

In a recent experimental work, Zhao *et al.* [69] observed that droplets deforming in stronger turbulent counterflows tend to feature larger lengths and widths, as shown in fig. 2.9. Figure 2.10 shows the shapes of the bags recorded in their study, which are found to become strongly distorted by the ambient turbulence, which is explained using

an RT instability analysis. Xu *et al.* [70, 71] placed droplets within a shear flow, where they identified two new breakup modes: butterfly and swing breakup. The former occurs at small We values, when the lower part of the droplet first enters the shear layer and is deflected by strong aerodynamic pressure, resulting in a butterfly-shaped bag; while the latter occurs at high We values and involves complex physical mechanisms including surface wave propagation, rim shrinkage and ligament stretching. Transverse RT instability is shown to govern swing breakup, and the log-normal distribution is found to best describe the fragment size distribution over the entire size range. Increasing Oh values impedes aerobreakup by increasing the transverse RT wavelength and the thickness of the deformed drop, leading to the formation of tail bag structures [71].

In the numerical study of Jiao *et al.* [68], which to our knowledge is the only numerical investigation of turbulent aerobreakup phenomena, homogeneous isotropic turbulent (HIT) fluctuations with various integral scales are imposed on uniform inflows. The deformation patterns of the drops interacting with ambient turbulence become highly asymmetric, demonstrating various types of behaviour including turning, rotating or squeezing not observed in laminar aerobreakup studies. The specific deformation patterns depend on the comparison between the droplet radius and the integral length scale L_0 of the gas-phase turbulence.

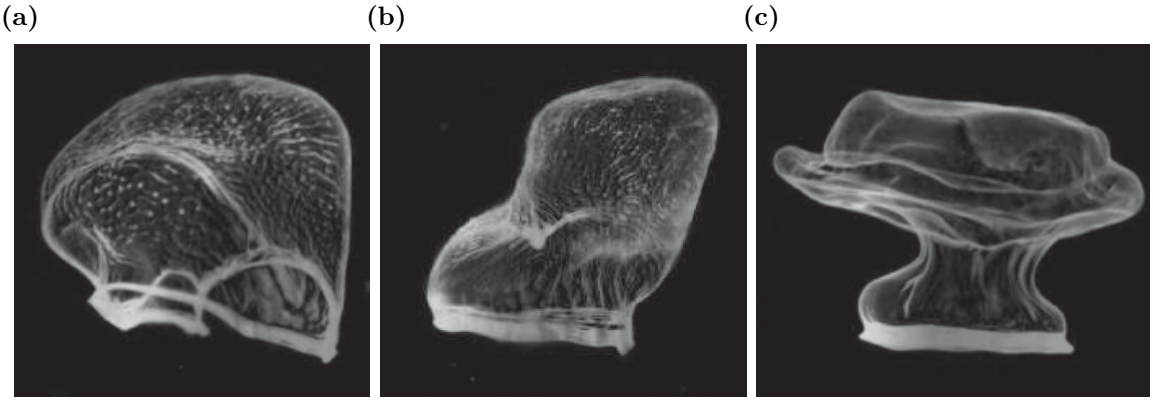

Figure 2.10: Experimental photographs showing bag shapes observed during turbulent bag breakup. Drops in (a) and (b) are photographed for an ambient turbulence intensity $u_{\mathrm{rms}}/U_0 = 0.034$, and are observed to feature relatively subtle distortions, whereas the drop in (c) is photographed for $u_{\mathrm{rms}}/U_0 = 0.061$ and found to feature a more strongly distorted, jellyfish-like shape. Reproduced from Ref. [69] with permission.

The studies reviewed above present valuable information about the general trends and characteristics of turbulent aerobreakup, yet these are qualitative in nature and do not allow for detailed, quantitative analysis of turbulence-droplet interactions. Moreover, few of these works address the influence of turbulence on the development and breakup of bag films, thus little is known about the statistics of fragments generated from turbulent aerobreakup.

2.2 Transverse collision of liquid rims

The generation of splash drops is closely tied to the inertial collapse of breaking waves. As is shown in fig. 2.11, during the lifetime of a deep-water plunging breaker [9], the frontal jet first impacts the sea surface below and produces a decelerated and highly corrugated splash-up. The yet unbroken wave bulk retains its high speed and catches up with the decelerated splash-up afterwards, now separated by a narrow indentation region. The rapid closure of this indentation region leads to the 'secondary splashing' phenomenon, which is characterised by a wall of vertically projected small droplets along the transverse direction. Under the effects of gravity, the secondary splashing phenomena are usually short-lived and succeeded by a prolonged phase of individual splash events, with secondary splash drops produced falling back to the sea surface [17, 74].

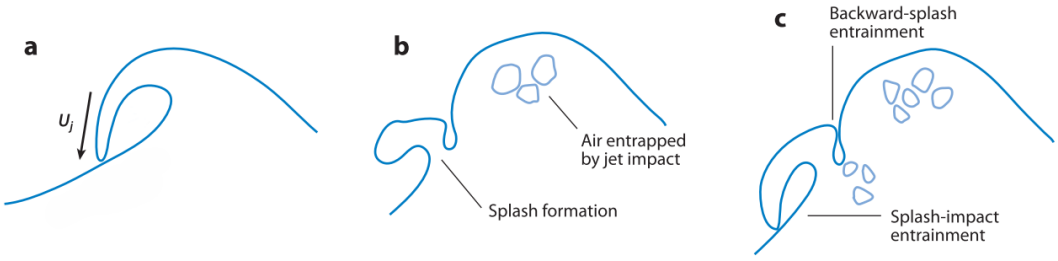

Figure 2.11: Schematic diagrams showing different phases of wave splashing. Following the impact of the overturning wave jet with speed U_j onto the sea surface (a), air is trapped beneath the jet, while a highly corrugated initial splash-up forms at the location of jet impact (b). As the initial splash-up grows, it will connect with the unbroken wave bulk ('backward-splash entrainment') and the sea surface further upstream ('splash-impact entrainment'). Adapted from Kiger and Duncan [9] with permission.

Currently, few works have investigated the generation mechanisms of such secondary splash drops in particular. Taking into account that the early-time evolution of plunging

breakers is largely two-dimensional [17, 75], and neglecting the size difference between the initial splash-up and the wave bulk as a further simplification, the secondary splashing phenomena can then be modelled as the collision between two identical liquid cylinders with initial interface perturbation and under gravitational effects. Liquid rim collision belongs to the larger class of liquid body impact problems, the most familiar example of which is the impact of droplets. The latter is ubiquitous in and significant to natural and industrial processes including soil erosion, airborne pathogen dispersion and material processing [76]. Within the droplet impact literature, the recent experimental works of Wang and Bourouiba [60, 77–80] investigate droplet impact with a solid surface of comparable size, which provide valuable insights into various aspects of droplet collision in the limit of large We. The theoretical analysis of Gordillo *et al.* [81] successfully predicts the evolution of the spreading liquid lamella after drop impact, which is also of great reference value for the present study.

In general, the impact of liquid rims has not received much scholarly attention, although also attested in several transient fragmentation processes, including liquid shell expansion and droplet bag film breakup [51]. To date, the only studies investigating the rim collision include the experimental study of Néel *et al.* [62] and the numerical work of Agbaglah [63]. In these works, the moving rims feature smooth surfaces and originate from holes expanding on thin films at the Taylor-Culick velocity (2.13).

2.2.1 Dimensional analysis

We consider the following scenario where two infinitely long cylindrical liquid rims with diameter d_0, density ρ_l and viscosity μ_l are aligned parallel to each other, and set with uniform initial velocities of opposite signs and the same magnitude U_0. These two rims are placed under a gravitational field g, and surrounded by an inert gas phase with density ρ_g and viscosity μ_g. The surface tension coefficient at the liquid-gas interface is σ. Consequently, five non-dimensional controlling parameters can be proposed,

$$We \equiv \frac{\rho_l (2U_0)^2 d_0}{\sigma}, \quad Oh \equiv \frac{\mu_l}{\sqrt{\rho_l d_0 \sigma}}, \quad Bo \equiv \frac{\rho_l g d_0^2}{\sigma}, \quad \rho^* \equiv \frac{\rho_l}{\rho_g}, \quad \mu^* = \frac{\mu_l}{\mu_g}, \tag{2.17}$$

where the definitions of We, Oh, ρ^* and μ^* are identical with those of Eq. (2.1), the only differences being that for the Weber number We, the liquid-phase density ρ_l and the relative speed between the two cylinders $2U_0$ are used as the characteristic density and velocity scales, since it is the liquid phase bulk flow that drives the evolution of the entire system. Here we note that most of the droplet and rim collision studies have neglected the influence of Bo due to the collision process being extremely fast. In our regime of interest corresponding to secondary wave splashing, the value of Bo is estimated to be 100-200, and we therefore expect effects of gravity on the problem to be significant.

2.2.2 Ligament generation and dynamics

Upon coming into contact, the two colliding liquid rims start to merge along the contact line, forming a liquid lamella which keeps expanding in the transverse direction. This lamella expansion process is known to be largely inviscid except close to the bordering rim region on the lamella, where viscous and capillary effects are significant [82]. In the absence of gravity, the inviscid nature of the lamella spreading motion allows self-similar velocity and interface profiles for the lamella, greatly facilitating its prediction [77, 81]. For droplet impact configurations, the maximum spread radius of the bordering rim has seen widespread investigation [83]. Analytical models based on mass and momentum conservation predicting their unsteady motion have also reached excellent agreement with experimental results [81].

As for liquid rim collision, according to the experimental work of Néel *et al.* [62], there exists a critical collision Weber number $We_c = 66$ that determines the subsequent evolution of the bordering rim. For $We \leq We_c$, the bordering rim remains largely smooth, and lamella expansion will eventually be curbed by capillary effects. The fused liquid bulk may undergo multiple oscillation periods and eventually pinch off to form a number of fragments with different sizes, as is also reported by Agbaglah [63]. On the other hand, for $We \geq We_c$, the rim will develop transverse indentations which give rise to regularly-spaced ligaments, whose formation is attributed to the RT instability developing on the decelerating bordering rim by Néel *et al.* [62], and to the combined effect of RT and RP instabilities by Liu *et al* [84]. For our study where rim collision is

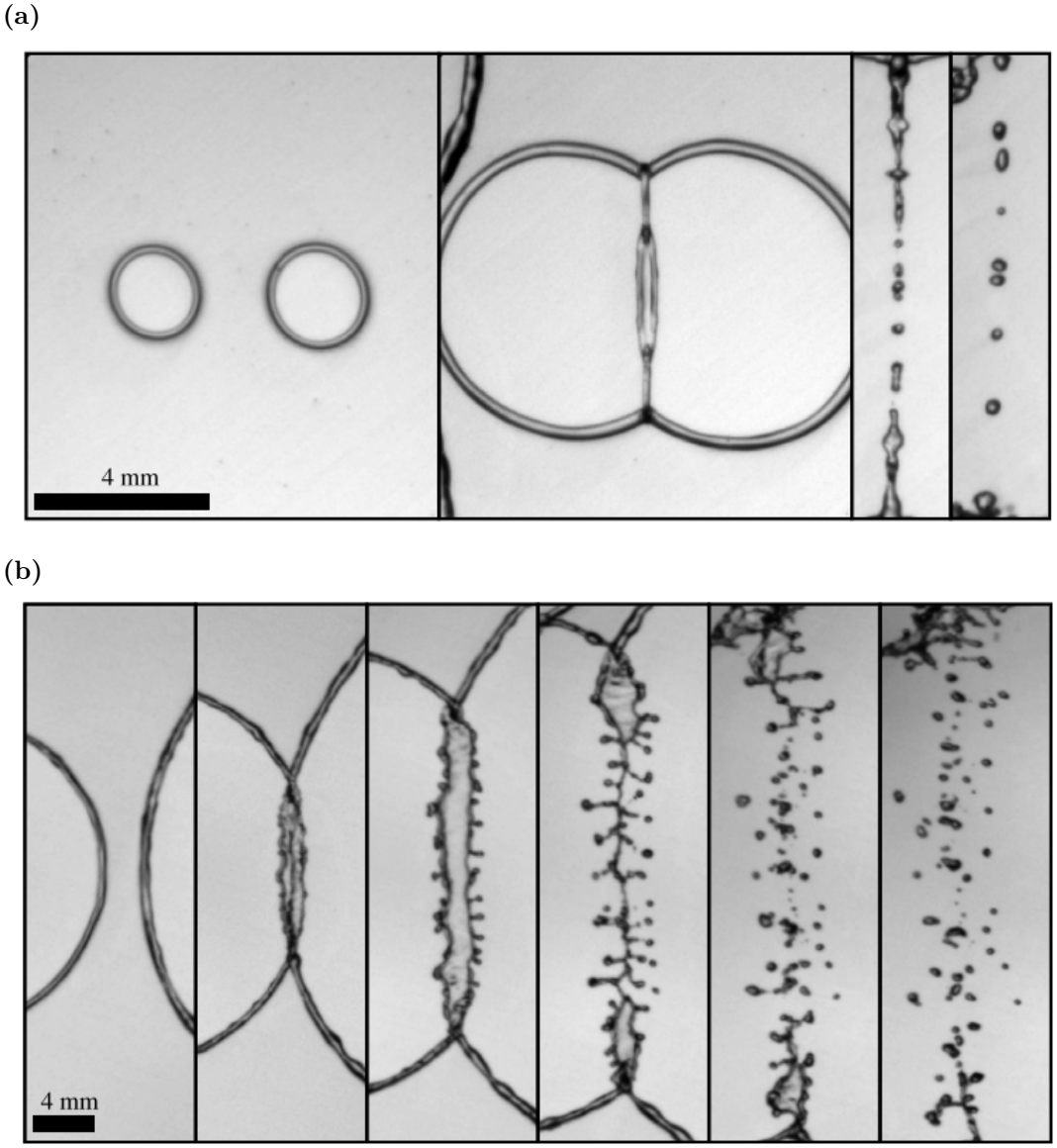

Figure 2.12: Experimental photographs showing the breakup of colliding hole rims at impact Weber number $We = 51$ (a) and 120 (b), reproduced from Ref. [62] with permission. Neighbouring frames are separated by 1 ms. A laminar circular jet impacts a small flat surface to form a horizontal thin Savart sheet. This liquid sheet is subsequently perforated by two simultaneous sparks from a pair of electrodes. The holes formed then expand and eventually merge with one another, forming a fused lamella where they initially contact. The fused lamella in the middle frame of (a) forms a transverse splash, but its development is curbed by capillary force. The lamella undergoes multiple periods of oscillation while thinning and breaks up into a series of primary and secondary drops. The lamella in (b) features a sufficiently high We so that ligaments develop on its edge, which pinch off to form many 'fine drops'.

used to model wave splashing phenomena, the collision Weber number We is estimated to be 200-300 based on available studies investigating wave breaking [17, 74, 85]; thus the latter high-We regime featuring ligament growth and pinch-off will be of major interest.

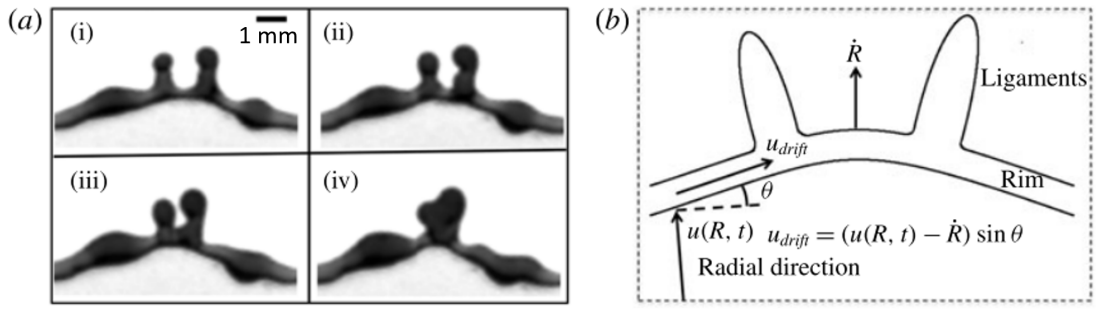

Figure 2.13: Experimental photograph (a) and schematic diagram (b) showing the ligament merging behaviour, adapted from Ref. [78] with permission. Neighbouring frames in (a) are separated by 0.25 ms. Two ligaments are observed on the edge of a thin lamella sheet generated from the impact of a drop with diameters $d_0 = 4.33$ mm with a small flat surface. These ligaments are found to approach and merge with one another, producing a thicker ligament. The schematic in (b) suggests that the ligaments merge because the rim is not perfectly perpendicular to the radial liquid influx from the lamella sheet into the rim. Here, the rim expands at speed $\dot{R}$, slower than the local liquid outgoing velocity $u(R, t)$ within the lamella sheet. The tangential component of the velocity difference $(u(R, t) - \dot{R}) \sin\theta$ gives the drifting speed of rim ligaments.

The presence of liquid ligaments on top of a corrugated bordering rim ('cusps') is reported by Kim *et al.* [86], Wang and Bourouiba [78] and Gordillo *et al.* [87]. Kim *et al.* [86] observed that the average spacing between neighbouring ligaments decreases with increasing initial impact speed, and ligaments may migrate in the transverse direction. Wang *et al.* [78] ascribed the transverse migration to the tangential component of liquid inflow from the lamella into the liquid rim, which gives rise to thicker and more corrugated ligaments. Gordillo [87] found that the rim corrugation slope $\theta \approx 26.6°$ remains constant, which is explained based on an argument of momentum balance at the rim position. However, while the structure and flow field associated with individual Worthington jets have been well studied [88–90], to our knowledge no existing study has investigated the detailed generation and migration dynamics of such ligaments, which is key to understanding the rim splashing behaviour.

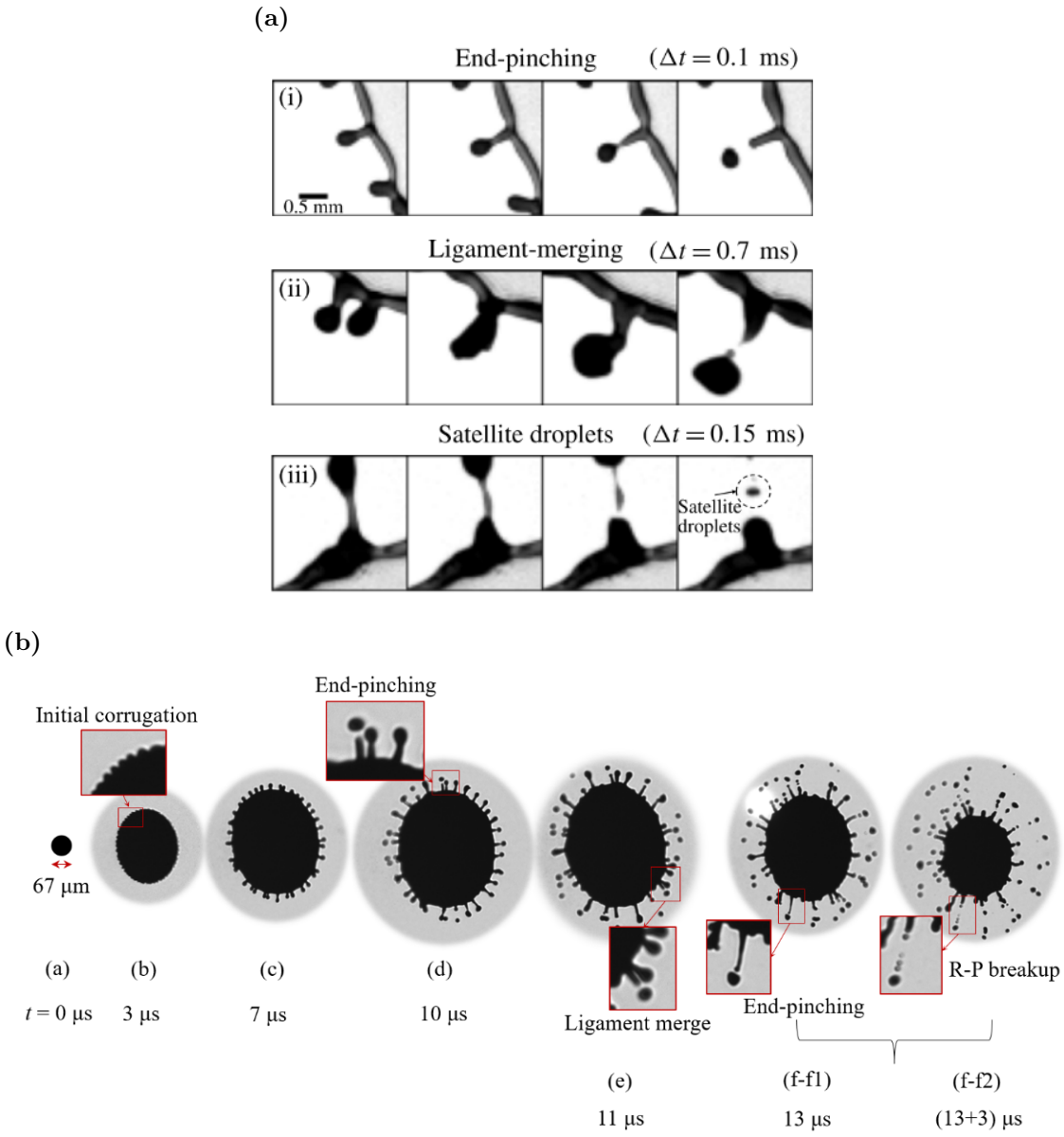

Figure 2.14: Experimental photographs showing the fragmentation mechanisms associated with droplet collision, reproduced from Ref. [78] (a) and Ref. [84] (b) with permission. Ref. [78] reports three types of droplet formation mechanisms as shown in (a). Namely, individual ligaments may pinch off at their ends forming one drop at a time (i), and two ligaments may merge and produce one large droplet at their end via end-pinching (ii), as the fused ligaments become sufficiently corrugated. End-pinching may also generate small satellite drops (iii) if the necking region is very long. Ref. [84] reports the same three drop formation mechanisms found in (a), but also argues that the rim ligaments may undergo R-P instability to produce multiple drops when they grow long enough.

2.2.3 Fragment behaviour and statistics

As the liquid ligaments continue to elongate, their free ends are decelerated by capillary force. This deceleration causes capillary waves to travel downstream towards the ligament bases [91], while fluid parcels elsewhere within the ligaments undergo ballistic acceleration [88]. A rounded tip takes shape, adjacent to a thin 'neck' region where the liquid is continuously depleted under pressure-induced suction effects. A finite-time singularity occurs as the neck radius approaches zero [92], causing the rounded tip to detach from its parent ligament and form secondary droplets, which is known as the 'end-pinching' mechanism for droplet formation. The first such end-pinching event during the lifetime of a ligament, together with the size and velocity characteristics of the first droplet, has seen thorough investigation in recent years within the context of Worthington jets produced from bursting surface bubbles [90, 91, 93, 94]. In droplet collision configurations, ligaments tend to elongate and pinch off repeatedly to form multiple droplets. Extremely thin necks may pinch off at both ends before they could retract into the ligament base, forming much smaller fragments termed 'satellite drops', as is shown in fig. 2.14a reproduced from Wang and Bourouiba [60]. These phenomena are much less investigated compared with those associated with the first droplets, with Berny *et al.* [95] showing the sensitivity of the formation of satellite drops to initial perturbations within the two-phase system. We also point out that, while Wang and Bourouiba [78] rules out the possibility of RP instability contributing to ligament breakup based on limited ligament length and mismatch in predicted fragment sizes, the more recent work of Liu *et al.* reported long ligaments breaking up and forming multiple primary droplets under the RP instability, as shown in fig. 2.14b. This is most likely due to the difference in the impact Weber numbers of the two studies [84].

Since ligament dynamics are crucial to fragment production in rim and droplet collision problems, the overall fragment size distributions can then be viewed as a superposition of the respective size distributions of fragments produced from individual ligaments and those of the ligaments themselves [62]. The size distributions of fragments arising from ligament breakup are skewed towards large fragment sizes, which are

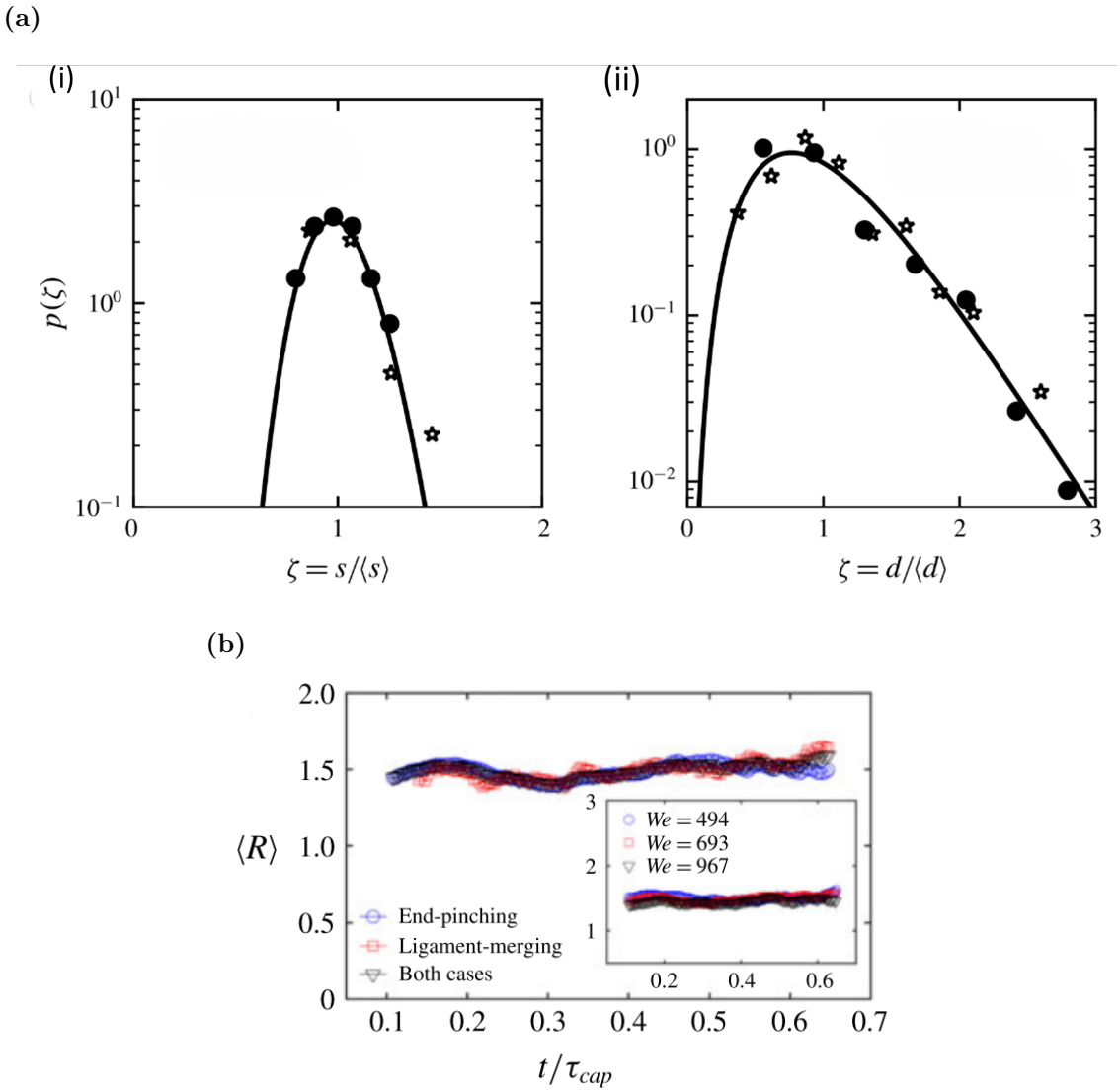

Figure 2.15: (a): Normalised probability density functions of ligament widths s (i) and fragment diameter d (ii) measured at $We = 193$ for hole rim collision. Solid lines represent Gamma functions fitted to the size distributions. For (ii), solid circles and hollow stars indicate measurements before and after fragmentation, whereas for (ii), the same symbols correspond to drops whose origin cannot be specified, and those produced from ligaments measured for (i). Adapted from Ref. [62] with permission. (b): The evolution of the ensemble-averaged ratio $\langle R \rangle$ between the diameters of drops and the widths of their parent ligaments. Time is non-dimensionalised by the capillary timescale of the impacting drop $\tau_{\text{cap}} \equiv \sqrt{\rho_l d_0^3 / 6\sigma}$. In the main plot, blue circles and red squares indicate measurements for drops produced from end-pinching or merging of ligaments, respectively, whereas the balck trangle indicates the average of these two scenarios. In the inset, blue circles, red squares and black trangles correspond to measurements for all fragments produced at $We = 494$, 693, and 967, respectively. Reproduced from Ref. [78] with permission.

typically modelled with a Gamma distribution [8, 96–98]. Moreover, under the end-pinching mechanism, the ratio between the fragments and the widths of their parent ligaments remains a fixed constant which only depends on the ligament stretching rate [93], which for the droplet collision configuration is close to 1.5 across a wide range of We [78]. It is therefore expected that the overall fragment size distributions associated with rim and droplet collision are also skewed in shape. It has also been found that increasing We causes the fragment size distributions to broaden [62, 78]. However, despite the seemingly simple explanation presented above, it remains difficult to propose theoretical models for fragment size distributions, due to the presence of multiple types of fragments produced and the unsteady nature of the collision process [78], reflected in evolving ligament size distributions and total numbers over time which are not yet well modelled themselves, as discussed above. This transient nature of liquid fragmentation is particularly important to consider in the current work, since the wave splash-up may not have time to fully flatten and produce all splash drops before it is destroyed by gravitational pulling. It is also noted that size distributions of droplets produced from breaking surface waves have been presented as different power-law regimes with abrupt breaks in the exponents [17, 74], which is also considerably different from the Gamma functions traditionally used to represent those produced from ligament breakup and droplet/rim collision; bridging these two scenarios thus remains a major challenge for the present work.

Wang and Bourouiba [78] also showed the fragment velocity distributions to be double-peaked, as in fig. 2.16. Since the ejection speeds of fragments are independent of the mode of ejection and the instantaneous fragment velocity distributions are Gaussian, they ascribed the double-peaked shape of fragment velocity distributions to unsteady effects associated with lamella expansion. The population mean speed of droplets at a given time is also identical to that of the ligament tips one necking time prior, which is confirmed by Liu *et al.* [84]. It is also known that the fragment ejection velocity decays over time at a rate slower than that of the bordering rim lying at the base of liquid ligaments [84]. Nonetheless, accurate prediction of fragment velocity distributions remains challenging, even though end-pinching is the dominant

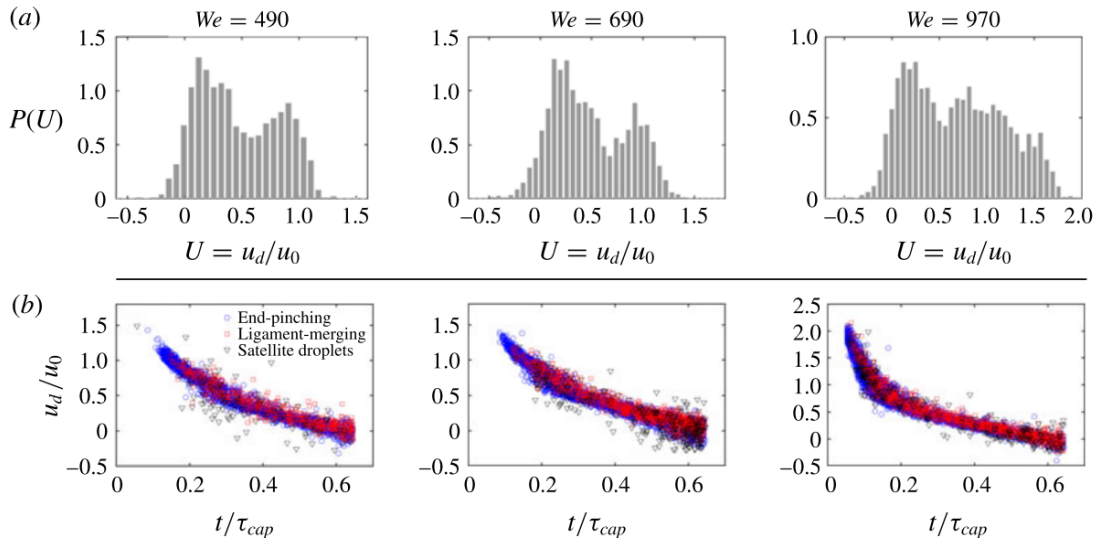

Figure 2.16: (a): Probability density functions of fragment speed recorded for droplet impact configurations with We = 490, 690 and 970, where the fragment speed u_d is non-dimensionalised by the initial droplet impact speed u. All three distributions are found to be multimodal. (b): Scattered plot showing the decay of fragment speed over time for the same three We values as (a), where blue, red and black colours indicate the origin of fragments: ligament end-pinching, merging or satellite drop formation, respectively. Reproduced from Ref. [78] with permission.

droplet generation mechanism for droplet collision [78], and analytical models based on mass and momentum conservation exist for describing the motions of both the bordering rim [81] and the ligaments [91]. This is because ligaments feature different lengths, meaning that individual droplets produced from end-pinching feature different initial speeds as their constituent fluid parcels are transported through the ligaments under ballistic acceleration.

2.3 Summaries

Currently available studies on the aerobreakup phenomenon span over the entire duration of droplet fragmentation. However, fragment size and velocity statistics remain scarce; and the governing mechanisms of bag film fragmentation, especially those leading to the formation of film holes, are still under intense debate. Furthermore, existing models of fragment size distributions rely heavily on empirical prescriptions obtained from idealised experimental conditions, and may not be directly applicable to spume drop generation with turbulent ambient flows. The numerical modelling of

droplet aerobreakup has largely been limited to axisymmetric configurations due to the extremely high cost of three-dimensional DNS. Where three-dimensional DNS studies are conducted, they are handicapped by the spurious breakup of thin bag films which prevents the fragment size distributions from reaching grid independence. In view of these limitations, we first establish grid convergence of film fragment statistics in §4, and analyse film fragmentation mechanisms establishing such statistics. §5 further quantifies how the bag morphology is modified by the ambient turbulence. With grid convergence achieved and effects of ambient turbulence clarified, these results allow for obtaining fully grid converged bag breakup fragment statistics, which are essential for developing SSGFs corresponding to ocean spume drops.

Very few studies have focused specifically on the transverse collision of liquid rims apart from Refs. [62] and [63], which investigate the merging of hole rims expanding on thin liquid films and provide an overview of the behaviour of the fused liquid lamellae following rim impact. However, hole rims are largely smooth and therefore differ significantly from the highly corrugated shape of the wave splash-up, the precursor to ocean splash drops. This initial corrugation will very likely modify the development of the liquid lamellae and the subsequent ejection of splash drops, which is not covered in the theoretical analysis of Ref. [62]. While there exists a large corpus of research works on the droplet impact problem, they have not examined the impact of liquid bulks as models for the wave splashing problem. These droplet impact studies, therefore, focus on impact regimes and physical properties not directly relevant to the current project. Here, we first develop a consistent, quasi-steady theoretical framework for the post-collision development of the liquid lamellae in §6, where the merging and pinch-off of lamella rim ligaments are found to regulate the statistics of the splash fragments. In §7 we extend this analysis to fully unsteady splashing under gravity and derive estimations of SSGFs corresponding to ocean splash drop formation.

3 Methodology

In this chapter, we first introduce the governing equations for our two-phase flow configurations. Afterwards, we provide an overview of the key numerical tools we have employed, namely the open-source numerical solver Basilisk, which we used to run all numerical simulations in this project; the Manifold Death (MD) algorithm proposed by Chirco *et al.*, [20] which is pivotal to our modelling of bag film fragmentation (Chapter 4); and the synthetic turbulence generation method of Xie and Castro [21], which is used for generating turbulent airflow in Chapter 5. While some aspects of these methods are also presented in the methodology sections of Chapters 4-7, here we present them in a more detailed and coherent manner.

3.1 Governing equations

Corresponding to the air-water system, two phases of incompressible fluids with drastically different densities and viscosities are included for both of our prototype flow configurations. We further assume these two phases to be immiscible and isothermal, neglecting mass and heat transfer across the fluid interface. Incompressibility and the absence of inter-phase mass transfer render the fluid velocity field $\boldsymbol{u}$ continuous across the fluid interface, which itself evolves under the dictation of local velocity values [99]. This allows us to describe the fluid motion within the entire simulation domain using

the Navier-Stokes equations written in the variable-density form,

$$\nabla \cdot \boldsymbol{u} = 0, \tag{3.1}$$

$$\frac{\partial \rho}{\partial t} + \nabla \cdot (\rho \boldsymbol{u}) = 0, \tag{3.2}$$

$$\rho \left(\frac{\partial \boldsymbol{u}}{\partial t} + \boldsymbol{u} \cdot \nabla \boldsymbol{u} \right) = -\nabla p + \nabla \cdot \left[\mu (\nabla \boldsymbol{u} + \nabla \boldsymbol{u}^T) \right] + \sigma \kappa \delta_s \boldsymbol{n}. \tag{3.3}$$

Here, Eq. (3.1) arises from the definition of fluid incompressibility, whereas Eqs. (3.2) and (3.3) are respectively the mass and momentum conservation equations. Eq. (3.1) indicates that the density of any particular fluid parcel is constant, although Eq. (3.2) allows the two fluids to have different densities. In Eq. (3.3), p is the fluid pressure, which loses its thermodynamic definition and reduces to the constraint for a divergence-free velocity field under the assumption of flow incompressibility [100]. Surface tension effects are incorporated in the volumetric form $\sigma \kappa \delta_s \boldsymbol{n}$ within Eq. (4.3), where σ is the surface-tension coefficient, and κ and $\boldsymbol{n}$ are respectively the local interface curvature and normal vector. The Dirac delta δ_s is non-zero only on the fluid interface, indicating the singular nature of the concentration of surface tension effects [99–101]. It is noted that Eq. (3.2) can be replaced by the following advection equation,

$$\frac{\partial f}{\partial t} + \boldsymbol{u} \cdot \nabla f = 0, \tag{3.4}$$

where f is a colour function that distinguishes the liquid and gaseous phases, taking the value of 1 and 0 in the former and latter, respectively. This is further coupled to Eq. (3.3) via the density and viscosity values ρ and μ, which are volume-averaged arithmetically across the two phases,

$$\rho = f\rho_l + (1 - f)\rho_g, \tag{3.5}$$

$$\mu = f\mu_l + (1 - f)\mu_g. \tag{3.6}$$

3.2 The Basilisk numerical solver

We use the open-source numerical solver Basilisk to solve the governing equation system (3.1)-(3.4), which is the successor of the Gerris numerical solver developed by the same

authors and has been utilised to solve a variety of partial differential equation (PDE) systems on regular adaptive Cartesian meshes [101, 102].

The geometric volume-of-fluid (VOF) method is applied in Basilisk to solve the interface advection equation (3.4) and minimise the spurious oscillation patterns in the discretised velocity field $\boldsymbol{u}$ [100]. This method incorporates the piecewise linear interface construction (PLIC) framework, which uses disjointed line segments to ensure a sharp interface representation. The local interface normals $\boldsymbol{n}$ are determined directly from the segments stored by the PLIC framework. The interface location, local curvature κ and δ_s in Eq. (3.3) is calculated from the VOF colour function f following Ref. [101].

The momentum equation (3.3) is solved at each discrete timestep as follows. Firstly, an auxiliary velocity field $\boldsymbol{u}^*$ is computed over the *advection step* using the Bell-Colella-Glaz scheme [75, 103]. Afterwards, the *diffusion step* solves a Helmholtz-Poisson-like equation iteratively to yield an estimated velocity field $\boldsymbol{u}_{\mathbf{est}}^{\boldsymbol{n+1}}$. In practice, this step can encounter stiffness issues at large fluid viscosities, although this is not a concern for the present project due to our focus on the small-Oh limit. Lastly, during the *projection step* the estimated velocity field $\boldsymbol{u}_{\mathbf{est}}^{\boldsymbol{n+1}}$ is corrected to satisfy the incompressibility condition (3.1), using the pressure field calculated with the multigrid iterative Poisson solver [104].

A key feature of Basilisk is its implementation of Adaptive Mesh Refinement (AMR), which is especially important to the present project. An adapted mesh allows local variations in size and/or orientation of the grid cells, with the aim of automatically concentrating the computational resources on active changes in local flow features which are usually distributed inhomogeneously within the simulation domain [105], while alleviating them elsewhere. Globally, the application of AMR should either improve the accuracy of the numerical solution without significantly increasing computational costs, or reduce computational efforts without loss in the solution accuracy [104].

As is shown in fig. 3.1, Basilisk employs a quad/octree-based, hierarchical Cartesian mesh structure to accommodate the non-uniform grid resolution associated with the AMR scheme. The nested grid mesh contains multiple coexisting resolution levels within the simulation domain, ranging from zero to a local maximum; and the global maximum resolution $L_{\max}$ is set by the user. Grid cells at different resolution levels

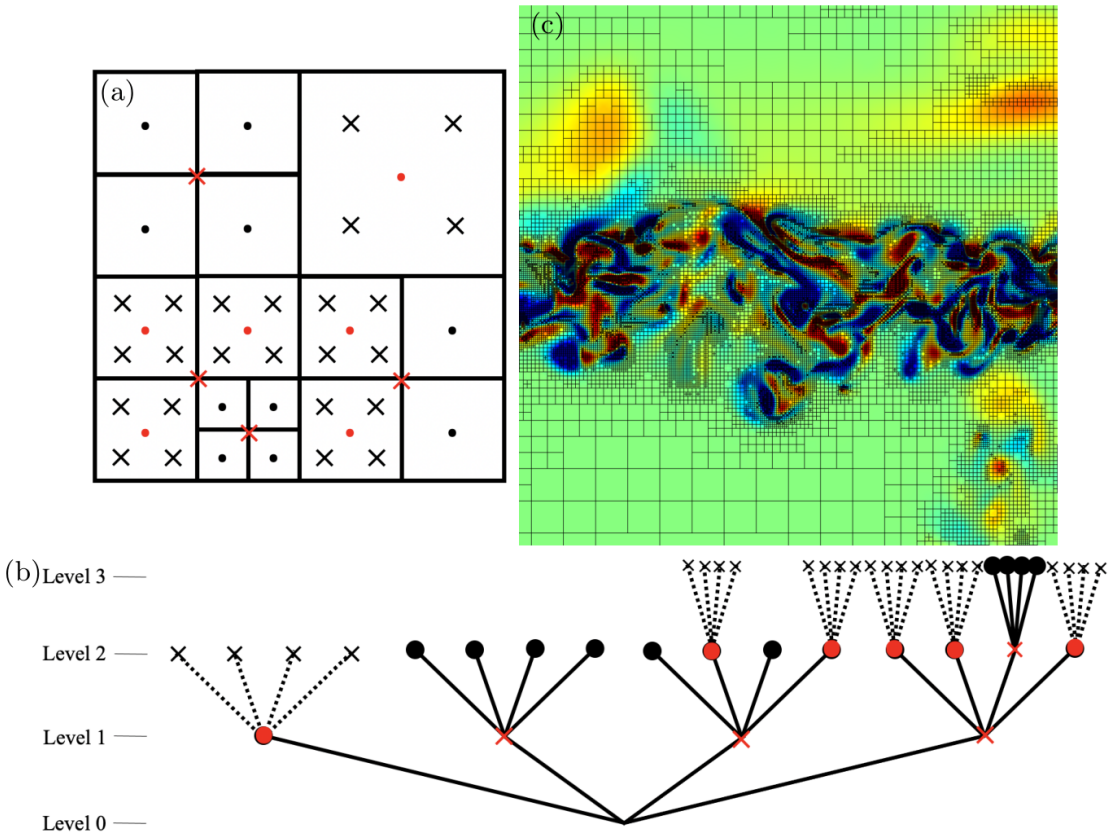

Figure 3.1: (a) Schematic illustration showing the Basilisk adaptive mesh refinement (AMR) grid structure, where black and red dots represent leaf and halo cell centres, respectively. Crosses indicate ghost cell centres. (b) Tree structure corresponding to the grid cells shown in (a), which is organised in different grid resolution levels. (c) Cross-sectional view of a Basilisk breaking wave simulation using the AMR scheme with the octree-based cell structure shown in grids with different sizes. The flow field is coloured based on the local vorticity strength, suggesting that the AMR scheme centres computational resources around the liquid-gas interface with large vorticity amplitudes. Reproduced from Mostert *et al.* [17].

are organised as a quad/octree structure, thus cells at a given location and resolution are the children of those at the next lower level, and the parents of those at the next higher level. Cells without any children are termed leaf cells. The grid size between parent and children cells varies by a factor of two. Spatially neighbouring leaf cells may differ by up to one level. Where they indeed feature different resolution levels, the coarser leaf cells are called halo cells (red dots in fig. 3.1a and b) and assigned children cells (the so-called ghost cells, shown as crosses in fig. 3.1a and b) at the same resolution level as the neighbouring finer leaf cells. The flow variables of interest in the ghost cells are interpolated based on information stored in their parent halo

cells. The introduction of these ghost and halo cells allows Basilisk to define a local regular Cartesian stencil for each cell using matrix-like indexations, which greatly simplifies the formulation of numerical methods and in particular the computing of various gradients and fluxes at the cell boundaries [17, 104].

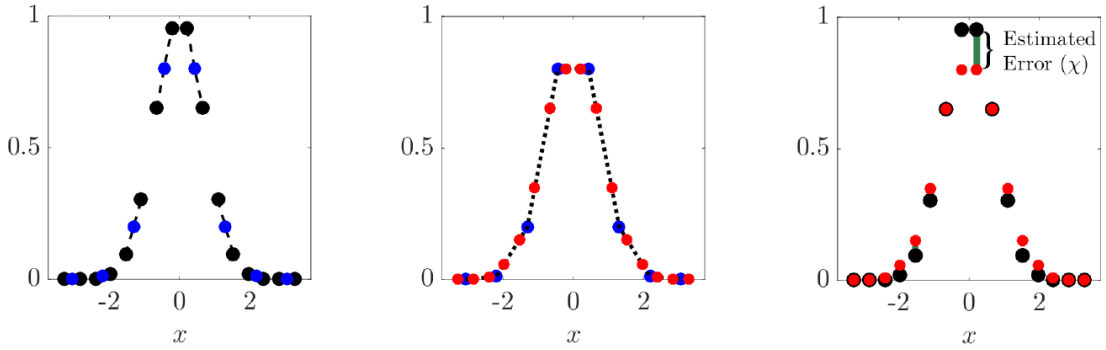

(a) Downsampling (b) Upsampling (c) Error estimation

Figure 3.2: A sketch demonstrating the discretisation error calculation method for a one-dimensional field $f(x)$ employed by the Basilisk AMR scheme. (a): A coarser-level estimation (blue dots) of the discretized solution (black dots) is obtained via the downsampling operation. (b) Based on these coarse-level estimations, the discretized solution at the original finer level can be reconstructed with the upsampling operation, shown in red dots. (c) The difference between the reconstructed (red dots) and original values (black dots) is used to estimate the discretisation error χ at the finer level. Reproduced from Ref. [104].

The refinement and coarsening of grid cells within the AMR scheme are based on a given criterion, which in this project is most commonly selected as the maximum tolerated discretisation errors ε of the VOF colour function f and/or the velocity field $\boldsymbol{u}$ due to the significant evolution of fluid interface over time. At each timestep, local discretisation errors in a given flow variable are estimated using a second-order accurate wavelet-based algorithm. Namely, the finest mesh representation of the variable is locally *downsampled* onto a coarser resolution. This new coarse representation is then re-interpolated (*upsampled*) onto the same grid points as the original fine representation. The absolute difference between the original and re-interpolated sample variables forms an estimate for the local discretization error of the fine representation, as is shown in fig. 3.2. The grid will then refine or coarsen by one level based on whether the local estimated error is greater or smaller than the tolerance criterion ε [17, 106]. The application of AMR indeed improves the efficiency of computational resource

distribution throughout simulation runtime, although the simulation speed is often not linearly dependent on the total amount of grid cells [106].

3.3 The Manifold Death (MD) algorithm

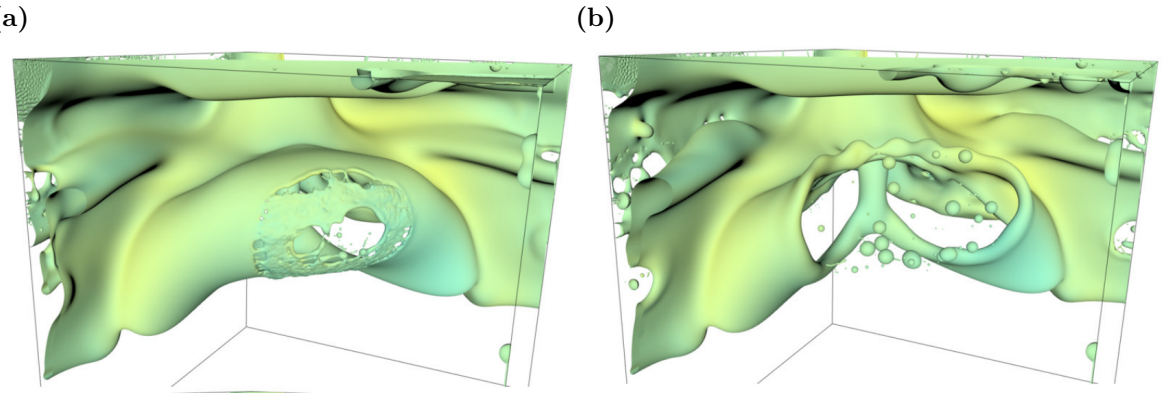

Figure 3.3: Examples from the simulations of phase inversion showing VOF-breakup (a) and controlled MD perforation (b) on a thin film [20]. The green liquid indicates oil with density $\rho_o = 900\,\mathrm{kg}\cdot\mathrm{m}^{-3}$ and viscosity $\mu_0 = 0.01958\,\mathrm{Pa}\cdot\mathrm{s}$, while the uncoloured ambient phase is water with $\rho_w = 1000\,\mathrm{kg}\cdot\mathrm{m}^{-3}$ and viscosity $\mu_w = \mu_o$. Reproduced from Chirco *et al.* [20].

While the geometrical VOF method incorporated in Basilisk renders sharp interface representations, it also suffers from major drawbacks centred around this singularity at the interface. One of these drawbacks concerns the breakup of thin films. When the VOF method is used to reconstruct the fluid interface, breakup is triggered as the local film thickness decreases to the finest grid size [107], which is characterised by small-scale irregular corrugation patterns and hole formation as shown in fig. 3.3a. Since the film fragmentation process is intrinsically tied to the first perforation events, this causes the initiation time of breakup and the size of the finest fragments to be grid-dependent. Indeed, as noted in a recent study [37], VOF methods tend to generate too many droplets in an intermediate range around the grid size Δ, where the probability density functions (PDFs) of droplet sizes are overestimated. To circumvent this unphysical and numerically uncontrolled phenomenon, we adopt the manifold death (MD) algorithm developed by Chirco *et al.* [20], whose idea is to artificially perforate thin films once their thickness decreases to a critical value independent of the grid size, bearing some resemblance to the breakup of thin films under the Level-Set

interface reconstruction method [37]. As both the perforation rate and the critical thickness are prescribed by the user, this enables us to establish grid convergence of the fragment size distributions and related quantities [20].

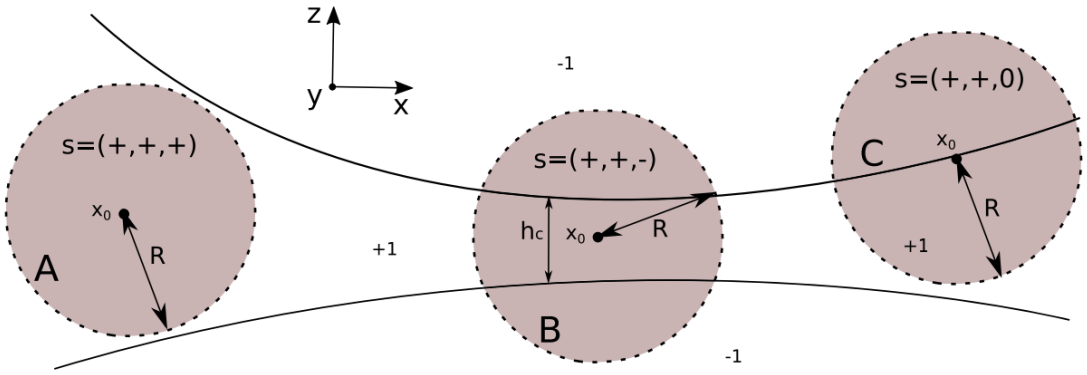

Figure 3.4: Schematic illustration showing the local signs s of the eigenvalues of the quadratic moment T_{ij} at location x_0 on a thin liquid film with a minimum thickness h_c. s are calculated within a sphere with radius R, and the MD algorithm uses them to determine the local two-phase flow geometry.

Reproduced from Chirco *et al.* [20].

The MD algorithm has been implemented in the Basilisk AMR framework by Chirco *et al.* [20], where the authors have validated this algorithm with a variety of flow configurations, including an axisymmetric droplet bag breakup problem. Here, we adapt it to the current project by tuning the controlling parameters L_{sig} and p_{perf} (defined below) to allow for the formation of $O(10)$ holes on the bag film, which is sufficient to prevent spurious bag film breakup in the 3D configuration. We now provide a brief overview of this algorithm as follows, while more detailed discussions are presented in §4.

Grid cells whose resolution equals a prescribed signature level L_{sig} are regularly scanned at a given time interval T_{MD}. Here, the signature level L_{sig} determines the critical film thickness $h_c \equiv 3D/2^{L_{\text{sig}}}$ (D being the simulation domain size), below which liquid films will be subject to artificial perforation by the MD algorithm. For each of these cells, their position $\boldsymbol{x_0}$ is set as the origin of the new coordinate system $O - x'y'z'$, based on which quadratic moments T_{ij} of the symmetric indicator function $\phi \equiv 2f - 1$ are computed,

$$T_{ij} = \int_V x'_i x'_j \phi(\boldsymbol{x'}) d\boldsymbol{x'}. \tag{3.7}$$

Compatible with the Cartesian stencil structure of Basilisk AMR mesh grids, the integration domain V for (3.7) is selected as a cube centred at $\boldsymbol{x_0}$ with a size of $5D/2^{L_{\text{sig}}}$. The signs of the eigenvalues of the computed quadratic moments T_{ij} indicate the local interface geometry, where a thin film is represented by two positive and one negative eigenvalue. All eligible film cells are recorded, and the algorithm proceeds to randomly create cubic cavities on the film by directly setting the value of f within eligible cells to that of the other phase with a probability p_{perf}. While the total fluid mass is changed, the MD algorithm minimises this breach of mass conservation by creating cavities with minimum sizes that allow for Taylor-Culick expansion, and limiting the maximum number of holes perforated at every iteration. As is shown in fig. 3.3b, the application of the MD algorithm successfully creates expanding holes on thin films before the onset of VOF breakup, and establishes grid convergence for the size distribution of large fragments [20].

It should be noted that while the MD algorithm enables the establishment of grid convergence, its controlling parameters need further tuning in comparison with experimental observations to obtain *physically correct* fragment statistics. This requires a sufficiently high grid resolution level at which thin films can be properly represented. Within the context of droplet aerobreakup, the thickness of bag films immediately before perforation is found to be around 1 μm [41, 51], a thousand times smaller than the initial drop radius. For the current laminar bag breakup configuration employed in §4, resolving a bag film of a thickness equivalent to experimental conditions requires a maximum grid resolution level of 16-17, which is beyond our computational capacities. Further tunings of the MD algorithm for physically correct bag film statistics are therefore reserved for future work.

3.4 The synthetic turbulence generation algorithm

For various types of turbulence simulations, accurately prescribing the incoming turbulent eddies as a function of time is a prerequisite for obtaining physically valid unsteady solutions within the simulation domain. However, setting up turbulent inflow conditions remains challenging. While it is possible to extract turbulent

flow field information from an auxiliary simulation and map this onto the inlet of the main simulation (recycling methods), an alternative approach is to impose coherence constraints on a random number field generated *ad hoc*, or by adding random perturbations to a deterministic coherent field (synthetic turbulence generation methods). The synthetic turbulence generation methods tend to be easier to implement, although their outputs are not solutions of the Navier-Stokes equation system in the strict sense [108].

In order to generate air-phase turbulence for Chapter 5, we implement and validate the synthetic turbulence generation method proposed by Xie and Castro [21] within the numerical framework of Basilisk, the details of which are presented in §5. This method is originally proposed for Large Eddy Simulations (LES) of small-scale urban canopy flows, and has also been used to simulate shock-induced separation bubbles [109] and bluff-body wake flows [110]. Here, we apply this method to the direct numerical simulation of two-phase flows. It is briefly reviewed as follows.

Firstly, at each timestep, a two-dimensional random number matrix R_{ij} with zero mean and unit variance is generated, and then filtered and normalised to produce two-dimensional space-correlated velocity fluctuation matrices ψ_{ij} for each velocity component,

$$\psi_{m,l} = \sum_{j=-N}^{N} \sum_{k=-N}^{N} b_j b_k R_{m+j,\, l+k}, \quad 0 \leq m,\, l \leq N_{\text{grid}}, \tag{3.8}$$

where $N_{\text{grid}} \equiv 2^L$ is determined by the maximum grid level L for resolving turbulence, and the filter size $N = 3L_{\text{La}}/\Delta$ is proportional to the number of grid cells spanned by the turbulence integral length L_{La}. The filter coefficients b_j are prescribed as,

$$b_j = \frac{e^{-\frac{\pi|j|}{2n}}}{\sqrt{\sum_{i=-N}^{N} e^{-\frac{\pi|i|}{n}}}}, \tag{3.9}$$

which ensures that the turbulence velocity correlation function R_{uu} can be approximated as an exponential,

$$\frac{\overline{u_m u_{m+k}}}{\overline{u_m u_m}} = R_{uu}(k\Delta) = e^{-\frac{\pi|k|\Delta}{L_{\text{La}}}}. \tag{3.10}$$

It is noted by Xie and Castro [21] that the behaviour of exponential forms of R_{uu} is not correct at asymptotically small length scales r, rendering a velocity spectrum

that decays like $(1/r)^{-2}$ rather than the correct power law of $(1/r)^{-5/3}$. Nevertheless, the large-scale turbulence behaviour is faithfully captured, which supports our usage of this model in the current project.

Time correlation is imposed between turbulent inlet conditions at successive timesteps by computing the new normalised fluctuating velocity components $\Psi(t)|_{m,l}$ based on those of the previous timestep $\Psi(t-\Delta t)|_{m,l}$ and newly synthesised fluctuation matrices $\psi_{m,l}$,

$$\Psi(t)|_{m,l} = \Psi(t-\Delta t)|_{m,l} e^{-\frac{\pi \Delta t}{4T_{\mathrm{La}}}} + \psi_{m,l}\sqrt{1-e^{-\frac{\pi \Delta t}{2T_{\mathrm{La}}}}}, \quad 0 \leq m,\, l \leq N_{\mathrm{grid}}, \tag{3.11}$$

where $T_{\mathrm{La}} \equiv L_{\mathrm{La}}/U_0$ is the Lagrangian time scale prescribed by users. Since $\psi_{m,l}$ is independent of $\Psi(t-\Delta t)|_{m,l}$, the variance of $\Psi(t)|_{m,l}$ is unity. Afterwards, the new inlet velocity profile is generated as follows:

$$U_{\mathrm{in}}|_{m,l} = U_0 + u_{\mathrm{rms}}^2 \Psi(t)|_{m,l}, \quad 0 \leq m,\, l \leq N_{\mathrm{grid}}, \tag{3.12}$$

where the constant coefficient u_{rms}^2 is a simplification of the Cholesky decomposition of the Reynolds stress tensor [110, 111] for HIT fluctuations. U_{in} is then corrected following Kim *et al.* [111] to ensure constant mass influx, and superimposed at the left boundary of the simulation domain as a time-variant Dirichlet boundary condition. This synthetic turbulence generation method significantly reduces the filter size compared with the earlier Klein's method [112], and therefore the computational overhead spent on it for producing the turbulent inlet profile decreases correspondingly. Note that while (3.12) assumes a uniform mesh at the inlet, it is also compatible with the AMR scheme of Basilisk, where the pointwise inlet velocity value required is interpolated from (3.12).

4

Droplet Bag Breakup in Uniform Airflows

Reproduced entirely from a published journal article: Tang, K., Adcock, T. A. A., & Mostert, W. (2023). Bag film breakup of droplets in uniform airflows. *Journal of Fluid Mechanics*, 970, A9.

4.1 Introduction

Liquid atomisation refers to the process where a bulk volume of liquid disintegrates into fragments featuring various sizes and shapes [25, 113]. The fragments generated are described as sprays, which are involved in many natural and industrial processes, including ocean-atmosphere interactions [10, 114], precipitation and rain-drop dynamics [10, 49, 115], combustion of liquid propellant in aerospace applications [18], pharmaceutical spray generation [116], and pathogen transmission [19, 38]. It has recently been found that the atomisation of small-scale sea surface perturbations dominates ocean spume generation under extreme wind conditions, producing large droplets with typical sizes of $10^2 \sim 10^3\,\mu$m [14, 23]. In this size range, the currently-available sea-spray generation functions (SSGF), crucial for calculations of air-sea momentum and heat exchange in earth-system modelling, show large range of scatter [10]. However, since the physics governing the fragmentation of bag films have not yet been firmly established, their

influences on SSGFs have been difficult to quantify. Improving this understanding is the primary motivation of the present work.

Two stages of liquid atomisation have been identified within literature, namely the primary and secondary atomisation. Sheets, ligaments and droplets are stripped from a bulk fluid during primary atomisation, which further decompose until stabilising capillary effects take over during secondary atomisation [113]. Secondary atomisation is typically modelled by the droplet aerobreakup problem characterised by the interaction between an initially spherical droplet with density ρ_l, viscosity μ_l and diameter d_0, and an ambient gas flow with density ρ_g, viscosity μ_g and uniform velocity U_0 [25]. Based on these physical properties, together with surface tension σ at the liquid-gas interface, four non-dimensional controlling parameters have been proposed using Buckingham's Pi Theorem (see e.g. Table 1 in Ref. [26]):

$$We \equiv \frac{\rho_g U_0^2 d_0}{\sigma}, \quad Oh \equiv \frac{\mu_l}{\sqrt{\rho_l d_0 \sigma}}, \quad \rho^* \equiv \frac{\rho_l}{\rho_g}, \quad \mu^* \equiv \frac{\mu_l}{\mu_g}. \tag{4.1}$$

Among these, We and Oh are respectively the Weber and Ohnesorge number quantifying the ratio of inertial to capillary and viscous to capillary forces, and ρ^* and μ^* are respectively the density and viscosity ratios of the liquid and gas phase.

Within literature, various droplet aerobreakup regimes have been observed where the droplet shows different deformation patterns, and the transition thresholds between these regimes have traditionally been delineated using We and Oh [27–29], although some recent works have shown that the density ratio ρ^* may also play an important role [29–31]. The aerobreakup regime is controlled by the competition between inertia and capillary effects, as reflected by We, for sufficiently small liquid viscosity μ_l satisfying $Oh < 0.1$ [32]. As We increases, the breakup becomes more violent and vibrational, bag, multi-mode (bag-stamen), sheet-thinning and catastrophic breakup regimes are observed in succession [26, 33]. Alternatively, based on the governing hydrodynamic instability involved in the process, the four breakup regimes mentioned above can be re-grouped into two major categories: Rayleigh-Taylor piercing (RTP) and shear-induced entrainment (SIE) [34]. However, despite the extensive amount of related work, the underlying physics governing the transient drop deformation in each regime are still

largely unclear. Furthermore, the empirical transition criteria proposed so far are often contradictory [27, 34], with the notable exception of a consensus that the critical Weber number beyond which bag breakup initiates is $We_c = 11 \pm 2$ when $Oh < 0.1$ [25, 27].

In the bag breakup regime, the initially spherical droplet first flattens and forms a disc, whose centre is then blown downstream and inflates into a hollow bag attached to a toroidal rim. The time it takes for the drop to reach breakup Δt_d typically falls within the range of $\tau \leq \Delta t_d \leq 2\tau$, where $\tau \equiv \sqrt{\rho^*} d_0/U_0$ is the characteristic deformation time proposed by Nicholls and Ranger [40]. The swollen bag first ruptures near its centre, triggering expansion of holes on the surface of the bag and eventually bursting into a large number of fragments, which is then followed by the breakup of the remnant toroidal rim into smaller amounts of fragments [25, 41, 117]. Droplet bag breakup and its associated fragment size and velocity distribution functions are of specific interest as they bear a strong resemblance to the previously mentioned bag-mediated fragmentation of small-scale sea-surface perturbations under extreme wind conditions [14, 23].

Droplet aerobreakup involves a complex interplay of aerodynamic, capillary and viscous effects that is still poorly understood [118]. The prevalent theoretical understanding is that hydrodynamic instabilities, particularly Kelvin-Helmholtz (KH) and Rayleigh-Taylor (RT) instability, play an important role in the aerobreakup process [25, 34, 42, 119]. KH instability occurs at the interface between two different streams of fluid with different velocities and densities [120]. In the context of large-We droplet aerobreakup, it governs the SIE breakup category [34], and is typically found near the drop periphery where the relative velocity between the liquid and gas phases is the largest [26, 121]. However, due to strong capillary effects, KH instability is unable to influence droplet deformation in the bag breakup regime [26, 119]. RT instability occurs when a corrugated interface separating fluids with different densities undergoes constant acceleration [43], and is hypothesised to cause interfacial perturbation growth on the windward surface of the droplet. The wave number of such perturbations determines whether the droplet undergoes oscillatory deformation, bag breakup or multi-mode breakup [27]. However, instability theories have difficulty in accounting for the viscous effects [26], flow dynamics prior to drop flattening, and finite thickness and peripheral

boundary of the flattened disc [42]. Alternatively, some works highlight the influence of the internal flow within the droplets on the deformation process [25, 42, 49, 50, 122]. The internal flow model compensates for the drawback of the RT instability model in predicting early-time drop deformation; however, this approach is somewhat simplified and cannot account for the complex interaction between wake vortices and drop surface [29]. The late-time breakup behaviour, however, is delineated into a bag-film rupturing event, and the fragmentation of the remnant rim at a later time. The bag film rupture occurs more rapidly and produces much smaller fragments compared with the remnant rim breakup, and is thus more difficult to capture [25]. It has only recently been clarified experimentally [51] that the major pathways leading to bag fragmentation are the destabilisation and collision of hole rims as they recede over the curved bag and experience centripetal acceleration, which is also observed in the numerical simulations of Ling and Mahmood [122], where they investigated in detail the morphological changes of the droplet in the moderate We regime, and benchmarked them against existing theoretical and experimental results; based on which they improved the internal flow model of Jackiw and Ashgriz [42] for prediction of drop deformation. Nevertheless, ensemble-averaged size and velocity statistics of aerobreakup fragments are still scarce [65]; and given the large span in time and length scales, the understanding of what types of physical mechanisms are involved in the bag film breakup process and how each of them contributes to the statistics of fragments and dictates their subsequent behaviour remains unsatisfactory. Furthermore, the effects of the Oh value on the bag breakup phenomena remain largely unexplored [51].

The earliest studies on droplet aerobreakup are mostly experimental, where the droplet breakup behaviour is recorded and analysed using shadowgraphs, high-speed cameras and particle image velocimetry (PIV) [25, 47, 67, 115]. Thanks to the recent development of computational power, numerical studies have provided a way to investigate atomisation phenomena and gain insight into fundamental mechanisms that are otherwise difficult to achieve experimentally [121, 123]. However, serious challenges are also present for computational studies on droplet aerobreakup, including reaching numerical convergence at large density ratio ρ^* [28, 29]; high computational

cost of fully resolving small-scale fragmentation processes in two-phase turbulence simulations at high We values [26, 121, 124], where the smallest droplet size may be much less than the Kolmogorov scale [124]. There is also a potential need for ensemble averaging when fragments produced from an individual realisation are not sufficient for obtaining statistically meaningful results [17]. In particular, as the Navier-Stokes equations do not describe the physical mechanisms that control topological changes at phase boundaries, thin films are subject to uncontrolled numerical perforation when their thickness approaches the minimum grid size [20]. As a result, the fragment statistics are dependent on grid sizes [51], and numerical convergence with respect to bag fragment statistics has not previously been obtained to our knowledge. It is therefore of paramount importance to improve the grid resolution level and make the onset of breakup independent of the grid size, even though the exact physical mechanism initiating the breakup events remains elusive [38]. A few attempts have been made to improve the numerical resolution of fragmentation or coalescence phenomena. Among these, Coyagee and Boersma [125] first proposed a modified VOF scheme that utilises multiple marker functions for different fluid interfaces to minimise spurious coalescence on coarse meshes. Afterwards, Zhang *et al.* [126] built a topology-based numerical scheme which automatically refines grid cells containing the liquid film bordered by two adjacent bubble interfaces. Finally, Chirco *et al.* [20] developed an algorithm that randomly perforates thin films once their thickness reduces to a prescribed critical value independent of the grid size. This algorithm is controllable via a set of tuning parameters and has been shown to improve grid convergence behaviour for various two-phase problems including droplet aerobreakup.

We present results of novel multiphase direct numerical simulation of droplet bag breakup using both axisymmetric and fully three-dimensional configurations. We conduct axisymmetric simulations to study pre-breakup deformation dynamics, and three-dimensional studies coupled with the MD algorithm of Ref. [20] to shed light on the breakup dynamics of bag films and acquire statistics of bag film fragments for further analysis of their behaviour, while leaving the validation of the MD algorithm with appropriately tuned parameters for the aerobreakup problem to future work. Our

study is structured as follows. We present in §4.2.1 the configuration of our problem and the parameter space we explore, and then introduce the numerical method in §4.2.2. We analyse the axisymmetric simulation results in §4.3 and compare them with previous theoretical predictions, focusing on the early-time deformation period where Jackiw and Ashgriz [42] predicted a constant spanwise growth rate (§4.3.1), and the film-thinning period immediately before bag breakup where an exponential decay model of film thickness is available [49] (§4.3.2). We then investigate the breakup of the bag film based on the three-dimensional simulation results, where we first show grid convergence of fragment statistics using the MD algorithm [20] (§4.4.1). We then analyse the size and velocity distributions, and provide an overview for the breakup mechanisms leading to bag disintegration in §4.4.2. Afterwards, we track and reconstruct the evolution of individual fragments, and study the dependence of their ejection velocity, lifetime and oscillation patterns in §4.4.3. Finally, we investigate the influence of Oh values on the breakup of bag films (§4.4.4). We provide a summary of the numerical convergence of bag fragment statistics in §4.5, and conclude the study in §4.6 with some remarks on future work.

4.2 Formulation and methodology

4.2.1 Problem description

The flow configurations for axisymmetric and three-dimensional simulations are shown in figs. 4.1a and 4.1b, respectively. For both axisymmetric and three-dimensional simulations, a stationary liquid droplet with diameter d_0, density ρ_l and viscosity μ_l is placed close to the left boundary, surrounded by an initially quiescent gas phase with density ρ_g and viscosity μ_g. The domain width D is set as $10d_0$ and $15d_0$ for axisymmetric and three-dimensional simulations, respectively, so as to eliminate the influence of finite domain size on the aerobreakup process. A zero-gradient velocity boundary condition is applied at the right boundary and a uniform incoming velocity U_0 is imposed on the left boundary, while no-penetration conditions are applied at the other domain boundaries. This velocity initialisation results in an impulsive acceleration of the

droplet at the first time step, and induces a flow field satisfying both incompressibility and conservation of linear momentum [26, 29].

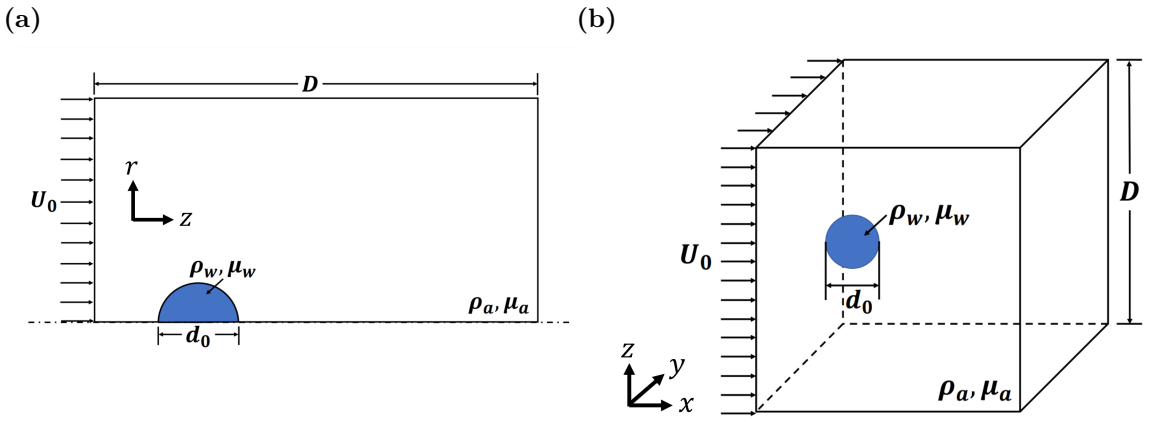

Figure 4.1: Sketches showing the initial configurations of axisymmetric (a) and three-dimensional (b) droplet aerobreakup simulations. The axis of symmetry is located at the bottom in (a).

As discussed in §4.1, the problem is defined by four non-dimensional parameters, namely the Weber number We, the Ohnesorge number Oh, the density ratio ρ^* and the viscosity ratio μ^*. Since we are interested in air-water systems, ρ^* and μ^* are set as 830 and 55, respectively, following the earlier work of Pairetti *et al.* [113]. We vary We between 12 and 25 in our axisymmetric simulations covering the bag breakup regime, while in our current 3D simulations we fix it at 15. In the meantime, Oh is varied between 10^{-4} and 0.075, which allows for a comprehensive investigation of small to moderate viscous effects on bag breakup.

4.2.2 Numerical method

We use the open-source Basilisk numerical library [102] to solve the Navier-Stokes equations for two-phase incompressible, immiscible and isothermal flows, which are written in the following variable-density form,

$$\nabla \cdot \boldsymbol{u} = 0, \tag{4.2}$$

$$\rho\left(\frac{\partial \boldsymbol{u}}{\partial t} + \boldsymbol{u}\cdot\nabla\boldsymbol{u}\right) = -\nabla p + \nabla\cdot\left[\mu(\nabla\boldsymbol{u} + \nabla\boldsymbol{u}^T)\right] + \sigma\kappa\delta_s\boldsymbol{n}. \tag{4.3}$$

Equations (4.2) and (4.3) are respectively the continuity and momentum equations, where $\boldsymbol{u}$ is the flow velocity and p is the fluid pressure. Surface tension effects are incorporated in the volumetric form $\sigma\kappa\delta_s\boldsymbol{n}$ within Eq. (4.3), where σ is the surface-tension coefficient and κ and $\boldsymbol{n}$ are respectively the local curvature and normal vector on the interface. The Dirac delta δ_s is non-zero only on the interface, indicating the local concentration of surface tension effects [100, 101].

The geometric volume-of-fluid (VOF) method is applied in Basilisk to reconstruct the interface and minimize the parasitic currents induced by surface tension [100], which solves the following advective equation,

$$\frac{\partial f}{\partial t} + \boldsymbol{u} \cdot \nabla f = 0, \tag{4.4}$$

where f is the VOF function that distinguishes the liquid and gaseous phases, taking the value of 1 and 0 in the former and latter respectively. For modelling of surface tension effects, $\delta_s\boldsymbol{n}$ in Eq. (4.3) is approximated as ∇f using an adaptation of Brackbill's method [101, 127], and the curvature κ is calculated by taking the finite-difference discretisation of the derivatives of interface height functions [101]. The quad/octree-based AMR scheme based on the estimation of local discretisation errors of ∇f and $\boldsymbol{u}$ is adopted so as to reduce the computational cost at high resolution levels L, which is defined using the minimum grid size Δ,

$$\Delta = \frac{D}{2^L}. \tag{4.5}$$

As Δ is the smallest length scale at which necks of thinning filaments can be represented, L sets the length scale at which liquid filament breakup occurs.

In the bag breakup regime, the onset of fragmentation is preceded by the inflation of bag structure whose thickness reduces considerably over time. While the mechanism responsible for the puncture of the bag film has been extensively discussed [20, 38, 54], in VOF simulations this is initiated when the local thickness of the bag decreases to the finest grid size [107], causing the initiation time of breakup and the size of the finest fragments to be grid-dependent. To circumvent this unphysical and numerically uncontrolled phenomenon, we adopt the manifold death (MD) algorithm recently

developed by Chirco *et al.* [20], which artificially perforates thin films once their thickness decreases to a prescribed critical value independent of the grid size. This enables grid convergence to be reached in the fragment size distributions and related quantities [20]. This is realised in the Basilisk framework by first computing quadratic moments of the VOF colour function f on grid cells with a given signature level $L_{\text{sig}} \leq L$, which defines the critical thickness $h_c \equiv 3D/2^{L_{\text{sig}}}$, the smallest length scale at which liquid films can be presented as below it they will be artificially perforated by the MD algorithm. The signs of the computed quadratic moments indicate the local shape of the interface. If a film with thickness not larger than h_c is detected, the algorithm randomly creates cubic cavities on the ligament by directly setting the value of f to that of the other phase with a probability p_{perf}. While the total fluid mass is changed when holes are created on thin films, the MD algorithm minimises this side effect by creating cavities with minimum sizes that allow for Taylor-Culick expansion, and limiting the maximum number of holes perforated at every iteration. Further discussion and details of the parameters used for the MD algorithm in our study are supplied in §4.4.1.

Before the formation of thin bag films and their subsequent breakup, the smallest length scale in the aerobreakup problem is the thickness δ of the viscous air boundary layer around the droplet, through which momentum diffuses from the surrounding airflow into the droplet and drives its deformation. Batchelor's estimation with the defining length scale of the droplet d_0 yields $\delta \sim d_0/\sqrt{Re}$, where $Re \equiv \rho_g U_0 d_0/\mu_g$ is the freestream Reynolds number. For a typical droplet in the bag breakup regime, characterised by Weber and Ohnesorge numbers $We = 15$ and $Oh = 10^{-3}$, this corresponds to $\delta \sim 1.2 \times 10^{-2} d_0$. The recommended criterion of $\delta/\Delta \geq 2$ [75] then requires the grid resolution level satisfy $L \geq 12$ for simulations with domain size $D = 15d_0$. The highest grid resolution level we set in our present simulations is $L = 14$, at which the droplet contour in our axisymmetric simulations has reached grid independence. The numerical convergence of fragment statistics is discussed in detail in §4.4.1.

Finally, the droplet diameter d_0, incoming flow velocity U_0, dynamic flow pressure $p_0 \equiv \rho_g U_0^2$ and the characteristic deformation time τ introduced in §4.1 provide the natural reference scales for the length, mass and time quantities that appear in Eqs. (4.2)

and (4.3), and will be used to non-dimensionalise the numerical results in the remainder of this study unless otherwise specified.

4.3 Pre-breakup deformation dynamics

Before the onset of bag breakup, the shape of the deforming droplet remains largely axisymmetric, although the wake region may have become fully turbulent and three-dimensional. Many previous numerical aerobreakup studies therefore conducted axisymmetric simulations for a parametric study [27, 29, 31]. In this section, we present our axisymmetric results to provide an overview of the pre-breakup deformation characteristics of the droplet, while also verifying our simulation results by comparing with available analytic models and experimental results.

4.3.1 Early-time deformation

We first discuss the initiation period of aerobreakup, defined by Jackiw and Ashgriz [42] as $0 \leq t \leq T_i$, where T_i is the time when the droplet reaches its minimal streamwise thickness. To provide an overview of the early-time droplet deformation process characterised by spanwise flattening, we first present in fig. 4.2 the droplet contours extracted from our axisymmetric simulations at various instants within $0 \leq t/\tau \leq 0.8$ for two different Ohnesorge numbers, $Oh = 10^{-3}$ and 10^{-2}, with the same Weber number $We = 15$. The radial profile is shown with $y = 0$ as the axis of symmetry. It is found that during the early deformation stage, the windward surface of the droplet continues moving downstream and pushing liquid to the drop periphery, leading to the gradual spanwise flattening of the droplet. In the meantime, a dimple develops on the windward surface that moves towards the axis of symmetry and eventually evolves into a crater for $Oh = 10^{-3}$, as shown in fig. 4.2a. The leeward side of the droplet remains relatively stationary after an initial movement to the left. In contrast, fig. 4.2b shows that the increase of viscosity postpones the dimple formation on the windward surface significantly, which only begins to appear at $t/\tau = 0.8$. Previous works have attributed the spanwise flattening of the drop to the aerodynamic pressure difference between the frontal stagnation point and the equatorial periphery [42], which drives the internal

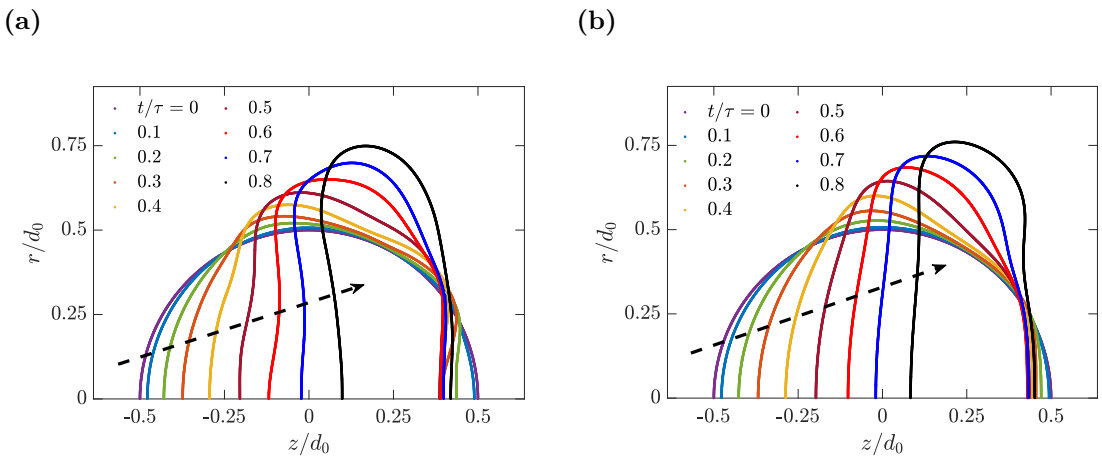

Figure 4.2: Early-time development of droplet contours for axisymmetric simulations with Ohnesorge number $Oh = 10^{-3}$ (a) and 10^{-2} (b), with the Weber number $We = 15$. The axis of symmetry is at $y = 0$.

flow within the droplet against the restoring effects of surface tension [29]. The airflow quickly separates from the leeward surface, creating a re-circulation region with low pressure which induces little movement at the leeward interface [118]. Formation of similar dimple structures on the windward surface can also be observed in fig. 1 of Ref. [29] for $11.3 \leq We \leq 24$, corresponding to bag and bag-stamen breakup.

We briefly examine whether the dimple is a result of RT instability developing on the windward surface due to wind acceleration. Li *et al.* [128] predicted a critical instantaneous Bond number $Bo_c \equiv \rho_l \alpha d_0^2/4\sigma = 11.2$, beyond which the windward surface is destabilised. Here α is the instantaneous acceleration of the liquid droplet. For a droplet with $We = 15$ and $Oh = 10^{-3}$, our results show $Bo_c = 0.57$ at $t/\tau = 0.4$ when the dimple is first observed in fig. 4.2a, much smaller than the threshold value of 11.2 predicted in Ref. [128]. Taking into account that the liquid is being primarily pushed from the frontal stagnation point to the windward side of the periphery around the time of dimple formation ($t/\tau \sim 0.4$ in fig. 4.2a), together with the We range where it is observed in Ref. [29], it is more likely that the dimple formation is caused by the capillary pinching effects against fluid influx, and should therefore be viewed as a precursor of later rim formation.

For validation of our numerical results, we present in fig. 4.3 the evolution of the maximum spanwise radius of the drop R_m and the streamwise length of the bag

L_{bag} measured from our axisymmetric and 3D numerical simulations at $We = 15$ and $Oh = 2.5 \times 10^{-3}$, and compare them with the experimental results of Refs. [42] and [129]. It can first be seen that the axisymmetric and 3D numerical results agree excellently until $t \approx 1.5\tau$, when the axisymmetric simulation shows a smaller bag length in fig. 4.3b. This late-time deviation most likely arises from the lack of 3D flow instability development in axisymmetric simulations [29], which may break the symmetry of the bag and limits its streamwise growth. Both our axisymmetric and 3D simulation results agree well with the experimental data of Ref. [42] up to $t/\tau = 1$, after which the experimental results show faster growth in both R_m and L_{bag}. This may be due to the sensitivity of the flattened drop to difference in the ambient flow conditions, as in our numerical simulations the air-phase flow remains laminar, whereas the experimental configuration of Refs. [129] and [42] in fact produces air-phase turbulence, which has been shown by Zhao *et al.* [69] to be capable of increasing the height and width of bags at late time (see e.g., their fig. 6). More specifically, Ref. [42] used a 5-gauge air needle (whose diameter D_n is only 2.48 times of the droplet diameter d_0) to generate air jets with centreline Reynolds number Re_a of $5.2 \times 10^3 \sim 2.5 \times 10^4$, apart from needles for suspending the drop within such air jets. In the case of Ref. [129], air jets are produced through a nozzle with diameter $D_n \approx 11d_0$, but the airflow is also turbulent with $Re_a = 1.8 \times 10^4$. The results of Ref. [51] are obtained from single experimental runs without being ensemble-averaged, which may lead to larger variations in their results, as also noted in the comparison of numerical results by Ling and Mahmood [122]. Additionally, note that in fig. 4.3a, the experimental results of Refs. [42] and [129] show some mutual disagreement in the spanwise radius values within the range of $t/\tau \leq 1.5$.

The bag lengths and widths recorded at various Oh values at the point of breakup are also included as scattered points in fig. 4.3, which we will return to in §4.4.4. It can be seen that our bags approach breakup within the time range of $1.74 \leq t/\tau \leq 1.91$, earlier than the experimental results of Ref. [42] ($t = 2.2\tau$ for $We = 15.3$). However, Ref. [129] did not report the exact time at which bag breakup is initiated. This earlier breakup time is associated with the limit of grid resolution, and hence L_{sig}, on the critical thickness at which the bag film is perforated by the MD algorithm, as

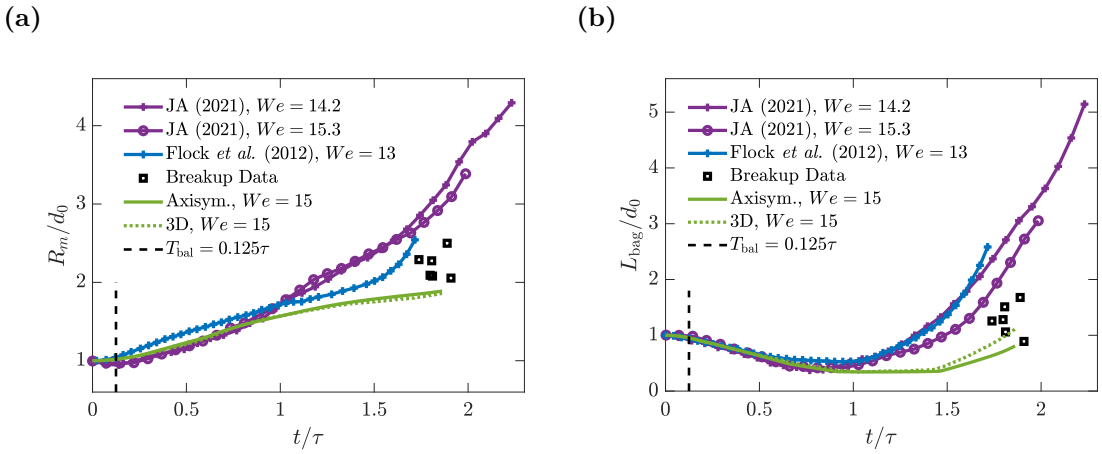

Figure 4.3: Comparison of our axisymmetric and 3D simulation results for the evolution of bag length (a) and width (b) at $We = 15$ and $Oh = 2.5 \times 10^{-3}$ with the experimental data of Jackiw and Ashgriz [42] and Flock *et al.* [129]. The breakup lengths and widths for various Oh values extracted from our simulations are included as scattered points, and the balance time $T_{\text{bal}} = 0.125\tau$ proposed by Ref. [42] is also plotted for reference.

at $L_{\text{sig}} = 13$, the critical thickness is $3D/2^{L_{\text{sig}}} = 5.5 \times 10^{-3} d_0$, which is a few times larger than the experimental value of $h/d_0 = 1.2 \times 10^{-3}$ as found in Ref. [51], and $5 \times 10^{-5} \leq h/d_0 \leq 5 \times 10^{-4}$ in Ref. [41]. The premature breakup of thick bag films is a limitation present in all numerical simulations of droplet aerobreakup, as is also noted in the recent work of Ref. [122].

Furthermore, Jackiw and Ashgriz [42] found experimentally that there exists an early period featuring constant growth rate of the maximum spanwise radius of the droplet R_m, and proposed the following model for its prediction,

$$\dot{R}_m = \frac{d_0 T_{\text{bal}}}{8\tau^2} \left(a^2 - \frac{128}{We} \right), \tag{4.6}$$

where $a \equiv du_z/dz$ is the air-phase axial stretching rate near the frontal stagnation point of the droplet and approximated as $a \simeq 6$; τ is the characteristic deformation time introduced in §4.1; and T_{bal} is the time when a constant streamwise deformation rate is reached, taken as 0.125τ according to the experimental results [42]. We note that this model is derived assuming ellipsoidal or cylindrical droplet shape and a balance between aerodynamic and capillary forces during deformation, which leads to a purely radial internal velocity profile that cancels out the viscous effects.

We now investigate Eq. (4.6) using our axisymmetric numerical results. Figs 4.4(a) and (b) show respectively the influence of We and Oh on the measured instantaneous spanwise growth rate $\tilde{\dot{R}}_m$), where the tilde indicates normalisation by the theoretical value from Eq. (4.6). We also include the growth rate evolution obtained by numerically differentiating the experimental data presented in fig. 28 of Ref. [42] for comparison. For the small Oh value of 10^{-3}, fig. 4.4a indicates that the spanwise growth rate $\tilde{\dot{R}}_m$) reaches a plateau with relatively small variations around $t = 0.3\tau$, where the prediction of Eq. (4.6) matches qualitatively with the measured $\tilde{\dot{R}}_m$) values. We note that while Jackiw and Ashgriz [42] set $T_{\text{bal}} = 0.125\tau$ as an *a posteriori* estimation based on the evolution of R_m rather than $\tilde{\dot{R}}_m$ when analysing their fig. 17(b), our results agree well with the spanwise growth rate computed from their experimental data up to $t = 0.74\tau$, with their data also reaching a plateau around $t = 0.3\tau$. The growth rate reported in Ref. [42] becomes much larger than ours for $t > 0.74\tau$, corresponding to the larger R_m values observed in fig. 4.3a, which is possibly a result of air-phase turbulence as previously discussed. For cases at $Oh = 10^{-3}$, this period of constant $\tilde{\dot{R}}_m$) ends around $t = 0.55\tau$, after which $\tilde{\dot{R}}_m$) reaches a peak aound $t = 0.6\tau$ and then decreases, indicating a deviation from Eq. (4.6) absent in the analyses of Ref. [42]. However, fig. 4.4b suggests that as Oh increases beyond 2.5×10^{-3}, the late-time peaking of $\tilde{\dot{R}}_m$) gradually attenuates, while the match with Eq. (4.6) is improved and maintained for longer periods of time, which is particularly interesting as Eq. (4.6) is derived based on inviscid flow assumptions and cannot account for viscous influences. Finally, Jackiw and Ashgriz [42] tested droplets for which $Oh = 2.7 \times 10^{-3}$; our numerical results are therefore consistent with their experiment.

Returning to fig. 4.2a suggests that during the period $0.3\tau \leq t \leq 0.55\tau$ when the constant growth rate $\tilde{\dot{R}}_m$ is observed, the liquid is being pushed from the frontal surface to the windward side of the periphery, where the maximum spanwise radius is reached. However, at $t = 0.6\tau$ when the peaking behaviour is observed, a bulge appears downstream and causes a location shift where the maximum spanwise radius R is reached. This bulging behaviour is also present in the growth rate evolution computed from the experimental data of Ref. [42] at $Oh = 2.7 \times 10^{-3}$, but virtually

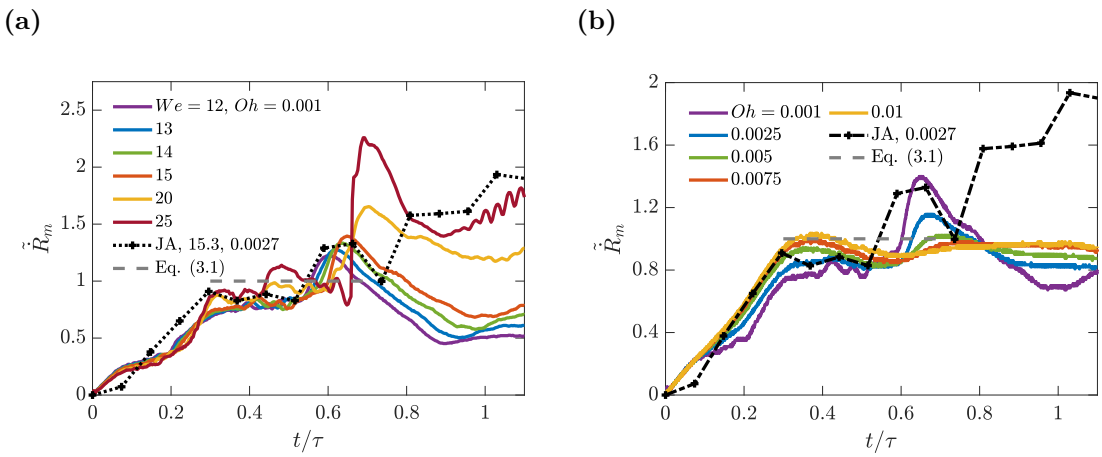

Figure 4.4: Measured droplet spanwise growth rate compared with the experimental data of Jackiw and Ashgriz [42]. Evolution of instantaneous spanwise growth rate $\tilde{\dot{R}}_m$) with various We and $Oh = 10^{-3}$ (a) and various Oh with $We = 15$ (b) are plotted; and the results are normalised using Eq. (4.6).

absent when $Oh = 10^{-2}$ in our numerical simulations, as shown in fig. 4.2b, where the periphery of the droplet contour only flattens over time.

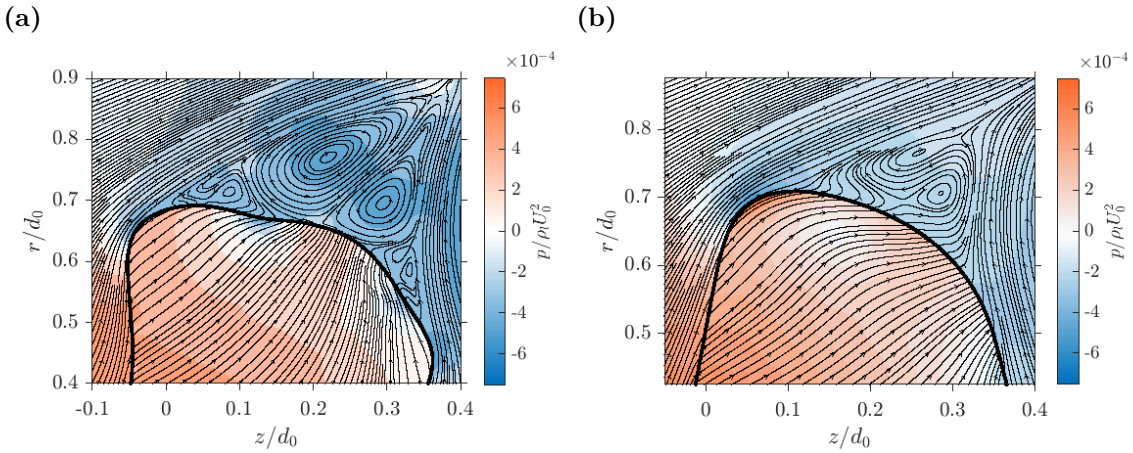

Figure 4.5: Flow fields near the tip of a droplet with $We = 20$, $Oh = 10^{-3}$ (a) and $We = 15$, $Oh = 10^{-2}$ (b) when the peaks in $\tilde{\dot{R}}_m$) are reached. The non-dimensional times at which (a) and (b) are taken are respectively $t/\tau = 0.62$ and 0.66.

To provide insights into physical mechanisms governing the peak in the spanwise growth rate observed for low Oh values in fig. 4.4, we plot in fig. 4.5 the pressure distribution and streamlines near the drop periphery, when the peaks in the spanwise growth rate $\tilde{\dot{R}}_m$ are reached in fig. 4.4b for $We = 20$ and $Oh = 10^{-3}$, and for $We = 15$

and $Oh = 10^{-2}$. It can be seen that the surrounding gas flow separates from the droplet surface at the windward side of the periphery, creating attached recirculating vortices in its wake with low pressure and slow fluid motion [29, 31], where the bulges are located. The pressure difference in the surrounding flow between the frontal stagnation point and the recirculating region drives the internal flow within the droplet from the windward surface to the periphery. Furthermore, the peaks in $\tilde{\dot{R}}_m$ observed for $Oh \leq 0.005$ are associated with the formation of a high-pressure region at the bulge on the droplet periphery, as can be seen in fig. 4.5a, which is caused by surface tension and decelerates the flow into the bulge. Further development of the bulge leads to an increase in the local capillary pressure, which causes the decrease in $\tilde{\dot{R}}_m$ after the peak. Notably, the droplet contour in fig. 4.5b at $Oh = 10^{-2}$ lacks craters at the axis of symmetry and bulges at the periphery, and therefore more closely resembles the cylindrical shape of the deforming drop assumed in the derivations of Ref. [42], which may explain why the match with the inviscid model (4.6) is improved as Oh is increased.

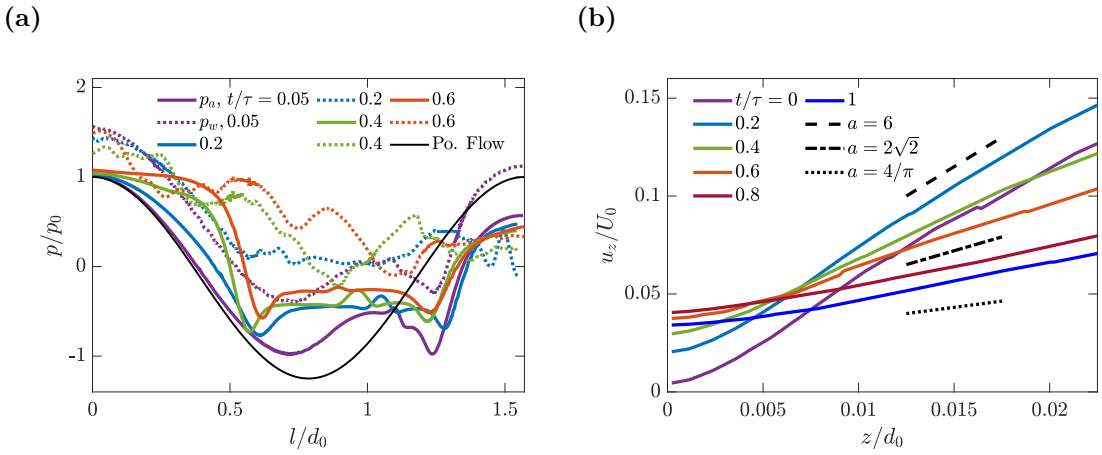

Figure 4.6: (a): Evolution of air (p_a, solid lines) and liquid pressures (p_w, dotted lines) on either side of the droplet interface as functions of the interfacial arc length l; (b): axial airflow velocity u_z on the axis of symmetry as a function of the distance to the windward stagnation point of the droplet z. The values of We and Oh are respectively 15 and 10^{-3}.

We further investigate the distribution patterns of flow pressure and velocity in the vicinity of the droplet, and their association with Eq. (4.6) of Ref. [42]. Figure 4.6a shows the air- and liquid-phase pressure on either side of the drop surface as functions of the arclength l traversing along the axisymmetric droplet contour in the clockwise

direction. At very early time ($t/\tau = 0.05$), the air-phase pressure profile closely follows the sinusoidal potential-flow solution for $l/d_0 \leq 0.6$, which corresponds to the windward face of the drop; whereas the profile at $l/d_0 > 0.6$ deviates from the potential-flow solution due to flow separation, characterised by a second minimum around $l/d_0 = 1.2$. At $t/\tau = 0.05$ the shape of the liquid-phase pressure profile bears strong resemblance to its airphase counterpart, with a nearly-uniform upshift due to the constant capillary pressure difference $4\sigma/d_0 = 0.28p_0$. As the droplet flattens over time, the air-phase pressure profile on the windward surface increases and the first minimum moves upstream, deviating from the potential-flow solution. In the meantime, the change in liquid-phase pressure for $l/d_0 \leq 0.37$ is relatively small, and the air- and liquid-phase pressure profiles cross at $l/d_0 = 0.37$ and $t/\tau = 0.4$, signalling dimple formation on the windward surface as the local radius of curvature reaches infinity. Note also that the minimum of the liquid-phase pressure profile around $l/d_0 = 0.85$ observed at $t/\tau = 0.4$ becomes a maximum at $t/\tau = 0.6$, which corresponds to the bulge formation observed in fig. 4.5a that leads to the deviation from (4.6) [42].

Figure 4.6b shows the airphase axial velocity u_x measured on the axis of symmetry as a function of the distance to the windward stagnation point of the drop z/d_0, where the slope of the curves corresponds to the axial stretching rate a used in model (4.6). It is first observed that the axial velocity value at $z/d_0 = 0$ increases gradually over time, which is because the measuring point is located in the airphase boundary layer attached to the accelerating droplet. The axial stretching rate a is found to gradually decrease from 6 and approach $4/\pi$, the extreme values corresponding to spherical and pancake drop shapes as noted in Ref. [42]; crossing over the intermediate value of $2\sqrt{2}$ proposed by Kulkani and Sojka [130]. The decrease of a corresponds to the air-phase pressure increase on the windward surface as observed in fig. 4.6a via

$$p_g(r) - p_g(0) = -\rho_g \frac{a^2 U_0^2}{8 d_0^2} r^2. \tag{4.7}$$

Consequently, we conclude that our numerical results reproduce the prediction (4.6) of Ref. [42] that there exists a period characterised by a constant spanwise radius growth rate $\tilde{\dot{R}}_m$. Furthermore, we find that the later deviation from (4.6) is characterised by

a peak in $\tilde{\dot{R}}_m$, which is caused by the capillary deceleration of liquid influx into the drop periphery that causes bulge formation at low Oh values. The increase in Oh eliminates the bulge and the frontal crater on the droplet surface, and the droplet acquires a nearly cylindrical shape which is one of the underlying assumptions by [42] when deriving (4.6), hence the better match with their model.

4.3.2 Film drainage and onset of bag breakup

When the droplet deforms into a disc at the end of the early-time deformation period, corrugations develop on its frontal surface, which have generally been considered as RT perturbation waves [27]. This appears in fig. 4.7a for $t/\tau = 0.95$, $We = 15$, in the form of waves on the windward surface of the droplet. Later on, thick rims are observed to form at the drop periphery due to deceleration by capillary force, which extract liquid from the drop centre and contribute to the formation of bag films near the axis of symmetry. Subject to the aerodynamic pressure difference between their frontal and back surfaces, these films further bulge out from the rim [42] and cause exponential growth of streamwise bag length before breakup.

Figure 4.7a shows non-uniform profiles of the bag thickness h, featuring a neck where a local minimum in h is reached and the film breakup eventually occurs. The neck moves outwards radially at $We = 15$, leaving a thickening remnant stamen structure developing at the axis of symmetry [29]. Figure 4.7b, however, shows the deformed drop contours at $t/\tau = 1.73$ for various Oh values. As Oh increases, the neck becomes less obvious as the distribution of bag film thickness becomes more uniform. This is likely because stronger viscous effects at larger Oh values slow down liquid draining from the neck, which is driven by the capillarity-induced pressure difference between the peripheral rim and the central bag.

It has been argued that the breakup of bag films is due to an RT instability peculiar to thin films rather than a finite-time singularity of the Navier-Stokes equations [49]. Assuming inviscid flow and uniform bag thickness, Villermaux and Bossa [49] derived the following exponential decay model for the film thickness h,

$$h(t) \sim d_0 e^{-\lambda t}, \tag{4.8}$$

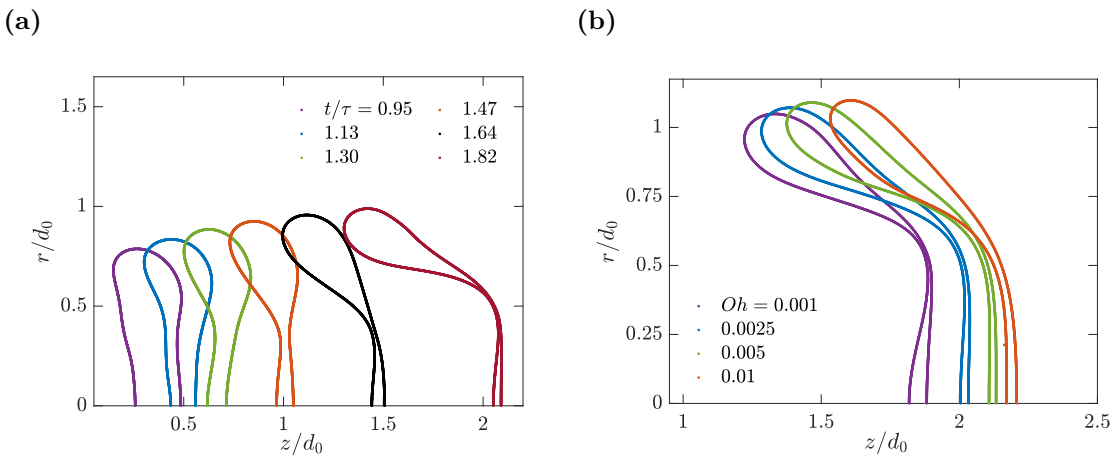

Figure 4.7: (a): Evolution of axisymmetric droplet contours with $We = 15$ and $Oh = 10^{-3}$, where the axis of symmetry is at $r = 0$. (b): droplet contours at $t/\tau = 1.73$ with various Oh values and $We = 15$.

where the exponential decay rate λ is given as $4/\tau$. We compare our numerical results with the predictions of Eq. (4.8) in fig. 4.8. The film thickness h is calculated by measuring the minimum distance between the windward and leeward surfaces of the deformed drop contour over a time period of $t_b - 0.87\tau \leq t \leq t_b$, where t_b is the time when film breakup is detected. Logarithmic scale is used for the vertical axis to facilitate comparison of the decay rate λ.

It can be seen that for the We and Oh range presented in fig. 4.8, the exponential decay rate λ is initially close to the prediction of (4.8). This phase, which features a constant thickness decay rate, roughly corresponds to the period of rim development prior to the 'bulging' of bag films, which is shown in fig. 4.7. However, the decay rate increases as the film continues thinning and approaches breakup, similar to the result of Kant *et al.* [38], which becomes more significant as We and Oh decrease. Most notably, at $We = 12$ the thinning rate continuously increases close to the onset of breakup, which suggests that an exponential decay law in the form of (4.8) does not fully capture the underlying physics for film drainage with strong surface tension.

Developing new theoretical models in place of (4.8) whose predictions match better with the late-time neck drainage behaviour observed within the We and Oh range of interest is out of the scope of the current work. We note briefly that the drainage behaviour of bag films under the influence of aerodynamic pressure difference observed

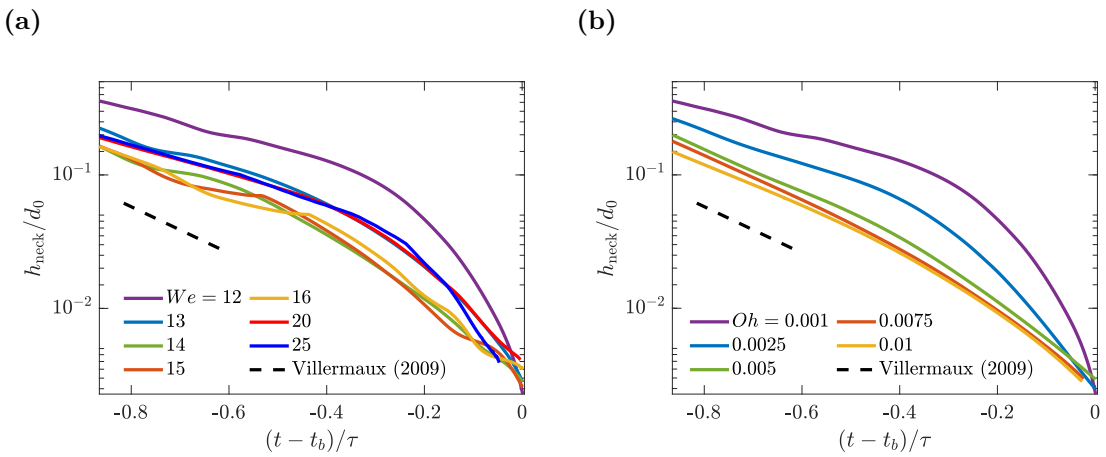

Figure 4.8: The evolution of film thickness h for $t_b - 0.87\tau \leq t \leq t_b$, measured from simulations with various We with $Oh = 10^{-3}$ (a) and various Oh with $We = 15$ (b). For a droplet with $We = 15$, $Oh = 0.001$, the breakup time is $t_b/\tau = 1.84$, and $t_b - 0.87\tau = 0.97\tau$. As fig. 4.7a shows, over this period a bag is blown out from the centre of the flattened disc. The prediction proposed by Villermaux and Bossa [49] (Eq. (4.8)) is also plotted for comparison.

here bears resemblance to the drainage of liquid films between a free air-water surface and a buoyancy-driven air bubble [55, 131, 132], where film drainage models are developed based on lubrication assumptions (see Section 4.2 of Ref. [56] and references therein for more detailed discussions). More specifically, Ref. [55] also showed a deviation from exponential decay of bubble film thickness under asymptotically large surface tension, which is ascribed to a finite-time singularity and contrasts with the thin-film RT instability mechanism proposed by Villermaux and Bossa [49]. However, the major difference between the bag and the bubble film drainage problem lies in the location of the neck. For the drainage of bag films, the neck can be formed some distance away from the axis of symmetry due to a competition of inertia between the outer rim and the inner stamen [29], which complicates theoretical modelling due to additional difficulties in predicting time-varying neck locations. In contrast, bubble film drainage always occurs on the axis of symmetry, as the thin bubble film is connected to an infinitely large and quiescent liquid domain.

4.4 Breakup of bag films

In this section, we analyse our three-dimensional simulation results during the period when the bag film undergoes disintegration to form small fragments, and the axisymmetric flow assumption completely breaks down. It is noted that the late stage of aerobreakup is not covered when the receding remnant bag collides with the surrounding main rim and triggers the fragmentation of the latter [51], which will be reserved for future work.

4.4.1 Grid convergence for fragment statistics

While the physical mechanisms responsible for the onset of liquid film breakup in general remain an active research topic, with various candidates proposed including chemical or thermal inhomogeneities [38], Marangoni effects [54] or presence of surface contamination [133], it has been argued that for bag films under normal acceleration, thickness modulations arise across the film due to the RT instability, resulting in perforation when the perturbation amplitude becomes comparable to the film thickness h [42, 49].

Numerically, the perforation and subsequent fragmentation of thin films in droplet breakup problems has historically been challenging to represent in a physically consistent manner. Given that perforation involves a topological change in the air-water interface, numerical studies have usually employed interface-capturing techniques such as the geometric VOF approach employed here [31, 118, 134]; such methods can represent interfacial topological change without a need for extensive special treatment. However, such techniques also tend to suffer from an unphysical and numerically uncontrolled perforation and fragmentation mode in thin films, which moreover compromises numerical convergence of the statistics of the resulting fragment populations [20]. In this phenomenon, when the film thickness approaches the local mesh size, it begins to destabilise, generating a large number of small fragments without a well-defined fragmentation mechanism; fig. 4.9a shows a qualitative illustration of this phenomenon in our own simulations. This phenomenon also appears in images of droplet breakup in Ref. [118]; unfortunately, information on numerical convergence of fragment statistics is not supplied in that study.

The manifold death (MD) algorithm constructed and implemented by Chirco *et al.* [20] in Basilisk aims to bypass this spurious mode of fragmentation. This algorithm detects and artificially perforates thin films periodically by removing liquid mass once their thickness decreases to a prescribed critical value. The key point is that VOF breakup is circumvented because the film is perforated at a thickness greater than what is required for VOF breakup to occur. A limitation of the MD method is that it removes mass from the droplet in order to generate the hole, which disturbs the momentum and mass conservation properties of the VOF scheme as implemented in Basilisk. We find in practice that the perforation rate of the MD algorithm can be adjusted so that sufficiently few holes are formed in these simulations and this mass loss becomes insignificant (see below).

The holes created by the MD perforation mechanism resemble those appearing in experiments (such as Refs. [38, 51, 61]) — see fig. 4.9b. The algorithm also affords considerable user control over the frequency and location, for example, of the perforations. In the present study, we control perforation frequency using a probabilistic approach which is scaled to be independent of parallelisation, resolution, and the calling interval of the algorithm, in order to minimise the number of free parameters governing the perforation problem. The appropriate choice of probability to match the efficiency of hole generation in experimental studies, such as those seen in Refs. [53, 54], is a complicated problem which is left for future work. Our aim in this study is instead to establish numerical convergence and verify various aspects of the resulting fragmentation process with experiment and theory, which in our knowledge has not been established in previous numerical studies.

All grid convergence test cases we conduct in this section are reloaded from a single three-dimensional simulation snapshot with an intact bag at $We = 15$, $Oh = 10^{-3}$, and the perforation probability and calling interval for the MD algorithm are set as $p_{\mathrm{perf}} = 5.7 \times 10^{-5}$ and $\Delta t_c = 0.5 d_0/U_0$, with grid level $L = 12$, 13, 14 and signature level $L_{\mathrm{sig}} = 11$, 12, 13 (see §4.2 for their definition). The fragment statistics are collected and output at fixed time intervals until the bags have fully disintegrated, and then post-processed to obtain time- and/or ensemble-averaged data. It is noted that as the

We	Oh	L	L_{sig}	Realisation No.	Category
15	10^{-3}	12	N/A	1	Convergence - VOF
15	10^{-3}	13	N/A	1	Convergence - VOF
15	10^{-3}	14	N/A	1	Convergence - VOF
15	10^{-3}	13	11	10	Convergence - MD
15	10^{-3}	13	12	5	Convergence - MD
15	10^{-3}	13	13	3	Convergence - MD
15	10^{-3}	14	13	7	Convergence - MD
15	10^{-3}	14	13	3	Oh Study
15	10^{-4}	14	13	2	Oh Study
15	5×10^{-4}	14	13	1	Oh Study
15	10^{-3}	14	13	3	Oh Study
15	5×10^{-3}	14	13	3	Oh Study
15	10^{-2}	14	13	3	Oh Study
15	2.5×10^{-2}	14	13	3	Oh Study
15	5×10^{-2}	14	13	3	Oh Study
15	7.5×10^{-2}	14	13	1	Oh Study

Table 4.1: List of ensemble realisations for three-dimensional numerical simulations carried out in this work, where the drop Weber and Ohnesorge numbers We and Oh, the grid and signature levels L and L_{sig}, the number of individual realisations, and the purpose for using the ensemble data (the grid convergence study for §4.4.1 and §4.4.2, or the Oh effect study in §4.4.4) are indicated.

test cases run without using the MD algorithm are deterministic in the sense that VOF breakup appears repeatably in the same locations of the thin film, while producing a large number of very small fragments, only one realisation is completed at each L value; whereas the MD algorithm introduces randomness in the perforation location and subsequent fragment formation, while also reducing the number of fragments, and therefore multiple realisations are completed for a given set of L and L_{sig} to generate sufficient total number of fragments for ensemble-averaging. A full list for the configurations of the three-dimensional numerical simulations is available in Table 4.1.

We first demonstrate the effects of the MD algorithm on the breakup behaviour of the bag film in fig. 4.9. The film rupture behaviour is qualitatively different with and without application of the MD algorithm. Figure 4.9a is a snapshot for a simulation case run without using the MD algorithm, featuring numerous small-scale irregular corrugations and ligament breaking on the bag, which reflect the uncontrolled nature of VOF breakup. Figures. 4.9b and 4.9c show that the MD algorithm is able to create

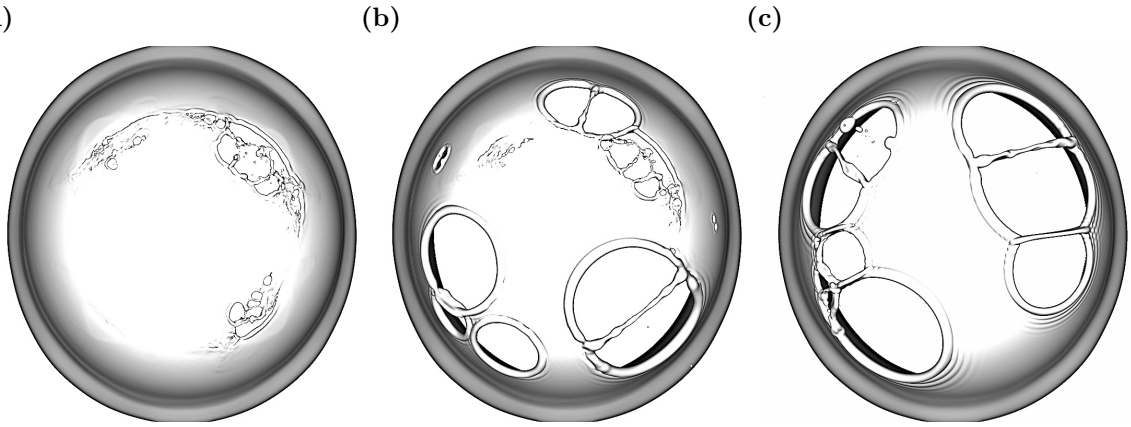

Figure 4.9: Effect of the MD algorithm on the bag breakup behaviour at grid level $L = 12$ and 13 for $We = 15$, $Oh = 10^{-3}$. (a)-(c): Simulation snapshots showing fragmenting bag films at $t/\tau = 1.909$ without (a) and with artificial perforation (b,c). VOF breakup characterised by small-scale corrugation and hole formation is observed on the bag films in (a,b). The MD algorithm generates expanding film holes in a regular pattern, as observed in (b,c). The grid resolution level is $L = 12$ for (a,b) and 13 for (c), while the MD signature level for (b,c) is $L_{\text{sig}} = 12$.

holes on the bag film in a controlled manner, and reduce the influence of VOF breakup on the bag dynamics. These holes created by the MD algorithm feature well-defined bordering rims that recede over the bag and create surface capillary waves ahead of them, and these may collide with one another and form a few long stretching liquid bridges [63], which are distinct from the numerous short and irregular bridges observed with VOF breakup. Note that fig. 4.9b still shows some VOF breakup behaviour which is absent in fig. 4.9c. This reflects the fact that, even though the film is perforated when the film thickness reaches the order of $3\Delta_{\text{sig}}$, the perforation probability and the rate of hole expansion are sufficiently low such that there are regions of the film that continue to thin down to the order of Δ, where VOF breakup begins. In fig. 4.9b, $\Delta = \Delta_{\text{sig}}$, so that VOF-induced fragmentation still appears, but this can be further minimized by choosing $L > L_{\text{sig}}$, such as in fig. 4.9c.

Figure 4.10 further compares the grid convergence behaviour for the size and velocity distribution of bag fragments without and with the MD algorithm applied. The fragment data are sampled at different times throughout the bag film breakup period, and then collected and binned based on the equivalent fragment diameter d to produce the size and velocity distribution functions. While the distribution functions presented in

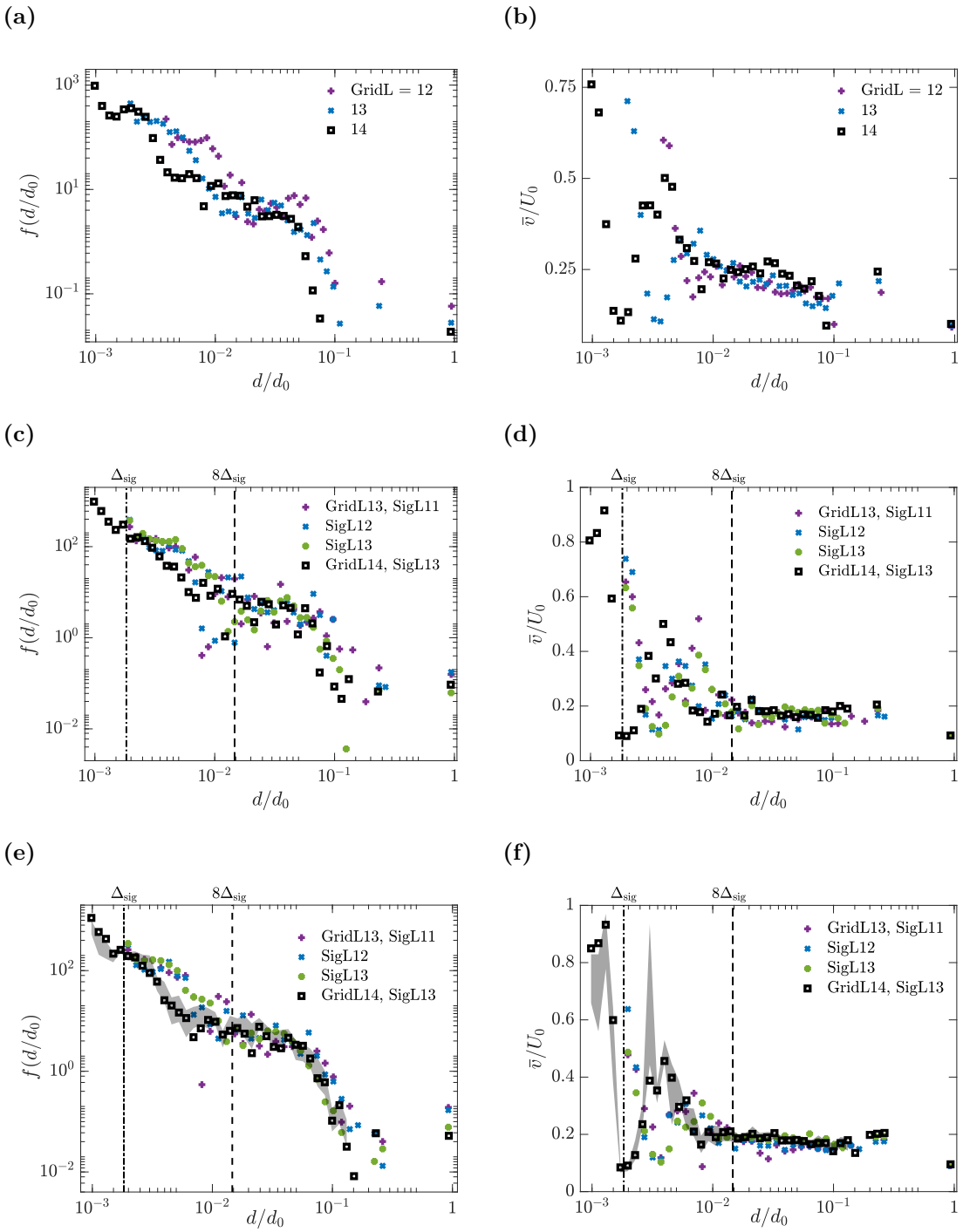

Figure 4.10: Time- and ensemble-averaged size (left column) and speed (right column) probability distribution functions of aerobreakup fragments obtained from simulations without using the MD algorithm (upper row), from an individual realisation (middle row) and from ensemble-averaged data across various realisations with the MD algorithm applied (lower row) at various grid resolution and signature levels. Confidence bounds for each bin are computed across different ensemble realisations at $L = 14$, $L_{\text{sig}} = 13$ using the bootstrapping method, and plotted in (e) and (f) using shaded area. For all test cases, $We = 15$ and $Oh = 10^{-3}$.

figs. 4.10a-d are for single realisations, those in figs. 4.10e-f are ensemble-averaged for each bin over different realisations; and we have verified that the total number of bins does not significantly influence the shape of size and velocity distributions. Figure 4.10a shows the fragment size distribution functions obtained from individual simulations without application of the MD algorithm. It can be seen that while the distributions have similar shapes at various grid levels L, that is, featuring large number densities of small fragments near the minimum grid size, followed by a fall-off at large fragment sizes, there is no clear indication of the distribution functions reaching grid convergence. In particular, it is observed that as L increases, the entire size distribution shifts to smaller sizes. In contrast, fig. 4.10c presents the fragment size distribution functions obtained from individual realisations within the range of $13 \leq L \leq 14$ and $11 \leq L_{\text{sig}} \leq 13$ when the MD algorithm is used. While more scatters in the size distribution functions are seen when compared with fig. 4.10a due to smaller amounts of fragments produced, we no longer observe the shift to small fragment sizes for the distribution tail with $d \geq 8\Delta_{\text{sig}}$, which is the range for well-resolved fragments as observed in Ref. [20]; and size distributions at different grid and signature levels appear to overlap for $d \geq 8\Delta_{\text{sig}}$ despite these scatters. Figure 4.10e further presents the ensemble-averaged size distribution functions obtained with the MD algorithm applied, which features much smaller range of scatter, as indicated by the confidence bounds represented by the grey shade at $L = 14$, $L_{\text{sig}} = 13$, showing clearly that the distributions of fragment statistics overlap for $d \geq 8\Delta_{\text{sig}}$ at different values of L and L_{sig}. From this we conclude that the ensemble-averaged data are grid-converged for $d \geq 8\Delta_{\text{sig}}$ and $13 \leq L \leq 14, L > L_{\text{sig}}$. Moreover, together figs. 4.10a, 4.10c and 4.10e establish that the lack of grid convergence in the no-MD case (fig. 4.10a) is attributable not to the scatter of individual realisations, but specifically to numerically uncontrolled VOF-breakup.

We also include the experimental data of Gildenbecher *et al.* [66] obtained with $We = 13.8$ and $Oh = 5.43 \times 10^{-3}$ in fig. 4.11, together with exponential and log-normal models fitted to their data. Guildenbecher *et al.* [66] noted the difference between the size distributions obtained using two experimental techniques with different resolution levels, and expressed most confidence in the upper tail of the distributions satisfying

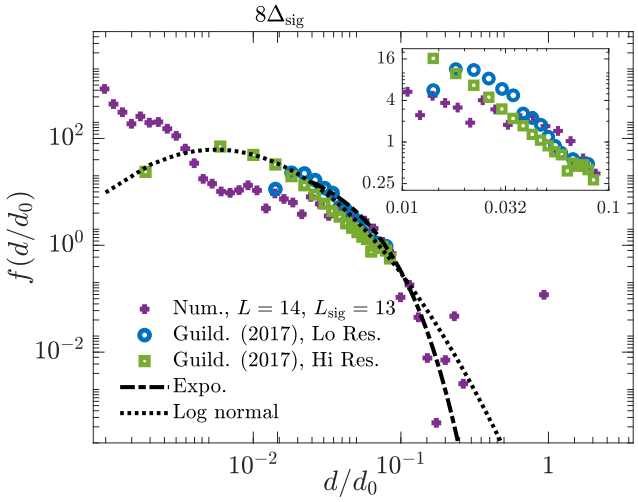

Figure 4.11: Fragment size distribution function measured from our $L = 14$, $L_{\text{sig}} = 13$ simulations, compared with the experimental data of Guildenbecher *et al.* [66] measured at two different apparatus resolutions. A zoom-in view is provided as an inset to facilitate comparison of different size distribution functions within the size range of $0.01 \leq d/d_0 \leq 0.1$. Exponential and log-normal functions fitted to the experimental size distribution function are also included.

$d \geq 0.01d_0$. Within this size range, the tails of our size distribution and those of Ref. [66] show excellent agreement, which further validates our numerical results within the size range of $d \geq 8\Delta_{\text{sig}}$. While we leave for future work the detailed investigation of possible differences in fragmentation mechanisms between our present results and the experiments of Refs. [66] and [42, 51], the present remarkable agreement with experimental data at larger fragment sizes suggests that the upper tails of the size distribution do not depend on whatever these differences may be. Both the exponential and the log-normal model are found to match well with the current size distribution functions for $d \geq 8\Delta$, while both differ from the current results within the range of $d < 8\Delta$, which may suggest that no single function can represent the complete spectrum of the current size distribution of bag fragments.

It is noted that in fig. 4.10e, the fragment statistics are not fully converged for $d \leq 8\Delta_{\text{sig}}$, where compared with its counterparts at $L = 13$, the size distribution at $L = 14$ shows more fragments satisfying $\Delta \leq d \leq \Delta_{\text{sig}}$, and fewer fragments with $\Delta_{\text{sig}} \leq d \leq 8\Delta_{\text{sig}}$. This is probably because the fragments within this range are primarily formed due to the breakup of liquid ligaments, especially the smallest fragments near

the grid size, which are most likely the satellite drops produced from the capillary breakup of corrugated slender ligaments [135]. These are controlled by the grid level L rather than the signature level L_{sig}, as the geometry-specific MD algorithm only targets thin liquid films in 3D simulations and do not act in the stretch-induced breakup of liquid ligaments. Our numerical results for $d \leq 8\Delta_{\text{sig}}$ also deviate from the log-normal function fit of Ref. [66], which may be due to multiple factors including the difference in We, the presence of additional flow perturbations in experiments, and possibly resolution limits in experimental equipment, as exemplified by a comparison performed in fig. 9 of Ref. [66]. However, the size distribution function of very large fragments satisfying $d \geq 0.1d_0$ shows relatively larger range of scatter compared with their smaller counterparts around $8\Delta_{\text{sig}}$, which likely arises from the smaller number of these fragments produced in each ensemble realisation and can be further reduced by increasing the ensemble size. Finally, we note that the influence of MD on mass conservation is minimal as the loss of liquid mass incurred by the MD algorithm does not exceed 0.023% for $t/\tau \leq 2.18$ at $L = 13$ and 14.

Figures 4.10b, 4.10d and 4.10f show the average speed $\bar{v}$ of fragments as functions of the fragment diameter d obtained from simulations without and with the MD algorithm applied. Similar to the size distribution functions, the shapes of the distribution of $\bar{v}$ clearly indicate grid convergence for the tail constituted by the well-resolved fragments with $d \geq 8\Delta_{\text{sig}}$ in fig. 4.10f, which is not observed in fig. 4.10b where large scatters across various grid levels are present. Interestingly, in fig. 4.10f, fragments with diameter $d \geq 8\Delta_{\text{sig}}$ show little variation in the average speed, which appears to be a constant independent of the values of L and L_{sig}; whereas a peak can be observed within the range of $\Delta_{\text{sig}} \leq d \leq 8\Delta_{\text{sig}}$ which is grid-dependent, along with the large increase of the speed of tiny fragments close to Δ_{sig} which approaches the freestream velocity U_0. While it is clear therefore that the production mechanisms of droplets satisfying $d \leq 8\Delta_{\text{sig}}$ may not be grid-converged, the resulting dynamics of these small droplets turn out to be well-resolved; more detailed analysis establishing this will follow in §4.4.2.

In summary, our results in this section demonstrate that the application of the MD algorithm helps to establish grid convergence of fragment size and speed statistics for

well-resolved fragments with diameter $d \geq 8\Delta_{\text{sig}}$, which is not achieved when VOF breakup is dominant. Based on these results, all following three-dimensional studies of bag film breakup are conducted at $L = 14$ and $L_{\text{sig}} = 13$.

4.4.2 Mechanisms leading to bag fragmentation

In this section, we further analyse the fragment statistics obtained from our grid convergence tests run at $L = 14$ and $L_{\text{sig}} = 13$, to provide insight into the shapes of the size and distribution functions observed in §4.4.1, and the physical mechanisms governing the formation of fragments and their subsequent evolution patterns. These choices of L and L_{sig}, together with the MD parameters specified in §4.4.1, allow the creation of only a few holes on the bag film, which are not only enough to avoid the onset of VOF breakup, but also preserves abundant film breakup phenomena including rim recession, collision and destabilisation behaviour that would otherwise be hard to recover with more holes created, where rim collision would dominate [53]. As is noted in §4.3.1, our film is thicker and breaks up earlier compared with experimental results due to the limit of grid resolution. This leads to smaller Taylor-Culick velocity values, which reduces the probability of destabilisation of receding liquid rims [51] and production of fine drops [133]; but our results show that many interesting breakup mechanisms can already be captured with this choice of L_{sig}, which we will present further below.

We first show in fig. 4.12 the time evolution of the instantaneous distributions of the size, axial and radial speed distributions of the fragments produced from bag breakup. Figure 4.12a indicates that immediately after the onset of bag breakup ($t/\tau = 1.96$) only small fragments close to the minimum grid size are produced, and well-resolved larger fragments satisfying $d \geq 8\Delta_{\text{sig}}$ only come into existence as time elapses, and are always fewer compared with small fragments near the grid size. The shape of the size distribution function gradually stabilises, and reaches a steady state by $t/\tau = 2.11$ that is very close to the ensemble- and time-averaged size distribution function. These findings suggest that the smaller and larger fragments are produced through different physical mechanisms that arise at different stages of bag breakup, and eventually these fragmentation mechanisms die out as the bag approaches full disintegration and the

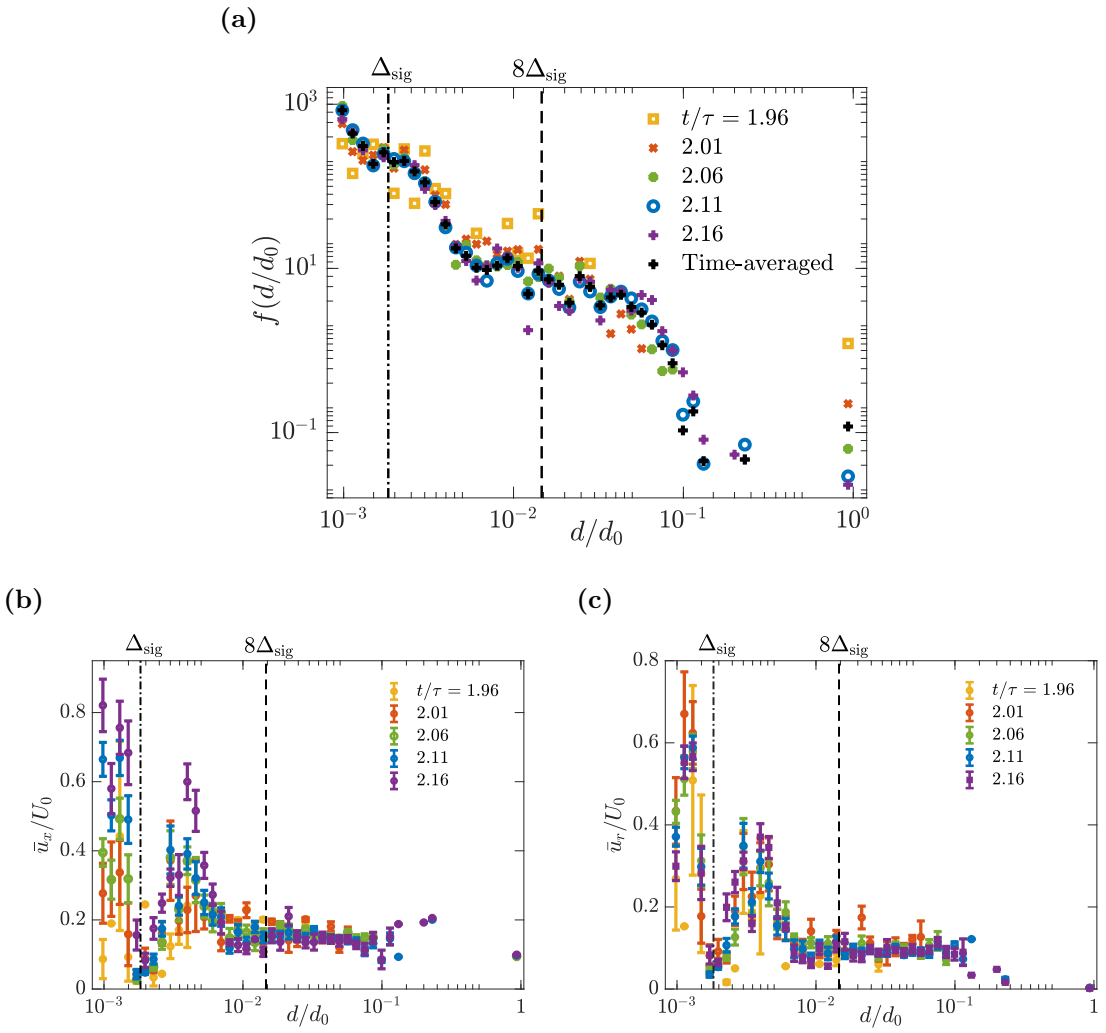

Figure 4.12: Ensemble-averaged instantaneous size distribution functions (a), and probability distribution functions of axial (b) and radial (c) speed of aerobreakup fragments calculated at $L = 14$ and $L_{sig} = 13$. Ensemble- and time-averaged fragment size distribution function is also plotted in (a) for reference.

fragment size distribution is well-represented by time-averaged results. The remaining rim will then disintegrate at still later times, whose investigation we leave for future work.

Figures 4.12b and 4.12c show the instantaneous distribution of fragment axial and radial speeds u_x and $u_r \equiv \sqrt{u_y^2 + u_z^2}$ as functions of their sizes, with the ensemble-wide variations of velocity components in each averaging bin shown in error bars. It can be seen that the speed of well-resolved fragments satisfying $d \geq 8\Delta_{sig}$ remains close to a constant value without significant variations. While the statistics of smaller fragments with $d \leq 8\Delta_{sig}$ are not fully numerically converged, they do show considerably larger variation around the binned average value in qualitative agreement with the

experimental results of Ref. [66]. Interestingly, we observe peaks around $d/d_0 = 5 \times 10^{-3}$ in the distributions of both u_x and u_r, whose location does not appear to vary with time. Moreover, despite the presence of velocity variations, fig. 4.12b suggests that the average axial speed u_x of smaller fragments with $d \leq 8\Delta_{\text{sig}}$ increases over time, whereas the radial speed u_r does not show similar increasing trend in fig. 4.12c. This is most likely because the smaller fragments are generated earlier and therefore are exposed to the airflow for much longer periods of time compared with larger fragments; together with their smaller mass, this means that they are much more easily accelerated by the axial velocity component of the airflow, hence the continuous increase in their u_x values. However, u_r does not increase significantly over time, likely because the airflow in the wake region does not have a large radial velocity component that can accelerate bag fragments as they migrate downstream.

We will hereafter discuss qualitatively several mechanisms through which the bag film undergoes fragmentation and form small droplets, which can be identified by inspecting typical simulation snapshots taken from our $L = 14$, $L_{\text{sig}} = 13$ simulations. Firstly, fig. 4.13 shows the breakup of a stretched long ligament neighbouring two enlarging holes into a series of small drops. As the ligament is itself connected to the main drop, there is a significant size difference between the parent and child drops produced from its breakup, which is an example of *non-local* breakup events (see Eq. (4.11) in §4.4.3 for a definition of non-local breakup). It can be seen from fig. 4.13a that significant cross-sectional diameter variations have developed on the ligament before the onset of its breakup, which can be viewed as the result of the nonlinear development of the RP instability [135]. Afterwards, the ligament shrinks to form sharp tips and then breaks up on multiple sites, as shown in fig. 4.13b, and forms a primary drop which continues to undergo periodic prolate-oblate shape oscillations resembling droplets produced by breaking Rayleigh jets [136], as highlighted in the red boxes in figs. 4.13b-4.13h. This is because the pinch-off of the stretching ligament induces an inner velocity field within the detaching droplet that drives it in the oblate direction (see e.g. fig. 7b in Ref. [136]), matching the perturbation shape of the second Rayleigh mode, which then excites oscillation modulated by capillary effects. In the meantime, the other parts

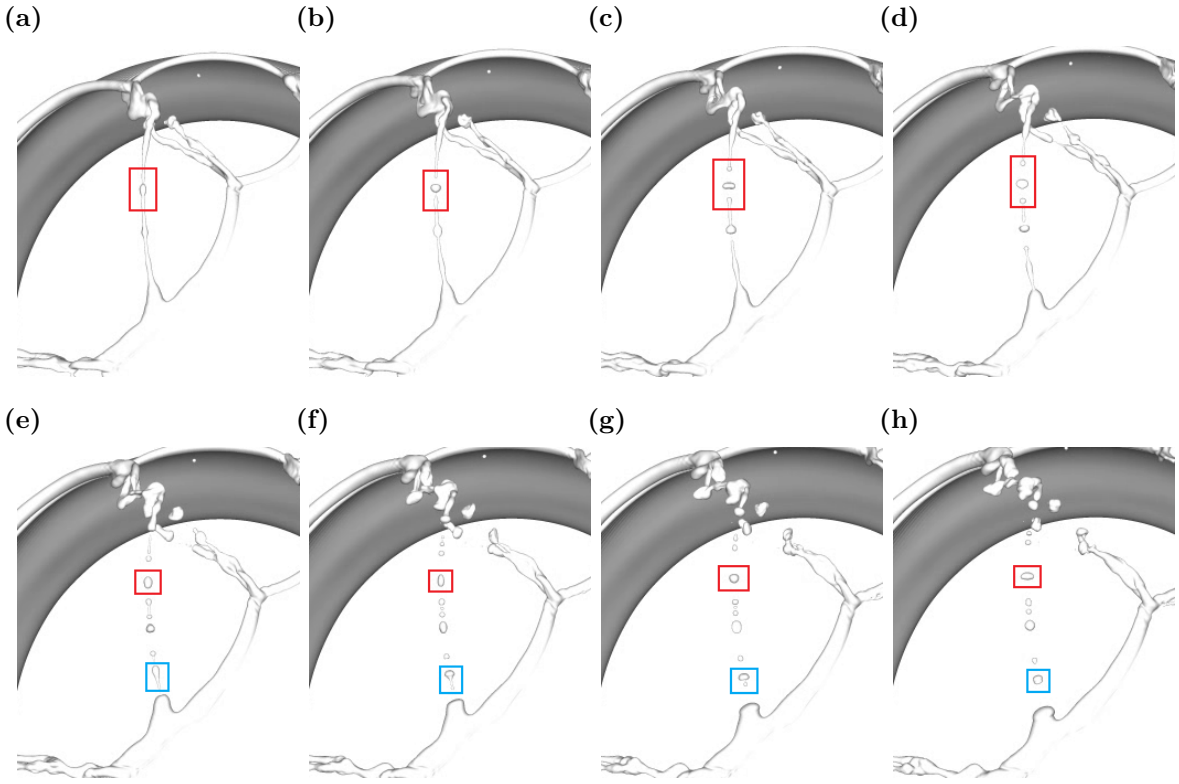

Figure 4.13: Snapshots showing the non-local breakup of a long ligament into multiple fragments during bag film fragmentation with $We = 15$ and $Oh = 10^{-3}$. Frame (a) is taken at non-dimensional time $U_0 t/d_0 = 110.1$ after the simulation starts, and neighbouring frames are separated by $\Delta t = 0.1 d_0/U_0$. The red boxes show the formation of a single fragment through non-local end-pinching and its subsequent oscillation, and the blue boxes show the formation of two fragments through a local breakup event and their subsequent coalescence.

of the ligament do not pinch off to form a series of fragments at once, but first break up into several elongated debris, and then split into large primary and small satellite drops via the well-known end-pinching mechanism [135, 137], which is an example of *local* breakup events as the parent (the elongated debris) and child (satellite drops) do not differ significantly in their sizes. Under certain circumstances, the primary and satellite drops might coalesce and form a larger fragment as highlighted in the blue boxes, resembling the 'immediate satellite merge' mechanism discussed in Ref. [138].

Figure 4.14 first shows an example of short ligament breakup and its eventual contraction into a single droplet, as highlighted in the blue boxes. Compared with the breakup of long ligaments demonstrated in fig. 4.13, this type of short ligament breakup bears stronger resemblance to the breakup phenomena of liquid bridges studied by

Agbaglah [63], where fragments produced from the same liquid bridge do not feature significant size variations. This is most likely because the initial holes are placed very close to each other in Ref. [63], and the receding rim does not have enough time to grow in size and momentum before their impact.

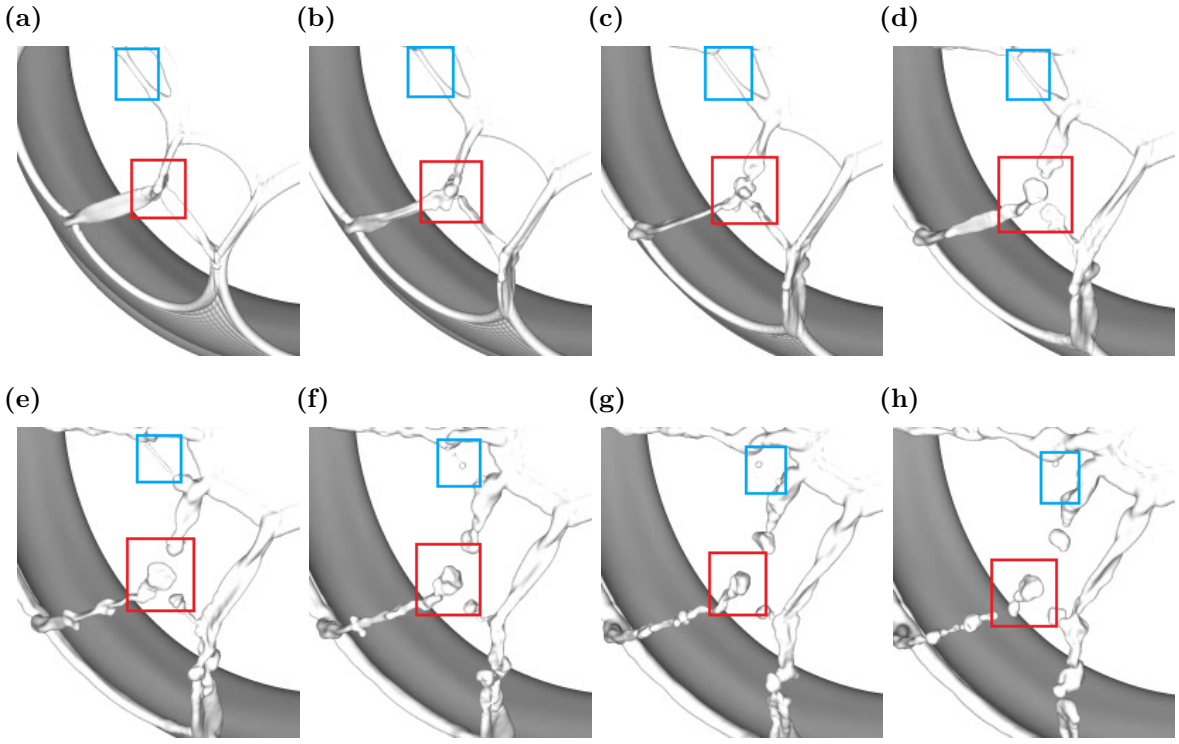

Figure 4.14: Snapshots showing the detachment of a liquid node from ligament webs (red boxes) and the evolution of a short ligament into a single drop (blue boxes) during bag film fragmentation with $We = 15$ and $Oh = 10^{-3}$. Frames (a) and (e) are taken at non-dimensional times $U_0 t/d_0 = 109.5$ and 110.3 after the simulation starts, respectively. Neighbouring frames in each row are separated by $\Delta t = 0.2 d_0/U_0$.

Another type of fragmentation mechanism can also be identified in fig. 4.14; as highlighted in the red boxes, three adjacent holes have merged with each other, and their three bordering rims converge on a common 'node' as they are stretched, which is also observed in the breakup of ligament webs formed on Savart sheets by Lhuissier and Villermaux [61]. Compared with the ligament pinch-off mechanism discussed earlier, the surface evolution of this 'node' shows much more complicated corrugation patterns as the rims it was connected to are gradually detached, and therefore is not dominated by the second Rayleigh mode alone. The 'node' drop that eventually forms in this

case also has a much larger size compared with its counterparts formed from ligament pinch-off events. However, different from an earlier study by Vledouts *et al.* [53], our choice of $L = 14$ and $L_{\text{sig}} = 13$ does not produce holes on the bag film with as high a number density, and therefore we are not able to directly measure the wavelength of the RT instability responsible for the film fragmentation from the average distance between the centres of adjacent holes. The relatively smaller number density of holes formed also means that the larger 'node' drops formed due to the merging of three or more adjacent and similarly sized holes are relatively rare compared with generally smaller fragments formed from ligament breakup, which require the collision of only two adjacent liquid rims. Furthermore, no less than three holes should fully expand and arrive at the same region on the bag film where the node is located, and each of the connecting rims need to break off successively before the node can be treated as a seperate fragment by the fragment counting algorithm. These factors help explain the tail of the size distribution function of aerobreakup fragments taking shape at much later time as we observed in fig. 4.12a; namely, that larger droplets are relatively few, and produced at generally later times during the fragmentation process.

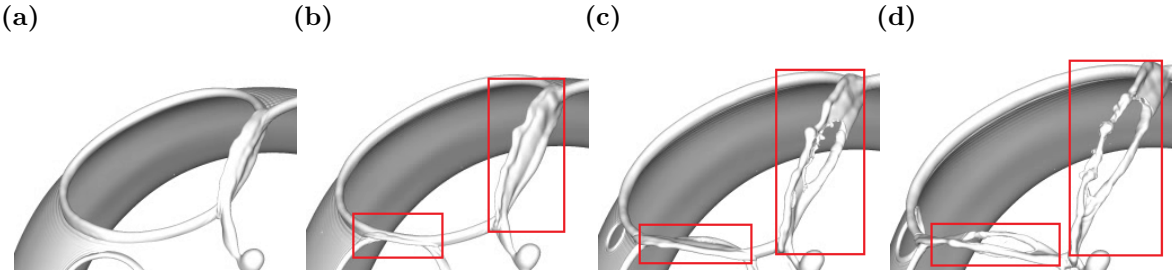

Figure 4.15: Snapshots showing the evolution of 'fingering' liquid lamellae during bag film fragmentation with $We = 15$ and $Oh = 10^{-3}$. Frame (a) is taken at non-dimensional time $U_0 t/d_0 = 110$ after the simulation starts, and neighbouring frames are separated by $\Delta t = 0.25 d_0/U_0$.

We also note that while we often observe the formation, oscillation and subsequent corrugation development of liquid ligaments after the impact of receding rims, as shown on the ligament to the left of the red box in fig. 4.14, destabilisation of such structure due to the RT instability and its subsequent evolution into fully developed transverse 'fingers' and 'fine drops' are only occasionally observed in our current simulations.

According to Neel *et al.* [62], these two regimes are separated by a critical local Weber number for rim collision $We_c \equiv \rho_l(2v_{\mathrm{TC}})^2 d_l/\sigma = 66$, where d_l is the rim diameter. Neglecting the curved geometry of the bag film, liquid mass conservation further yields $We_c = 8\sqrt{D_c/\pi h}$, where D_c and h are respectively the distance between the centre of two neighbouring holes and the film thickness. Taking $h = 3D/2^{L_{\mathrm{sig}}} = 3D/2^{13}$, we find that $We_c = 66$ corresponds to $D_c = 1.2d_0$, which we expect might be reached for some pairs of sufficiently separated holes, as the bag diameter d_f before the onset of fragmentation typically approaches $2d_0$, as shown in both our numerical results and the experimental data of Ref. [42] (see e.g. their fig. 30). Figure 4.15 highlights two such examples in red boxes, where we observe the transverse growth of the lamella and the growth of finger-shaped corrugations on its edges; however, before the fingers fully develop and detach as 'fine' drops, holes are observed to form on the thinning lamella, which then expand and collide with the fingering lamella edges, turning them into isolated breaking ligaments. Similar phenomena of lamellae rupture and their edges forming corrugated ligaments can also be observed in fig. 14 of Ref. [53], although in that case the lamellae appear to remain within the plane of the film surface, and do not experience transverse growth; and VOF breakup may play a role in the present examples. Nevertheless, the liquid ligaments found in the current simulations have already displayed a variety of well-documented physical phenomena that collectively contribute to the large span of fragment sizes found in our fragment distribution functions.

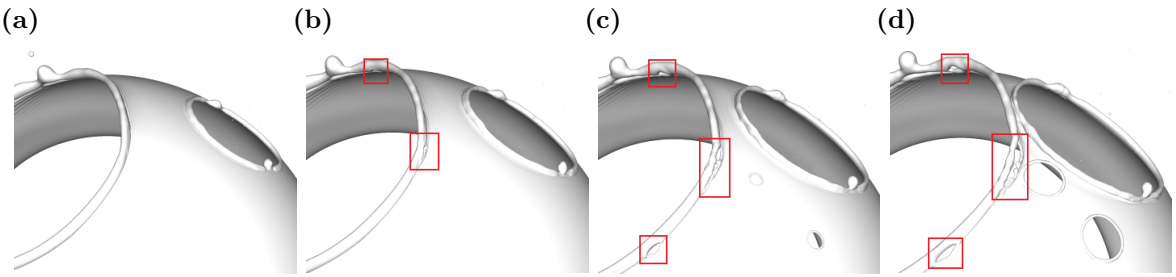

Figure 4.16: Snapshots showing the receding liquid rim destabilisation during bag film fragmentation with $We = 15$ and $Oh = 10^{-3}$. The sites where the rim is detached from its base is highlighted in red boxes. Frame (a) is taken at non-dimensional time $U_0 t/d_0 = 111$ after the simulation starts, and neighbouring frames are separated by $\Delta t = 0.25 d_0/U_0$.

Lastly, we observed a few examples showing the destabilisation of receding liquid rims, as demonstrated in fig. 4.16. These destabilisation phenomena are absent in the recent work of Ref. [63] where holes expand over a flat liquid film, and are therefore most likely linked with the influence of centrifugal acceleration caused by the curved bag film [51, 54]. While we are not yet able to measure the wavelength or the linear growth rate of the instability, and therefore have not identified the type of hydrodynamic instability involved here; we observe in fig. 4.16d regular-spaced holes highlighted in the red boxes forming at the foot of the rim bordering the hole on the left. These are not attributable to VOF breakup because they are not observed to appear elsewhere on the bag at the same time; while the rim bordering the larger hole on the right is seen to develop regular corrugation patterns, which might be an indication that the receding liquid rim is experiencing the RP instability. Any further development of the instability is interrupted by the eventual collision between adjacent rims (not shown in fig. 4.16). The readers are referred to [51] for a more comprehensive discussion on rim destabilisation. There a few candidates are proposed, including the RT instability mechanism governing the 'fingering' behaviour on bursting surface bubbles [54]; and it is concluded that the centrifugal acceleration does not govern the instability of the rim directly, but instead regulates the thickness of the rim via a local-Bond-number criterion [60], with the rim in turn susceptible to the RP instability. With the present methodology, these rim instabilities can be investigated in more detail with higher signature levels L_{sig}, and concomitantly higher L. Given the large computational expense of such simulations, it is not feasible to include such an analysis in the present study.

4.4.3 Behaviour of bag fragments

In the following, we move away from considering the dynamics and numerical characteristics of the production mechanisms of fragments to examine instead those of the fragments themselves. To provide further insight into the evolution of individual fragments rather than their collective behaviour, we utilise the droplet tracking algorithm proposed by Chan *et al.* [139] in post-processing to reconstruct their breakup lineage. This toolbox assumes breakup and coalescing events to be binary (i.e. at most two parent droplets

may collide and form one large child droplet, or two child droplets may be produced from the breakup of one parent droplet in a single breakup/coalescing event), and is capable of identifying all coalesce/breakup events and differentiating between the new drops produced from these events and those which do not undergo such changes. It requires only the instantaneous fragment size, location and velocity output from the simulation at given time intervals, instead of knowledge of the entire flow field at successive simulation time steps, and therefore incur only limited computational cost [139].

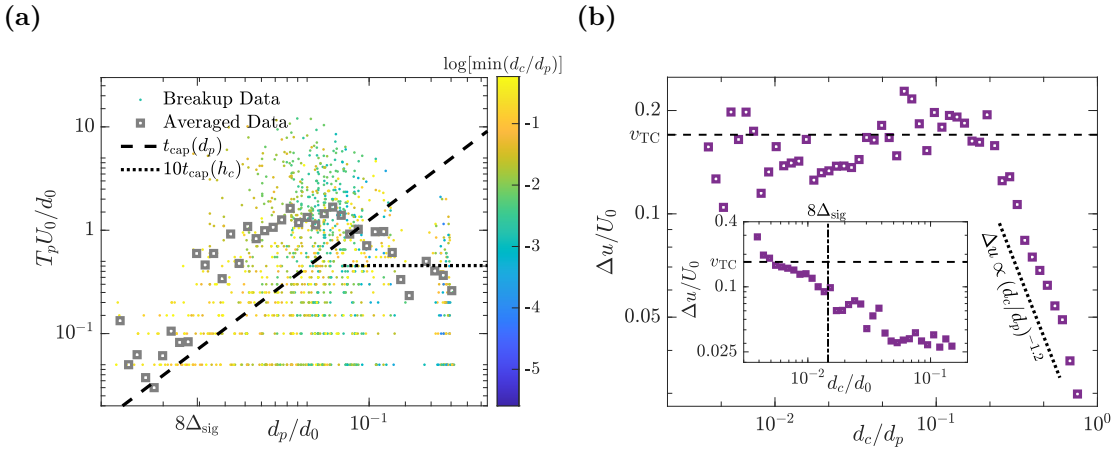

Figure 4.17: (a): The lifetime of the parent fragments T_p as a function of their diameter d_p for $We = 15$ and $Oh = 10^{-3}$. The bin-averaged results are shown in grey hollow squares, and the original data are shown as solid dots, whose colour represents the value of the child/parent diameter ratio. Note that this plot does not include the main drop as a parent which features $d_p/d_0 \approx 1$. (b): Velocity difference between parent and child fragments Δu as a function of the child/parent diameter ratio d_c/d_p is shown in the main plot, whereas the inset plots Δu as a function of the diameter of child fragments d_c.

As the fragments produced from bag breakup are much smaller compared with the parent drop, and therefore have a much smaller Weber number, it is highly unlikely that they will undergo another bag breakup event. However, they may still experience secondary breakup to form smaller fragments as they evolve over time. It is therefore of interest to determine the lifetime of breaking parent fragments T_p using the toolbox of Ref. [139], defined as the interval between their birth and death in two successive breakup events [73]. Figure 4.17a shows T_p as a function of the diameter d_p of parent fragments, with the bin-averaged values of T_p shown in grey squares. The solid dots plotted in the background represent recorded individual breakup events, and are colour-coded

by the logarithm of the diameter ratio d_c/d_p between the parent and the smaller child drop, highlighting a broad distribution of parent fragment lifetime. For comparison, the characteristic capillary time of fragments t_{cap} is also plotted in fig. 4.17a as a function of d_p, which is defined as follows:

$$t_{\text{cap}}(d_p) = \sqrt{\frac{\rho_l d_p^3}{8\sigma}}. \tag{4.9}$$

It can first be seen from the scattered original data that most of the bag film fragments that undergo a secondary breakup fall within the range of $d_p \geq 8\Delta_{\text{sig}}$, which correspond to the 'well resolved' fragments discussed in §4.4.1. Furthermore, the lifetime of fragments T_p satisfying $d_p \leq 0.05d_0$ shows a dependency on r_p that roughly scales with the characteristic capillary time, but this trend breaks down for even larger fragments with $d_p \geq 0.05d_0$. It is noted that the capillary time defined in Eq. (4.9) is proportional to the oscillation period of droplet spherical harmonic modes (Eq. (4.12)). Therefore, the scaling of T_p with t_{cap} for $d_p \leq 0.05d_0$ may suggest that the fragmentation of these fragments is primarily due to large-amplitude nonlinear oscillations which can trigger a capillary breakup [140]. This also explains the large scatters we observe in the lifetime of parent fragments within this size range, as when nonlinearity becomes dominant, the surface oscillations cannot be represented by a single mode, and different modes of perturbation with different oscillation periods might trigger breakup depending on specific fragments. As for even larger fragments with $d_p \geq 0.05d_0$, their lifetime T_p appears to scatter around an average value of $10t_{\text{cap}}(h_c)$, where $t_{\text{cap}}(h_c)$ is the characteristic capillary time based on the critical film thickness $h_c = 3D/2^{L_{\text{sig}}}$. Here $10t_{\text{cap}}(h_c)$ is an estimation of the inertial timescale leading to the capillary breakup of stretching liquid ligaments, which are formed due to hole collision [63]. This suggests that this type of non-local breakup is only dependent on the topological evolution of the stretching liquid ligament, rather than that of the entire parent drop from which the child fragments are torn off; but this remains to be verified in future work.

We also compute the magnitude of the velocity differences Δu between fragment parents and their children at two successive instants when the fragment statistics are collected, and plot them in fig. 4.17b as a function of the ratio between the child and

parent diameter d_c/d_p. It is found that for breakup events where a small child/parent size ratio ($d_c/d_p \leq 0.22$) are detected, the velocity difference Δu appear to show little dependence on d_c/d_p, despite significant scatter. Based on our findings in fig. 4.17a, these breakup events with $d_c/d_p \leq 0.22$ mostly feature small children with large parents. However, breakup events satisfying $d_c/d_p \geq 0.22$ are dominated by small parents and children, and their Δu decreases with increasing values of d_c/d_p, roughly following a power-law scaling $\Delta u \propto (d_c/d_p)^{-1.2}$. We further note that the Δu values of breakup events satisfying $d_c/d_p \leq 0.22$ roughly coincides with the inviscid Taylor-Culick velocity v_{TC}, with an estimation for the bag film thickness h based on the signature level L_{sig}:

$$v_{\mathrm{TC}} \equiv \sqrt{\frac{2\sigma}{\rho_l h}} = \sqrt{\frac{2^{L_{\mathrm{sig}}+1}\sigma}{3\rho_l D}} \approx 0.17 U_0. \tag{4.10}$$

This agrees with the recent confirmation by Neel and Deike [141] that the speed of film drops produced from bubble-bursting can be estimated by v_{TC} to an order of magnitude. An explanation for this approximate agreement is as follows. Prior and up to collision between adjacent hole rims, each rim travels at the Taylor-Culick velocity. The colliding rims of these holes then form liquid ligaments, which exhibit an axial stretching rate comparable to the pre-collision rim speed (i.e. the Taylor-Culick velocity). This stretching rate in turn sets the relative speed of sufficiently small fragments ejected from the parent ligament. The parent ligaments may constitute part of the parent drop, or may themselves have separated from it. Therefore, for a given child droplet size produced by this mechanism, the ratio d_c/d_p may see considerable variation. Consequently, we observe the large range of $d_c/d_p \leq 10^{-2}$ where the parent/child velocity difference remains close to v_{TC}. The inset of fig. 4.17b further shows the velocity difference in breakup events as a function of the child diameter d_c alone; and this time we find that it is the small fragments satisfying $d_c \leq 8\Delta_{\mathrm{sig}}$ that appear to approach v_{TC}, agreeing with our analysis that it is the fragments produced from liquid ligament breakup that are represented within the range of $d_c/d_p \leq 0.22$. Note however that in the inset of fig. 4.17b, Δu continues to increase beyond v_{TC} with decreasing d_c, and does not scatter around v_{TC} as in the main plot. This is most likely because the droplet tracking algorithm has a finite calling frequency [139], and the smallest fragments may

be generated and accelerated by the ambient airflow between two successive instants when this algorithm is called for their detection. The nominal velocity difference Δu for the smallest fragments therefore includes contributions from both the initial ejection velocity (primarily in the radial direction) and the increment due to airflow acceleration (primarily in the axial direction), which causes Δu to increase steadily beyond u_{TC}. As these smallest fragments are scattered in different averaging bins according to the child/parent diameter ratio of the breakup events, the contribution of airflow acceleration to Δu becomes less obvious.

Based on our findings in fig. 4.17b, we introduce the following criteria for determining 'non-local' breakup and coalescing events, respectively:

$$\max\left(\frac{d_{c,i}}{d_p}\right) \leq 0.22, \quad \max\left(\frac{d_c}{d_{p,i}}\right) \leq 4.64, \quad i = 1, 2. \tag{4.11}$$

Otherwise, we term the breakup or coalescing events 'local'. Here the critical child/parent diameter ratio of 0.22 for fragment breakup (and analogously 4.64 for coalescence) separates the two breakup regimes found in fig. 4.17b, where the velocity difference Δu either scatters around v_{TC} or scales with d_c/d_p. Note that the term 'local' here does not mean the parent and child fragments are close to each other in terms of their locations in the physical space, which all such events satisfy; but rather in the sense of the parent and its two children being close in their respective sizes [142]. Equation (4.11) serves as a heuristic criterion for differentiating different types of breakup events. For example, droplets shed directly from the bag feature relatively small $d_{c,i}/d_p$ values as $d_p = d_0$, and their generation events are more likely characterised as non-local breakup. Whereas liquid ligaments or nodes already detached from the bag break up to form secondary fragments, this type of breakup events are more likely characterised as local breakup.

We further plot in fig. 4.18 the ensemble-averaged number density of breakup and coalescing events detected during the bag fragmentation period. It is found that both breakup and coalescing events occur most frequently around $t/\tau = 2.10$. This is most likely when the receding rims fully absorb the bag film and collide with each other, which then triggers a series of corrugated ligament breakup and fragment coalescing events. After this the breakup and coalescing behaviour become less frequent, as the

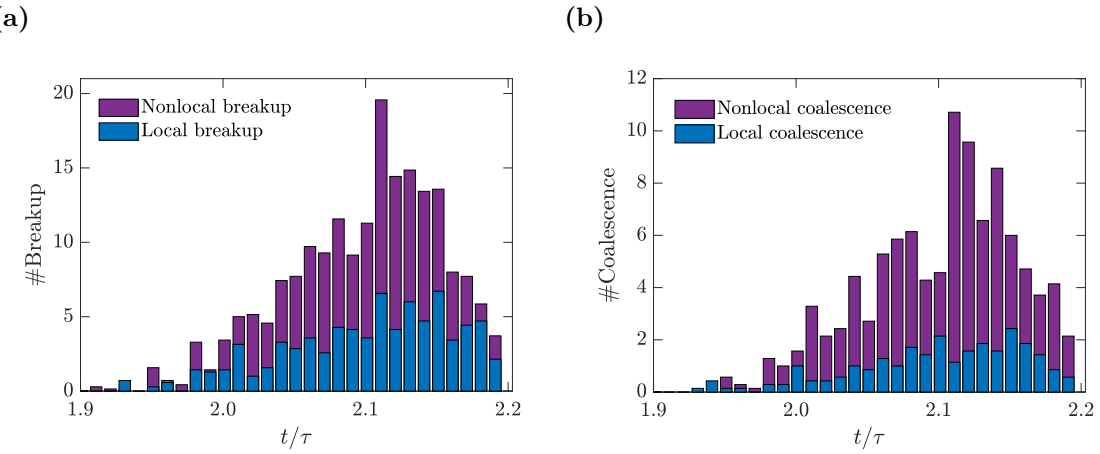

Figure 4.18: Stacked bar charts showing the ensemble-averaged evolution of the number of breakup (a) and coalesce (b) events during the breakup of bag films produced from an initial droplet with $We = 15$ and $Oh = 10^{-3}$. All ensemble realisations are run at $L = 14$, $L_{\text{sig}} = 13$.

corrugated ligaments gradually disintegrate without liquid mass input from the bag film. While there exist 'multistep' breakup events in our aerobreakup simulation outputs, our results in fig. 4.18 suggest that the fragmentation process involved in the aerobreakup problem cannot be well described by a breakup cascade model [142, 143], as non-local breakup and coalescing events producing children with sizes drastically different from their parents are found to dominate this problem, which is different from the entrained air bubble breakup scenario in breaking wave studies [17, 142–145] where the prevalence of local breakup events leads to a well-defined bubble-mass flux supporting breakup cascade models. Note also that breakup events occur much more frequently than coalescing events for bag films, which is expected as the latter requires two adjacent fragments to cross paths at the same time, which only happen for a small portion of neighbouring fragments with specific initial position and velocity configurations.

Apart from identifying all breakup and coalescing events in the spray formed due to aerobreakup, the toolbox developed by Chan *et al.* [139] also enables us to track the evolution of properties of individual fragments during their lifetime. For example, fig. 4.19a shows the evolution of surface energy E_s of individual small fragments recorded from simulations run at $L = 14$ and $L_{\text{sig}} = 13$, with the records of only a few representative fragments highlighted for clarity. The steady-state values of surface energy is also computed based on the volume of corresponding fragments, and plotted in grey

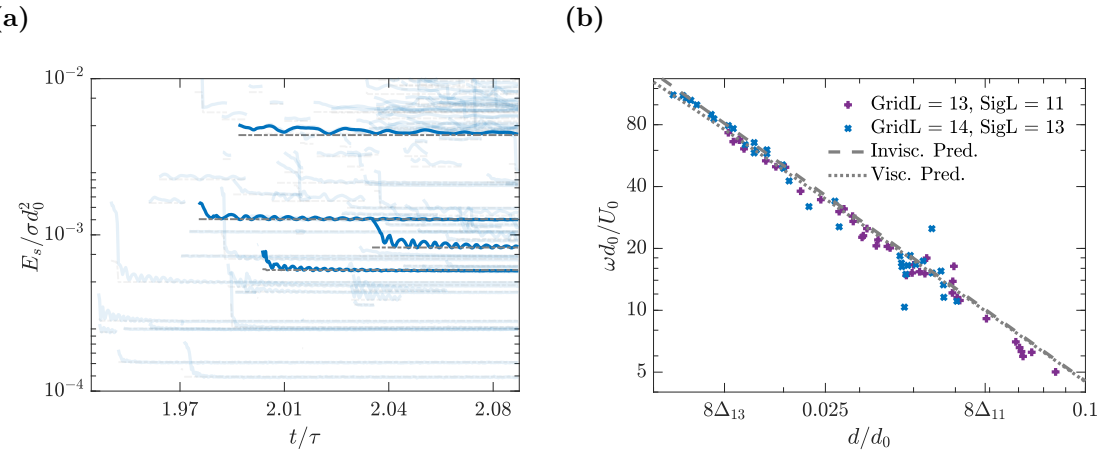

Figure 4.19: Oscillatory behaviour of very small aerobreakup fragments produced from an initial droplet with $We = 15$ and $Oh = 10^{-3}$, with the simulation run at $L = 14$ and $L_{\text{sig}} = 13$. Left: surface energy evolution of individual fragments (blue curves) with their steady-state surface energy values plotted (dashed lines) for reference, with the records of only a few representative fragments highlighted for clarity; right: frequency of the dominant fragment oscillation mode as a function of the fragment radius. Theoretical predictions for inviscid and viscous droplet oscillation frequencies by Prosperetti [146] are also included as dashed and dotted lines, respectively.

dashed lines for reference. It is seen that the oscillation frequency and amplitude vary for each fragment, but all of them clearly demonstrate decaying oscillation behaviour, with their oscillation frequency generally increasing with decreasing fragment radius r (hence decreasing steady-state surface energy values). We further extract the frequency of the dominant oscillation mode of these small fragments at two different grid resolution configurations ($L = 14$, $L_{\text{sig}} = 13$ and $L = 13$, $L_{\text{sig}} = 11$), and plot them against the fragment radius in fig. 4.19b, where an excellent agreement is found for small fragments within the diameter range of $0.01d_0 \leq d \leq 0.1d_0$ with the theoretical predictions of Ref. [146] for the second Rayleigh mode, which is given as follows for an inviscid droplet with density ρ_l and radius R^* at equilibrium:

$$\omega_{n,0} = \sqrt{(n-1)n(n+2)\frac{\sigma}{\rho_l R^*}}, \tag{4.12}$$

where n is the spherical harmonic mode number at which the interface of the droplet is perturbed. The second Rayleigh mode corresponds with $n = 2$, and this mode number is associated with the oblate-prolate shape perturbations which we observed in fig. 4.13. Both the viscous and inviscid theoretical model of Ref. [146] are plotted

in fig. 4.19, which almost completely overlap except for small fragments below $8\Delta_{13}$, where the viscous model shows a slightly better match with the numerical results. This is because the Oh value of 10^{-3} at which simulations discussed in this section are run is very low, such that viscous effects become non-trivial only for very small fragments. Furthermore, for results at both resolution levels shown in fig. 4.19b, the agreement between numerical and theoretical results reaches into their corresponding range of small fragments with $d \leq 8\Delta_{\text{sig}}$, although the fragment size and velocity distributions within this range have not reached grid convergence. Overall, these results demonstrate that fragments satisfying $d \leq 8\Delta_{\text{sig}}$ are governed by well-documented physical mechanisms, for example, rim retraction at the Taylor-Culick velocity and the Rayleigh oscillation theory [146], even though full grid independence in terms of fragment size and velocity statistics is still to be established. It is, therefore, the small droplet production mechanism through ligament fragmentation that remains somewhat grid-dependent, while the droplets resulting from these production events are themselves well-resolved. Nevertheless, we highlight that the film fragmentation process is well-resolved in our numerical simulations with the aid of the MD algorithm [20].

4.4.4 Viscous effects on bag breakup

Having provided an overview of the physical mechanisms governing bag breakup and the subsequent evolution patterns of the fragments at a specific low Oh value of 10^{-3} in §4.4.2, in this section we increase Oh up to 0.05 where viscous effects become moderate, and examine its influence on the bag breakup phenomena. This has not been examined in depth in currently available aerobreakup studies, as most research efforts have been carried out in the inviscid limit featuring very low Oh values [38, 51, 66].

We first provide in fig. 4.20 simulation snapshots showing the bag breakup process for $Oh = 10^{-4}$, 10^{-3}, 10^{-2} and 5×10^{-2} for a qualitative analysis, with $We = 15$ for all cases. As Oh increases from very low ($Oh \leq 0.005$) to moderate ($0.005 \leq Oh \leq 0.05$) values, the bag becomes more 'flattened' and its surface area becomes smaller, and correspondingly the surrounding rim around the bag becomes more prominent. This implies that the inviscid model proposed by Jackiw and Ashgriz [42] predicting the

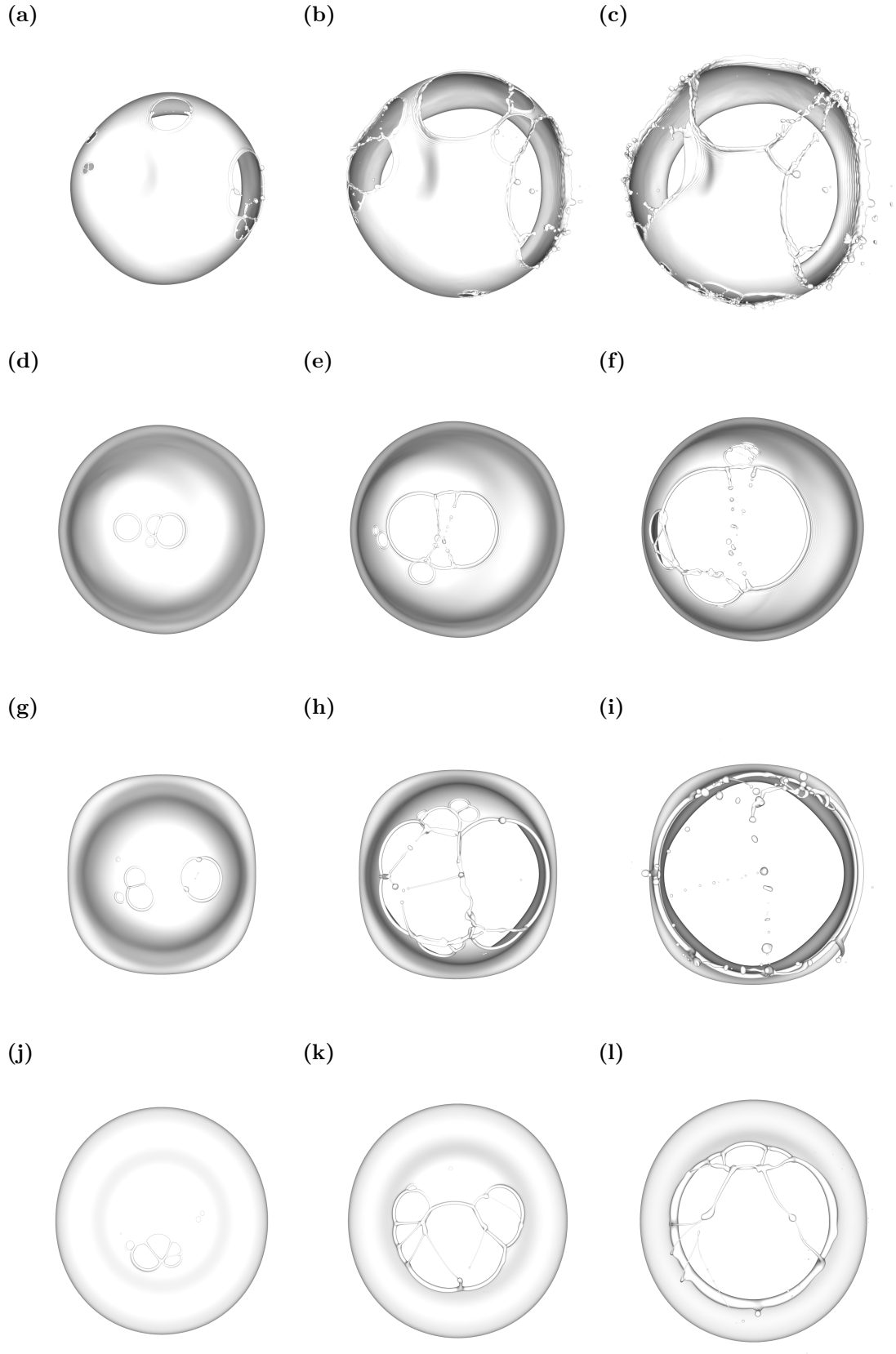

Figure 4.20: Simulation snapshots showing the bag breakup process at different Oh values (10^{-4}, 10^{-3}, 10^{-2} and 5×10^{-2} from the top to the bottom row), where We is fixed as 15. For all cases, $L = 14$ and $L_{\text{sig}} = 13$.

volume of the bag film and rim may need to be extended for a generalisation to the moderate-Oh regime. Furthermore, it is observed that the ligament breakup behaviour changes significantly as the Oh value increases. While at $Oh = 10^{-4}$ the receding liquid rims generate capillary waves propagating through the entire bag [59], and undergo destabilisation patterns similar to what we observed in fig. 4.16, these are not found at higher Oh values, which suggests that these phenomena are highly sensitive to viscous damping effects, and their contribution to fragment statistics becomes negligible with increasing Oh. At $Oh = 10^{-3}$, liquid ligaments typically show long periods of radial oscillation after their formation out of colliding hole rims, and then break up into 'primary' and 'satellite' drops that differ significantly in their sizes. When Oh increases to the moderate value of 10^{-2}, it is found that far fewer satellite drops are produced from ligament breakup, and the 'end-pinching' breakup mechanism comes to dominate as the ligaments now tend to break up on one end repeatedly and form small drops. This may be because the ligaments can be stretched longer and thinner with a higher Oh, and the smaller ligament radius impedes the formation of satellite drops. According to Vassallo and Ashgriz [138], smaller radius of ligaments induces a larger pressure difference that pushes their free ends back in the axial direction much quicker, hence preventing capillary pinch-off in the radial direction that produces the satellite drops. Further increasing Oh to 5×10^{-2} causes the ligaments to be stretched even thinner and produce smaller fragments once they break up, which is because increased viscosity smooths out the variation of the axial velocity along the ligament that drive the pinch-off events [136]. Another side effect appearing at $Oh = 5 \times 10^{-2}$ is that fewer node fragments are observed, which is because the decreased bag area leaves smaller room for generation and mutual collision of more than three holes which produce node fragments. Savva and Bush [59] suggest that at even higher Oh values the liquid rims will disappear, and the thickness of the entire bag film will correspondingly increase as the holes enlarge, although we do not reach this limit in our current numerical simulations.

Figure 4.21 further shows the evolution of the number of fragments satisfying $d \geq \Delta_{\text{sig}}$, the dependence of bag length and width at the onset of bag breakup on the Oh values, and the time- and ensemble-averaged size and speed distribution functions

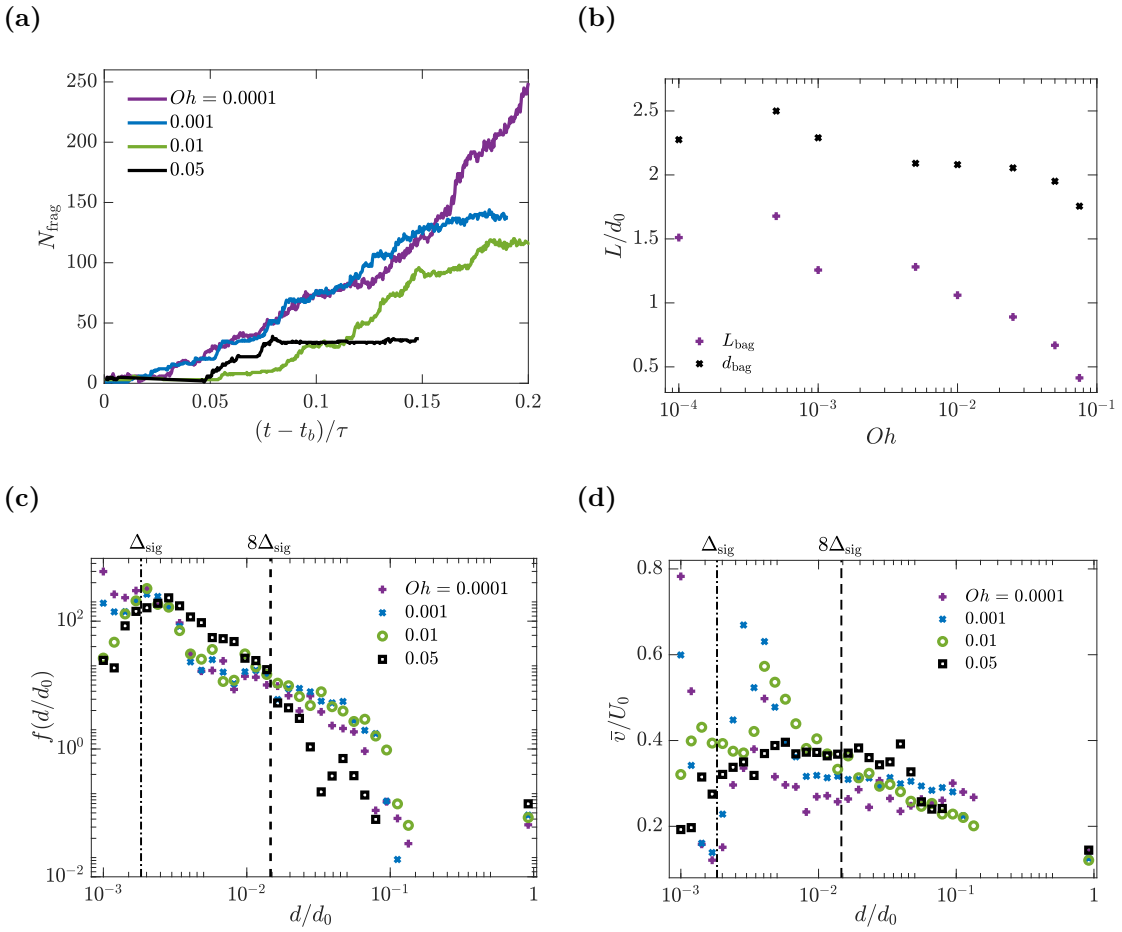

Figure 4.21: (a): Time evolution of the total number of film fragments after the onset of bag breakup for one ensemble realisation with different Oh values. (b): The bag length L_{bag} and width d_{bag} just before the breakup of bag films as functions of the Oh values. (c)(d): Time- and ensemble-averaged size (c) and speed (d) probability distribution functions of aerobreakup fragments with $We = 15$ and various Oh values.

for the three specific Oh values selected in fig. 4.20. Figure 4.21a shows that as the Oh value increases, the number of fragments N_{frag} reached when the bag fully disintegrates decreases, which is because the total area of the bag film decreases, leaving less amount of liquid that feeds the film breakup process. While N_{frag} generally increases over time despite small-scale local oscillations, which most likely arise from relatively rare coalescing events, long periods of time where N_{frag} remains nearly constant can be clearly seen for $Oh = 5 \times 10^{-2}$, as the highly-viscous liquid ligaments can now be sustained for much longer under stretching, and it is their intermittent breakup events that contribute to the isolated sharp growth events in N_{frag}. The length L_{bag} and width

d_{bag} of the bags just before their breakup for different Oh values are measured and shown in fig. 4.21b (which were also presented in fig. 4.3 as scattered points for validation of our numerical results), where it can be seen that our bags are 'flattened' in shape (satisfying $d_{\text{bag}} > L_{\text{bag}}$), and that for $Oh \geq 5 \times 10^{-4}$, both L_{bag} and d_{bag} decrease with increasing Oh, suggesting that the bag area indeed becomes smaller as Oh increases.

Figure 4.21c shows that the fragment size distribution functions for $10^{-4} \leq Oh \leq 10^{-2}$ remain very close to each other. When Oh is further increased to 5×10^{-2}, it is observed that the size distribution function for $d \geq \Delta_{\text{sig}}$ becomes much more convex-shaped, with more 'intermediate' fragments produced within the range of $\Delta_{\text{sig}} \leq d \leq 8\Delta_{\text{sig}}$, and fewer large fragments with $d \geq 8\Delta_{\text{sig}}$. This arises from the coupled effects of reduction of bag film area (hence smaller chance for formation of 'node' fragments, as observed in fig. 4.20l) and breakup of long viscous ligaments into smaller fragments, and implies a reduction in the average fragment size which will be discussed in more details further below. Finally, fig. 4.21d suggests that increasing the Oh value causes the fragment speed to become more evenly-distributed across different fragment sizes, which is probably due to the combined effects of viscous damping of the internal axial velocity distributions of pre-breakup ligaments [136], and the ambient airflow becoming much less turbulent as its viscosity also increases under a fixed viscosity ratio μ^*.

We now analyse the influence of Oh on the ensemble-averaged breakup time $\bar{t}_b$ (defined as the time when the first hole is generated on the film by the MD algorithm) and the ensemble-averaged instantaneous diameter of fragments $\bar{d}_{\text{frag}}$ in fig. 4.22. It should be noted that due to the significant runtime required on supercomputers, the results at a few Oh values in fig. 4.22 are obtained from only one realisation instead of being ensemble-averaged, and these results are differentiated from the others by a cross mark. Nevertheless, from fig. 4.22a, it is seen that $\bar{t}_b$ first remains almost independent of Oh as the latter increases from the low value of 10^{-4} to the moderate value of 10^{-2}, which is likely because the wake flow remains separated from the drop surface, and the thinning process of the bag before the onset of its breakup is determined by capillary and inertial effects, as discussed in §4.3.2. When Oh exceeds the moderate value of

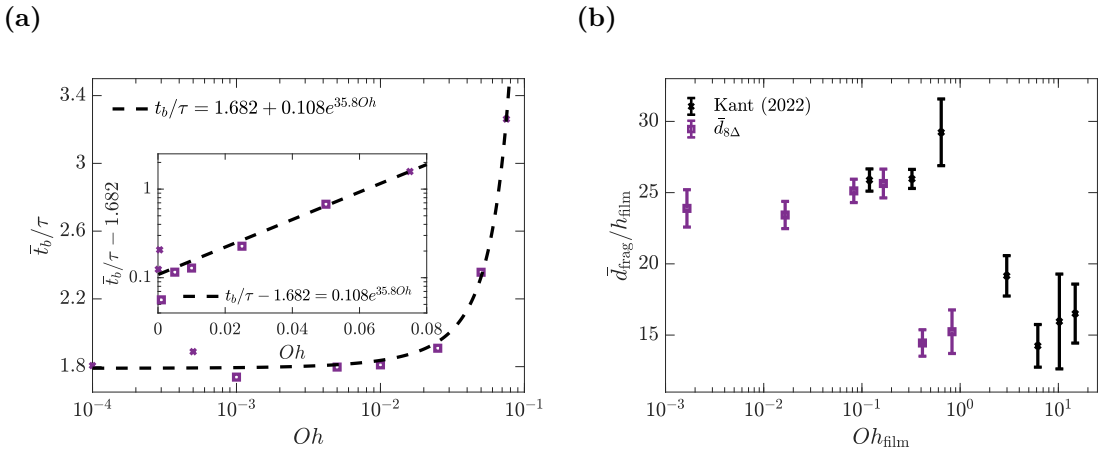

Figure 4.22: The breakup onset time t_b (a) and the instantaneous average diameter $\bar{d}$ of fragments satisfying $d \geq 8\Delta_{\mathrm{sig}}$ (b) as functions of the Oh values, with an exponential model fit for (a). The non-dimensionalised experimental data of Kant *et al.* [38] are included in (b) for comparison. Squares mean the results have been ensemble-averaged over three individual realisations, and crosses mean data from only one realisation is available. For all cases $We = 15$.

10^{-2}, $\bar{t}_b$ is found to increase exponentially with Oh as shown by the fitted model, which may be the consequence of both the transition of the wake region from a turbulent to a laminar status (hence smaller fore-aft pressure difference on the deforming drop that pushes out the bag), and the bag thinning process coming under the domination of a capillary-viscous balance. The hypothesis of the influence of wake region on the growth of t_b is further supported by examining the freestream Reynolds number Re:

$$Re \equiv \frac{\rho_g U_0 d_0}{\mu_g} = \frac{\mu^* \sqrt{We}}{\sqrt{\rho^*} Oh} = \frac{7.381}{Oh}, \tag{4.13}$$

where the critical Oh value of 10^{-2} corresponds to $Re = 7.38 \times 10^2$, which agrees with the order of magnitude of previously-reported Re values at which the wake regions behind a sphere transits to turbulence and vortex shedding is initiated [147]. Overall, this sharp increase of the breakup time $\bar{t}_b$ with increasing Oh beyond 10^{-2} agrees with the early findings that the Oh values do not have significant influence over breakup regimes when they are below 0.1 [47].

Finally, we compute the instantaneous average diameter $\bar{d}_{\mathrm{frag}}$ at the end of film breakup. The averaging is completed for fragments satisfying $d \geq 8\Delta_{\mathrm{sig}}$ over different individual realisations with the same Oh value, which enables us to acquire sufficient

amounts of numerically converged statistics to produce meaningful results. In fig. 4.22b, $\bar{d}_{\text{frag}}$ shows a non-monotonic dependence on the film Ohnesorge number, defined as $Oh_{\text{film}} \equiv \mu_l/\sqrt{\rho_l \sigma h_f}$. While the bag films continues thinning as they undergo fragmentation, we select a constant characteristic film thickness value $h_f = D/2^{L_{\text{sig}}}$ so that our computed average fragment diameters, non-dimensionalised by h_f, match the order of magnitude of the thin-film fragment statistics studied by Kant *et al.* [38], which are also included in fig. 4.22b for comparison. Namely, as Oh_{film} increases from 1.65×10^{-3} to 0.826, $\bar{d}_{\text{frag}}$ first remains close to $25h_f$, followed by an abrupt decrease as it approaches $Oh_{\text{film}} = 0.4$, which corresponds to the drop Oh value exceeding the moderate value of 0.01. This non-monotonic dependency on Oh is also observed in the results of Ref. [38], where an initial increase of $\bar{d}_{\text{frag}}$ to $29.2h_f$ is followed by an abrupt decrease to $14.2h_f$ when Oh_{film} increases beyond unity. Based on our analysis of fig. 4.20 and fig. 4.21, we ascribe the abrupt decrease of $\bar{d}_{\text{frag}}$ with increasing Oh values to the formation of much fewer large 'node' fragments due to the decrease of bag area, and the breakup of ligaments that are stretched much thinner under high viscosity.

4.5 Summary of numerical convergence considerations

Here we provide a brief summary for the influence of the MD algorithm [20] on the numerical convergence behaviour of bag film fragment statistics, which is of reference value for future works on two-phase flows involving topological changes. It is noted that in the aerobreakup simulations, fragments are produced following a sequence of film perforation, hole expansion, rim collision and ligament breakup, regardless of whether the MD algorithm is applied. However, the MD algorithm controls hole formation through a signature level L_{sig}, thereby perforating thin films at a controlled thickness independent of the mesh resolution. Typically, holes are initially isolated and grow for some time before their bordering rims collide with each other. When they do, ligaments form and break up to produce droplets, including primary and satellite drops directly formed out of breaking ligaments (fig. 4.13) and liquid nodes when their neighbouring ligaments break down completely (fig. 4.14). The independence

of the critical film thickness from mesh resolution opens up the possible formation of fragments whose sizes are also grid-independent.

It is observed in fig. 4.10e that when the MD algorithm is applied, droplets greater than $8\Delta_{\text{sig}}$ show grid-converged size statistics; while those smaller than $8\Delta_{\text{sig}}$ do not. Apart from the present results and Ref. [20], empirical lower bounds for grid convergence in the form of 8Δ have also been proposed in other works involving two-phase breakup phenomena (see e.g., Ref. [72]). However, to the knowledge of the authors, there has been no underlying physical mechanism proposed for this lower bound. We suggest a possible explanation as follows. As can be seen in figs. 4.13 and 4.14, bag fragments originate from the breakup of liquid ligaments formed from colliding hole rims. When the MD algorithm [20] is applied, regions on the bag film with thickness around the critical value of $3\Delta_{\text{sig}}$ are perforated, and the diameters of the hole rims gradually increase as they recede over the bag film [63]. Consequently, the diameters of colliding rims should satisfy $d_{\text{rim}} \geq 3\Delta_{\text{sig}}$. Conservation of liquid volume then yields $d_{\text{lig}} = \sqrt{2}d_{\text{rim}}$, where d_{lig} is the diameter of the fused ligament produced from colliding liquid rims. Further assuming that the fused ligament does not generate transverse liquid lamellae which pinch off into 'fine' drops (as seen in Ref. [62]), but instead break up under the Rayleigh-Plateau (RP) Instability, the size of the primary fragments should then satisfy [135],

$$d_{\text{RP}} = 1.9d_{\text{lig}} \geq 8.0\Delta_{\text{sig}}, \tag{4.14}$$

which leads to the lower bound of $8\Delta_{\text{sig}}$ observed in Figs. 4.10c and 4.10e.

However, the statistics of the smallest droplets are still grid dependent when the MD algorithm is applied, which is also noted by Ref. [20]. These small droplets are most likely satellite drops produced from ligament breakup and not directly controlled by the MD algorithm, whose typical size and number have a strong dependence on the initial perturbations present on the ligament [135] which are under mesh-regularized effects. However, even though their production mechanism is not well-resolved, these droplets themselves are sufficiently large to have well-resolved dynamics captured by the numerical mesh (as discussed in §4.4.3, see especially fig. 4.19).

4.6 Conclusions

We have presented in this study the results of both axisymmetric and three-dimensional numerical simulations of droplet aerobreakup. For the axisymmetric simulations, our results were validated by a good agreement with the experimental results of Jackiw and Ashgriz [42], and we were able to explain deviation from their theoretical model (4.6) based on the interaction between the drop surface and the wake vortices. We also look into the thinning of bag films before the onset of bag breakup, and found that at small Oh values capillary effects will cause the thinning rate to exceed that predicted by Villermaux and Bossa [49].

For the three-dimensional aerobreakup simulations, we utilised the MD algorithm [20] for artificial perforation of thin films, which enabled us to minimise pollution of fragment statistics by spurious numerical breakup, and establish grid convergence of fragment statistics for aerobreakup studies for the first time. Afterwards, we analysed the output fragment statistics, and were able to reconstruct the breakup lineage and evolution of individual fragment properties using the postprocessing toolbox proposed by Chan *et al.* [139]. It is found that smaller fragments with their diameters satisfying $d \leq 8\Delta_{\text{sig}}$ are most likely satellite drops produced from ligament breakup and tend to undergo decaying surface oscillations dominated by the second Rayleigh mode, with their ejection velocity set by the colliding liquid rims receding at the Taylor-Culick velocity; while larger fragments satisfying $8\Delta_{\text{sig}} \leq d \leq 0.05d_0$ are most likely primary drops produced from ligament breakup or detached liquid 'nodes' bordering three or more holes, and tend to experience secondary local breakup events due to large-amplitude nonlinear oscillations. Destabilisation of receding rims is also found in some individual realisations, although they do not contribute significantly to fragment production under current simulation configurations.

We find in particular that the bag-breakup problems feature subtle numerical convergence properties:

1. Without the MD algorithm, numerical convergence cannot be achieved for thin film fragmentation owing to the VOF-breakup phenomenon.

2. With the MD algorithm, the production of fragments through thin film fragmentation shows grid convergence for droplet children with diameter $d > 8\Delta_{\text{sig}}$.

3. With or without the MD algorithm, the production of small droplets close to the resolution limit resulting from ligament fragmentation occurs independent of VOF- or MD-induced breakup, and numerical convergence for these production mechanisms is yet to be established in the present study.

4. However, once they are produced, the subsequent evolution of small fragments is well-resolved in the present simulations, even for small fragments approaching the grid resolution.

Finally, we investigated the influence of drop Oh on bag film breakup, and it is found that increasing Oh within the moderate range of $0.005 \leq Oh \leq 0.05$ causes the bag area to decrease and the liquid ligaments to be stretched much thinner, which generally lead to production of fewer fragments with smaller average diameters.

Overall, these results show the utility of the MD algorithm in improving the grid convergence behaviour of fragment statistics and helping to recover previously unresolved fluid physics in two-phase numerical simulations involving breakup of thin films [38], and also shed light on the effect of moderate viscosity on bag breakup which has not been discussed in detail in previous aerobreakup studies [51]. They also pave the way for future studies investigating the later development of the remnant rim and the effects of airphase turbulence and initial perturbations on the deformation and breakup of droplets, while also serving as a stepping stone towards a full-scale numerical study of spume drop generation on the air-sea interface under high wind conditions.

5

Droplet Bag Formation in Turbulent Airflows

Reproduced entirely from a published journal article: Tang, K., Adcock, T. A. A., & Mostert, W. (2025). Droplet Bag Formation in Turbulent Airflows. *Physical Review Fluids.* 10(3), 033604.

5.1 Introduction

Atomisation involves the morphological evolution of the liquid bulk driven by external forces, followed by the formation of corrugated ligaments subject to capillary pinch-off, and terminates in a number of fragments featuring a broad size distribution [8]. The aerobreakup of spherical liquid droplets in uniform airflows is a canonical problem of atomisation and two-phase fluid dynamics [15, 51], and a fragmentation mechanism found in numerous natural and industrial processes, including precipitation [49], sea spume production [23], disease transmission [19, 38], liquid fuel combustion [148] and inkjet printing [149]. In a uniform airflow, droplet aerobreakup can be parameterised by the following four non-dimensional controlling parameters [26]:

$$We \equiv \frac{\rho_g U_0^2 d_0}{\sigma}, \quad Oh \equiv \frac{\mu_l}{\sqrt{\rho_l d_0 \sigma}}, \quad \rho^* \equiv \frac{\rho_l}{\rho_g}, \quad \mu^* \equiv \frac{\mu_l}{\mu_g}. \tag{5.1}$$

Among these, We and Oh are respectively the Weber and Ohnesorge numbers quantifying the ratio of inertial to capillary and viscous to capillary forces, and ρ^* and μ^* are respectively the density and viscosity ratios of the liquid and gas phases. ρ_l, μ_l and ρ_g, μ_g are respectively the density and viscosity for the liquid and gas phase, d_0 is the initial diameter of the droplet, U_0 is the velocity of the ambient airflow, and σ is the surface tension at the liquid-gas interface [25].

The effects of We and Oh on the morphological evolution of droplets undergoing aerobreakup have been extensively investigated in many experimental and numerical studies [29]. Various aerobreakup regimes, including bag, multi-mode (bag-stamen), sheet-thinning and catastrophic breakup, have been observed and the transition thresholds between them have been delineated using these two non-dimensional parameters [27, 32, 34]. Among these regimes, the investigation of the bag breakup regime can potentially shed light on the mechanism of ocean spray production [10], as the bag-shaped geometry of the late-time deformed drops bears a strong resemblance to the small-scale sea-surface perturbations, whose breakup dominates sea spume generation under extreme wind conditions [14, 23]. Most of the early works investigating droplet aerobreakup focus on the analysis of bag formation using hydrodynamic instability models [150], while discussions on the late-time bag breakup mechanisms and fragment statistics are still scarce [42, 65]. The recent experimental work by Jackiw and Ashgriz [51] discussed in detail the physical mechanisms governing the early-time droplet deformation patterns, which are not captured by the simplified hydrodynamic instability models. They also observed that the major pathways leading to film fragment generation are the destabilisation and collision of receding hole rims under centripetal acceleration, and an analytical model predicting the overall volume probability distribution of aerobreakup fragments is developed and verified at various We values [64]. Numerical investigations into fragment statistics, especially those exploiting the flexible Volume-of-Fluid (VoF) interface reconstruction method, have historically been handicapped by the lack of grid convergence, which arises from uncontrolled numerical perforation of bag films when they reach the minimum grid size. However, recently Chirco *et al.* [20] developed a Manifold Death (MD) algorithm that prevents such spurious breakup of thin films

by artificially perforating them once their thickness reduces to a prescribed critical value. This algorithm improves the grid convergence behaviour of the statistics of large bag film fragments, allowing further investigation into the generation mechanism and behaviour of individual aerobreakup fragments [15, 37].

Nevertheless, despite the progress made against these limitations, a complete accounting of the realistic physical environment around droplet breakup has not yet been achieved. One important effect is that of turbulence in the freestream gas flow. In most of the natural phenomena as well as previous experimental studies, droplet breakup occurs in turbulent gas flows. For example, combustion chamber flows may feature a variety of integral length scales [68], and spume generation at the air-sea interface occurs within the turbulent atmospheric boundary layer [14], which can be further modified over time due to coupled wind-wave interactions [4, 151]. In these scenarios, apart from the aerodynamic force exerted by the mean flow, accelerating, shearing and fluctuating effects of the turbulent flow can also affect the deformation and breakup of the droplet [152]. In particular, a detailed and quantitative analysis approach is still lacking for the interaction between the droplet surface and the turbulent vortices present in the ambient gas flow. It is also noted that, although droplet-turbulence interactions have seen some investigation in recent years with important findings, for example, droplets larger and smaller than the Hinze scale demonstrate different behaviour: the former tend to break up through a memoryless process [153] and absorb energy from the ambient flow, while the latter oscillate rapidly or coalesce to release energy to the environment [154]; these studies lack a base flow and are mostly carried out at low density ratios close to 1, which differ from the air-sea interaction scenario featuring finite wind speeds and large density contrasts.

Despite the difficulty in accurately measuring turbulent flow properties [68] and quantifying the response of droplets to external turbulence forcing, there have been a few experimental studies of turbulent aerobreakup in recent years [69, 71, 152]. Among these, Zhao *et al.* [69] utilised perforated plates to generate turbulent counterflows, which in turn drives the deformation of droplets falling from above. It is found that increasing turbulence intensity results in larger lengths and widths of the bag, which

then breaks up to form smaller fragments compared with uniform flow conditions. Xu *et al.* [71, 152] placed droplets within the shear layer of a turbulent air jet, where two new breakup regimes with complicated morphological patterns are identified: butterfly and swing breakup.

Numerical studies of the turbulent aerobreakup problem are even more scarce, most likely due to the difficulty in imposing turbulent fluctuations on a uniform mean flow, and the high computational cost of resolving all turbulence length scales apart from the droplet dynamics. The linear-forcing method proposed by Rosales and Meneveau [155] cannot be directly applied to the aerobreakup problem, despite its recent successful application to turbulent bubble breakup studies [73, 156]. This is because the linear-forcing method is usually implemented with triply-periodic boundary conditions, while in the aerobreakup problem the droplet produces a separated wake region that breaks the fore-aft symmetry of the ambient flow field; in other words, a droplet undergoing aerobreakup can be affected by the wake of its preceding periodic image [157]. On the other hand, synthetic turbulence generation methods produce pseudo-turbulence fluctuation by summation of random Fourier modes (Synthetic Random Fourier Method), or superposition of spatial and temporal coherence on initially uncorrelated random number series (Synthetic Digital Filtering Method). Jiao *et al.* [68], to our knowledge the only investigation of the turbulent aerobreakup problem utilising direct numerical simulations, applied the LEMOS inflow generator [158] at the inlet with outflow boundary conditions. This generator represents turbulence as a series of random spots whose inner velocity distributions are determined by prescribed autocorrelation functions, which enables generation of turbulence structures with prescribed integral length scales and fluctuating velocities on the mean flow [158]. Their results suggest that superimposed air-phase turbulence leads to rapid redistribution of flow pressure around the droplet, which can cause asymmetric deformation patterns coupled with various forms of rotational motion; while the bag film breakup process and associated fragment statistics are not investigated due to limited grid resolution level. It is also noted that this work is carried out at a relatively low liquid-gas density ratio $\rho^* = 20$,

which means that their results might not be directly applicable to air-water systems where the density ratio is much larger.

Overall, it can be seen that currently available results of the turbulent aerobreakup studies are very limited and obtained under considerably different flow configurations. A well-defined methodological framework is still lacking, based on which systematic investigations of this problem can be carried out. Droplet bag breakup within a uniform incoming flow with a superimposed, well-characterised turbulent fluctuation features a simple configuration and therefore serves as a first step towards understanding aerobreakup in more complicated turbulent flow environments, for example, boundary-layer flows where shear effects dominate. We investigate the turbulent aerobreakup problem using two-phase and three-dimensional direct numerical simulations. Our focus is on elucidating the droplet deformation mechanisms up to the point of bag formation, which serves as a basis for future analysis of the breakup behaviour and fragment statistics. Our study is structured as follows. We present in §5.2.1 our problem configuration and parameter space, and then introduce the numerical method in §5.2.2, with a focus on the synthetic turbulence generation method [21] we adopt for producing turbulent incoming airflows. We proceed to present in §5.3 a brief overview of the droplet-turbulence interactions. We then discuss in §5.4 the evolution of the droplet centre-of-mass dynamic properties, and the air-phase pressure distributions giving rise to such evolution trends. Afterwards, we analyse in §5.5 various droplet deformation patterns, including the aspect ratio (§5.5.1), the tilting behaviour (§5.5.2) and the surface curvature and velocity increment distributions (§5.5.3). Finally, we discuss the possible influences of the liquid-gas viscosity ratio in §5.6, and conclude the study in §5.7 with some remarks on future work.

5.2 Formulation and methodology

5.2.1 Problem description

The configuration for our fully three-dimensional direct numerical simulations is shown in fig. 5.1. A liquid droplet with initial diameter d_0, density ρ_l and viscosity μ_l is inserted close to the left boundary, within a turbulent gas phase featuring density

ρ_g and viscosity μ_g. The domain width D is set as $10d_0$, at which the influence of finite domain size on the aerobreakup process can be considered negligible. Outlet flow conditions are applied at the right boundary and a turbulent inflow with mean velocity U_0, fluctuating velocity u^* and injection length scale L_0 is introduced at the left boundary, while zero-gradient conditions are applied at the other domain boundaries.

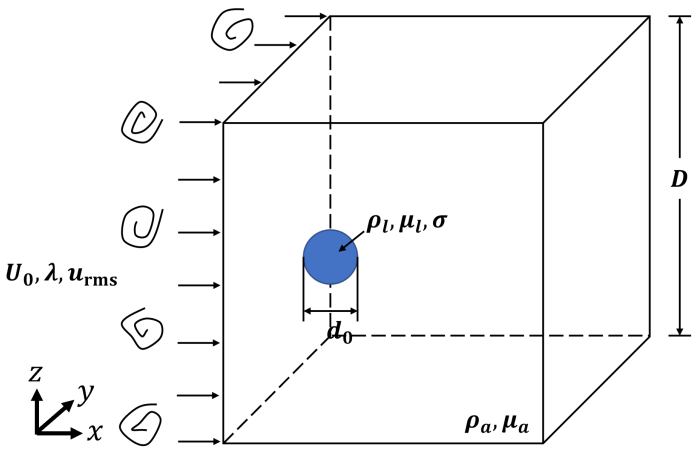

Figure 5.1: Sketch showing the configuration of the turbulent droplet aerobreakup problem.

Among the dimensional parameters introduced above, the fluctuation velocity u^* and the injection length scale L_0 characterises the swirling motion of the largest eddies within the synthesised air-phase turbulence. These in turn lead to two additional non-dimensional groups [72] apart from those already introduced in Eq. (5.1),

$$\widetilde{We} \equiv \frac{2\rho_g \varepsilon^{2/3} d_0^{5/3}}{\sigma} = \frac{2\rho_g u^{*2} d_0^{5/3}{}^{2/3}}{\sigma L_0} \quad , \tag{5.2}$$

$$\frac{d_h}{d_0} \propto \left(\frac{\sigma}{\rho_g}\right)^{3/5} \varepsilon^{-2/5} = We^{-3/5} \left(\frac{u^*}{U_0}\right)^{-6/5} \left(\frac{L_0}{d_0}\right)^{2/5}, \tag{5.3}$$

where $\widetilde{We}$ and d_h/d_0 are respectively the turbulent Weber number and the Hinze scale non-dimensionalised by the initial droplet diameter; and ε is the turbulence dissipation rate per unit volume, which we scale using the nominal value of u^{*3}/L_0 for the turbulent fluctuations we produce. Note that the Hinze scale d_h is a length scale at which turbulence forcing is strong enough to overcome surface tension and break up droplets. The resulting turbulence reaches statistical stationarity after an initial startup transient. It is unforced in the interior of the numerical domain, and shows a gradual decay in the

streamwise direction (parallel to the mean flow), but is homogeneous in the spanwise plane. The turbulence is further characterised in §5.2.2 below.

As for the four non-dimensional parameters defined in Eq. (5.1), namely the mean flow Weber number We, the Ohnesorge number Oh, the density ratio ρ^* and the viscosity ratio μ^*, we fix $We = 15$, $Oh = 0.005$ and $\rho^* = 833$, as is typical for air-water droplet bag breakup. We test three values of μ^*, namely 55, 20 and 10, which allows us to analyse the influence of the liquid-gas viscosity ratio on turbulent aerobreakup in §5.6. Note that the single configuration with $\mu^* = 10$ only serves to examine the effects of μ^* and can be difficult to obtain for liquid-gas systems under experimental conditions. For reference, note that these three viscosity ratios correspond to gas-phase Reynolds numbers $Re \equiv \rho_g U_0 d_0/\mu_g = 1476$, 537 and 268, respectively. At this magnitude of Re, flows past a solid sphere would begin to transition to turbulence [15, 147]. A full list showing the parameter space of this study is provided as Table 5.1, featuring a wide range of $\widetilde{We}$ and d_h/d_0 values including both super- and sub-Hinze-Scale droplets. The presence of significant variations within the turbulent ambient flow necessitates ensemble averaging across multiple realisations, thus enabling us to determine the statistically converged evolution patterns or distributions for physical properties under a certain turbulence configuration. We have therefore provided the number of ensemble realisations in the last column of Table 5.1.

Among the physical properties introduced in Table 5.1, the Taylor microscale λ, the Taylor Reynolds number Re_λ, and the Kolmogorov microscale η are defined as follows [72],

$$\lambda \equiv \sqrt{\frac{15\nu_g}{\varepsilon}}u^*, \quad Re_\lambda \equiv \frac{u^*\lambda}{\nu_g}, \quad \eta \equiv \left(\frac{\nu_g^3}{\varepsilon}\right)^{1/4}, \tag{5.4}$$

where $\nu_g \equiv \mu_g/\rho_g$ is the kinematic viscosity of the gas phase. According to Table 5.1, our turbulence configurations feature Taylor Reynolds number Re_λ ranging from 31.7 to 149, which becomes stronger than the turbulence-bubble interaction studies carried out by Rivière *et al.* [72] for simulations with large u^* or L_0, but remains typical of two-phase turbulence simulations [159, 160].

u^*/U_0	L_0/R_0	μ^*	Re	$\widetilde{We}$	d_h/d_0	λ/d_0	Re_λ	η/d_0	Real. No.
0	0	55	1476	-	-	-	-	-	1
0.25	1	55	1476	2.976	1.008	0.142	52.8	0.0100	5
0.25	1.5	55	1476	2.271	1.186	0.174	64.6	0.0110	5
0.25	2	55	1476	1.875	1.331	0.202	74.6	0.0119	5
0.25	4	55	1476	1.181	1.756	0.284	106	0.0141	5
0.25	8	55	1476	0.744	2.317	0.402	149	0.0167	5
0.5	1	55	1476	11.90	0.439	0.101	74.6	0.0059	5
0.65	1	55	1476	20.12	0.320	0.088	85.0	0.0049	5
0.8	1	55	1476	30.48	0.249	0.080	94.4	0.0042	5
0.25	1	20	537	2.976	1.008	0.236	31.7	0.0213	3
0.5	1	20	537	11.90	0.439	0.167	44.9	0.0127	3
0.65	1	20	537	20.12	0.320	0.146	51.2	0.0104	3
0.8	1	20	537	30.48	0.249	0.132	56.8	0.0089	3
0.25	1	10	268	2.976	1.008	0.334	11.2	0.0359	3

Table 5.1: List showing the parameter space for three-dimensional numerical simulations of turbulent bag formation carried out in this work. For all configurations, $We = 15$, $Oh = 0.005$ and $\rho^* = 833$.

5.2.2 Numerical method

We use the open-source Basilisk numerical library [102] to solve the two-phase incompressible Navier-Stokes equations, which utilises a finite-volume numerical scheme coupled with the geometric volume-of-fluid (VOF) method for fluid interface reconstruction [100]. Usage of an octree-based adaptive mesh refinement (AMR) technique significantly reduces the computational cost for such two-phase simulations. Readers are referred to our previous works [15, 161] for a detailed description of the aforementioned numerical methods. Here we focus on the synthetic digital filtering method proposed by Xie and Castro [21], which we adopt for generating turbulent fluctuations at the inlet.

As is mentioned in §5.1, the linear forcing method of Rosales and Meneveau [155] has seen successful applications in turbulence-bubble interaction studies [72, 156]. It adds a volumetric forcing term to the Navier-Stokes equation in the physical space, which leads to the transition from an Arnold-Beltrami-Childress (ABC) flow at initialisation to well-characterised HIT fluctuations at steady-state. However, this method cannot be applied to the present turbulent aerobreakup problem, otherwise the deformation and breakup of the drop will be affected by the wake of its preceding mirror image. To show

this, a scaling analysis can be made based on existing works on wake velocity defects (the difference between velocities at the same location with and without the obstacle) of spherical obstacles immersed in a turbulent carrier phase [157, 162]. Namely, as the distance to a solid spherical obstacle z increases, the magnitude of the velocity defect Δu decays following a power law of z^{-1} within the range of $z \leq 13d_0$, which asymptotes to z^{-2} at larger z values. In our case where the liquid-gas density ratio ρ^* is large, the droplet can be approximated as a solid obstacle, and the velocity defect caused by the droplet's preceding mirror image reads

$$\frac{\Delta u_i}{u^*} \propto \frac{U_0}{u^*}\left(\frac{D}{d_0}\right)^{-1}. \tag{5.5}$$

For a typical simulation configuration considered in the current work, where $U_0/u^* \approx 10$ and $D/d_0 = 10$, Eq. (5.5) suggests that the magnitude of velocity defect caused by the preceding periodic image of the droplet is the same as the turbulent fluctuating velocity of the ambient airflow. In other words, significant mutual interactions between neighbouring drops would arise across periodic boundaries. While such interactions may be eliminated by further increasing the domain size D, this would incur higher computational costs for resolving turbulence in an enlarged simulation domain, which suggests that the linear forcing method cannot be applied directly with our current computational capabilities. In addition, the turbulent flows generated by this method feature a fixed injection length scale $L_0 = 0.19D$, which does not meet our need to change it as a variable.

Based on the discussions above, it would be ideal to generate and maintain homogeneous and isotropic airphase turbulence in a simulation domain with inflow and outflow conditions. Wu [108] provides an overview of currently available inlet turbulence generation methods and their applications, where at each timestep the inlet velocity condition can be set using flow-field slices imported from an external auxiliary simulation (Strong Recycling Method), slices extracted from a downstream location within the current simulation domain (Weak Recycling Method), or synthesised using random number series or Fourier modes filtered by an approximate correlation function (Synthetic Turbulence Generation). Here we select the synthetic turbulence generation method

proposed by Xie and Castro [21] due to its simplicity, high efficiency and well-validated turbulence statistics including inertial subrange and two-point velocity correlations [110].

The framework of this turbulence generation method is briefly reviewed as follows. Firstly, at each timestep, a two-dimensional random matrix R_{ij} with zero mean and unit variance is generated, and then filtered and normalised to produce two-dimensional space-correlated velocity fluctuation matrices ψ_{ij} for each velocity component,

$$\psi_{m,l} = \sum_{j=-N}^{N} \sum_{k=-N}^{N} b_j b_k R_{m+j,l+k}, \quad 0 \leq m,\, l \leq N_{grid}, \tag{5.6}$$

where $N_{grid} \equiv 2^L$ is determined by the maximum grid level L for resolving turbulence, and $N = 3n = 3L_0/\Delta$ is proportional to the number of grid cells spanned by the turbulence integral length L_0. The filter coefficients b_j are prescribed as follows to approximate exponential velocity correlation functions,

$$b_j = \frac{e^{-\frac{\pi|j|}{2n}}}{\sqrt{\sum_{i=-N}^{N} e^{-\frac{\pi|i|}{n}}}}. \tag{5.7}$$

Time correlation is imposed between turbulent inlet conditions at successive timesteps by computing the new normalised fluctuating velocity components $\Psi(t)|_{m,l}$ based on that of the previous timestep $\Psi(t-\Delta t)|_{m,l}$ and newly synthesised fluctuation matrices $\psi_{m,l}$,

$$\Psi(t)|_{m,l} = \Psi(t-\Delta t)|_{m,l} e^{-\frac{\pi\Delta t}{4T_0}} + \psi_{m,l}\sqrt{1-e^{-\frac{\pi\Delta t}{2T_0}}}, \quad 0 \leq m,\, l \leq N_{grid}, \tag{5.8}$$

where $T_0 \equiv L_0/U_0$ is the injection time scale. Afterwards, the full inlet velocity profile is generated as follows:

$$U_{in}|_{m,l} = U_0 + u_{\text{rms}}^2 \Psi(t)|_{m,l}, \quad 0 \leq m,\, l \leq N_{grid}, \tag{5.9}$$

where the constant coefficient u_{rms}^2 is a simplification of the Cholesky decomposition of the Reynolds stress tensor [110, 111] for homogeneous and isotropic turbulence (HIT) fluctuations. U_{in} is then corrected following Kim *et al.* [111] to ensure constant mass influx, and superimposed at the left boundary of the simulation domain as a time-variant Dirichlet boundary condition.

Following Rivière *et al.* [72], we first run precursor simulations without droplets to create statistically stationary turbulent airflows within the entire simulation domain,

where the maximum grid resolution level for the AMR scheme is set as $L_{turb} = 8$ for simulations with $\mu^* = 55$, and 9 for those with $\mu^* = 20$. In the latter case, we reach a minimum grid size of $\Delta_{turb} = D/2^{L_{turb}} = 0.0195d_0$, allowing us to resolve the air-phase turbulence down to the Kolmogorov microscale η as shown in Table 5.1. Afterwards, we insert the droplet which is allowed to interact freely with the ambient air-phase turbulence, and in the meantime increase the maximum grid resolution level to $L_{drop} = 12$ for resolving the droplet surface, thus obtaining high-fidelity droplet deformation patterns up to the initiation of bag formation.

Finally, the droplet diameter d_0, incoming flow velocity U_0, dynamic flow pressure $p_0 \equiv \rho_g U_0^2/2$, and the characteristic droplet deformation time $\tau \equiv \sqrt{\rho_l/\rho_g} d_0/U_0$ provide the natural reference scales for the length, mass and time quantities associated with the turbulent aerobreakup process. We will henceforth use these to non-dimensionalise the numerical results in the remainder of this study unless otherwise specified.

Verification of air-phase turbulence statistics

Upon the start of the simulation, a turbulent airflow is produced at the left boundary and transported downstream through the initially quiescent simulation domain, eventually reaching a statistical stationary state before the droplet is inserted. Here we inspect a few characteristics of the stationary-state turbulent airflow to evaluate its homogeneity and isotropy. In particular, Table 5.1 shows that the Kolmogorov microscale η/d_0 can be as small as 0.004 for simulations with viscosity ratios $\mu^* = 55$, while the minimum bulk grid size is only $\Delta_{turb}/d_0 = D/d_0/2^{L_{turb}} = 0.078$. This suggests that for simulations with the most severe turbulence fluctuations, we are not yet able to resolve the smallest turbulence length scales where viscous dissipation dominates. Previous studies conclude that only strong airphase eddies at the large turbulence integral scale will impact droplet deformation [68, 69, 71], which indicates that under-resolved small eddies at the Kolmogorov length scale will not be likely to affect the fidelity of the droplet deformation data. Nonetheless, we evaluate the influence of reducing μ^* on the turbulence statistics here, and further investigate its effects on droplet surface statistics in §5.6.

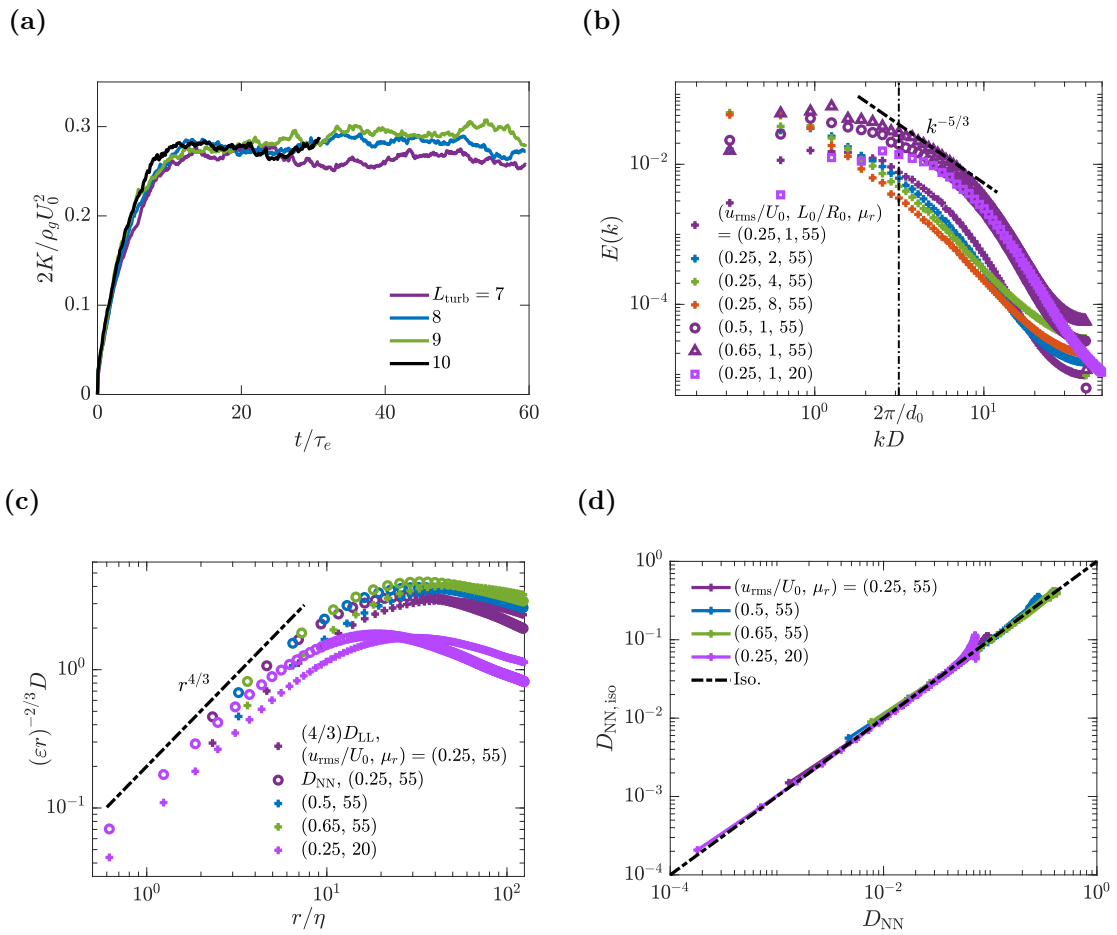

Figure 5.2: (a): Grid convergence test for the air-phase turbulent kinetic energy K for the turbulence configuration of $u^*/U_0 = 0.8$ and $L_0/R_0 = 1$. (b): Power spectrum density of fluctuating velocities u, v and w calculated from time series recorded near the inlet. (c): Compensated second-order turbulence structure functions D_{LL} and D_{NN} as a function of the dimensionless distance r/η, where η is the Kolmogorov length scale. (d): Comparison between $D_{NN}|_{iso}$ and D_{NN} at different values of u^* as a test for flow isotropy.

Figure 5.2a shows the evolution of the averaged air-phase turbulent kinetic energy K within the simulation domain at various values of L_{turb} for $u^*/U_0 = 0.8$ and $L_0/R_0 = 1$, where time is non-dimensionalised by the turnover time $\tau_e \equiv d_0^{2/3}\varepsilon^{-1/3}$ of eddies comparable to the size of the droplet. The turbulent kinetic energy first increases and then saturates as the turbulent airflow fully develops, with the steady-state value reaching grid convergence at a bulk resolution level of $L_{turb} = 8$. This suggests that at $L_{turb} = 8$, the mid-to-large-scale turbulent velocity fluctuations are already well-resolved, although the dissipation behaviour associated with smaller length scales requires further examination. Figure 5.2b shows the turbulence power spectrum $E(k)$ sampled from

the entire simulation domain; where we observe the $-5/3$ power law characteristic of the inertial subrange, and the wavelength corresponding to the droplet diameter $2\pi/d_0$ is found to either fall within or remain close to the inertial regime. The slope of $E(k)$ steepens at higher frequencies, and diminishes again towards the upper bound of the wavenumber k for spectra with $\mu^* = 55$; the latter behaviour is also present in fig. 13 of Xie and Castro's original paper [21]. Indeed, this is most likely because the Kolmogorov microscale and the associated dissipative action at that scale are not fully resolved for $\mu^* = 55$. This behaviour in the spectrum does not appear for $\mu^* = 20$, where the Kolmogorov microscale and dissipation behaviour are well resolved.

We now proceed to assess the isotropy of the turbulence we generate. For this purpose, we introduce the second-order structure functions measured in both the longitudinal (D_{LL}) and transverse (D_{RR}) directions [72, 156, 163] to characterise turbulence fluctuations,

$$D_{LL}(r) = \frac{1}{3}\sum_i \left\langle [u_i(\boldsymbol{x},t) - u_i(\boldsymbol{x} + r\hat{\boldsymbol{x}}_{\boldsymbol{i}},t)]^2 \right\rangle, \tag{5.10}$$

$$D_{NN}(r) = \frac{1}{6}\sum_{i\neq j} \left\langle [u_i(\boldsymbol{x},t) - u_i(\boldsymbol{x} + r\hat{\boldsymbol{x}}_{\boldsymbol{j}},t)]^2 \right\rangle, \tag{5.11}$$

Figure 5.2c shows the structure functions D_{LL} and D_{NN} compensated by the theoretical scaling $(\varepsilon r)^{2/3}$ for HIT fluctuations. Similar to Rivière *et al.* [72], we recover the $D_{LL} = (3/4)D_{NN}$ relationship and the $D_{LL} \propto r^2$ scaling (corresponding to the $r^{4/3}$ scaling observed for the compensated structure functions in fig. 5.2c) at small length scales regardless of the value of μ^*. The compensated structure functions reach their maxima within the range of $20 \leq r/\eta \leq 40$, and for $\mu^* = 20$ their peak values are close to 2, agreeing with theoretical predictions [72, 163]. For $\mu^* = 55$, the peak values become greater than 2, which suggests that the turbulence dissipation ε is underpredicted at the set grid resolution. This is because we are not yet resolving the air-phase turbulence down to the Kolmogorov microscale η in these simulations. At larger values of r both D_{LL} and D_{NN} start to decrease, where flow isotropy is no longer expected, especially along the streamwise direction due to the decay of turbulence intensity.

As an additional test for flow isotropy, we calculate the transverse structure function $D_{NN}|_{iso}$ corresponding to HIT fluctuations from its longitudinal counterpart,

$$D_{NN}|_{iso} = D_{LL} + \frac{r}{2}\frac{\partial}{\partial r}D_{LL}(r). \tag{5.12}$$

Figure 5.2d compares the computed values of $D_{NN}|_{iso}$ according to (5.12) and those of D_{NN} directly determined from our turbulence data according to (5.11), showing an excellent agreement between the two regardless of the specific value of μ^*.

Overall, the results presented in fig. 5.2 suggest that the air-phase synthetic turbulence features satisfactory homogeneity and isotropy. The turbulent energy budget might not be fully recovered due to under-resolved viscous dissipation at small length scales, especially with large values of u^* and μ^*. Similar to grid-generated turbulence [164], the intensity of synthetically generated turbulence also decays further away from the inlet due to the lack of turbulence forcing in the simulation domain, causing large-scale inhomogeneity in the spanwise direction. However, we anticipate that these limitations should not affect the integrity of our results at $\mu^* = 55$, since eddies at the Kolmogorov microscales do not have any discernible influence on droplet deformation, and we do not consider energy exchange between the droplet and ambient turbulent flow in this work.

5.3 Phenomenology of droplet-turbulence interactions

After the air-phase turbulence reaches the statistically stationary state, we insert the droplet and immediately release it to freely interact with the surrounding airflow, while recording its motion and deformation history. In this section, we discuss the influence of air-phase turbulence on droplet morphology qualitatively by inspecting snapshots produced from various individual simulations, with the aim of summarising general patterns of such influences and providing the basis for further quantitative analyses in the following sections.

In fig. 5.3 we first compare the morphological evolution of droplets within a laminar airflow (figs. 5.3a-d) and a typical turbulent airflow (figs. 5.3e-h) with $u^*/U_0 = 0.25$

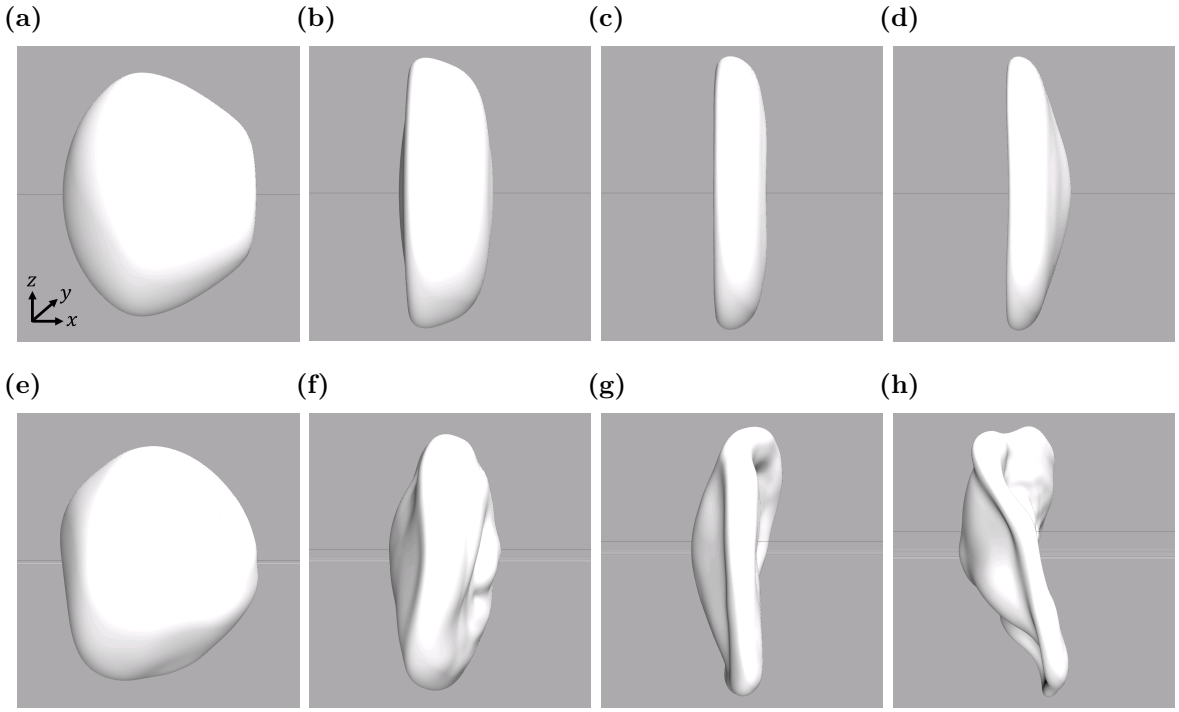

Figure 5.3: Snapshots showing the bag formation process in the laminar airflow case (a-d) in comparison with a typical turbulent airflow case with $u^*/U_0 = 0.5$, $L_0/R_0 = 1$ (e-h). The snapshots are taken at $t/\tau = 0.28$ (a,e), 0.69 (b,f), 1.11 (c,g) and 1.52 (d,h).

and $L_0/R_0 = 1$. While the droplet shape remains axisymmetric until the blow-out of the bag in the laminar aerobreakup case, this symmetry about the streamwise minor axis of the drop can be lost at very early times when turbulence is introduced. As the droplet flattens in the turbulent airflow, its minor axis no longer aligns with the streamwise direction in fig. 5.3h, which will be covered in §5.5.2. Furthermore, significant corrugations arise across the entire droplet surface and disrupt the well-defined bag shape observed in laminar aerobreakup scenarios, which we will discuss in detail in §5.5.3.

Due to the chaotic nature of the ambient airflow, droplets forced by turbulence with identical configurations may exhibit different deformation histories. Figure 5.4 shows the bag shapes from two different turbulence configurations: $(u^*/U_0,\ L_0/R_0) = (0.25,\ 1)$ (a-c), and (0.65, 1) (d-f), where the snapshots in the same row correspond to bag shapes taken from different individual ensemble realisations at the same simulation time. While the bag shapes and orientations vary significantly among different realisations, some common features are still observed for those with the same turbulence configurations.

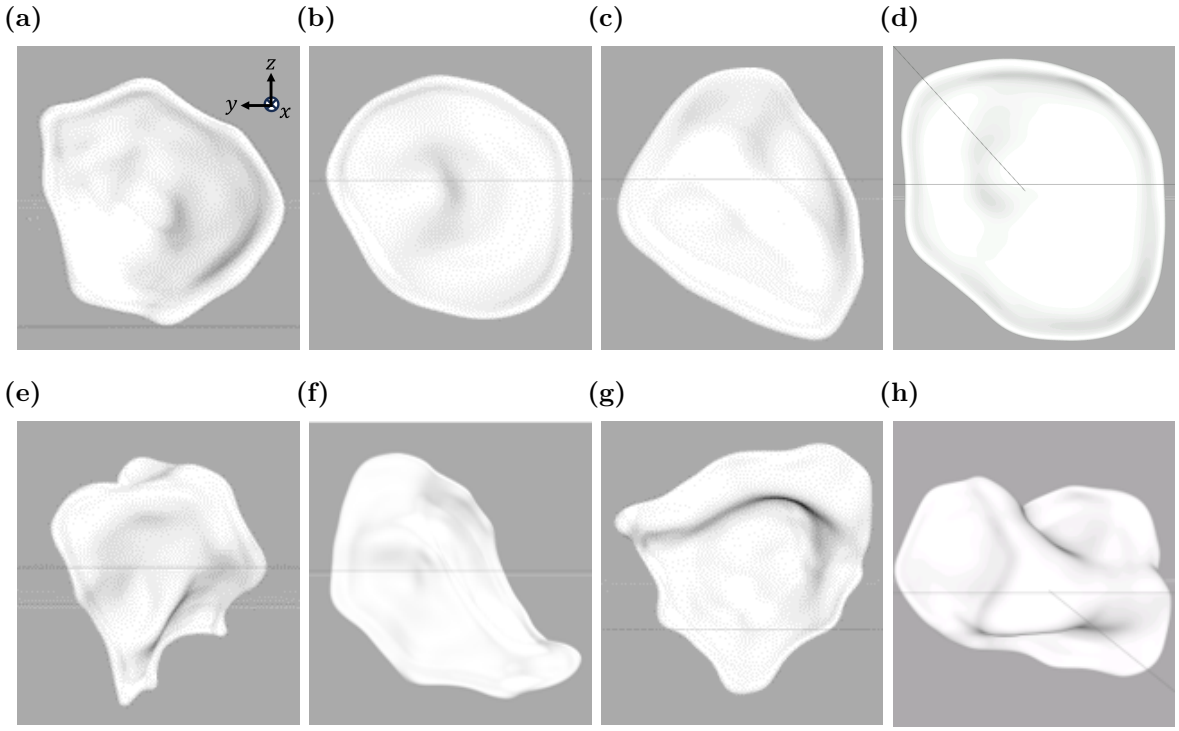

Figure 5.4: Snapshots showing the bags formed at late times, retrieved from different ensemble realisations with the same turbulence configurations. For (a) to (d): $(u^*/U_0,\, L_0/R_0) = (0.25,\, 1)$. For (e) to (h): $(u^*/U_0,\, L_0/R_0) = (0.65,\, 1)$.

Namely, at $u^*/U_0 = 0.25$ we find the bags to feature well-defined peripheral rims and inflating central films similar to laminar bag breakup phenomena observed in previous studies [15, 122], despite mild stretching across the entire bag. However, we find the flattened drops severely distorted at $u^*/U_0 = 0.65$, and the distinction between the peripheral rim and the central bag becomes much less prominent. Ensemble-averaging across different turbulence realisations is therefore necessary for obtaining statistically meaningful data [15, 17].

Apart from the fluctuating velocity u^*, variations in the injection length scale L_0 also lead to qualitative changes in droplet deformation. Figure 5.5 shows the typical late-time bag shapes across a wide range of turbulence configurations $(u^*,\, L_0)$. It is observed that as the turbulence intensity u^* increases (figs. 5.5a-d) or the injection length scale L_0 decreases (figs. 5.5e-h) such that the non-dimensionalised Hinze scale d_h/d_0 becomes smaller than unity, the shape of the deformed droplet deviates further away from the well-defined laminar aerobreakup morphology, as is already observed

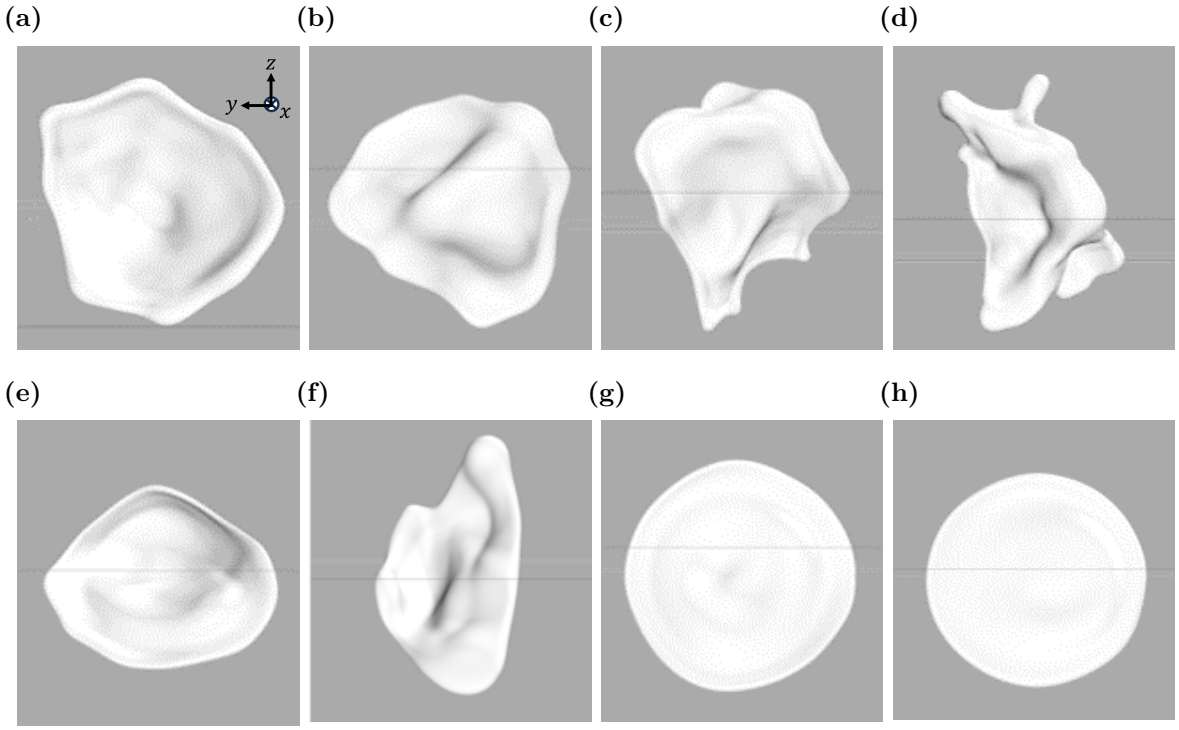

Figure 5.5: Snapshots showing the bag morphology under different turbulence configurations. For (a) to (d): $L_0/R_0 = 1$, while $u^*/U_0 = 0.25$ (a), 0.5 (b), 0.65 (c), and 0.8 (d). For (e) to (h): $u^*/U_0 = 0.25$, while $L_0/R_0 = 1.5$ (e), 2 (f), 4 (g), and 8 (h). The Hinze scales d_h/d_0 for (a)-(h) are respectively: 1.008 (a), 0.439 (b), 0.320 (c), 0.249 (d), 1.186 (e), 1.331 (f), 1.756 (g), 2.317 (h).

in fig. 5.4. Instead, large-scale distortion arises across the bag, and the peripheral rim becomes increasingly corrugated, forming sharp protrusions (fig. 5.5c) which evolve into liquid nodes (fig. 5.5d) [51] bearing some resemblance to the 'handle' structures observed by Cannon *et al.* [165] for $\rho^* = \mu^* = 1$. This also matches qualitatively with previous multiphase turbulence studies [72, 73], where the morphological evolution and breakup behaviour of the bubble or droplet relies strongly on d_h/d_0. Similar rim protrusions are not observed in previous numerical studies of laminar aerobreakup [15, 122] but reported in experimental bag breakup studies, as they eventually pinch off to produce node drops. It is found that either the Rayleigh-Plateau (RP) or the Rayleigh-Taylor (RT) instability can explain their formation [44, 51].

It is also noted that as the injection length scale L_0 increases, the late-time bags recover the laminar axisymmetric shape with only an overall tilting motion, resembling the bag morphologies reported by Jiao *et al.* [68]. This is expected as the droplet now

interacts with turbulent eddies of larger size in individual realisations, and therefore experiences less severe ambient flow velocity variation across its diameter with a fixed turbulent fluctuation intensity. Indeed, this agrees with Wang *et al.* [166] and Xu *et al.* [167] that eddies interact preferentially with particles featuring diameters closest to their sizes. Overall, the bag morphologies observed in fig. 5.5 suggest that 'mild' or 'severe' modifications of the bag shape by ambient turbulence can be predicted based on the non-dimensionalised Hinze scale value d_h/d_0: the former occurs when $d_h/d_0 > 1$, whereas the latter occurs when $d_h/d_0 \leq 1$. The validation of this heuristic criterion requires ensemble realisations at more ambient turbulence configurations, and is therefore outside the scope of the current work.

5.4 Droplet dynamics

We now seek to inspect the evolution of the centre-of-mass dynamic properties of the droplet, including both velocity and acceleration, which is closely tied to the droplet deformation history and will shed light on the overall effect of the ambient turbulence on the droplet.

In fig. 5.6, we present the streamwise and radial components of the droplet centre-of-mass velocity U_x and $\dot{r} \equiv \sqrt{U_y^2 + U_z^2}$ at both viscosity ratios $\mu^* = 55$ and 20. Here, $\dot{r}$ is the component of the droplet velocity orthogonal to the mean flow. For example, in a laminar freestream flow which remains strictly axisymmetric, such as early times, this component would be zero. The results have been ensemble-averaged to reduce variations across different individual realisations. It is observed that the introduction of air-phase turbulence leads to an increase of both U_x and $\dot{r}$; in other words, ambient turbulence intermittency contributes to droplet acceleration in both the axial and radial directions. It is particularly interesting to note that, according to figs. 5.6a and 5.6c, the evolution patterns of the streamwise velocity U_x do not depend strongly on the air-phase turbulence configurations within our parameter space, including u^*, L_0 and μ^*; and compared with the laminar aerobreakup case, a consistent enhancement in the increasing rate of U_x is reached at around $t = 0.6\tau$ for all turbulent aerobreakup cases, when the droplet is about to become fully flattened. However, fig. 5.6c suggests that increasing

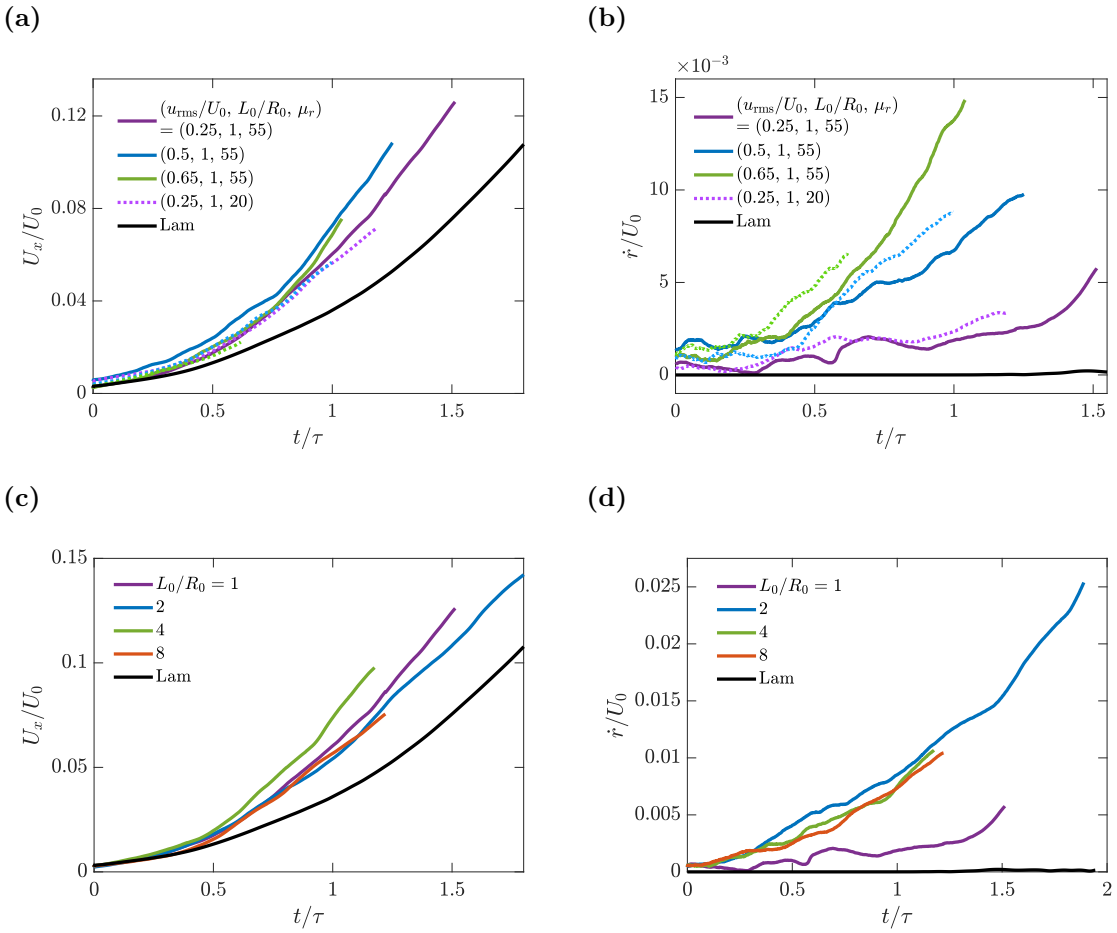

Figure 5.6: Evolution of the ensemble-averaged droplet centre-of-mass velocity U_x (a,c) and radial velocity $\dot{r}$ (b,d), measured at different fluctuating velocities u^* (a,b) and injection length scales L_0 (c,d).

u^* causes the radial component of the droplet velocity $\dot{r}$ to increase, although the magnitude of $\dot{r}$ still remains much smaller than its streamwise counterpart U_x, meaning that the droplet is transported mostly in the mean flow direction. This is expected since the large liquid-gas density ratio ρ^* ensures flow separation and hence a large pressure difference between the frontal and leeward sides of the droplet, which dominates droplet acceleration even when large turbulence fluctuations in the cross-stream directions are present. It is also likely that the increase in $\dot{r}$ incorporates the contribution of irregularity in the droplet internal flows, which causes the droplet morphology to deviate further away from axisymmetry at large turbulence fluctuating speeds u^*/U_0.

To allow for detailed analysis of the droplet streamwise acceleration patterns,

especially around $t/\tau = 0.5$ where the significant acceleration by ambient turbulence is observed, we differentiate U_x numerically in time to obtain streamwise acceleration a_x, and non-dimensionalise the results as a drag coefficient $C_{D,x}$ [122],

$$C_{D,x} \equiv \frac{2m_d}{\rho_g U_0^2 \pi R_0^2} a_x = \frac{8}{3}\frac{\rho_l}{\rho_g}\frac{R_0}{U_0^2} a_x. \tag{5.13}$$

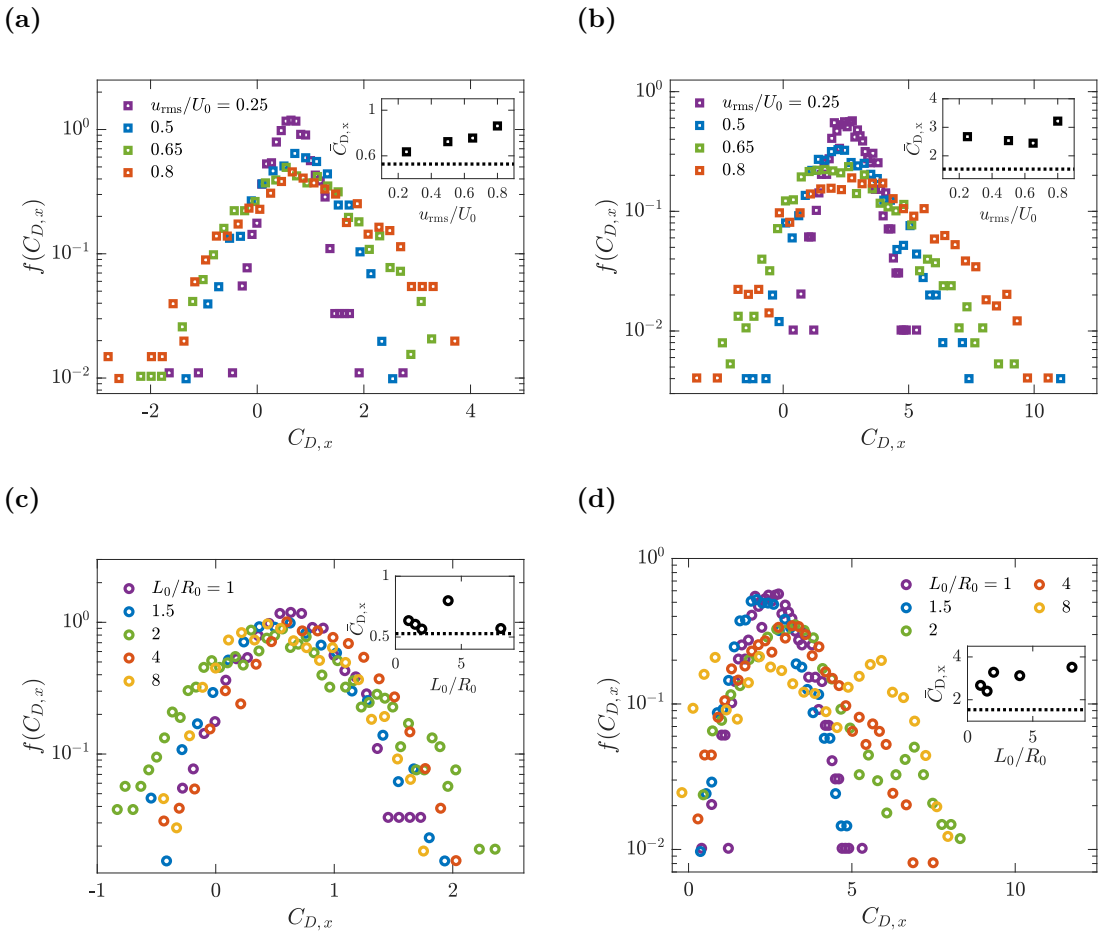

Figure 5.7: Distributions of droplet streamwise drag coefficients $C_{D,x}$ measured at different turbulence configurations. (a,c) and (b,d) are sampled within time windows $0 \leq t/\tau \leq 0.173$ and $0.485 \leq t/\tau \leq 0.693$, respectively. For (a,b), $L_0/R_0 = 1$ and for (c,d) $u^*/U_0 = 0.25$. The insets show averaged drag coefficients of turbulent aerobreakup cases (scattered data) compared with their laminar counterparts (dashed line).

Due to the presence of strong fluctuations in the instantaneous streamwise droplet acceleration a_x, we select two time-windows for comparison: $0 \leq t/\tau \leq 0.173$ and $0.485 \leq t/\tau \leq 0.693$, which correspond to the early and intermediate deformation stage respectively, and present in fig. 5.7 the distributions of instantaneous streamwise

drag coefficients $C_{D,x}$ sampled across all ensemble realisations, rather than directly showing the original time sequence of streamwise acceleration. Figure 5.7a show that at early times, the distributions of $C_{D,x}$ are largely symmetric. The mean values of $C_{D,x}$ increase over time, as indicated by the shift of the maxima of $C_{D,x}$ towards larger values. Figure 5.7b suggests that while the distribution of $C_{D,x}$ is still largely symmetric for $u_{rms}/U_0 \leq 0.5$, a skew towards larger $C_{D,x}$ values occurs at larger turbulence fluctuating velocities. Interestingly, while increasing turbulence intensity u^* causes the $C_{D,x}$ distribution to broaden, it does not significantly influence the mean value of $C_{D,x}$ as shown in the inset of fig. 5.7b, agreeing with our earlier observations of fig. 5.6a. On the other hand, fig. 5.7c suggests that increasing L_0 does not cause any consistent change in the shape of the $C_{D,x}$ distribution at early times. For turbulent aerobreakup cases with $L_0/R_0 \geq 2$, fig. 5.7d suggests that the $C_{D,x}$ distributions become double-peaked, which is especially prominent for $L_0/R_0 = 2$ and 8. The distribution for $L_0/R_0 = 4$ also features a skew towards large $C_{D,x}$, while the mean values for $C_{D,x}$ remain largely unaffected by L_0. We consider this change in the distribution shape of $C_{D,x}$ to be most likely associated with the increased occurrence of large-scale velocity fluctuations within the ambient turbulence. Indeed, as the injection length scale of the turbulence becomes larger than the droplet, it is expected that the interior structure of the turbulent eddies becomes more important in controlling the instantaneous droplet acceleration. A detailed investigation of this phenomenon is left for future work.

Agreeing with our observations in fig. 5.6, the insets of fig. 5.7 show that turbulent aerobreakup cases (shown in scattered data points) indeed feature larger $\bar{C}_{D,x}$ values compared with their laminar aerobreakup counterparts, while our current results do not indicate any clear dependence of $\bar{C}_{D,x}$ on the turbulence parameters u^* and L_0. We also find that while the magnitudes of instantaneous $C_{D,y}$ and $C_{D,z}$ values are comparable with $C_{D,x}$ [168], their mean values remain close to zero without any obvious evolution over time (not shown here). Overall, these results confirm our observation in fig. 5.6 that introducing air-phase turbulence causes a nontrivial streamwise mean acceleration effect, which most likely arises from a qualitative change in the ambient flow field that does not depend significantly on specific turbulence configurations.

The recorded extreme values in $C_{D,x}$, on the other hand, are found to appear more frequently at large values of u^* and L_0, which are probably associated with more extreme fluctuations in the ambient turbulence.

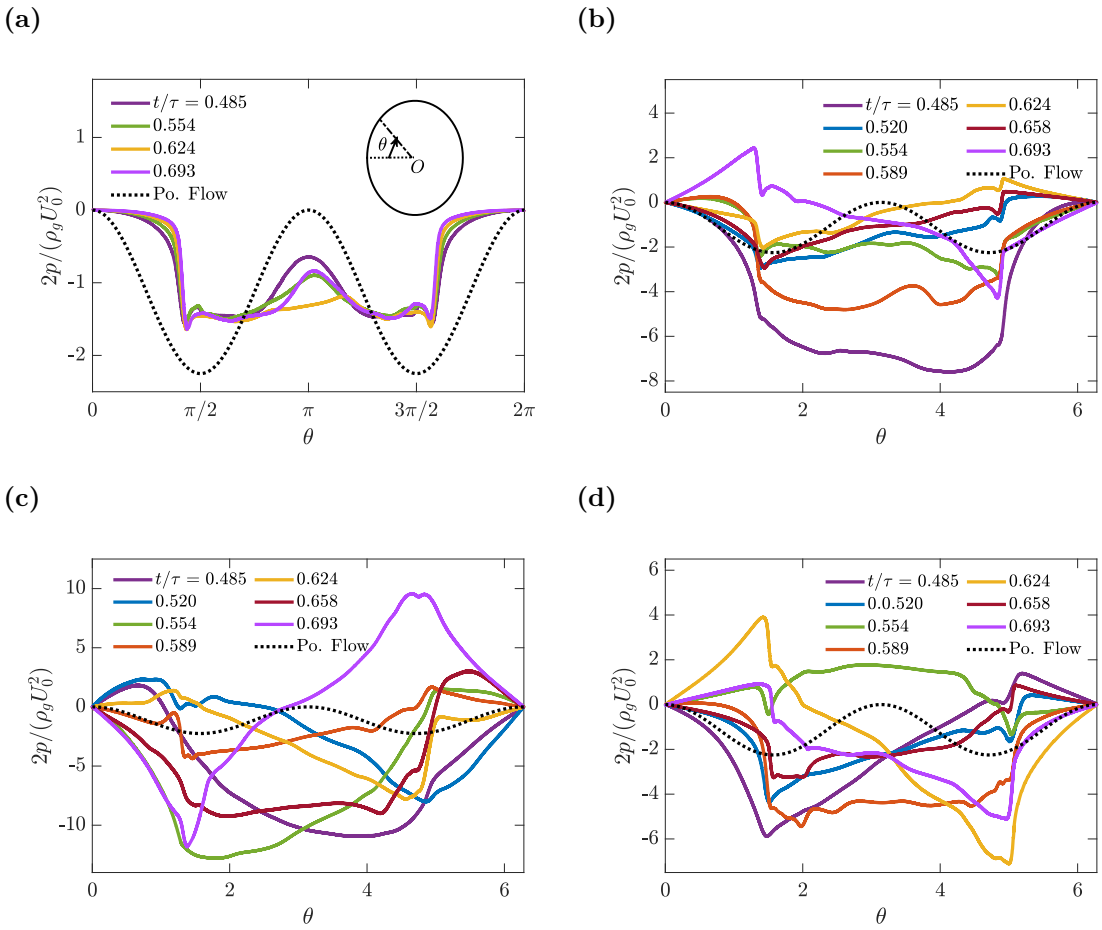

Figure 5.8: The air-phase pressure profiles close to the droplet surface, sampled within the plane $z = 0$ at different turbulent fluctuating velocities u^*. From (a) to (d): laminar airflow (a), $(u^*/U_0,\, L_0/R_0) = (0.25,\, 1)$ (b), $(0.5,\, 1)$ (c) and $(0.25,\, 4)$ (d). The inset of fig. 5.8a shows how the angle θ is calculated along the drop surface, and the potential flow solution for laminar airflow around a sphere is included in all subfigures for comparison.

To further elucidate the physical mechanism leading to the droplet acceleration patterns we observed, we now inspect the distribution of air-phase pressure around the droplet. In fig. 5.8 we show the evolution of pressure profiles within the period of $0.485 \leq t/\tau \leq 0.693$ for individual realisations, when the flattened droplet is further accelerated by airphase turbulence. These pressure profiles are sampled close to the droplet surface within the reference plane $z = 0$, and plotted as a function of polar

angle θ traversing the droplet surface in the clockwise direction as shown in the inset of fig. 5.8a. Here, $\theta = 0$ corresponds to the leftmost point on the windward surface, where the pressure values have been referenced to $p = 0$ to facilitate comparison across different turbulence configurations. Figure 5.8a shows the pressure profiles obtained from laminar aerobreakup, where the minima at $\theta = \pi/2$ and $3\pi/2$ increase compared with the potential flow solution, a known effect of wake flow separation [15]. These laminar profiles are relatively stable without significant changes over time. Unique to the laminar aerobreakup case is the pressure maximum at $\theta = \pi$, which is present at all times therein except $t/\tau = 0.624$, when it briefly disappears. This most likely corresponds to the attached wake vortices, which oppose the movement of the leeward side of the droplet at early times [15, 118].

As airphase turbulence is introduced, the pressure maxima at $\theta = \pi$ are no longer consistently observed, indicating that the attached vortices are now disrupted by external turbulent forcing. Moreover, figs. 5.8b and 5.8c show that the minima in the wake region decrease and become significantly more negative than the potential-flow prediction as the turbulent fluctuating velocity u^* increases, corresponding to an increase in the instantaneous pressure-induced force felt by the droplet. While our problem is transient in nature and differs from the configuration of Peng and Wang [169] where the spherical particles are fixed in turbulent ambient flows, our observations match their report of pressure-drag amplification by external turbulence. An earlier study by Rind and Castro [170] discussed this pressure decrease in the wake of a disc-shaped obstacle in detail, where it is ascribed to increased entrainment of external turbulent fluid into the separated region and the wake vortices forming closer to the drop surface. The pressure profiles are also found to change significantly within and between the sampling periods when ambient turbulence is present. While our limited pressure-field data do not permit high-frequency time averaging to fully confirm this, the time-averaged turbulent flow field in the droplet wake might feature similar pressure profiles that do not depend strongly on either u^* or L_0, thus preventing accumulation of streamwise acceleration at larger u^* or L_0 values and leading to the universal acceleration rate we observed in fig. 5.7. Indeed, while increased turbulent fluctuations lead to temporary

peaks in the pressure profiles (e.g. as seen in the $t/\tau = 0.693$ curve of fig. 5.8c), the rate of pressure redistribution around the droplet increases as the ambient turbulence becomes more severe [68], so that these momentary peaks are approximately smoothed out over time, thus ensuring a net acceleration effect largely insensitive to the external turbulent forcing conditions as we observed here.

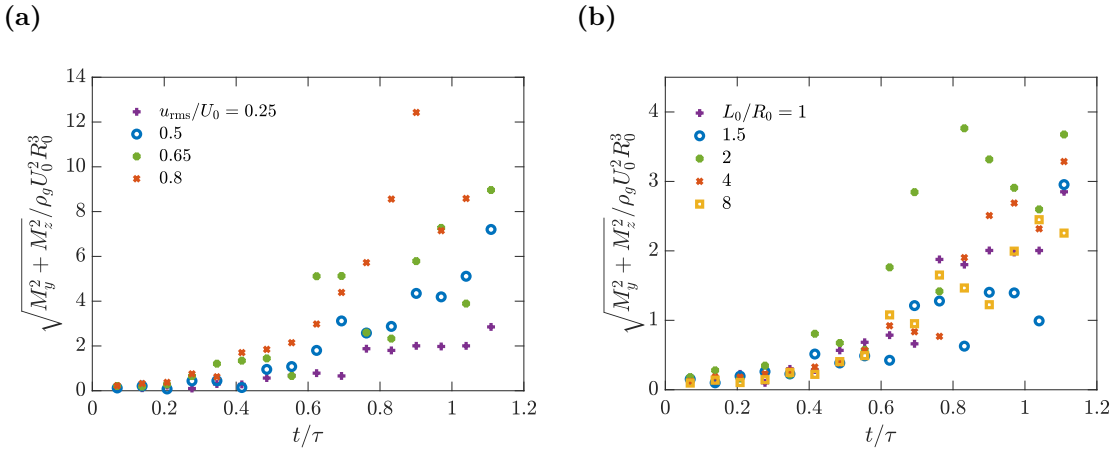

Figure 5.9: The evolution of the hydrodynamic torque $\sqrt{M_y^2 + M_z^2}$ acting on the droplet at different turbulence fluctuating velocities u^* (a) and L_0 (b), calculated using the pressure field in the vicinity of the droplet surface.

Another interesting observation from fig. 5.8 is that the pressure maxima do not always occur at $\theta = 0$. In other words, the stagnation point may drift away from the centre of the droplet frontal face under the disruption of ambient turbulence. Moreover, many instantaneous pressure profiles show extreme values appearing at $\theta = \pi/4$ and $3\pi/4$ in an anti-symmetric pattern (e.g., $t/\tau = 0.693$ in fig. 5.8b), suggesting a net torque acting on the flattened droplet. To further explore this, we compute the evolution of the hydrodynamic torque $\boldsymbol{M}$ acting upon the droplet,

$$\boldsymbol{M} = \iint_S \boldsymbol{r} \times (-p\delta_{mn} + 2\mu_g S_{mn}) d\boldsymbol{S}, \tag{5.14}$$

where $\boldsymbol{r}$ is the displacement vector from the droplet centre-of-mass to a point on its surface, δ_{mn} is the Kronecker symbol, and S_{ij} is the strain-rate tensor of the ambient airflow [171]. It is found that the streamwise torque component of M_x remains close to zero at all times, regardless of the turbulence configuration. The evolution patterns of

the other two cross-stream torque components M_y and M_z are similar to each other while differing considerably from that of M_x, and thus we present the evolution of $\sqrt{M_y^2 + M_z^2}$ in fig. 5.9. Initially, $\sqrt{M_y^2 + M_z^2}$ remains small and comparable in magnitude to M_x (not shown in the figure) for all simulation cases up to $t/\tau \approx 0.5$, as is the case for the fixed particle study of Wang *et al.* [166] (see e.g. their fig. 3). For $t/\tau \geq 0.5$, the fluctuation in $\sqrt{M_y^2 + M_z^2}$ becomes significantly amplified. Since according to fig. 5.3, the droplet is being compressed in the streamwise direction over this period, the results shown in fig. 5.9a suggest that the droplet experiences much greater hydrodynamic torques as it undergoes flattening. This rapid growth in $\sqrt{M_y^2 + M_z^2}$ can potentially lead to droplet rotation and is thus the direct cause of its tilting behaviour, which we will analyse in more detail later in §5.5.2, alongside the possible origins of such growth patterns.

5.5 Droplet deformation patterns

In this section, we provide a quantitative analysis of the deformation patterns of droplets interacting with turbulent ambient airflows up to the point of bag formation. We start with quantifying the global extent and characteristics of droplet deformation using spherical harmonic decomposition in §5.5.1, and move on to examine the droplet tilting behaviour in §5.5.2. We finish this section with a discussion on the droplet surface corrugation patterns in §5.5.3.

5.5.1 Global features

We first analyse the deformation characteristics of the droplet using spherical harmonic decomposition following Perrard *et al.* [156], which allows us to investigate how surface deformation patterns of different length scales evolve as the droplet undergoes strongly nonlinear surface deformation. To assess the overall droplet deformation, we introduce the root-mean-squared deformation ζ_Ω measured from an integration over all solid angles $d\Omega \equiv dA/(r - R_0)^2$,

$$\zeta_\Omega^2 = \frac{1}{4\pi} \iint_S (r - R_0)^2 d\Omega, \tag{5.15}$$

Where R_0 is the radius of the undeformed droplet, and $r - R_0$ reflects the local deformation extent on the droplet interface, which is assumed to be single-valued. Figs. 5.10a and 5.10b show the ensemble-averaged early-time evolution of ζ_Ω for different airphase turbulence configurations. ζ_Ω is found to undergo an accelerated increase over time for all cases recorded, without saturating or oscillating trends observed at smaller We values in the absence of ambient mean flows [156, 172]. Moreover, turbulence is found to cause a slight increase in the total deformation for most of the turbulent aerobreakup cases in comparison with their laminar aerobreakup counterpart; except $(u^*/U_0,\, L_0/R_0) = (0.25,\, 8)$ where ζ_Ω is found to decrease instead, which is probably an effect of the ensemble size. These changes in ζ_Ω are not dramatic, which is most likely because the turbulence-induced deformation corresponds to small-amplitude high-mode perturbations, and does not significantly modify the dominant mode-2 perturbations corresponding to droplet flattening, as will be discussed below.

Here we introduce the spherical harmonics $Y_l^m(\theta,\, \phi)$, and the deformation coefficient corresponding to each spherical harmonic mode $a_{l,\,m}$ can be calculated as follows,

$$a_{l,\,m} = \frac{1}{4\pi} \iint_S (r - R_0) Y_l^m(\theta,\, \phi) d\Omega, \tag{5.16}$$

which is realised through a Voronoi decomposition of the droplet surface during postprocessing. In the absence of a mean flow and within the limits of linear deformation, the coefficients $a_{l,\,m}$ are solutions to a set of damped oscillator equations [146, 156]. As harmonic modes with the same value of l feature the same oscillation frequency, we introduce the global coefficient a_l quantifying the total potential energy contained in all spherical harmonic modes l,

$$a_l^2 = \sum_{m=-l}^{l} a_{l,\,m}^2, \tag{5.17}$$

which is in turn associated with the root-mean-squared global deformation ζ_Ω (5.15) as follows via the orthogonality of the spherical harmonic bases,

$$\zeta_\Omega^2 = \sum_{l=1}^{+\infty} a_l^2. \tag{5.18}$$

Among these global coefficients, we select the droplet centre position $\boldsymbol{r_c}$ as the origin for the spherical coordinate system such that $a_1 = 0$. The mode-2 deformation

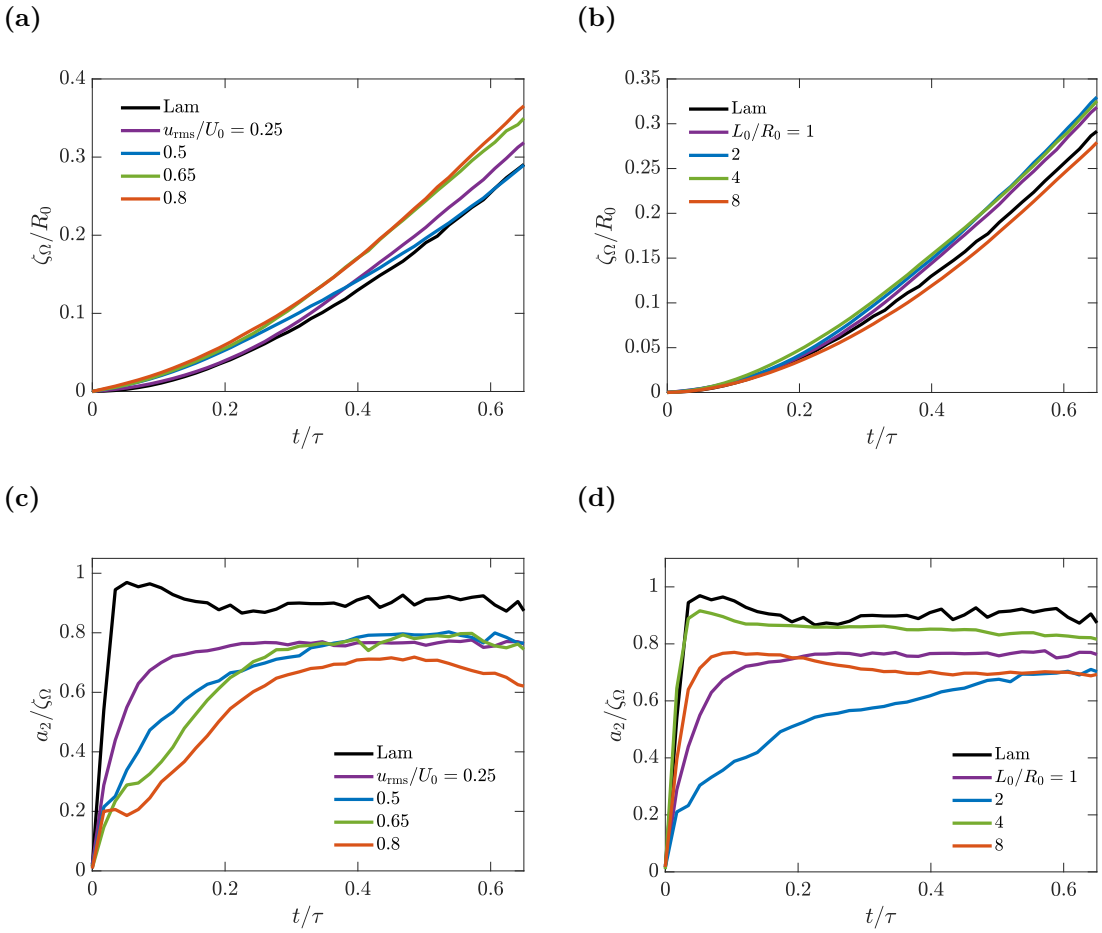

Figure 5.10: Evolution of the ensemble-averaged droplet total spherical harmonic deformation ζ_Ω (a,b) and mode-2 deformation a_2 (c,d) at different values of u^* (a,c) and L_0 (b,d).

coefficient a_2 is found to dominate all global coefficients a_i and evolve with an increasing growth rate similar to that of ζ_Ω. To facilitate comparison between a_2 and ζ_Ω, we plot the evolution of their ratios over time in figs. 5.10c and 5.10d. For most of the turbulent aerobreakup cases, a_2/ζ_Ω reaches a plateau value between 0.7 and 0.8, smaller than its laminar aerobreakup counterpart of 0.9. Since mode-2 spherical harmonic deformation corresponds to prolate-oblate shape changes, this slight decrease in a_2/ζ_Ω suggests that while the flattening of the droplet still largely follows a prolate-oblate pattern, the introduction of air-phase turbulence fluctuations excites higher-mode deformation patterns with smaller length scales, as we have already observed in fig. 5.3. Figure 5.10c also suggests that with increasing values of u^*, the growth of a_2/ζ_Ω for $t/\tau \leq 0.3$ becomes slower. This might be associated with stronger surface corrugation patterns as

the ambient turbulent fluctuations intensify. The influence of L_0 on the evolution of a_2/ζ_Ω is less obvious. The evolution patterns of a_2/ζ_Ω at $L_0/R_0 \geq 4$ closely resemble their laminar aerobreakup counterpart, which is expected as the droplets experience much milder ambient flow velocity variation at $d_h/d_0 > 1$ (see our discussions of fig. 5.5). For $(u^*/U_0,\, L_0/R_0) = (0.25,\, 2)$, a_2/ζ_Ω becomes much smaller at very early times as shown in fig. 5.10d, but have exceeded 0.5 by $t/\tau = 0.3$. These smaller values of a_2/ζ_Ω at early times correspond to a phase reversal in some of the individual realisations, that is, for these cases the droplets first elongate upon insertion, and higher-mode deformation arises as the droplet relaxes from this initial elongation and begins to flatten.

Given that the early-time droplet deformation can still be largely described as a prolate-oblate shape change despite corrugation formation, we now seek to quantify the global influence of turbulence corresponding to the mode-2 spherical harmonics, while leaving local higher-order corrugation features for the curvature distribution analysis in §5.5.3. It should be noted that, since the droplet can become distorted and/or tilted during its deformation process under strong air-phase turbulence, the definitions of bag length and width [15, 42, 122] as the streamwise and spanwise extents of the bag are not strictly applicable here. Instead, following Cannon *et al.* [165], we define the droplet aspect ratio $\sqrt{I_1/I_3}$, which is the ratio between the smallest and largest eigenvalues of the moment-of-inertia tensor for the droplet,

$$\boldsymbol{T_I} = \int_V \rho(\boldsymbol{r}^2 \boldsymbol{I} - \boldsymbol{r} \otimes \boldsymbol{r}) dV, \tag{5.19}$$

and show their evolution in fig. 5.11. We note here that $\sqrt{I_1}$ and $\sqrt{I_3}$ are proportional to the lengths of the minor and major axes of the spheroid, respectively.

It is first observed that $\sqrt{I_1/I_3}$ initially decreases over time and stabilises around $t/\tau = 0.75$, for laminar and turbulent airflows satisfying $u^*/U_0 \leq 0.5$. This corresponds to the flattening stage of the droplet where the bag width increases and the bag length decreases. At later stages, the laminar flow case shows a slight increase in the aspect ratio, corresponding to the late-time bag blowout phenomenon where the bag length significantly increases. The introduction of air-phase turbulence does not significantly affect the evolution of $\sqrt{I_1/I_3}$ at early times except for $u^* = 0.65$; while at mid-to-late

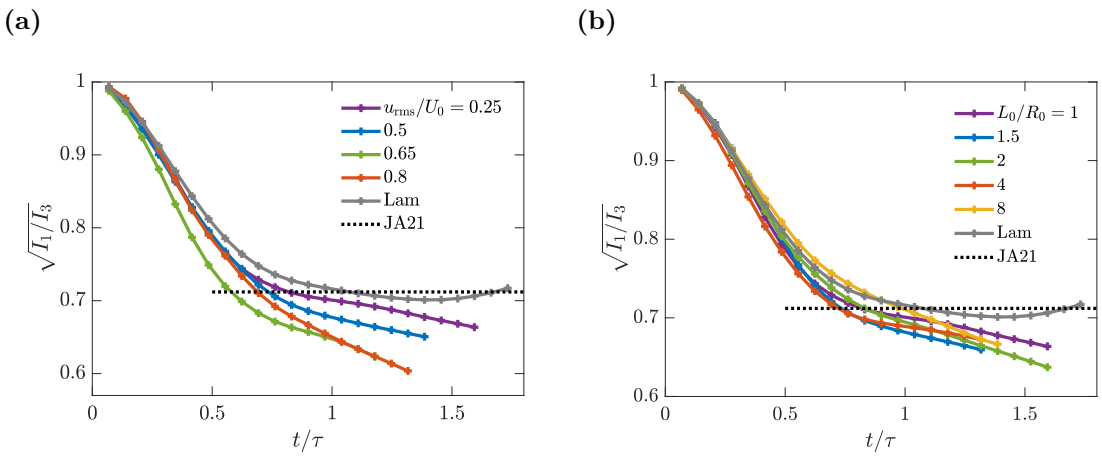

Figure 5.11: Evolution of the ensemble-averaged droplet aspect ratio $\sqrt{I_1/I_3}$ at different values of u^* (a) and L_0 (b). The theoretical value according to Jackiw and Ashgriz [42] is included as dotted lines.

times it is found to cause a decrease in $\sqrt{I_1/I_3}$ compared with the laminar airflow case. Taking into account the observation of Zhao *et al.* [69] that liquid bags are stretched longer and wider in turbulent ambient flows, a decrease in $\sqrt{I_1/I_3}$ then suggests that the increase in bag width exceeds that of its length. Moreover, for turbulent ambient flows featuring $u^*/U_0 \geq 0.65$, fig. 5.11a shows a continued decrease of $\sqrt{I_1/I_3}$, which is possibly because the air-phase turbulence is now strong enough to distort the flattened droplet so significantly that both its orientation and bag blowout dynamics are modified, as observed in figs. 5.5c and 5.5d.

We also present in fig. 5.11 the aspect ratio at the onset of bag formation predicted by Jackiw and Ashgriz [42] for $We = 15$, which is determined as follows. According to that study, the major axis lengths for bag morphologies are approximately $2R_i/d_0 \approx 1.6$; whereas the minor axis length is given as follows,

$$\frac{d_i}{d_0} = \frac{4}{We_{\rm rim} + 10.4}, \tag{5.20}$$

where the rim Weber number is defined as $We_{\rm rim} \equiv \rho_l \dot{R}^2 d_0/\sigma$. Based on an analysis of pressure balance at the drop surface, Jackiw and Ashgriz [42] proposed the following prediction for the bag spanwise growth rate $\dot{R}$,

$$\frac{\dot{R}}{d_0/2} = \frac{1}{\tau}\frac{a^2}{4}\left(1 - \frac{128}{a^2 We}\right) T_{bal}, \tag{5.21}$$

where $a = 6$ is the stretching rate at the frontal stagnation point of the droplet, and the initial flow balancing time T_{bal} is set as $\tau/8$. As such, we are able to determine the theoretical aspect ratio $\sqrt{I_1/I_3}$ assuming an ellipsoidal shape with axis lengths $a_i = b_i = R_i$ and $c_i = d_i/2$,

$$\sqrt{\frac{I_1}{I_3}} = \sqrt{\frac{b_i^2 + c_i^2}{a_i^2 + b_i^2}} = 0.712, \tag{5.22}$$

which we plotted in fig. 5.11 for reference. It is found that the prediction of (5.22) is very close to the minimum in our laminar airflow case, thus validating our aspect ratio calculations. Overall, we consider the deviation of turbulent aerobreakup aspect ratios from Eq. (5.22) to result from the increased droplet fore-aft pressure difference, which modifies the spanwise growth rate $\dot{R}$, while the generation of higher-mode interfacial deformation might also play a role.

5.5.2 Droplet tilting behaviour

As the droplet flattens in the ambient air-phase turbulence, it may exhibit the tilting behaviour formerly reported by Jiao *et al.* [68]; namely, the principal axes of the deforming droplet no longer align with the streamwise direction. Similar phenomena have been observed in previous experimental studies of droplet aerobreakup [42, 51] and also investigations of sea spume generation [22]; which are analogous to the tumbling behaviour of anisotropic solid spheroids where the particle rotates around a non-symmetry axis [173]. In our current study, this behaviour is usually first observed at intermediate times as shown in fig. 5.12, when the droplet has fully flattened and not yet evolved into bag-rim structures at later times; although for one particular realisation with $(u^*/U_0,\, L_0/R_0) = (0.25,\, 2)$ this occurred at very early times when the droplet is still largely spherical. Here, we have coloured the background flow field using the magnitude of airflow velocity u^*/U_0. These snapshots reveal that the droplet tilting phenomenon is closely associated with turbulence intermittency: while the principal axis of the droplet initially aligns largely with the streamwise direction, as shown in fig. 5.12a, a cluster of high-speed air parcels approaches (fig. 5.12b) and bypasses (figs. 5.12c-d) the droplet asymmetrically from above. This high-speed air

parcel modifies the pressure distribution on the droplet surface to form a net torque (see our discussions in Sec. 5.4), causing it to tilt over in fig. 5.12e. It is also noted that this high-speed air parcel does not directly impact the droplet, which might correspond to the earlier observations of Vela-Martín and Avila [174] that non-local actions by outer eddies away from the drop surface contribute significantly to the surface energy increment. For most simulation cases, the droplet will retain this oblique orientation afterwards as the interaction with these high-speed air parcels is a rare event.

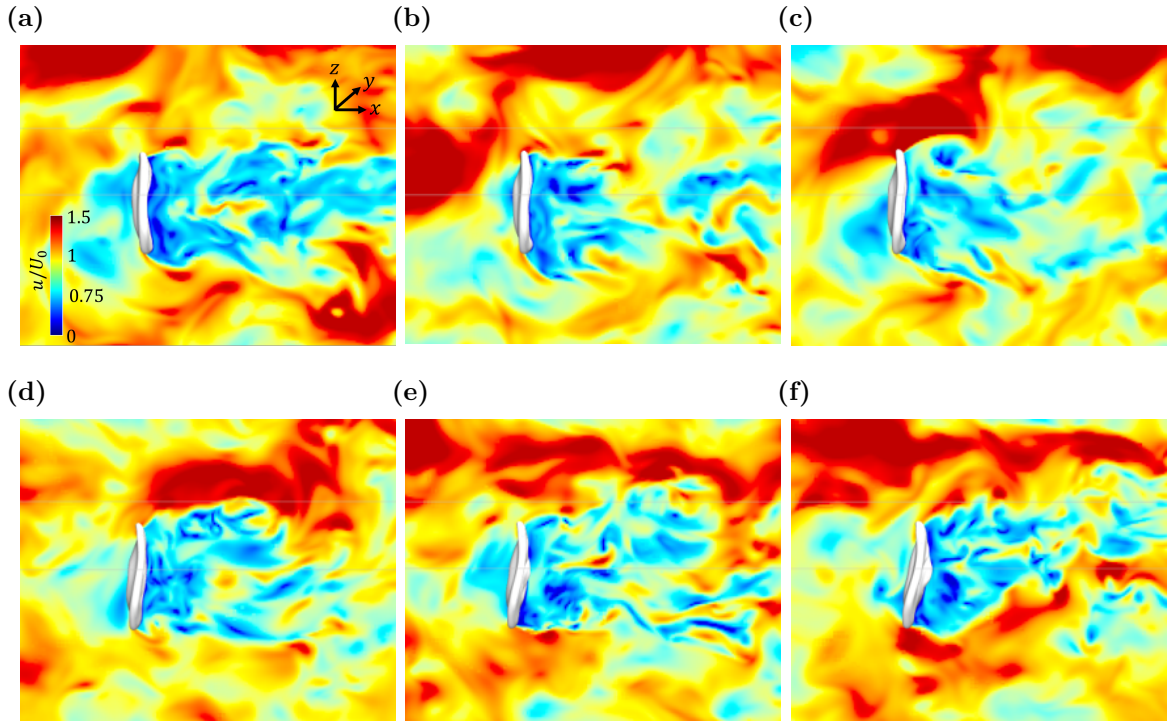

Figure 5.12: Snapshots showing the tilting of a droplet with air-phase turbulence characteristics $u^*/U_0 = 0.25$, $L_0/R_0 = 2$, where the background flow field is coloured based on the local airflow speed $u/U_0 = \sqrt{u_x^2 + u_y^2 + u_z^2}/U_0$. Warmer colour represents higher magnitudes of airflow velocity in these snapshots. From (a) to (f): $t/\tau = 1.03$, 1.09, 1.14, 1.20, 1.26, and 1.32.

To quantify the tilting phenomenon described above, we measure the droplet principal axis $\boldsymbol{e_1} \equiv (\theta_{11}, \theta_{12}, \theta_{13})$, which can be obtained by computing the eigenvectors of the moment of inertia tensor $\boldsymbol{T_I}$ (See Eq. (5.19)). Here, θ_{ij} is the angle between the droplet principal axis $\boldsymbol{e_i}$ and the lab-frame coordinate $\boldsymbol{j}$; and we are particularly interested in the orientation angle θ_{11} between the droplet minor axes and the streamwise direction, since its change most clearly reflects the droplet tilting dynamics.

We then explore the possible connections between the tilting behaviour and the turbulent airflow characteristics at the scale of the droplet diameter d_0. Following Masuk *et al.* [175, 176], we introduce the slip velocity $\boldsymbol{u_{slip}}$,

$$\boldsymbol{u_{slip}} = \bar{\boldsymbol{u}}_{\boldsymbol{i}}(\boldsymbol{x_0}) - \boldsymbol{u_c}. \tag{5.23}$$

Here, $\bar{\boldsymbol{u}}_{\boldsymbol{i}}(\boldsymbol{x_0})$ is the coarse-grained air-phase velocity at x_0, computed by averaging all velocity records within a shell enclosing the droplet given by $1.5R_0 \leq r \leq 2R_0$; and we have checked that changing the upper and lower boundaries of this sampling shell does not have any discernible effect on the value of $u_i(\bar{x}_0)$. As $\boldsymbol{u_c}$ is the droplet centre-of-mass velocity, the slip velocity $\boldsymbol{u_{slip}}$ represents the coarse-grained speed of the airflow felt by the droplet.

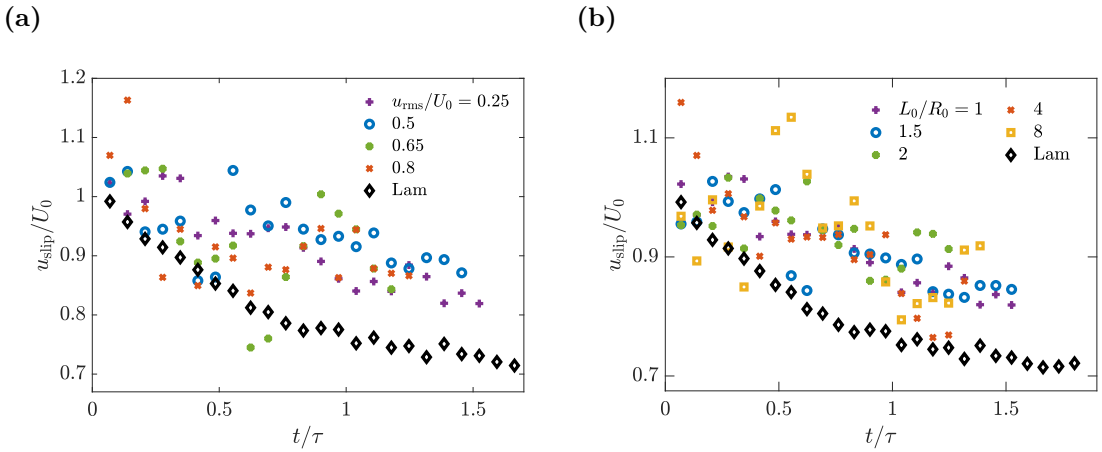

Figure 5.13: Evolution of the slip velocity u_{slip} over time at different air-phase turbulence configurations.

Figure 5.13 shows the evolution of the magnitude of slip velocity u_{slip}, where a decreasing trend is observed for all cases reported. This decrease is due to the acceleration of the droplet by the ambient airflow, and is most prominent for the early-time flattening stage where $t/\tau \leq 0.6$. Interestingly, we observe that at the same non-dimensional time t/τ, the slip velocities for the turbulent airflow cases mostly exceed their laminar airflow counterpart, and there does not appear to be any strong dependence of u_{slip} on the turbulence configurations. This increase in u_{slip} is most likely due to the high-speed turbulent fluid parcels bypassing the droplet, as we observed in

fig. 5.12; which is also associated with the increased centre-of-mass acceleration and deformation rates we discussed earlier in §5.4 and §5.5.1.

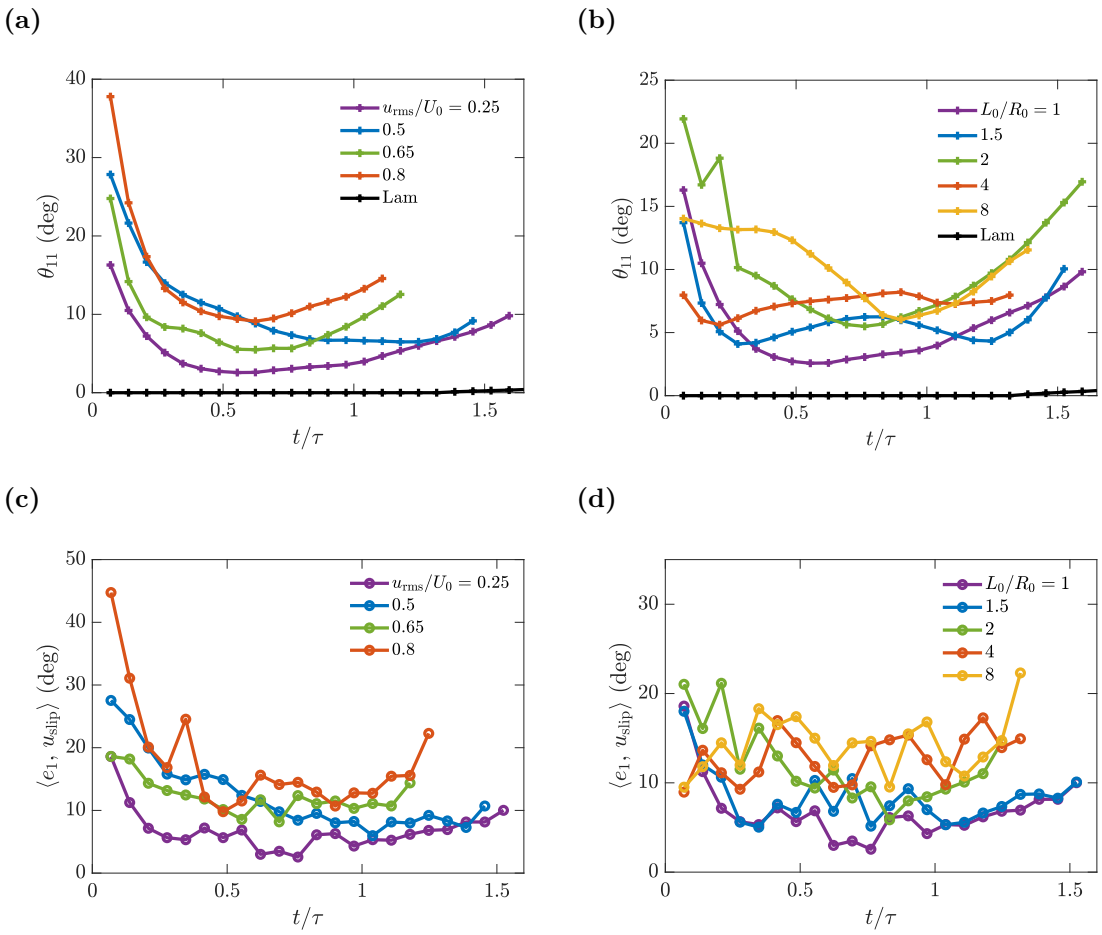

Figure 5.14: Evolution of ensemble-averaged droplet orientation angle θ_{11} (a,b), and the alignment angle $\langle \boldsymbol{e_1}, \boldsymbol{u_{slip}} \rangle$ between the droplet principal axis $\boldsymbol{e_1}$ and the slip velocity $\boldsymbol{u_{slip}}$ (c,d).

We now present the evolution patterns of the droplet orientation angle θ_{11} at different turbulence configurations in figs. 5.14a and 5.14b. While θ_{11} remains zero for the laminar airflow case, when turbulence is introduced, we first observe large initial values of θ_{11}, which are most likely caused by small-scale droplet surface perturbations imprinted by the turbulent airflow just after the insertion of the drop. We have already noted the effects of these small perturbations when discussing the decrease in a_2/ζ_Ω observed in figs. 5.10c and 5.10d, which decay rapidly as the droplet flattens. For most of the cases shown in figs. 5.14a and 5.14b, we observe an increase in θ_{11} for $t/\tau \geq 1$; since

the droplet has already finished flattening by this stage, we consider this increase in θ_{11} to represent the late-time tilting behaviour observed in fig. 5.12. It is also within this late stage that θ_{11} appears to mildly increase with increasing u^* and L_0, although exceptions exist when $(u^*/U_0,\, L_0/R_0) = (0.5,\, 1)$ and $(0.25,\, 2)$.

The previous study by Masuk *et al.* [176] reveals a strong preferential alignment between bubbles deforming in turbulence and the slip velocity. This is measured by the alignment angle $\langle \boldsymbol{e_1},\, \boldsymbol{u_{slip}} \rangle$ between the minor axis of the flattening drop and the slip velocity, which is defined as,

$$\langle \boldsymbol{e_1},\, \boldsymbol{u_{slip}} \rangle \equiv \arccos\left(\frac{\boldsymbol{e_1} \cdot \boldsymbol{u_{slip}}}{\|\boldsymbol{e_1}\| \|\boldsymbol{u_{slip}}\|} \right), \tag{5.24}$$

whose evolution we present in figs. 5.14c and 5.14d. While the values of $\langle \boldsymbol{e_1},\, \boldsymbol{u_{slip}} \rangle$ calculated are generally close to those of θ_{11}, larger fluctuations are observed in its evolution, which are expected due to the presence of variations in the ambient turbulent airflow and vortex shedding in the wake of the drop. Interestingly, despite the presence of scatter and the apparent increase of the alignment angle with increasing L_0 shown in fig. 5.14d, we still observe a largely decreasing trend in $\langle \boldsymbol{e_1},\, \boldsymbol{u_{slip}} \rangle$ at early time, similar to that of θ_{11}. This suggests a close connection between the two quantities, as the coarse-grained airflow velocity felt by the droplet becomes increasingly aligned with its minor primary axis $\boldsymbol{e_1}$ as it flattens. This agrees with Cui *et al.* [173], as they observed that under the influences of the fluid inertial torque, the symmetry axes of oblate spheroids tend to align with the slip velocity.

Referring back to fig. 5.9a, one observes that the amplitude of the hydrodynamic torque acting on the droplet begins to rapidly increase at around the same time when θ_{11} and $\langle \boldsymbol{e_1},\, \boldsymbol{u_{slip}} \rangle$ minimise. We believe this is due to the increased susceptibility of the flattened droplet to ambient flow field perturbations originating from the bypassing of high-speed ambient flow parcels as shown in fig. 5.12, even though the magnitude of the slip velocity felt by the droplet continues to decrease, as shown in fig. 5.13. To better demonstrate this argument, we note that previous studies prescribe the following functional form for hydrodynamic torques experienced by immersed oblate

particles [171, 173],

$$|\boldsymbol{M}_H| = \frac{1}{2}\rho_g |\boldsymbol{u_{slip}}|^2 a^3 F(\lambda) \sin 2 \langle \boldsymbol{e_1}, \boldsymbol{u_{slip}} \rangle , \tag{5.25}$$

where a is the length of the droplet major axis, and $F(\lambda)$ is a shape function dependent on the droplet aspect ratio λ. This prescription is strictly valid only for Stokes flow scenarios where the particle Reynolds number $Re_p \equiv \rho_g |\boldsymbol{u_{slip}}| a/\mu_g \ll 1$, but available results support its usage up to $Re_p \approx 10^2$ [171, 177]. We do not expect our simulations, which have Re_p around 10^3, to match this result, but we note a similarity in how it connects the turbulent properties of the surrounding flow to the torque experienced by the droplet. Since it is found in fig. 5.14 that when the droplet fully flattens, the alignment angle $\langle \boldsymbol{e_1}, \boldsymbol{u_{slip}} \rangle$ remains small and does not change significantly across different turbulence configurations, whereas the slip velocity amplitude $|\boldsymbol{u_{slip}}|$ keeps decreasing, the rapid growth of torque exerted on the droplet may be attributable to a significant growth in $a^3 F(\lambda)$, which is determined by the droplet geometry. Indeed, the shape function $F(\lambda)$ increases rapidly with decreasing aspect ratio within the range of $0.1 \leq \lambda \leq 1$, as shown in fig. 3 of Ref. [173], which supports our reasoning that the rapid torque growth and the droplet tilting behaviour are associated with decreasing droplet aspect ratio due to flattening. At the current stage, a more rigorous examination of the droplet tilting dynamics remains difficult compared with the tumbling behaviour of solid particles [173, 178], since the droplet is deforming and tilting at the same time. However, we consider that the discussion of θ_{11}, and the comparison with both $\langle \boldsymbol{e_1}, \boldsymbol{u_{slip}} \rangle$ and the hydrodynamic torque shed light on the influences of nearby extreme turbulence events on the droplet dynamics.

5.5.3 Formation of surface corrugations

In this section, we direct our attention towards more local morphological features present on the drop surface; more specifically the distributions of the surface velocity increment δu_s [156] and the local droplet interface curvature κ [179, 180]. Here, the surface velocity increment δu_s is defined on a reference envelope Γ encompassing the

droplet, as the difference between the radial components of the local air-phase velocity $\boldsymbol{u}$ and the mean air-phase velocity at all points located on this envelope; namely

$$\delta u_s(R,\,\theta,\,\phi) = \tilde{\boldsymbol{u}}(\boldsymbol{R}) \cdot \hat{r}, \tag{5.26}$$

$$\tilde{\boldsymbol{u}}(\boldsymbol{R}) = \boldsymbol{u} - \frac{1}{4\pi} \iint_{\Gamma} \boldsymbol{u}(\boldsymbol{R},\,\theta,\,\phi)\, d\Omega. \tag{5.27}$$

The distance between any point on Γ and the droplet surface is fixed as $\Delta l = 0.05R_0$. It should be noted that, in contrast to Perrard *et al.* [156] where Γ is a fixed spherical surface, in our case Γ follows the droplet and deforms along with it due to the presence of the mean flow. Positive δ_s indicates the ambient airflow moving at velocities higher than the average value, while negative δ_s values suggest lower-than-average ambient velocities. For the early stages of droplet aerobreakup characterised by spanwise flattening, it is expected that the peripheral region of the drop mainly features positive δ_s, while the frontal and back faces of the drop feature negative δ_s instead.

In fig. 5.15a we present the probability distribution functions of δu_s normalised by its standard deviation $\langle \delta u_s \rangle$ at different air-phase turbulence configurations before the insertion of the droplet, where the turbulent airflow has reached a statistical steady-state. The velocity increments are computed on the spherical surface $r = 1.05R_0$ and are found to abide by a normal distribution. In fig. 5.15b we inspect the correlation between δu_s and the droplet local curvature κ at a fixed time $t/\tau = 1.109$ after droplet insertion, when the droplet has fully flattened. It is found that δu_s mostly increases with κ, except for $(u^*/U_0,\, L_0/R_0) = (0.25,\, 4)$ and $\kappa d_0/2 \geq 15$. Moreover, this positive correlation does not appear to depend on the specific turbulence configurations within the range of $-2d_0/h_i \leq \kappa d_0/2 \leq 2d_0/h_i$, where $2d_0/h_i = 2d_0/d_i$ is the curvature of the peripheral rim according to (5.20). Figs. 5.15c-e present droplet surfaces at the point of bag initiation, which have been coloured to reveal the spatial distribution of the local curvature κ. Large values of κ are observed primarily at the outer edge of the peripheral rim, where large δu_s is also expected. Conversely, negative κ is found either on the 'neck' connecting the bag film and peripheral rim or the dimples on the bag film, and elsewhere on the bag film κ remains close to zero. This suggests that on the droplet surface, the development of highly-curved structures is closely associated

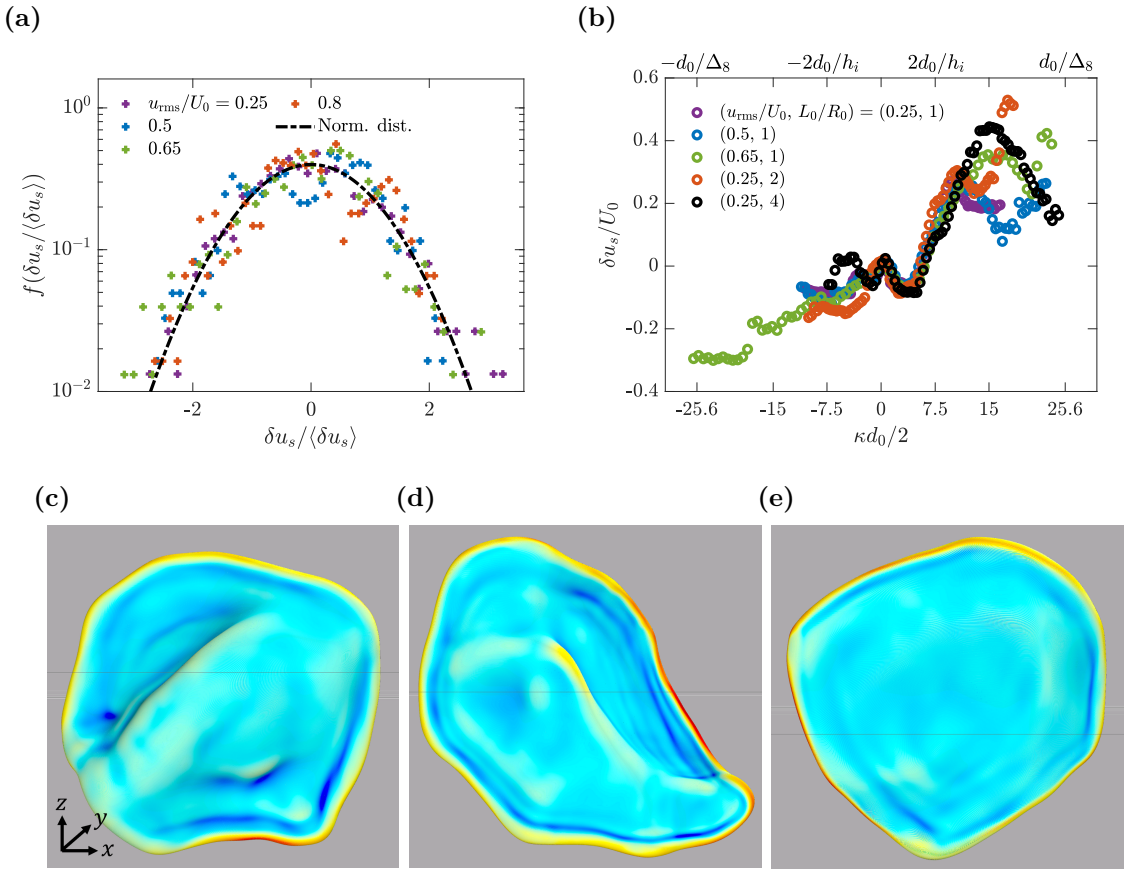

Figure 5.15: (a): Probability distribution functions of the surface velocity increment δu_s immediately before droplet insertion, measured at different u^* values. (b): Correlation between δu_s and local interface curvature κ, sampled at $t/\tau = 1.109$ and at different u^* values. The secondary axis on the top of fig. 5.15b shows reference curvature values corresponding to the turbulence grid size d_0/Δ_8 and droplet peripheral rim $2d_0/h_i$. (c)-(e): Colour-mapped droplet surfaces showing the spatial distribution of local interface curvature κ for $(u^*/U_0,\ L_0/R_0) = (0.65,\ 1)$ and $t/\tau = 1.11$, where warmer colour corresponds to larger κ.

with extreme events in ambient turbulence; whereas structures with medium to low local curvature are more likely associated with mean flow effects.

We further inspect the evolution of δu_s over time in fig. 5.16a. Initially, the distribution of δu_s spans over a quite wide range of $-0.75 \leq \delta u_s/U_0 \leq 0.5U_0$ with a flat plateau in the middle bordered by steep tails on either side, reflecting a large range of velocities present in the separated airflow around a largely spherical droplet. As time elapses, the distribution of δu_s narrows down with an increasingly steep left tail. Interestingly, while there are already two distinctive peaks present in the distribution of δu_s at a relatively early time $t/\tau = 0.069$, which gradually approach one another as

time elapses, the monotonically decreasing right tail has developed a shoulder around $\delta u_s/U_0 = 0.25$ by $t/\tau = 0.901$, which persists up to $t/\tau = 1.109$. Taking into account that the two early-time peaks are almost symmetric about $\delta u_s = 0$, we consider that they most likely correspond to the stagnation and separation points at the drop surface, since it is at these locations that the ambient airflow velocity minimises and maximises, respectively. The formation of the shoulder around $\delta u_s/U_0 = 0.25$ suggests a breakdown of symmetry in the probability distribution function so that large positive δu_s values are more likely to be observed. Since positive δu_s is associated with the droplet periphery, the formation of this shoulder can be understood as an indicator of the torque growth and droplet tilting patterns we discussed earlier in §5.4 and §5.5.2.

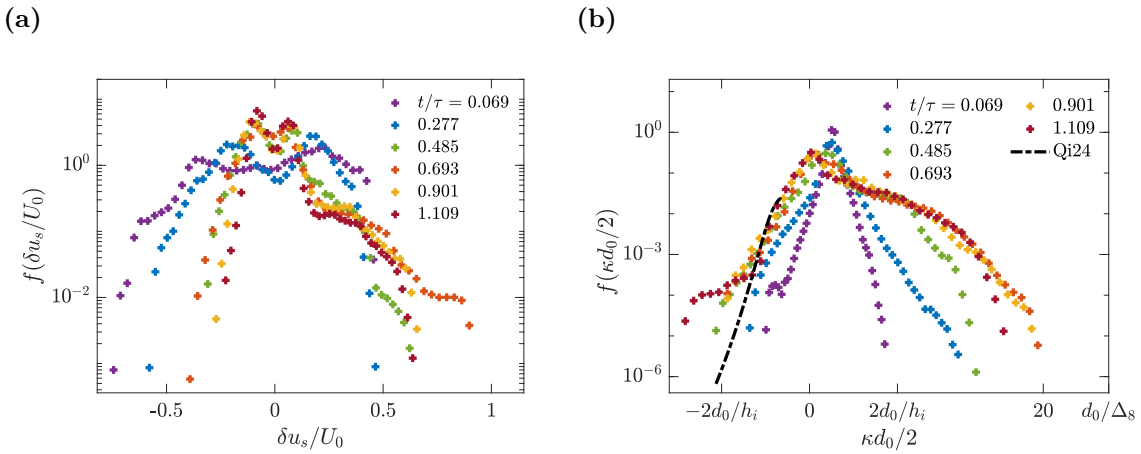

Figure 5.16: Evolution of the ensemble-averaged probability distribution functions of surface velocity increment δu_s (a) and local interface curvature κ (b) over time for $u^*/U_0 = 0.25$, $L_0/R_0 = 1$. We also include in fig. 5.16b the theoretical prediction of Qi *et al.* [180] for comparison, where the fitting parameter C_1 in Eq. (5.28) is set as 0.4.

In contrast to the narrowing trend observed in the distributions of δu_s, fig. 5.16b suggests that the distributions of the local interface curvature κ broaden over time. Initially, the distribution of κ is symmetric and peaks around $\kappa d_0/2 = 2$, which suggests the presence of small-scale perturbations on the largely spherical droplet surface due to interactions with the turbulent airflow. As the droplet deforms over time, the distribution of κ broadens and develops a skew towards large positive curvature values, representing bumps or ripple-like irregularities [179]. The peaks of κ distributions have

shifted to $\kappa = 0$ by $t/\tau = 0.901$, which most likely correspond to the flat surface on either side of the disk-shaped droplet before the bag blows out.

We also include in fig. 5.17b the theoretical prediction of Qi *et al.* [180] for turbulence-bubble interactions, where it is found to partially describe the intermediate-time curvature distribution of negative κ values. This theory assumes that the concave regions on the droplets result from their interactions with energetic, sub-droplet-scale eddies with size $D_e < d_0$, whose inertia $\rho_g u_e^2$ is sufficient to overcome the increase in surface energy σ/D_e caused by the local deformation. This yields the following lower bound for the characteristic speed of such eddies,

$$u_{e,\,d} = \sqrt{C_1 \sigma / \rho_g D_e}, \tag{5.28}$$

where C_1 is a fitting parameter. The distribution of instantaneous eddy velocity u_e is given as follows,

$$P(u_e|D_e) = \frac{3\sqrt{2}}{2} \varepsilon_e^{2/3} D_e^{-1/3} P(\varepsilon_e), \tag{5.29}$$

where the distribution of the local energy dissipation rate ε_e is in turn approximated as a log-normal function according to a multi-fractal model. Consequently, the distribution of the sizes of the eddies strong enough to deform the drop surface is expressed as

$$P(D_e) \propto D_e^2 \omega_c \int_{u_{e,d}}^{\infty} P(u_e|D_e) du_e, \tag{5.30}$$

where the droplet surface area deformed by the eddy is assumed to scale with D_e^2, and the frequency of collision between the droplet and the eddy is approximated as $\omega_c \propto \langle \varepsilon \rangle^{1/3} D^2 D_e^{-11/3}$ by analogy with the gas kinetic theory. As the local deformation curvature can be estimated by $\kappa \approx -2/D_e$, this allows one to write the distribution of the local negative curvature κ as

$$P(\kappa) \propto \kappa^{-2} P(D_e). \tag{5.31}$$

Similar to Qi *et al.* [180], we find that when setting $C_1 = 0.4$, (5.31) matches partially with the left tail of the simulation results up to $\kappa d_0/2 = -2.5$, where the former shows a kink. While the agreement here suggests that collision with sub-droplet-scale eddies

is an important physical mechanism responsible for the dimple formation in our study, we note that the contribution of other mechanisms, such as the balance between the deforming effects of the mean flow and surface tension, cannot be accounted for by this model and still awaits further analysis. Moreover, we note that while fig. 3 in Ref. [180] also shows a skew towards positive curvature values, the right tail of their curvature distribution functions are concave-shaped and extends to very large positive values ($\kappa d_0/2 \approx 40$); whereas our results at $t/\tau = 1.109$ feature convex-shaped right tails that tend to fall off abruptly at a finite value around $\kappa d_0/2 \approx 20$. This is likely because droplets take much longer to deform and elongate, and feature much fewer 'sharp' regions at the time of bag formation compared with bubbles with negligible inertia.

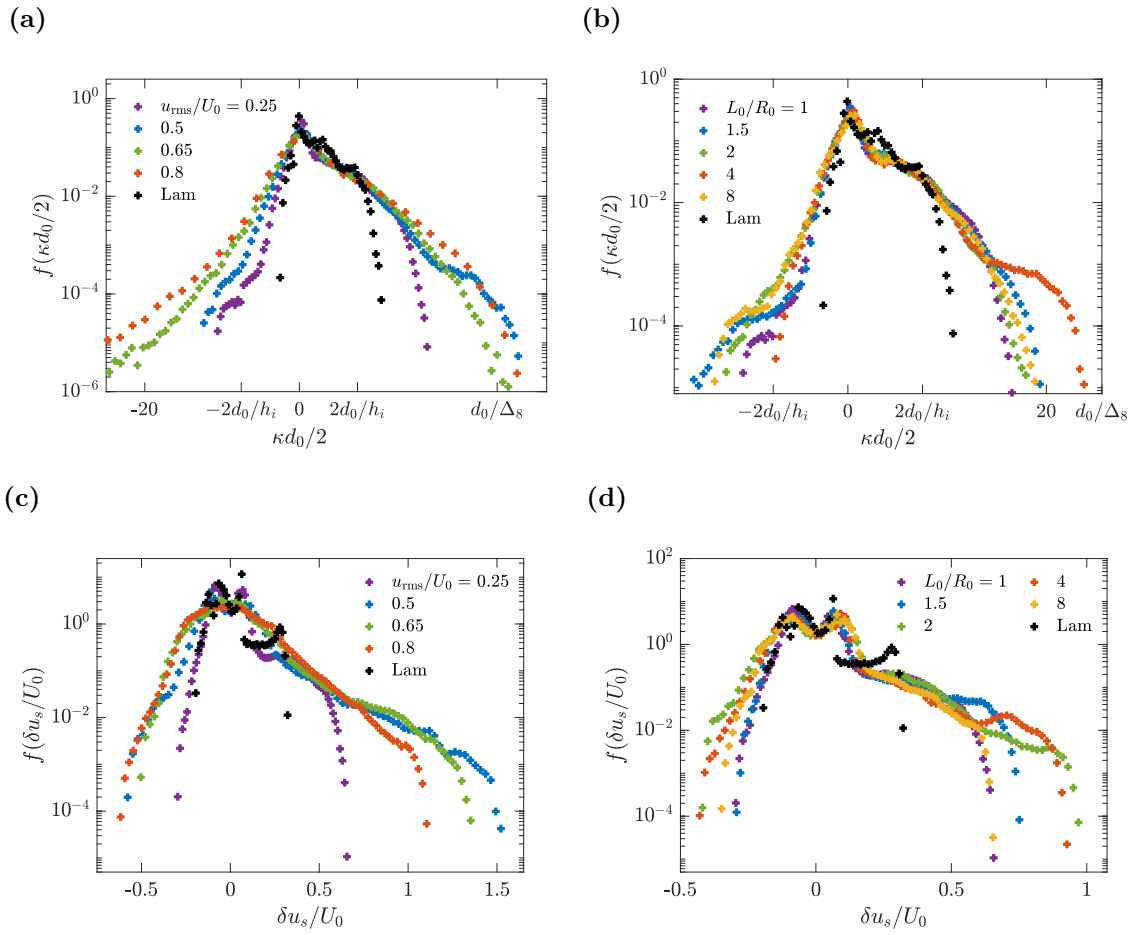

Figure 5.17: Ensemble-averaged probability distribution functions of local interface curvature κ (a,b) and surface velocity increment δu_s (c,d) sampled at $t/\tau = 1.11$ for air-phase turbulence with different fluctuating velocities u^* (a) and injection length scales L_0 (b).

In fig. 5.17 we further show the influence of air-phase turbulence on the distribution patterns of κ and δu_s. Figs. 5.17a and 5.17b suggest that the right tails of the κ distributions are most strongly influenced by air-phase turbulence; as compared with their laminar airflow counterpart, all turbulent aerobreakup cases feature an increased number of large positive curvature records. This indicates that local small-scale structures forming on the bag, for example, the protruding nodes observed in figs. 5.5c and 5.5d, become increasingly prominent as u^* increases. According to Jackiw and Ashgriz [51], the formation of these nodes and the subsequent generation of node drops can be attributed to either RT or RP instability developing on the periphery rim. The influence of air-phase turbulence on the left tails of the curvature distributions is not as prominent as the right tails, as the left tails only slightly broaden when u^* increases. This is most likely because the formation of convex regions on the drop surface with large local curvatures (rims and nodes) benefits jointly from the suction of low ambient gas pressure and capillary pinching effects, whereas creating the concave regions (dimples) requires strong small-scale eddies to act against capillary forces, as we have discussed for fig. 5.16b. Interestingly, we observe that the curvature distribution within the range of $0 \leq \kappa d_0/2 \leq 8$ does not appear to depend on the turbulence characteristics.

Figs. 5.17c and 5.17d show the velocity increment distributions at different air-phase turbulence configurations. Similar to the curvature distributions, it is found that the introduction of air-phase turbulence leads to a broadening effect, which becomes the strongest at the right tail for $\delta u_s/U_0 \geq 0.5$. Also, similar to the curvature distribution for $0 \leq \kappa d_0/2 \leq 8$, the velocity increment distribution for $0 \leq \delta u_s/U_0 \leq 0.5$ does not appear to depend strongly on the turbulence characteristics. We consider that both these turbulence-independent regimes correspond to the same droplet morphological feature present in all simulations carried out in this study, which is the flattened frontal and back faces of the droplet; since it is here that the most probable values of both κ and δu_s are found.

5.6 Influence of the liquid-gas viscosity ratio μ^*

As can be seen from Eq. (5.4), the Kolmogorov microscale η is directly linked with the air-phase kinematic viscosity ν_g; therefore a decrease of the viscosity ratio μ^* can cause an increase in η and allow the simulation to better resolve air-phase turbulence dissipation. The effects of μ^* on the air-phase turbulence characteristics and the droplet centre-of-mass properties have already been covered in §5.2.2 and §5.4, respectively. Here, we present distributions of droplet interface curvature κ and surface velocity increment δu_s obtained at different times with reduced μ^* values of 20 and 10 (only for $u^*/U_0 = 0.25$), and compare with those obtained for $\mu^* = 55$ in fig. 5.18. This allows us to provide some insight into the effects of the liquid-gas viscosity contrast on the deformation characteristics of the droplet and its interaction with the ambient turbulence.

It is observed that for all three turbulence configurations shown in fig. 5.18, the local interface curvature distribution does not show any consistent change with decreasing μ^*, with the only noticeable difference occurring in the left and right tails from time to time. Alongside results presented in §5.2.2 and §5.4, these data suggest that the liquid-gas viscosity ratio and small eddies at the Kolmogorov microscale do not significantly affect the droplet dynamics and global deformation patterns. Furthermore, the insensitivity of the droplet behaviour to μ^* justifies our use of $L_{turb} = 8$ for resolving only large eddies in the turbulent bulk flow. On the other hand, the velocity increment distributions show a stronger dependence on μ^*; especially at a very early time $t/\tau = 0.069$ immediately after droplet insertion, as we observe the distribution of δu_s broadens as μ^* increases. This is expected since larger values of μ^* correspond to larger gas-phase Reynolds numbers Re, which in turn lead to stronger turbulence and more extreme velocity values recorded around the droplet.

5.7 Concluding remarks

We have presented novel direct numerical simulations of droplet deformation in a turbulent mean flow, systematically investigating various aspects of the dynamic and morphological droplet evolution patterns. Utilising a robust synthetic turbulence

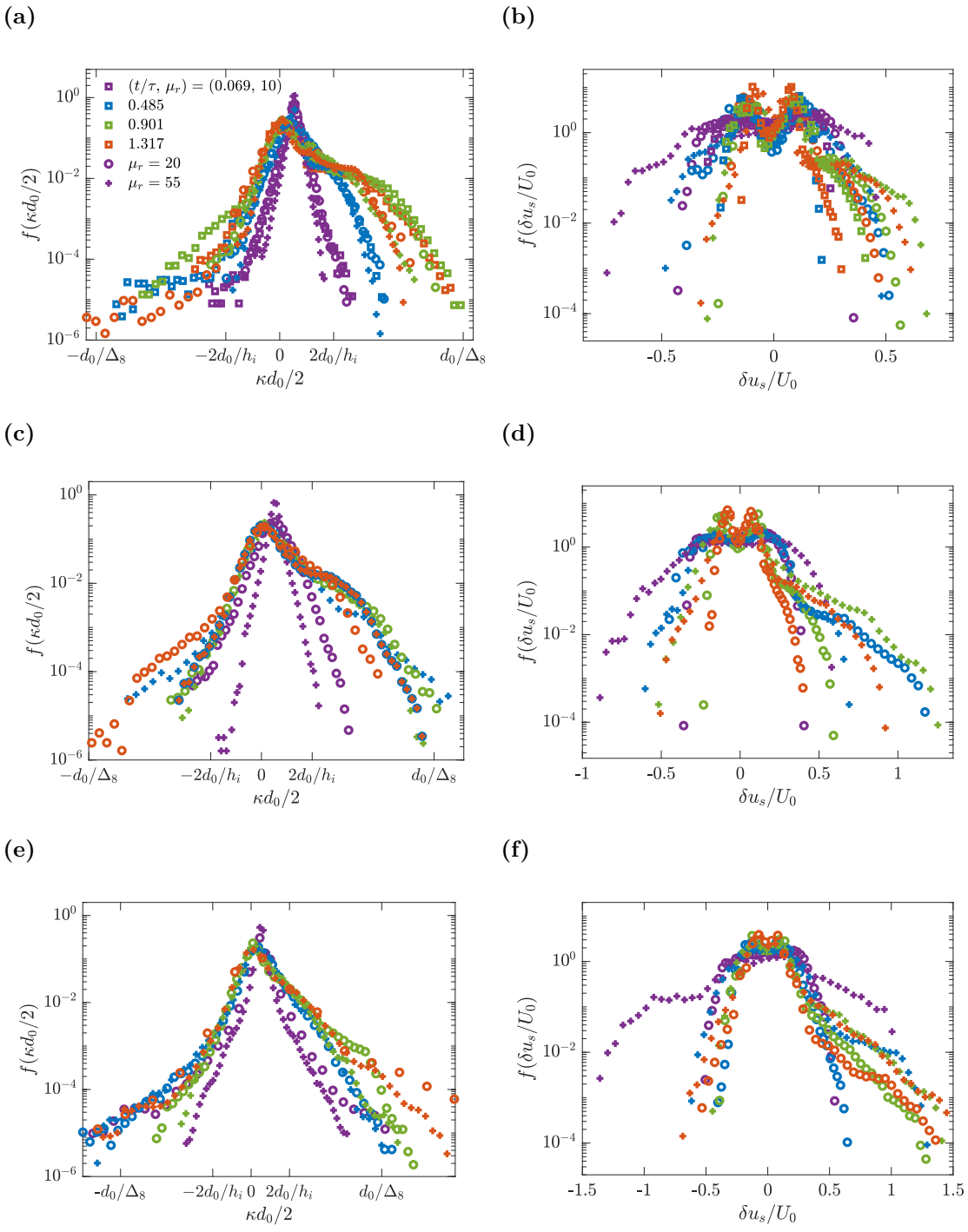

Figure 5.18: Comparison of ensemble-averaged probability distribution functions of local curvature and velocity increment at $t/\tau = 1.11$ and $\mu^* = 10$, 20 and 55. (a,b): $u^*/U_0 = 0.25$; (c,d): $u^*/U_0 = 0.5$; (e,f): $u^*/U_0 = 0.65$; while for all simulation cases $L_0/R_0 = 1$.

generation method [21], we obtained ambient airflows with validated turbulence statistics, and reproduced various aspects of droplet behaviour observed in pioneering works by Zhao *et al.* [69] and Jiao *et al.* [68], including the increase in bag size, tilting and formation of high-curvature local interfacial geometries. Our results shed light on the detailed physical mechanisms governing the droplet acceleration and deformation processes, thus laying the foundation for future works investigating the detailed turbulent bag breakup dynamics and associated fragment statistics. Here, we further discuss the possible implications of introducing air-phase turbulence on the fragment statistics resulting from bag breakup, which will be the focus of more detailed follow-up work.

First, our figs. 5.6 and 5.7 suggest that introducing turbulence causes the droplet to further accelerate in the streamwise direction, with some degree of randomness in the radial direction resulting from turbulence lift effects. We therefore expect promoted droplet surface instability development and draining of bag films, leading to an earlier perforation time of the latter; which is already reported in previous experimental studies [69].

Second, as is observed in the snapshots in fig. 5.5, the flattened droplet exhibits diverse morphological features not observed in laminar aerobreakup simulations [15, 122]. Among these are the distortion of the bordering rim and formation of protruding nodes, which we expect to eventually give rise to 'node drops' similar to the experimental observations of Jackiw and Ashgriz [51], and result in a reduction of the final volume fraction of rim drops resulting from Plateau-Rayleigh breakup [42]. Additionally, the formation of small-scale, highly-curved features on the droplet at late times, as observed in figs. 5.16 and 5.17, suggests a more corrugated bag film which will disrupt the hole expansion process governed by the Taylor-Culick mechanism [15], modifying the development of hole rim instabilities and the subsequent drop shedding processes [51, 53, 62, 161]. We therefore expect the final fragment size distribution arising from turbulent aerobreakup to become broader compared with laminar aerobreakup scenarios, since the parent features of such fragments become more varied. Nonetheless, it remains a challenge to properly resolve the bag film perforation process and obtain

high-fidelity fragment statistics, even with the aid of the MD algorithm for establishing grid-converged size distributions for large fragments [15, 20, 37].

Lastly, we note that the tilting behaviour of the droplet, as observed and analysed in figs. 5.12 and 5.14, implies more widespread trajectories and spatial distributions of the fragments compared with the laminar bag breakup case, as they are now ejected from a highly inclined and corrugated bag surface. A more detailed analysis of the tilting dynamics would therefore deepen our understanding of the breakup of bag-shaped sea surface perturbations which also feature oblique orientations, as discussed by Troitskaya *et al.* [14, 22, 23].

6
Purely Inertial Rim Splashing

Reproduced entirely from a published journal article: Tang, K., Adcock, T. A. A., & Mostert, W. (2024). Fragmentation of colliding liquid rims. *Journal of Fluid Mechanics*, 987, A18.

6.1 Introduction

Liquid atomisation is a class of challenging multiphase problems [50] featuring a large separation of scales and various interacting physical mechanisms, which is of significance to numerous fields of application including meteorology [49], ink-jet printing [92, 149, 181], internal combustion engines [83], and pharmaceutical manufacturing [116]. Within the context of air-sea interactions, liquid fragmentation is primarily associated with wave breaking events, and gives rise to ocean sprays. These spray drops are then transported within the atmospheric boundary layer while exchanging with the latter moisture, momentum and heat during their lifetime; thus leaving their impact on both global and regional climates [5, 10, 54]. Atomisation involves topological changes of the liquid bulk driven by external forces, typically followed by formation of corrugated ligaments subject to capillary breakup, and ends with a number of fragments featuring a broad size distribution, the knowledge of which is crucial for various areas of applications listed above [8].

Among various types of liquid atomisation problems, the impact of liquid droplets has received much scholarly attention for its ubiquitous presence, rich dynamics and vast range of applications [8, 76, 83] since the pioneering experimental study of Worthington [182]. The impact process features a competition between inertial and capillary forces, which together with the characteristics of the impacting object and the surrounding gas phase shapes the final outcome of the original droplet: bouncing, spreading or splashing. Empowered by the rapid pace of sensor developments and increasing computational capacities, past works have elucidated considerable details about the ephemeral kinematic and morphological development of drops impacting with various types of surfaces [76], including liquid films [183], deep pools [184, 185], smooth solid surfaces [82, 186], rough solid surfaces with friction [187], or an identical droplet [188, 189]. Some recent works have also probed the dynamic properties of drop impact including the distribution of impact force and stresses, providing an alternative approach to investigate impact dynamics at early times [76]. Specifically, there have been a series of recent experimental works studying the high-speed impact of droplets with a surface of comparable size as a canonical unsteady fragmentation problem [60, 77–80], providing valuable insights into various aspects of the impact process in the limit of large We, including the self-similar evolution of the liquid-phase thickness and velocity profile [77], the dynamics of the rim bordering the expanding liquid sheet [60], the growth of liquid ligaments and the detachment of liquid drops from their tips [78, 79], and the partition of mass, momentum and energy during the entire collision process [80].

However, the impact-induced fragmentation of liquid bulks featuring non-spherical initial shapes is also attested, which has received considerably less attention and remains less understood compared to drop impact problems [190]. Among these is the collision of liquid rims, which has seen some recent investigations experimentally [62] and numerically [63] and is also the focus of the present work. In the two works cited above, an initially intact liquid film is perforated to form small holes, which then expand under surface tension and develop bordering rims travelling at the Taylor-Culick velocity [191, 192]. Neighbouring film holes merge with one another when their bordering rims collide, oscillate and break up into small fragments, a process commonly observed during the

rupture of films, which may be induced by rapid radial expansion of liquid shells [53] or the inflation of a liquid drop interacting with a surrounding airflow [15, 51, 122]. Agbaglah [63] placed the two holes immediately adjacent to each other so that the two liquid rims collide at low impact Weber number We; and the fused liquid bridge is found to pinch off under oscillation and form only a few small droplets. Neel *et al.* [62] were able to investigate the rim collision phenomena by varying the initial distance between the two perforation sites, thus varying the impact We value within the range of $50 \leq We \leq 200$. Apart from the primary capillary breakup mechanism of fused liquid bridges as discussed by Agbaglah [63], Neel *et al.* [62] also identified a critical We value of 66 beyond which the decelerating transverse lamella rims develop elongating ligaments under the Rayleigh-Taylor (RT) instability, which then produce many secondary fine drops under capillary instabilities featuring a skewed size distribution. Additionally, there have been some early theoretical analyses on the capillary-driven coalescence of two liquid cylinders [193–195]; although these are conducted at the creeping flow limit with negligible liquid bulk velocity, and thus may not be directly applicable to the current problem featuring finite collision speeds.

Apart from its presence during the rupture of thin films, the collision of liquid rims is also of specific interest due to its strong resemblance to the secondary wave splashing phenomena observed in ocean wave breaking events [9, 17, 74]. Namely, two consecutive well-defined splashing phases have been identified [9] during the lifetime of a deep-water plunging breaker. The first is the 'forward splashing' mechanism occurring right upon the reconnection of the overturning wave front and the sea surface below, which according to [17] only produces small amounts of droplets. After this, as shown in fig. 6.1d, the wave bulk catches up with the decelerated splash-up generated from the initial impact at a relative speed u_r close to the phase speed of the unbroken wave U_g. At the indentation region between these two structures, the shape of the wave bulk and the splash-up can be approximated as two cylinders, whose cross sections feature radii of curvature r_b and r_s which are typically different. The rapid closure of the indentation region leads to the 'secondary splashing' phenomenon, which is characterised by a wall of vertically projected small droplets along the transverse direction as reproduced in

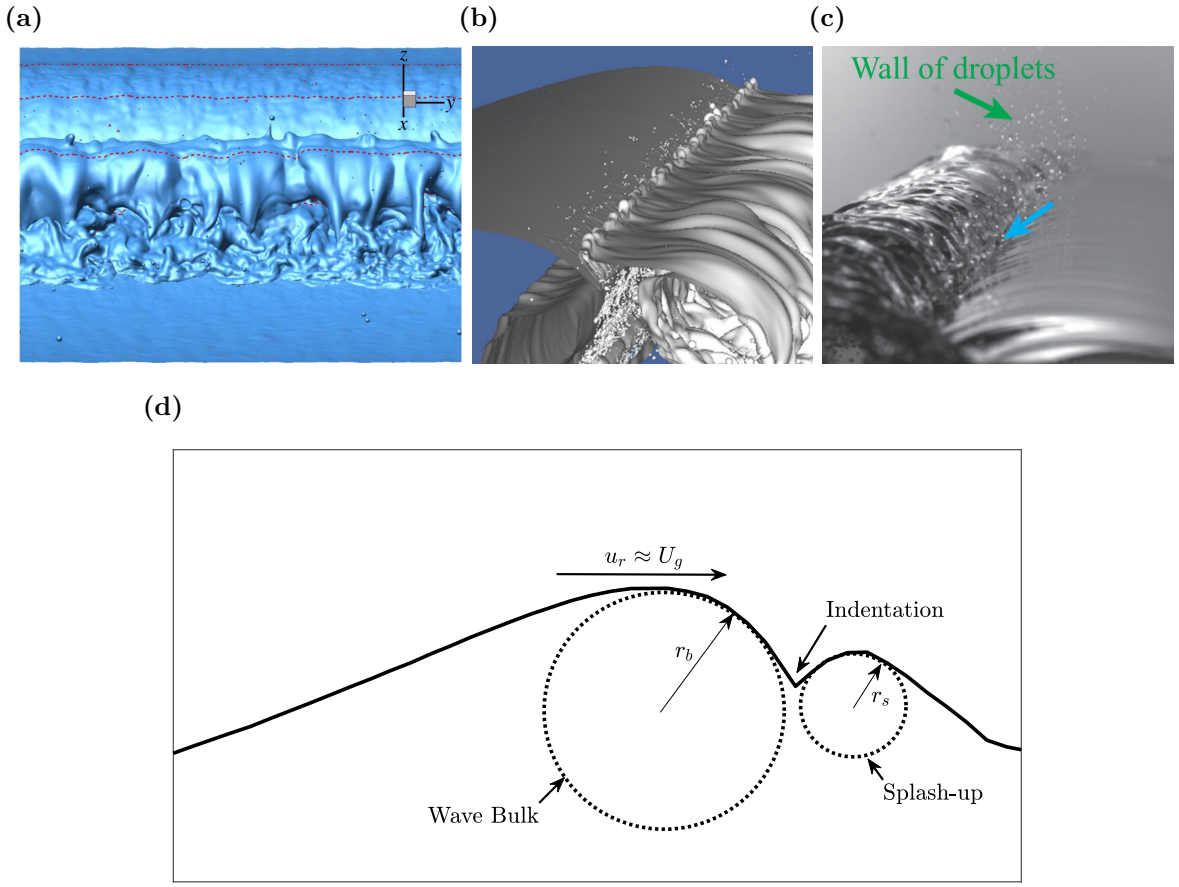

Figure 6.1: (a)-(c): Wave splashing observed in previous numerical (a,b) and experimental (c) studies, adapted from [196] (a), [17] (b) and [74] (c), respectively. Ligaments are obserced to form between the initial splash-up and the wave bulk, whose pinch-off gives rise to splash drops. (d): Sketch showing the ensemble-averaged breaking wave profile taken from [85] after the initial moment of impact in the breaking wave, at the moment of secondary splashing, where dashed lines indicate our simplification of the problem as the collision of two cylindrical rims with radii r_b and r_s. In this study we consider the basic case $r_s = r_b$. We also approximate the relative collision speed u_r between the wave bulk and the splash-up as the phase speed U_g of the unbroken gravity wave.

figs. 6.1a-c, accompanied by air entrainment within the former indentation region [9]. Under experimental conditions, fragments generated via this mechanism comprise about one third of the total amount of droplets produced over the entire wave-breaking process [74]; and Ref. [17] found that this splashing mechanism produces many fragments and can be curbed by strong surface tension (small Bo values). While Ref. [196] noted the connection between the corrugated surface of the splash-up and the vortical structures beneath the wave surface, to our knowledge no existing study has analysed the physical

mechanism governing the formation of these fragments, and their contribution to the overall droplet distribution associated with wave breaking remains unknown [9, 10, 16]. Furthermore, this splashing mechanism is found to produce many fragments close to the minimum grid size of Ref. [17]; together with the highly transient nature of wave breaking and the presence of other fragmentation mechanisms, this indicates considerable difficulty in investigating the secondary splashing phenomena directly within the context of wave breaking. While we do not yet reproduce the fragment statistics seen in the studies above, the present work serves as a first step towards understanding the more complex wave splashing phenomena by retaining the major generation mechanism of splash fragments while leaving out many complicating factors, including size difference between the wave bulk and the splash-up evolving with time, and internal turbulent flow within the liquid phase; as a similar approach taken by Gao *et al.* [197] reveals the connection between the bubble size distributions of destabilising air cylinders and air cavities entrained by plunging breakers.

In this work, we conduct a comprehensive investigation of the collision between two liquid cylinders with identical size, covering the entire deformation and fragmentation period. The direct comparison and establishment of connections between the rim collision results and the statistics of the secondary wave splashing phenomenon are left for future work, together with the role of gravity and the difference between the sizes of the wave bulk (r_b) and the splash-up (r_s) which complicate the early-time rim dynamics. Two-phase numerical simulations are conducted to derive detailed flow field information during this highly transient collision process. Our study is structured as follows. We first present in §6.2.1 the problem configuration and the parameter space of the current work, and then introduce the numerical method in §6.2.2. After providing an overview of the rim collision phenomena in §6.3, we quantitatively analyse the development of each part of the expanding liquid bulk successively following a spatial order, namely the kinematics of the spreading liquid sheet (§6.4.1) and its bordering rim (§6.4.2), the growth and merge of transverse ligaments topping the rim (§6.5), and the statistics of fragments shed from the ligaments (§6.6). We conclude the study in §6.7 with some remarks on future work.

6.2 Formulation and methodology

6.2.1 Problem description

The geometrical configuration for the rim collision problem is shown in fig. 6.2a, where two infinitely long cylindrical liquid rims with diameter d_0, density ρ_l and viscosity μ_l are aligned along the x axis, and set to travel along the z axis with uniform velocities of opposite sign and the same magnitude U_0. The liquid cylinders are surrounded by an inert gas phase with density ρ_g and viscosity μ_g, and the liquid-gas interface is characterised by a surface tension coefficient σ. Gravitational effects have been neglected in the current setup and, differing from the configurations of Refs. [62] and [63], there is no interstitial film connecting the two approaching cylinders. Consequently, four non-dimensional controlling parameters are relevant to this problem:

$$We \equiv \frac{\rho_l (2U_0)^2 d_0}{\sigma}, \quad Oh \equiv \frac{\mu_l}{\sqrt{\rho_l d_0 \sigma}}, \quad \rho^* \equiv \frac{\rho_l}{\rho_g}, \quad \mu^* = \frac{\mu_l}{\mu_g}, \tag{6.1}$$

where We and Oh are, respectively, the Weber and Ohnesorge numbers comparing inertial and viscous effects to capillary forces, and ρ^* and μ^* are respectively the density and viscosity ratios of the liquid and gas phase. In this work, Oh is set as 0.01 in most of the simulations, whereas its influence on the fragment statistics is briefly discussed in Appendix A. We take $\rho^* = 833$ and $\mu^* = 55$ as 830 and 55, respectively, which are typical values for the air-water system [113].

We set the width D of the cubic simulation domain as $10d_0$ to allow enough space for the morphological evolution of the coalesced liquid structure. Utilising the symmetry of the splashing phenomena about the xz-plane, we only model the merging of the upper halves of the two liquid cylinders to save computational resources. A symmetric boundary condition is therefore applied at the bottom, and an outflow boundary condition is imposed on the top boundary so that fragments produced from the collision can leave the domain from there at late time; the other boundary conditions are set as periodic.

To investigate the sensitivity of the fragmentation process to the initial conditions [95, 198], and also taking into account the surface corrugation of the splash-up in wave breaking events [9], which still has not been quantified according to our knowledge, we

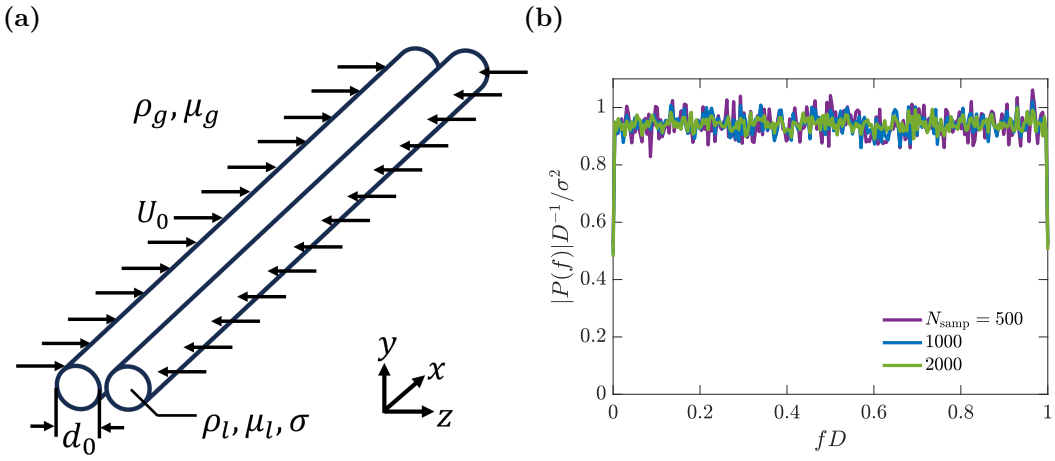

Figure 6.2: (a): Sketch showing the configuration of the liquid rim collision problem; (b): ensemble-averaged power density spectrum of the white noise signal for generating initial interface perturbations on the cylindrical rims.

introduce random transverse perturbation within a certain wavelength range on the cross-sectional radius of the two cylindrical rims [135], in the form of filtered white noise signals characterised by the following two parameters,

$$\varepsilon_0 \equiv \frac{2\epsilon_0}{d_0}, \quad N_{\max}, \tag{6.2}$$

where ε_0 is the non-dimensionalised characteristic amplitude of perturbation, and $N_{\max}$ defines the highest wavenumber among the spectrum of the perturbation signal. The filtered white noise signal is the default type of initial interface perturbation we impose on the rims, as Ref. [199] did for analysing the linear stability of the crown splash. Separately, we also consider single-wavelength sinusoidal perturbations with wavelengths $\lambda = D/8$, $D/16$ and $D/32$, or a superposition of sinusoidal perturbations with all these three wavelengths for comparison, which will be explicitly denoted by 'Sing.' and 'Sup.' when reported. In the case of single-wavelength perturbations, $N_{\max}$ corresponds to the perturbation wavenumber.

As discussed above, We, ε_0 and $N_{\max}$ constitute the parameter space for the present study. Among these, We is varied between 60 and 280 where the coalesced liquid bulk expands vertically to form a lamella, and ε_0 is set as 0.02, 0.04 and 0.06, within the limit of small radial perturbations. $N_{\max}$ varies between 15 and 80, whose influence will be discussed in detail in §6.5.2.

6.2.2 Numerical method

The open-source scientific computation toolbox Basilisk [102] is used in this work to solve the two-phase nonlinear, incompressible, variable-density Navier-Stokes equations. A second-order accurate discretisation is applied in both space and time, and a geometric volume-of-fluid (VOF) method in a momentum-conserving formulation is used to maintain a sharp representation of the liquid-gas interface while minimising the parasitic currents induced by surface tension [100, 134]. Capillary effects are modelled as source terms in the Navier-Stokes equations using an adaptation of Brackbill's method [101, 127], which calculates the interface curvature by taking the finite-difference discretisation of the derivatives of interface height functions [101]. The octree-based adaptive mesh refinement (AMR) scheme based on the estimation of local discretisation errors of the VOF function f and flow velocity $\boldsymbol{u}$ is adopted so as to reduce the computational cost at high resolution levels L, which is defined using the minimum grid size,

$$\Delta = \frac{D}{2^L}. \tag{6.3}$$

The results presented in the main body of this work are obtained from three-dimensional simulations at $L = 10$, at which the late-time evolution of interface profile and liquid-phase energetics have reached grid independence. The numerical convergence of fragment statistics is also established for fragments with diameter larger than $4\Delta_{10}$, which is discussed in detail in Appendix A. Results from some two-dimensional simulations are also presented for comparison with three-dimensional rim dynamics (§6.4.2), and to investigate lamella foot formation at very early time (Appendix B).

Since the present study focuses on the liquid-phase morphological development *after* the rims begin to coalesce, the distance between the symmetric axes of the two cylindrical rims are set at initialisation as $\Delta z_c = 0.95 d_0$, so that the slightly overlapped rims form a line of contact. The interfacial perturbations on the rims are introduced as follows. Firstly, discrete white noise signals with unit variance $\sigma^2 = 1$ are produced using the random number generator provided in Basilisk. Figure 6.2b shows the ensemble-averaged power density spectra of the white noise signals generated in Basilisk at different numbers of realisations N_{samp}. It is observed that the power density $P(f)$ is

close to the theoretical value of σ^2 at all frequencies f, matching the requirement of frequency independence for white noise signals. Next, we apply a low-pass filter on these signals so that only the lowest $N_{\max}$ wavelengths are preserved, and the filtered signal is normalised so that its standard deviation becomes $\epsilon_0 = 0.5\varepsilon d_0$. The normalised signals η are then mapped onto the transverse radius profile $R(x)$ of the liquid rims, in the form of $R(x) = R_0 + \eta(x)$. The two liquid cylinders being positioned close to each other ensures that they coalesce immediately when the simulation starts; there is not sufficient time for capillary effects to smooth out the perturbations, or to amplify them via the Rayleigh-Plateau (RP) instability [135].

6.3 Overview of rim splashing

Here we qualitatively describe the rim splashing process as observed in the simulations before analysing the detailed dynamics at each stage in the following sections. Figure 6.3 presents the isometric view of the splashing phenomenon at $We = 200$, $\varepsilon = 0.06$ and $N_{\max} = 25$, whereas fig. 6.4 shows the side view for a few different (We, ε) configurations with $N_{\max} = 25$. Tiny air bubbles are entrained within the indentation space between the two rims following the impact [74, 183, 200], which in our case have no known effects on the subsequent development of liquid-phase flow fields. The rims coalesce rapidly, causing a dramatic increase in the local liquid-phase pressure [62]. A very large pressure gradient arises at the surface 'indentation' between the two cylinders since the air-phase pressure remains unchanged, leading to the vertical acceleration of fluids near the surface [201]. The magnitude of the vertical velocity near the contact line can be a few times larger than the initial horizontal velocity U_0, causing the contact line to advance upwards rapidly with fluid particles nearby converging to it, while the high-pressure region follows it closely rather than remaining on the axis of symmetry [202]. A thin transverse liquid lamella [62] appears as shown in figs. 6.3b, and the location of the lamella foot agrees well with Eq. (B12) developed in Appendix B using potential flow theory [203]. The liquid lamella is also observed in the experimental study of Ref. [204] where two neighbouring drops impact with a solid surface simultaneously and expand into contact. Within the parameter space of the present study, this transverse

lamella continues to expand vertically under the pressure difference between the two phases and consumes the two impacting cylinders, evolving into a thin film aligned with the xy-plane; in the meantime it is continuously decelerated by capillary force, forming a thick rim at its upper border.

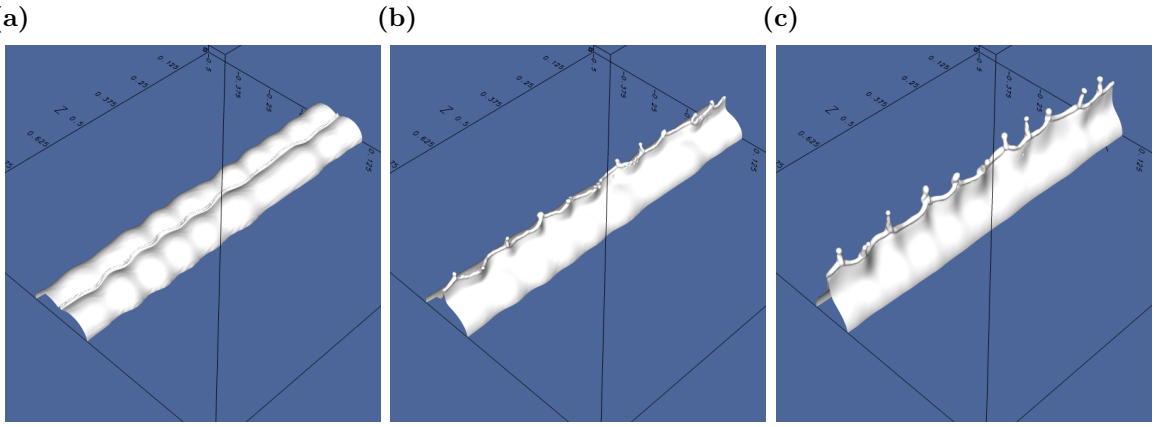

Figure 6.3: Isometric snapshots showing the liquid sheet expansion process at $We = 200$, $\varepsilon = 0.06$ and $N_{\max} = 25$. From left to right: $t/\tau_{\text{cap}} = 0.029$, 0.113 and 0.454.

Without the initial interface perturbation, the liquid rim would remain intact and mostly smooth during the entire simulation period up to $t/\tau_{\text{cap}} = 2.73$, where $\tau_{\text{cap}} \equiv \sqrt{\rho_l d_0^3/8\sigma}$ is the capillary time scale corresponding to the initial rim diameter. When perturbation is introduced, we observe the amplification of transverse perturbation waves on the rim as shown in fig. 6.4. Depending on the value of We, these waves will either slowly increase in amplitude and reach nonlinear development, whose growth rate increases with the initial perturbation amplitude ε_0, as shown in the first and last row of fig. 6.4; or generate slender ligaments which continue to elongate on the top of 'cusp' structures [87], as shown in fig. 6.3 and the middle row of fig. 6.4. It is noted that for all three cases presented in fig. 6.4, the number density of transverse ligaments (or the characteristic perturbation wave number when no such ligaments form) decreases over time rather than remaining a constant, a phenomenon which we will analyse in more details in §6.5. In the meantime, lamella expansion gradually slows down as the vertical position of its bordering rim reaches saturation, and begins to slightly retract at low We values as can be seen in figs. 6.4b and 6.4c. As is the paradigm of droplet formation in many previous fragmentation studies [8], here the transverse ligaments act

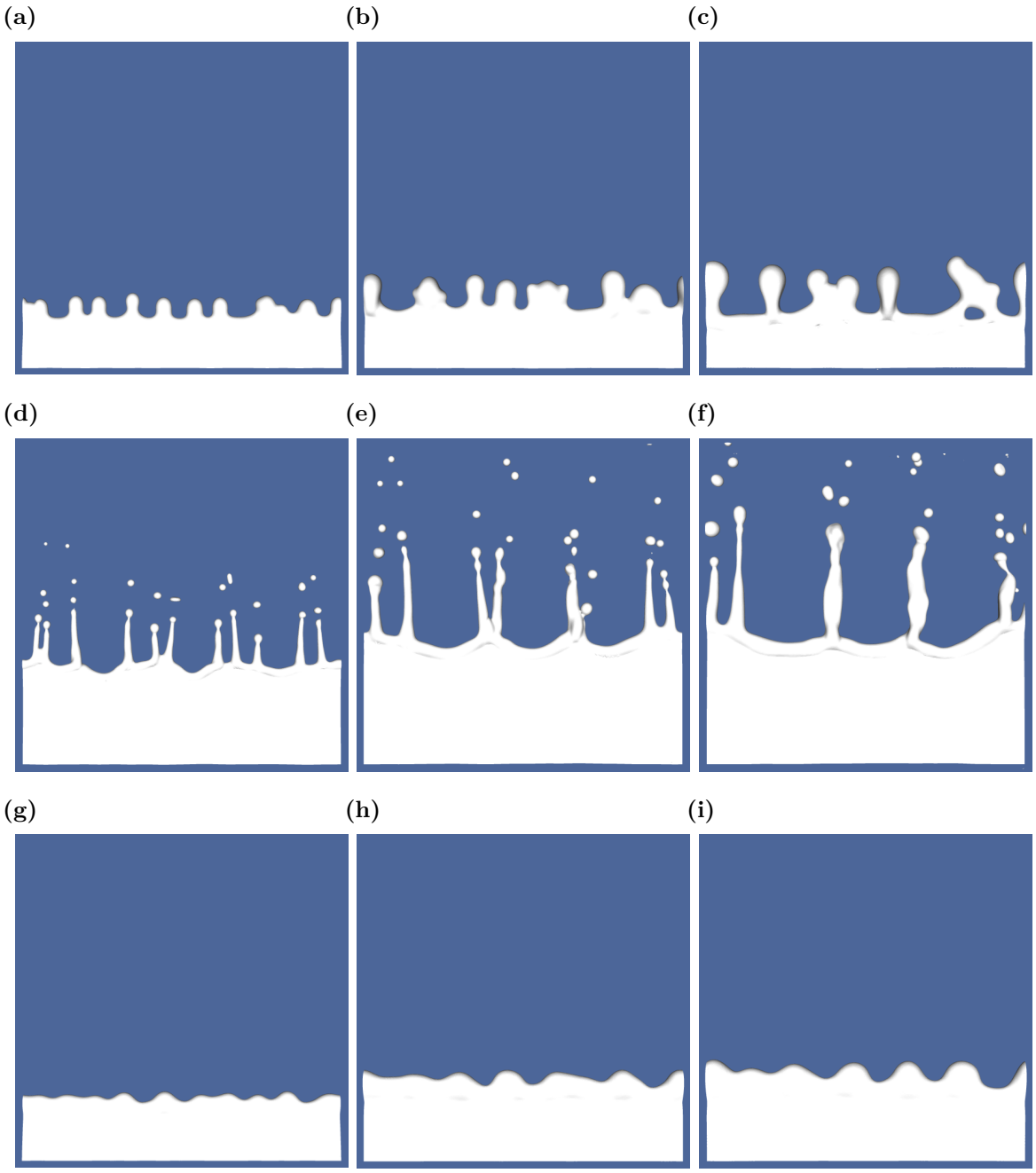

Figure 6.4: Snapshots showing the liquid sheet expansion process at $We = 60$, $\varepsilon = 0.06$ (top), $We = 200$, $\varepsilon = 0.06$ (middle), and $We = 60$, $\varepsilon = 0.02$ (bottom). From left to right: $t/\tau_{\text{cap}} = 0.91$, 1.82 and 2.73. For all three cases, $N_{\text{max}} = 25$.

as the direct and only source of fine drops as the latter intermittently detach from the ligament tips, whose statistics will be presented in §6.6. Under the restoring effects of capillary force, most of the fragments undergo prolate-oblate shape oscillations after their detachment, and a small portion of them may cross path and merge to form larger droplets during their flight [15]. Note that in our simulations all fragments keep moving upwards before crossing over the top boundary and leaving the simulation domain; while in wave splashing scenarios without wind forcing they will ultimately fall back to the sea surface under gravity and be destroyed [17].

6.4 Liquid lamella expansion

In this section, we study the dynamics of the liquid lamellae consisting of the expanding sheet (§6.4.1) and its bordering rim (§6.4.2). To simplify the problem which features random initial perturbation, here we do not consider the formation of liquid ligaments. Instead, we average the transverse cross section of the coalesced liquid bulk along the x axis following [77] so that the lamella expansion process can be described in a quasi-one-dimensional manner, characterised by one-dimensional velocity and thickness profiles $u_y(y,t)$ and $h(y,t)$.

6.4.1 Liquid sheet kinematics

The unsteady evolution of the expanding sheet profile is of both fundamental and practical importance for impact problems, especially for predicting their maximum spread radius [77, 83, 205], and the first step towards modelling the profile evolution of expanding sheets is to understand the fluid motion within them.

We first derive the velocity profile within liquid lamella sheets in Cartesian coordinates for $We \gg 1$ and $Oh \ll 1$. At early times, the vertically expanding sheet is bounded at its lower end by the line of collision between the two cylinders, which we call the lamella foot. The trajectory of this foot is given by $y_n = 2\sqrt{U_0 t/R_0}$, per the analysis given in Appendix B and following [81]. At later times, this lamella foot becomes increasingly indistinct as the colliding cylinders merge.

We now proceed to discuss the kinematics of the fluid within the vertical lamella sheet itself, subject to these considerations, following the general analytical strategy of Ref. [77]. After neglecting viscous, compressibility and capillary effects, the quasi-one-dimensional momentum equation in the vertical direction can be written as

$$\frac{\partial u_y}{\partial t} + u_y \frac{\partial u_y}{\partial y} = 0, \tag{6.4}$$

which may be presented alternatively in the Lagrangian form along the characteristics $dy/dt = u_y$,

$$\frac{Du_y}{Dt} = 0, \tag{6.5}$$

where D/Dt is the total derivative. Equation (6.5) suggests that the velocity of a fluid particle remains unchanged within the liquid sheet as it travels vertically upwards. We can then integrate along the characteristics and obtain the motion of fluid particles within a Lagrangian frame following it,

$$y = u_y t + \xi, \tag{6.6}$$

where u_y and ξ are the initial vertical velocity and position of fluid particles. Following Ref. [206], Ref. [77] assumes that the initial velocity is proportional to the initial position, namely $u_y = \beta\xi$, similar to the velocity field of a stagnation-point flow. Consequently, Eq. (6.6) may be rewritten in the Eulerian reference frame as

$$u_y(y,t) = \frac{y}{t + \frac{1}{\beta}}, \tag{6.7}$$

where $1/\beta$ corresponds to the time needed to set up the post-collisional velocity profile within the liquid bulk, which according to Ref. [77] is at the same order of the collision timescale d/U_0. As sheet expansion further progresses, so that $t \gg 1/\beta$, Eq. (6.7) asymptotes to

$$u_y(y,t) = \frac{y}{t}. \tag{6.8}$$

We measure the vertical velocity profile within the expanding sheet from our numerical simulations at different times for $We = 120$, and first plot them in the inset

of fig. 6.5a. Consistent with our assumption, the vertical velocity u_y is observed to scale linearly with the vertical position y, with the slope decreasing over time. In the main plot we rescale the horizontal axis by $U_0 t$, after which the velocity profiles at different times all collapse for $y \leq 2U_0 t$, agreeing with the prediction of Eq. (6.8). For $We = 120$, the collision timescale is $d/U_0 \approx 0.52\tau_{\text{cap}}$, while fig. 6.5a indicates that the velocity profile at $t/\tau_{\text{cap}} = 0.73$ is already very close to the analytical solution (6.8); which suggests that in fact the initialisation timescale $1/\beta \ll d/U_0$, and Eq. (6.8) is applicable to the early collision stage where $t \approx d/U_0$. Note that as time elapses, the vertical velocity deviates from Eq. (6.8) at progressively smaller values of $y/U_0 t$, where the fluid parcels move away from the sheet towards the bordering rim. Indeed, in fig. 6.5b we also plot the vertical velocity normalised by y/t at different times, We values and perturbation waveforms. All results presented therein feature a range where the normalised velocity $u_y t/y = 1$, suggesting that Eq. (6.8) remains valid at different initial configurations within our current parameter space.

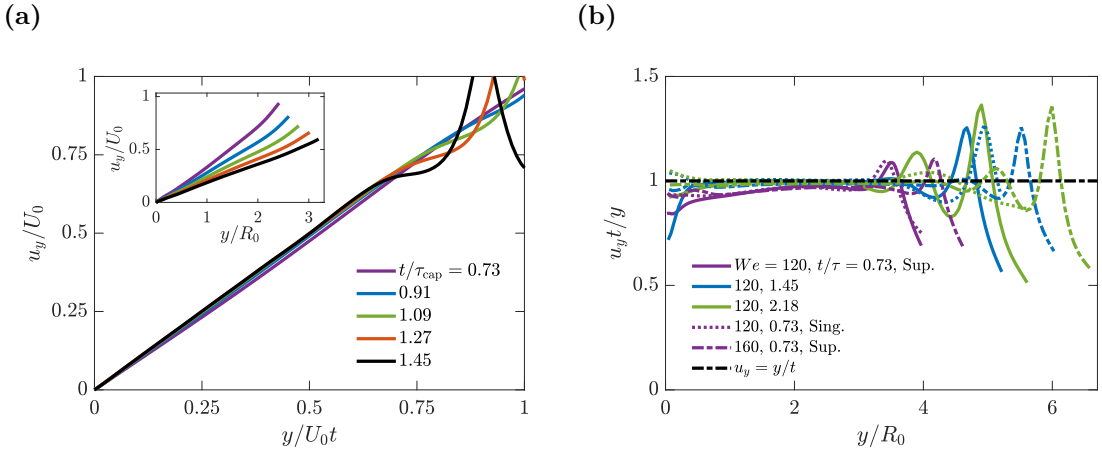

Figure 6.5: (a): Liquid sheet velocity profile at $We = 120$, scaled according to Eq. (6.8); (b): verification of Eq. (6.8) at different values of We, time and perturbation waveforms. 'Sing.' indicates that the initial perturbation we impose features a single wavenumber N_{max}, while 'Sup.' denotes a combination of sinusoidal perturbations with wavelengths $\lambda = D/8$, $D/16$ and $D/32$.

Having established the liquid velocity profile within the lamella sheet, we can further solve for its thickness profile utilising the continuity equation, which can be written

as follows for a thin sheet expanding in the y direction,

$$\frac{\partial h}{\partial t} + \frac{\partial (u_y h)}{\partial y} = 0, \tag{6.9}$$

combined with Eq. (6.8), this yields

$$t\frac{\partial h}{\partial t} + y\frac{\partial h}{\partial y} + h = 0. \tag{6.10}$$

This can be solved by separation of variables in the form of $h(y,t) = f(t)g(y)$ to obtain the evolution of sheet thickness h, which is written in a non-dimensional formulation as

$$\frac{hU_0 t}{R_0^2} = f\left(\frac{y}{U_0 t}\right). \tag{6.11}$$

Note that this result differs from the axisymmetric configuration where $hU_0^2 t^2/R_0^3$ evolves self-similarly without an explicit time dependence [77, 81].

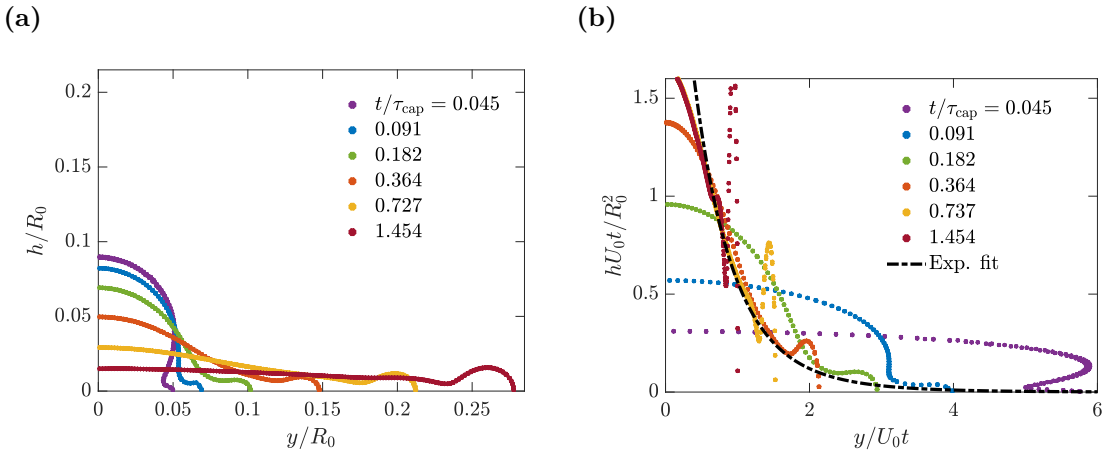

Figure 6.6: (a): Liquid sheet profiles at $We = 120$; (b): comparison between interface profiles non-dimensionalised according to Eq. (6.11) and the exponential fit in Eq. (6.12).

We plot the lamella thickness profiles for $We = 120$ in fig. 6.6a, where it can be seen that the 'bulge' centred around $y = 0$ gradually flattens into an extended thin liquid sheet, pushing the bordering rim further along the vertical direction. The bordering rim is connected to the sheet via a neck, reminiscent of capillary waves upstream of inviscid liquid rims receding at the Taylor-Culick velocity [59]. Figure 6.6b further shows the profiles rescaled by Eq. 6.11. The 'bulk' region where $y/R_0 \leq \sqrt{2U_0 t/R_0}$ initially retains its cylindrical shape during the initialisation period $t \sim 1/\beta$, and only

comes to agreement with Eq. (6.11) when the lamella foot disappears and the bulk can no longer be decisively told apart from the lamella. The non-dimensionalised lamella profile in fig. 6.6b is found to be well described by the following functional form $f(x)$,

$$f(x) = 0.5081e^{-x} + 2.782e^{-2x}. \tag{6.12}$$

Lastly, we note that although the liquid lamella expands vertically to form a thin film, the latter does not suffer from spontaneous perforation during our simulation period, although this is observed in fig. 14 of Ref. [53] and marks the onset of bag film fragmentation in droplet aerobreakup problems [15, 122], where the liquid films are subject to radial accelerations. Neither does the lamella film experience destabilisation under shear force arising from its interaction with the surrounding gas phase [207, 208], which may arise at larger We values. We therefore do not take special measures to artificially stabilise [198] or perforate [20] the expanding lamellae in this study.

6.4.2 Bordering rim evolution

As discussed in §6.4.1, while the expanding lamella sheet abides by the velocity profile in Eq. (6.8) and the self-similar thickness profile in Eq. (6.11), these two models break down for the bordering rim, which demands separate scaling laws to describe its kinematics. Similar rim structures are ubiquitous in impact problems and act as the crucial link between the expanding sheet and shedding droplets [60], and understanding their motion lays the foundation for further theoretical analysis of ligament merging, which we perform in §6.5.2.

In a quasi-one-dimensional framework, the kinematics of the bordering rim can be characterised by two parameters, namely its average vertical position y_{rim} and diameter b_{rim}. We first present their evolution at different We values in figs. 6.7a and 6.7b, respectively; where time and length are scaled using U_0/R_0 and R_0. It is seen that both y_{rim} and b_{rim} first increase with time and eventually saturate; and y_{rim} and b_{rim} show different dependence on We, as the former increases and the latter decreases with We, although these We-dependencies have become very subtle by $We = 200$. Further, the evolution of y_{rim} at $We = 200$ for $\varepsilon = 0.06$ and $\varepsilon = 0.04$ in fig. 6.7a

is virtually the same, which shows that the dynamic behaviour of the rim is largely independent of the initial perturbation amplitude ε.

We now seek to further compare our numerical results obtained in figs. 6.7a and 6.7b with available theoretical models. Following Ref. [81], the following mass- and momentum-conservation equations can be proposed in the non-dimensionalised form to describe the dynamic behaviour of the advancing lamella rim in the inviscid limit:

$$\frac{\pi}{8}\frac{db_{\mathrm{rim}}^2}{dt} = [u_y(y_{\mathrm{rim}},t) - v_{\mathrm{rim}}]h(y_{\mathrm{rim}},t), \tag{6.13}$$

$$\frac{dy_{\mathrm{rim}}}{dt} = v_{\mathrm{rim}}, \tag{6.14}$$

$$\frac{\pi}{8}\frac{d}{dt}(b_{\mathrm{rim}}^2 v_{\mathrm{rim}}) = u_y(y_{\mathrm{rim}},t)[u_y(y_{\mathrm{rim}},t) - v_{\mathrm{rim}}]h(y_{\mathrm{rim}},t) - \frac{8}{We}, \tag{6.15}$$

where the cylinder radius R_0, initial impact velocity U_0 and their quotient R_0/U_0 are chosen as the reference scales for length, velocity and time. The numerical solutions of the ordinary differential equation (ODE) system comprising Eqs. (6.13)–(6.15) at various We values, with initial conditions as defined in Appendix B, are presented in figs. 6.7a and 6.7b respectively as transparent solid lines. Since most of our measurements from 3D simulations are taken when $U_0 t/R_0 > 1$, we also present results of 2D simulations at $We = 80$ and 160 using solid dots, which extend to much earlier times. We find excellent agreement between the predictions of Eqs. (6.13)–(6.15) and the 2D results. Three-dimensional measurements of y_{rim} and b_{rim} are found to saturate earlier and become smaller than their 2D counterparts and theoretical predictions as time elapses. These observations can be explained by taking into account the formation of ligaments on the lamella rim. This mechanism arises due to highly nonlinear transverse perturbations imposed on the liquid rim, which is not present in 2D simulations. At sufficiently large times, the growth of ligaments causes a substantial mass flux away from the liquid rim, which becomes more prominent at higher We values as is shown in fig. 6.4. Other factors may also play a role, such as the initial overlapping between the two rims in 3D simulations.

In figs. 6.7c and 6.7d we present the evolution of y_{rim} and b_{rim} again, where time is now non-dimensionalised using the capillary timescale τ_{cap}. The growth of both y_{rim} and b_{rim} in 3D simulations is consistent with a power law of $\sqrt{t/\tau_{\mathrm{cap}}}$ up to $t/\tau_{\mathrm{cap}} \approx 1.4$,

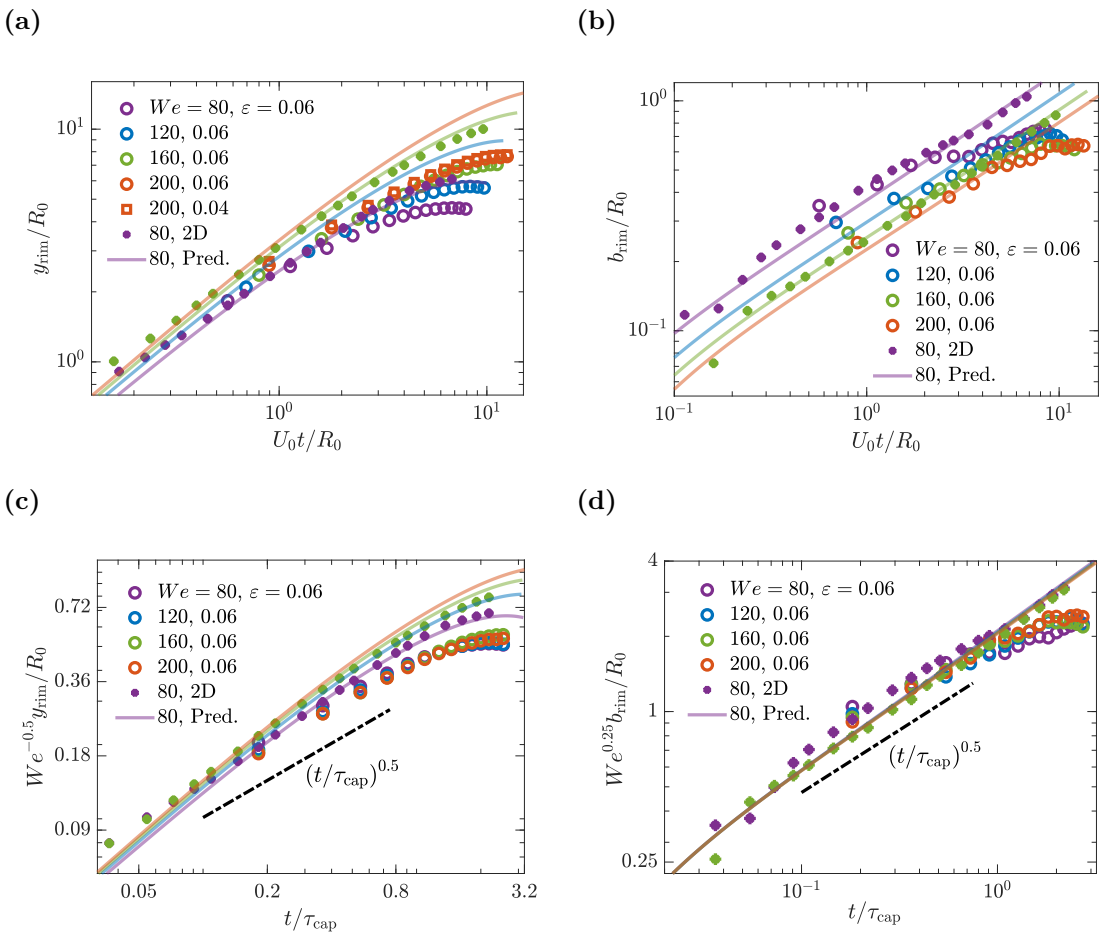

Figure 6.7: (a)(b): The evolution of the vertical position $y_{\rm rim}$ (a) and the rim thickness $b_{\rm rim}$ (b) over time, compared with solutions of Eqs. (6.13)–(6.15) at corresponding We values (solid lines). Early-time measurements from two 2D simulations with $We = 80$ and 160 are also included. (c)(d): Results in (a) and (b) rescaled using Eq. (6.16).

after which deviation from this power law is observed. It is also found that prefactors of $\sqrt{We}$ (for $y_{\rm rim}$) and $We^{-1/4}$ (for $b_{\rm rim}$) can collapse the evolution data reasonably well, especially for $b_{\rm rim}$ as a single master curve is clearly observed in fig. 6.7d, leading to the following scaling arguments:

$$\frac{y_{\rm rim}}{R_0} \propto \sqrt{We}\sqrt{\frac{t}{\tau_{\rm cap}}}, \quad \frac{b_{\rm rim}}{R_0} \propto We^{-1/4}\sqrt{\frac{t}{\tau_{\rm cap}}}, \tag{6.16}$$

which we use for further theoretical analysis of the ligament merging phenomenon in §6.5.2, while a complete determination for Eq. (6.16) valid for very late time remains for future work. The scaling of We in Eq. (6.16) agrees with the experimental results of Ref. [207] and Ref. [60] for drops impacting a small surface; although the dependence on

time is different, as their models aim at describing the entire sheet expansion-retraction motion. Nonetheless, similar empirical $\sqrt{t}$ scalings have been proposed in Refs. [209, 210] and [211] for quantifying the radial position of the expanding lamellae in the inertial regime, indicating that this simple form of time dependence can still describe the rim kinematics reasonably well between its formation and the onset of the retraction motion. Note that Eq. (6.16) implies that the evolution of the liquid momentum carried by the rim $p_{\mathrm{rim}} \equiv \pi \rho_l D b_{\mathrm{rim}}^2 \dot{y}_{\mathrm{rim}}$ is independent of the values of We, even though its average vertical velocity $\dot{y}_{\mathrm{rim}}$ and volume $\Omega_{\mathrm{rim}} \equiv \pi b_{\mathrm{rim}}^2 D$ do depend on We. This contrasts with the axisymmetric results of Ref. [80], where the rim volume remains independent of We due to their axisymmetric configuration.

6.5 Transverse liquid ligaments

6.5.1 Formation and growth

In the scenario considered by Wang and Bourouiba [79], liquid ligaments grow slowly out of the corrugated bordering rim along its azimuthal direction, which they ascribed to a combination of local geometry, pulling effects of inertial force associated with rim deceleration and the global liquid-phase mass conservation. For this study, and given our perturbation profile, we find the transverse ligaments form very early for $We \geq 120$, nearly at the same time when the lamella is born out of the indentation region between the two cylinders, as presented in the simulation snapshots of fig. 6.8. A closer look at fig. 6.8b reveals that the ligaments are produced preferentially from the concave regions along the two perturbed cylinders, suggesting that the ligament formation process is closely associated with the initial rim perturbation waveform. Indeed, a previous investigation by Gordillo *et al.* [212] suggests that the ligaments originate from the non-uniform initial distribution of normal interface velocity, which is in turn determined by the upstream liquid velocity and the curved initial cavity profile at the moment of impact. Note also that the nascent ligaments do not always project exactly vertically (i.e., in the y direction); rather, they can display complex twisting and surface oscillation motions, and may grow in an oblique direction. At the same time, the liquid sheet beneath its bordering rim also features a wavy surface

not perfectly aligned with the xy-plane. These are most likely due to the difference in the initial interface perturbations imposed on the two colliding rims, which gives rise to oscillatory motions under capillary effects.

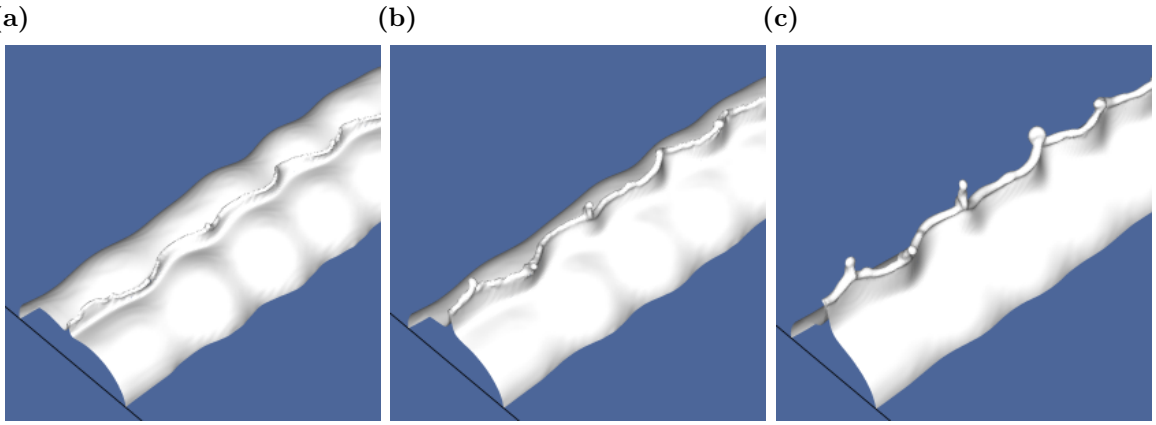

Figure 6.8: Snapshots taken from a simulation case at $We = 200$, $\varepsilon = 0.06$ and $N_{\max} = 25$ showing ligaments generated from the 'indentation' region between two colliding rims. From left to right: $t/\tau_{\text{cap}} = 0.045$, 0.091 and 0.136.

We next discuss the subsequent growth of the height of these ligaments after their formation, which is shown in fig. 6.9a for rim collision at $We = 120$ and 160, where we present the height evolution of three individual ligaments at each We. The shedding of the first fine drop from these ligaments is characterised by a kink around $t = 0.4\tau_{\text{cap}}$. While this initial pinch-off may happen at even earlier times as We increases, as shown in fig. 7 of Ref. [78]; this is still much later than the onset of the micro-splashing phenomena investigated by Thoroddsen *et al.* [210], which happens at $t/\tau_{\text{cap}} = O(10^{-4})$ (see, e.g., their fig. 5b). Before this first pinch-off event, the height h_{lig} of different ligaments increases following a similar trend, and the growth rate at $We = 160$ is higher than that at $We = 120$. Given that the initial phase of growth of these ligaments is governed primarily by inertio-capillary effects, we compare it in fig. 6.9a with the self-similar power law of $h \propto t^{2/3}$, proposed by Lai *et al.* [89] in their investigation of inertio-capillary-dominated collapse of small surface bubbles. It is found that the height increase of the majority of transverse ligaments (except Ligament 1 at $We = 120$) agrees better with the linear growth model. This is most likely because the formation of fast jets observed in Ref. [89] is preceded by focusing of interfacial capillary waves at the bottom

of the bubble cavity while the liquid bulk remains quiescent, whereas here the bulk velocity plays a vital role in driving the closure of rim indentation and may thus modify the rate of jet growth. In addition, a recent study by Gordillo and Blanco-Rodríguez [90] suggests that the exponent of power laws dictating the evolution of jet radius and speed is dependent on the initial geometry of the collapsing air cavity, which may also account for the difference between our results and those of Ref. [89] since the concave regions on our perturbed cylindrical surfaces do not feature a uniform radius of curvature.

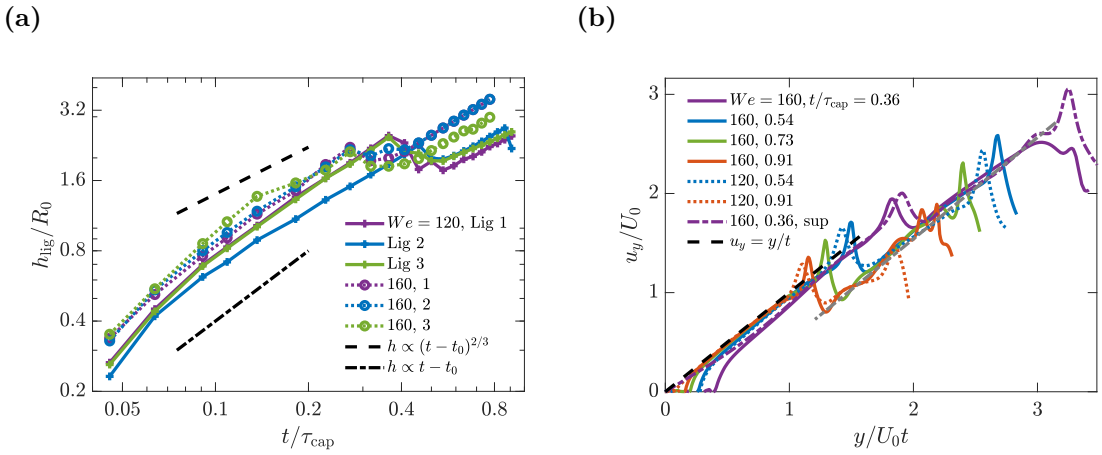

Figure 6.9: (a): The evolution of liquid ligament length measured at different We values, compared with the $t^{2/3}$ scaling law of Ref. [89] and a linear growth model. (b): Vertical component of liquid velocity u_y measured within liquid sheets and ligaments, showing the ballistic region within the ligament proposed in Ref. [88]. 'Sup' denotes that the initial rim perturbation is a superposition of sinusoidal signals with wavelengths $\lambda = D/8$, $D/16$ and $D/32$.

To better understand the fluid motion within the growing ligaments, we measure the liquid-phase vertical velocity u_y from the bottom of the expanding sheet up to the tip of a single ligament, and plot it in fig. 6.9b as a function of the vertical coordinate y. Two linear scaling regimes are observed; the first one is well described by $u_y = y/t$, which corresponds back to Eq. (6.8) we established for the expanding sheet. As the fluid particles move higher up and away from the sheet, its velocity first increases and then abruptly decreases as it enters the neck and rim region respectively; a similar abrupt deceleration is also noted by Wang and Bourouiba [80] for drop collision problems. Interestingly, the combination of the neck and rim causes a constant decrease in the vertical velocity of approximately $0.7U_0$ for different We values, times and perturbation

waveforms. This pattern is not explicable from Eq. (6.16) since according to it, the fluid velocity should be equal to the average rim velocity $\dot{y}_{\mathrm{rim}}$ after deceleration, which is always one half of the sheet velocity y_{rim}/t before deceleration. The implication is that the fluid velocity at the ligament root is always faster than the average rim velocity, which Ref. [79] ascribed to the additional acceleration due to the interface curvature at the rim-ligament junction. After this constant offset at the bordering rim which is most likely a viscous effect [213], u_y grows linearly again with the vertical position y with the same slope as the sheet region. This second linear scaling regime most likely corresponds to the ballistic region (although in the present study gravity is not included) in Worthington jets identified by Gekle and Gordillo [88], where the liquid particles travel at constant speed upwards before being slowed down once again at the bulb by capillary effects.

While Ref. [80] were able to demonstrate theoretically that energy dissipation at the bordering rim is responsible for the local rapid deceleration of fluid particles, which we also observed in fig. 6.9b, the detailed nonlinear dissipation mechanism is not captured by their one-dimensional model. As discussed in §6.1, there is still a dissipation deficit of 15% not covered by their calculations occurring at early-time. To help elucidate this discrepancy, we present contour plots in fig. 6.10 for a simulation case at $We = 200$, showing the distribution of the liquid-phase viscous dissipation rate $\epsilon_d \equiv \mu_l(\partial u_i/\partial x_j)(\partial u_j/\partial x_i)$ within the centre-plane $x = 0$ for $t/\tau_{\mathrm{cap}} \leq 0.36$, covering the early deformation period $t/\tau_{\mathrm{cap}} \leq 0.2$ where Ref. [80] observed the dissipation deficit (see their fig. 19). It is found that when the lamella is born at very early time and its bordering rim has not yet fully developed (fig. 6.10a), there is an extremely high concentration of ϵ_d located at the lamella foot, agreeing with the simulation results of Ref. [82] for drops impacting a smooth surface (see their fig. 4) and Eq. [214] for drops impacting a liquid pool (see their fig. 8b). As time elapses, the bordering rim takes shape with its neck featuring relatively high concentration of ϵ_d; whereas the dissipation at the lamella foot weakens and eventually becomes negligible by $t/\tau_{\mathrm{cap}} = 0.364$ (fig. 6.10d), matching the saturation trend shown in fig. 19 of Ref. [80] for the dissipation deficit. This decay pattern of liquid-phase dissipation may be explained as follows. The liquid

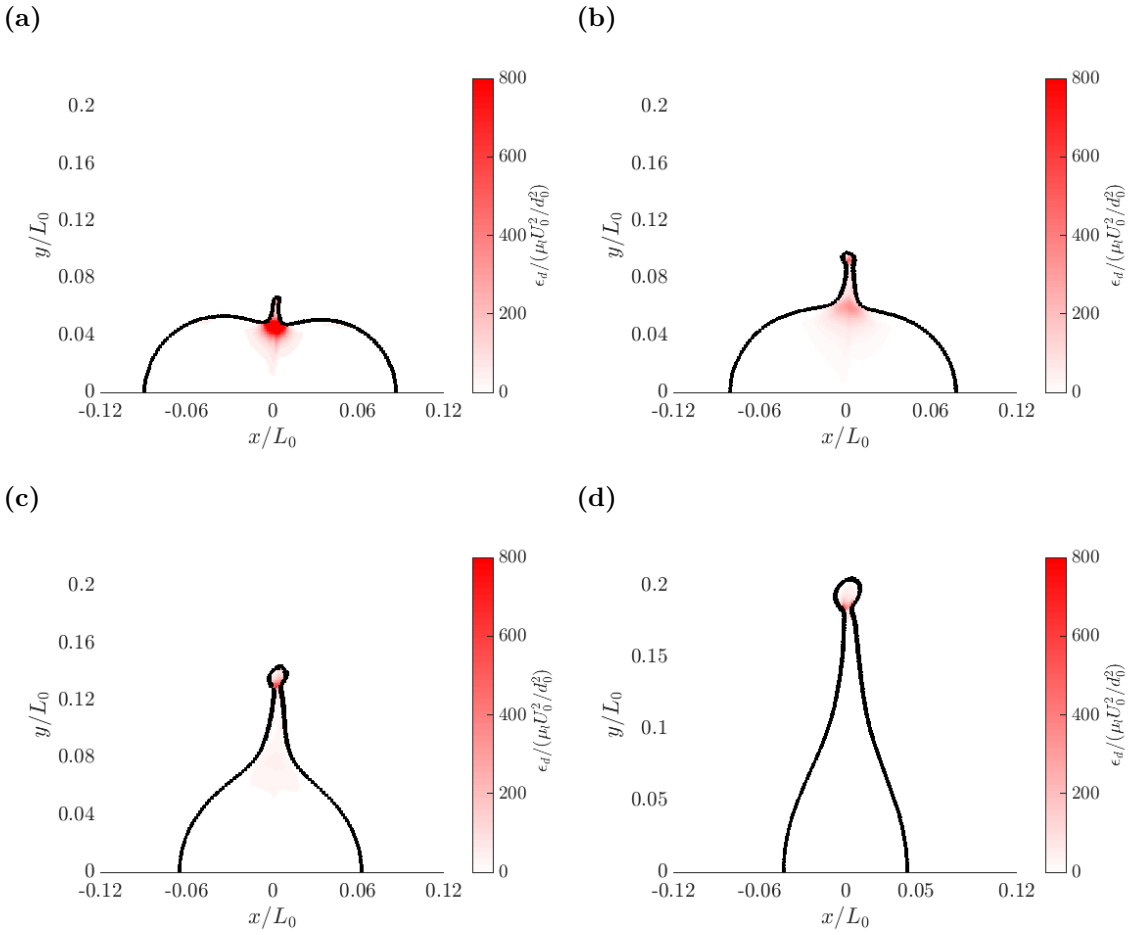

Figure 6.10: Contour plots visualising the 2D distribution of instantaneous liquid-phase dissipation rate ϵ_d within the centre-plane $x/D = 0.5$ for $t/\tau_{\text{cap}} = 0.045$ (a), 0.091 (b), 0.182 (c) and 0.364 (d), where $We = 200$ and $\varepsilon_0 = 0.06$.

particles feeding the lamella at early time mostly comes from a very narrow boundary straddling the corners on either side of the lamella foot [203]; and they generate vorticity [215, 216] and experience capillary deceleration while traversing the highly-curved free surface, leading to very large values of viscous dissipation. Since this early-time deceleration is geometry-induced, Ref. [214] further hypothesised that the magnitude of the velocity gradient remains largely unchanged at different flow configurations so that the early-time dissipation rate is proportional to the liquid viscosity μ_l; although this is not directly verified in the present work. As the liquid sheet extends further upwards, the interface curvature at the lamella foot decreases and capillary deceleration becomes much weaker, hence the decrease in the dissipation rate ϵ_d. Eventually, as the lamella

foot is no longer discernable from the flattened liquid bulk and the capillary effects become negligible, the inviscid sheet velocity profile in Eq. (6.8) will be established.

These observations of the liquid-phase dissipation evolution therefore suggest that the unidentified dissipation deficit found in Ref. [80] is most likely linked with the early-time lamella formation which also features strong viscous effects; and according to Refs. [82] and [217], this kind of dissipation is a type of 'general head loss' imposed by the deformation mode of the impacting object and independent of the detailed impact parameters. The head loss in impact problems dissipates a fixed fraction of the initial kinetic energy via recirculating flows [82, 217], which matches the observations of Ref. [80]. It is also noted that besides the early-time lamella foot and the late-time rim neck, the flow field elsewhere within the coalesced liquid bulk shown in fig. 6.10 is nearly inviscid, supporting our derivation of the centerline velocity profile within the liquid sheet (See Eq. (6.8)) based on inviscid flow assumptions. While we have not fully explored the influence of Oh on the lamella expansion process, it can be expected that in the inviscid limit where $Oh \ll 1$, its influence will be confined to the narrow 'viscous' regions identified in this section, and thus will not significantly affect the deformation of the droplet bulk, or the ligament dynamics and fragmentation mechanisms to be discussed below.

6.5.2 Ligament merging phenomenon

As is noted in §6.3, the number of transverse ligaments on the rim will decrease over time as they merge with their neighbours. This merging process is observed only when the initial perturbation is not monochromatic such that the nascent ligaments are not equidistantly spaced, and it turns out crucial in maintaining the growth of ligaments and the continuation of fragment shedding. Figs. 6.11a-c show the development of ligaments formed out of monochromatic perturbation waveforms, and it is observed that after two rounds of pinching-off events at their tips, the ligaments can no longer sustain their own growth and are re-absorbed back into the underlying liquid rim; whereas ligaments formed out of filtered white noise perturbations at the same values of We, ε

and $N_{\max}$ merge with their neighbours and survive end-pinching, continuing to grow and shed fragments until the end of simulation, as observed in figs. 6.11d-f.

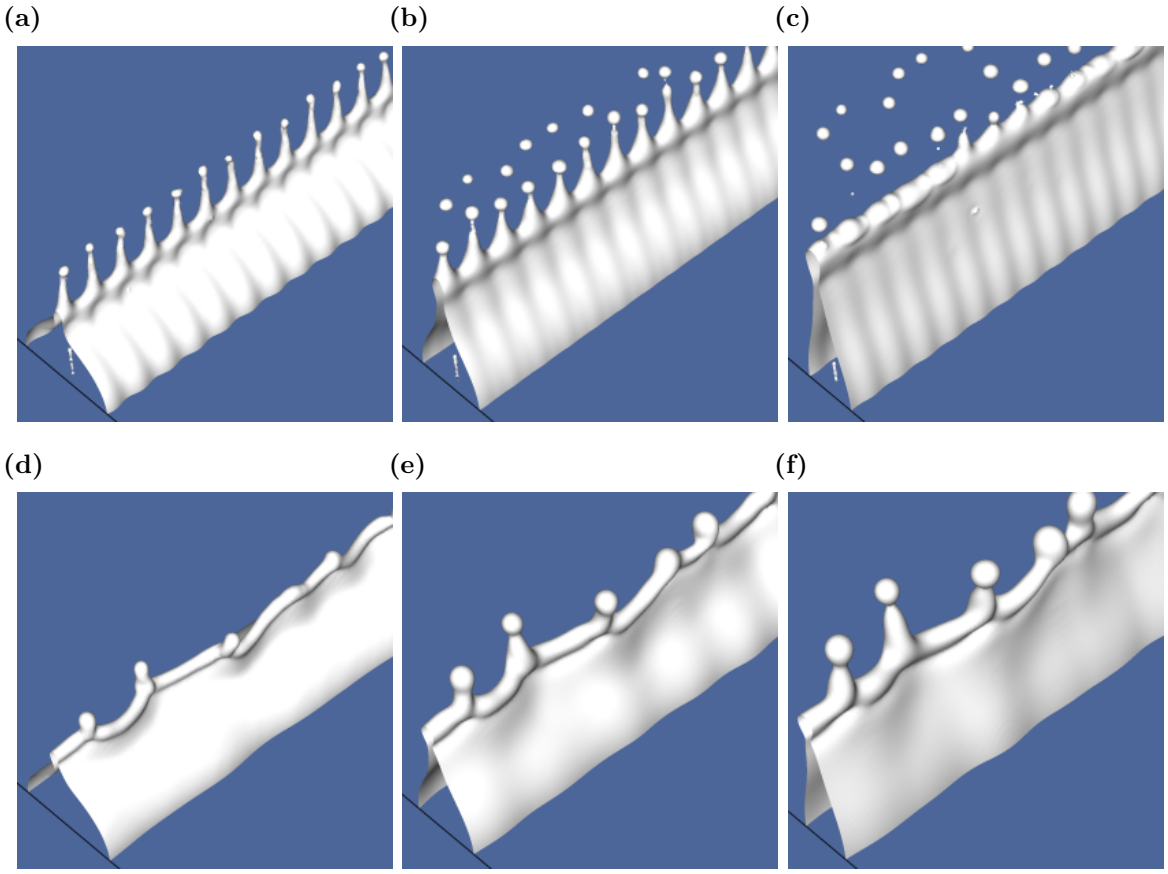

Figure 6.11: Snapshots at $We = 120$, $\varepsilon = 0.06$ and $N_{\max} = 25$ showing ligament evolution from monochromatic initial perturbations (upper row) and filtered white-noise perturbations (lower row). Re-absorption of ligaments back into the rim is observed for the monochromatic perturbation case after two cycles of drop shedding. From left to right: $t/\tau_{\text{cap}} = 0.2$, 0.4 and 0.6.

The ligament merging process is shown in more details in the snapshots of fig. 6.12, where the merging ligaments are observed to be located on rim 'cusp' structures extruding from the liquid sheet beneath, an indication of the non-uniform incoming mass distribution along the bordering rim [78, 87]. When ligament merging occurs, the roots of two neighbouring ligaments approach each other; liquid is then drawn upwards from the underlying cusp in between the two ligaments, causing them to coalesce into a thicker and more corrugated ligament; while the length of the fused ligament does not differ significantly from those of its parents. Ligament merging is thus capable of delaying

the next end-pinching event since the fused ligament takes longer to be stretched, thus allowing incoming fluid from the rim to sustain their growth and evade re-absorption into the rim when the depleted ligament becomes too short, as observed in fig. 6.11. Note that the monotonically decreasing trend of ligament numbers observed by us and in Ref. [79] differs from the early experimental work of Thoroddsen and Sakakibara [218] on drop impact, where they also observed splitting of liquid fingers aside from their merging behaviour, so that the total finger number remains approximately constant.

Figure 6.12: Snapshots taken from a simulation case at $We = 160$, $\varepsilon = 0.04$ and $N_{\max} = 25$ showing ligaments merging on the corrugated rim bordering the expanding sheet, while shedding fragments via the end-pinching mechanism. From left to right: $t/\tau_{\text{cap}} = 0.73$, 1.09 and 1.45.

To the knowledge of the authors, a scaling law for the ligament numbers accounting for their merging dynamics is not yet available. The early work of Marmanis and Thoroddsen [219] found that the number of liquid fingers at the maximum spread radius for high-speed drop impacts scales with $Re^{3/4}$ (Re being the impact Reynolds number), without accounting for their evolution over time; whereas the recent $We^{3/8}$ scaling model proposed by Wang and Bourouiba [79] is based on the understanding that the ligaments are formed from a subset of rim corrugations arising from a combined Rayleigh-Taylor (RT) and Rayleigh-Plateau (RP) instability; a physical mechanism which is most likely not yet active within our parameter space as we find the formation of ligaments more closely linked with the initial interface perturbation geometry. The early theoretical analysis of Yarin and Weiss [206] predicted that perturbed free rims will spontaneously develop 'cusp' structures due to nonlinearity, where two neighbouring rim sections impinge and give rise to free jets. This physical picture closely resembles our present observations, although they did not proceed to develop scaling models for the splashing

fragments. We therefore seek to derive a new ligament number scaling model accounting for the merging dynamics in this section, and compare it with the simulation results.

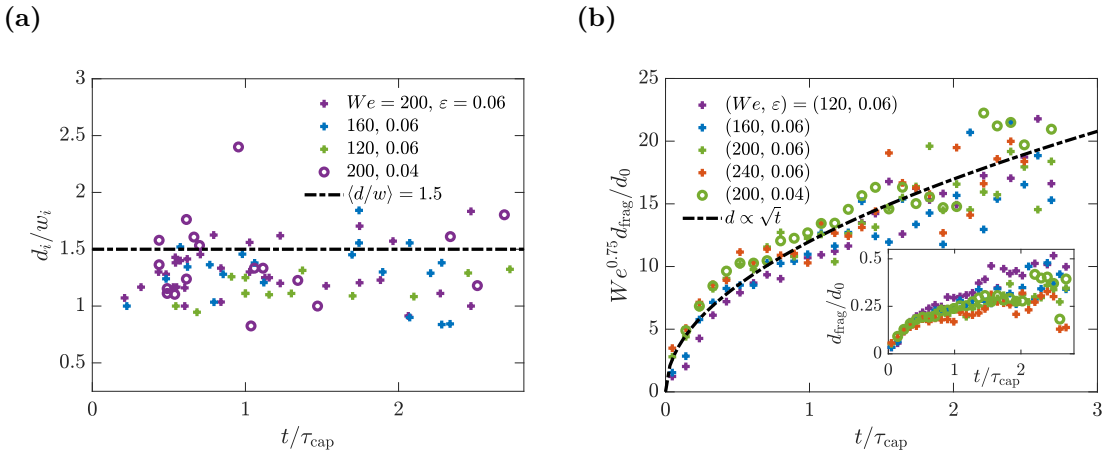

Figure 6.13: (a): Measurement of the ratio between the diameter d_i of the detaching fragment and the width w_i of its originating ligament at different ejection times. (b): The evolution of the fragment diameter d_{frag} of ejected fragments. The results in (b) have been ensemble-averaged across three realisations for each (We, ε) configuration, and rescaled by $We^{-0.75}$ in the main plot.

As the first step towards quantifying ligament dynamics, we seek to determine the evolution of the average ligament width w_{lig} over time by inspecting the evolution of fragment diameter d_{frag}, which can be easily reconstructed using the droplet-tracking algorithm of Chan *et al.* [139]. The connection between these two quantities is established in fig. 6.13a, where we plot the ratio between d_{frag} and w_{lig} at the instant of pinch-off. The ligament diameters are measured at the cross section corresponding to one half of the total ligament length. Most of the measured data are found to scatter between 1 and 2, centred around 1.4 which is close to the average value of 1.5 as found by Wang and Bourouiba [78]. These are below the theoretical value of 1.89 as predicted by the RP instability [93], indicating that end-pinching is indeed the dominant fragment production mechanism for the present study, and that the diameter of fragments d_{frag} remains in proportion to the width of their parent ligaments w_{lig}.

The inset of fig. 6.13b shows the diameters of the fragments d_{frag} versus their time of formation, where the data for each configuration of (We, ε) have been averaged across three individual realisations to reduce the range of scatter. It is found that

larger fragments are generally produced at later times and smaller We values. The scatter in data increases over time, which is most likely due to the increase in the diameter difference and the surface corrugation of remaining ligaments as they merge with one other. The main plot suggests that the evolution of individual fragment diameter in fig. 6.13b roughly scales with $We^{-3/4}\sqrt{t/\tau_{\text{cap}}}$, while noting that our fitted prefactor $We^{-3/4}$ is not conclusive and remains to be further validated at higher We values. Since the fragment size remains in proportional to the width of their parent ligament according to fig. 6.13a, it can be inferred that

$$w_{\text{lig}} \propto d_{\text{frag}} \propto \sqrt{\frac{t}{\tau_{\text{cap}}}}. \tag{6.17}$$

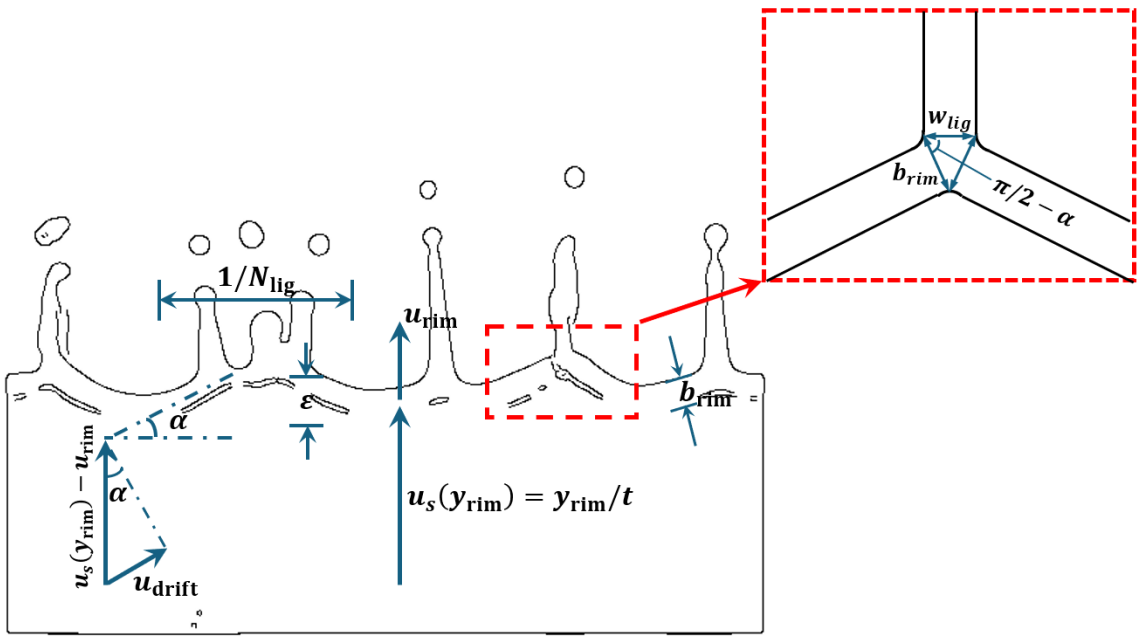

Figure 6.14: Main plot: Sketch showing the quantities defined in §6.5.2 for developing the ligament merging model in Eq. (6.22). Inset: Sketch showing the local geometry of the junction region at the ligament base.

Gordillo *et al.* [87] and Wang and Bourouiba [78] proposed the following drift velocity of ligaments u_{drift} on top of a liquid cusp to characterise their migration,

$$u_{\text{drift}} = [u_s(y_{\text{rim}}) - u_{\text{rim}}] \sin\alpha, \tag{6.18}$$

where $u_s(y_{\text{rim}}) = y_{\text{rim}}/t$ is the velocity at which liquids enters the rim from the expanding liquid sheet, calculated from Eq. (6.8); and u_{rim} is the vertical rim velocity determined by

differentiating the scaling law for y_{rim} in Eq. (6.16). It is noted that both $u_s(y_{\mathrm{rim}})$ and u_{rim} scale as $\sqrt{We}\cdot t^{-1/2}$, and α is the angle between the local rim and the horizontal plane as shown in fig. 6.14. Overall, Eq. (6.18) suggests that the migration of ligaments is driven by the tangential projection of the net incoming fluid velocity along the corrugated rim.

As u_{drift} drives the ligament migration and causes the ligament number density N_{lig} to decrease, the average transverse ligament spacing $1/N_{\mathrm{lig}}$ on the rim consequently increases. Therefore,

$$u_{\mathrm{drift}} \propto \frac{d}{dt}\left(\frac{1}{N_{\mathrm{lig}}}\right). \tag{6.19}$$

The averaged value of $\sin\alpha$ can be determined by inspecting the geometry of the junction region between the ejected ligaments and the lamella rim, which is shown in the inset of fig. 6.14. Making use of the law of cosines:

$$\frac{w_{\mathrm{lig}}}{2b_{\mathrm{rim}}} = \cos\left(\frac{\pi}{2}-\alpha\right) = \sin\alpha. \tag{6.20}$$

This combined with Eqs. (6.17) and (6.16) yields

$$\sin\alpha = C(We), \tag{6.21}$$

suggesting that the rim slope α remains unchanged over time and depends only upon the impact Weber number. Taking into account that $\tan\alpha \approx \varepsilon_{\mathrm{rim}}N_{\mathrm{lig}}$, α remaining constant also indicates that as the average ligament spacing $1/N_{\mathrm{lig}}$ becomes larger over time owing to the ongoing merging of ligaments, the rim corrugation $\varepsilon_{\mathrm{rim}}$ also increases proportionally to maintain a constant local slope.

By further incorporating Eqs. (6.19) and (6.18), the following model predicting the evolution of the ligament number density N_{lig} can be derived,

$$N_{\mathrm{lig}} \propto \left(\frac{t}{\tau_{\mathrm{cap}}}\right)^{-1/2}. \tag{6.22}$$

In the main plots of fig. 6.15 we show the decay of the ligament number density N_{lig} at different values of N_{max} and We. Figure 6.15a shows that while increasing N_{max} leads to the formation of more ligaments at early time, N_{lig} appears to reach saturation and does not increase proportionally with N_{max} when $t/\tau_{\mathrm{cap}} = 0.18$; and it is likely

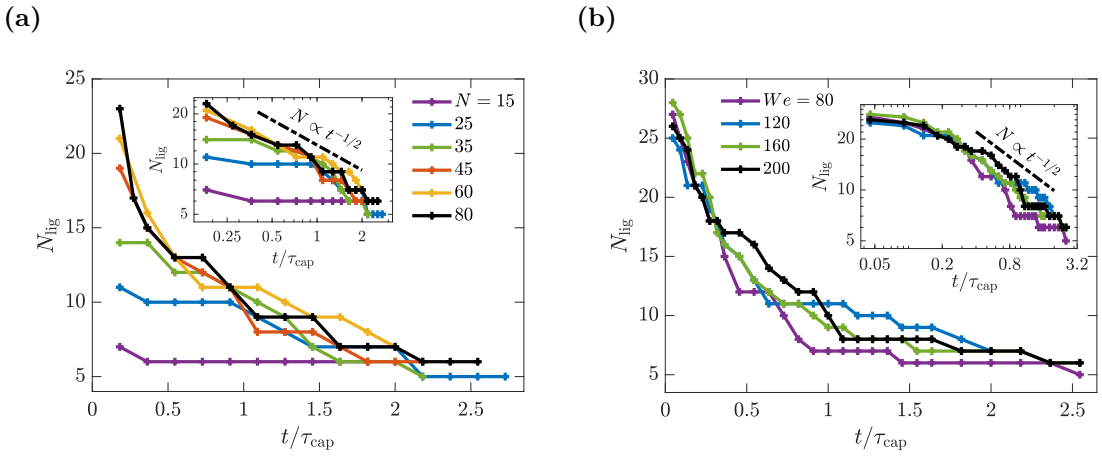

Figure 6.15: Evolution of the ligament number density N_{lig} at different values of $N_{\max}$ with $We = 120$ (a) and different We with $N_{\max} = 60$ (b). The insets compare the evolution of N_{lig} with Eq. (6.22).

that viscous damping effects are particularly strong when the lamella is ejected at the early impact stage, which may smooth out short-wavelength components in the initial perturbation spectra (see our fig. 6.10 and relevant discussions). Larger $N_{\max}$ also leads to faster decay of N_{lig} as expected, since the average distance between neighbouring ligaments becomes smaller; and for all values of $N_{\max}$, fig. 6.15a suggests that the evolution of N_{lig} becomes largely similar for $t/\tau_{\text{cap}} > 1.5$, where the remaining ligaments take much longer to migrate and merge. Figure 6.15b shows that the decay of N_{lig} does not appear to depend strongly on We and thus lends some support to the prediction of Eq. (6.22) that it is We-independent, although ensemble averaging would be needed to ascertain this due to the randomness in the initial perturbation waveform. The insets of fig. 6.15 show the evolution of N_{lig} again in log-log axes, which is also compared with Eq. (6.22). The inset of fig. 6.15a indicates that the measured results collapse well and agree with Eq. (6.22) for $N_{\max} \geq 35$ throughout the period of measurement, whereas at $N_{\max} = 25$ the decay of N_{lig} is initially slower, and only matches the prediction of $t^{-1/2}$ for $t/\tau_{\text{cap}} \geq 1$. The measurement of N_{lig} extends to earlier times in fig. 6.15b, and its inset suggests that the evolution of N_{lig} at different We is initially slower and matches Eq. (6.22) only after $t/\tau_{\text{cap}} \geq 0.2$. This slower decay at early times observed in both insets arises most likely because the rim slope α takes a finite period of time to develop before reaching the steady-state value given by Eq. (6.21). Overall, these results indicate

that Eq. (6.22) offers a good working description of the ligament merging phenomenon occurring within our parameter space. However, the approximations we make for its derivation restricts its application to the scenario when N_{lig} is large and the slope α of the corrugated rim has reached the steady-state value predicted by Eq. (6.21).

6.6 Droplet generation and characteristics

Since the expanding sheet remains intact during our simulation period, fragments are formed solely through the breakup of liquid ligaments originating from the bordering rim. The majority of fragments are produced via the end-pinching mechanism, a process that coincides with the ligament merging phenomena and is already visible in the snapshots presented in figs. 6.4 and 6.12. Namely, the ligament tips are decelerated by capillary force and produce surface corrugations, which in turn creates a local pressure gradient within the ligament neck that drains the liquid towards the tip and triggers pinch-off. After this, the enlarged ligament tip detaches as a primary drop [93], whose diameter is proportional to the parent ligament width as shown in fig. 6.13a. Occasionally, satellite drops are formed from the small amount of remnant liquid within the neck before it can be fully reabsorbed into the ligament after end-pinching, as also shown in fig. 5b of Ref. [78]. In contrast with the primary drops, the production of these satellite drops is sensitive to initial liquid-phase velocity perturbations, thus introducing randomness to the jet breakup process. However, they do not affect the size and velocity of the subsequent primary drops ejected, as shown by Berny *et al.* [95] in the instance of jet-droplet production by bubble-bursting. Possibly due to the difference in their generation mechanisms, our ligaments can grow much longer than those observed by Ref. [78] in their experiments. At late times, some particularly long ligaments may break up due to the RP instability and shed multiple primary fragments at a time, as can be seen in the rightmost ligament in fig. 6.4e and fig. 2f of Ref. [84]. The production of multiple drops from the end of ligaments appears inconsistent with the conclusion of Ref. [79] that a ligament can only pinch off to produce one primary drop at a time under the chaotic dripping regime.

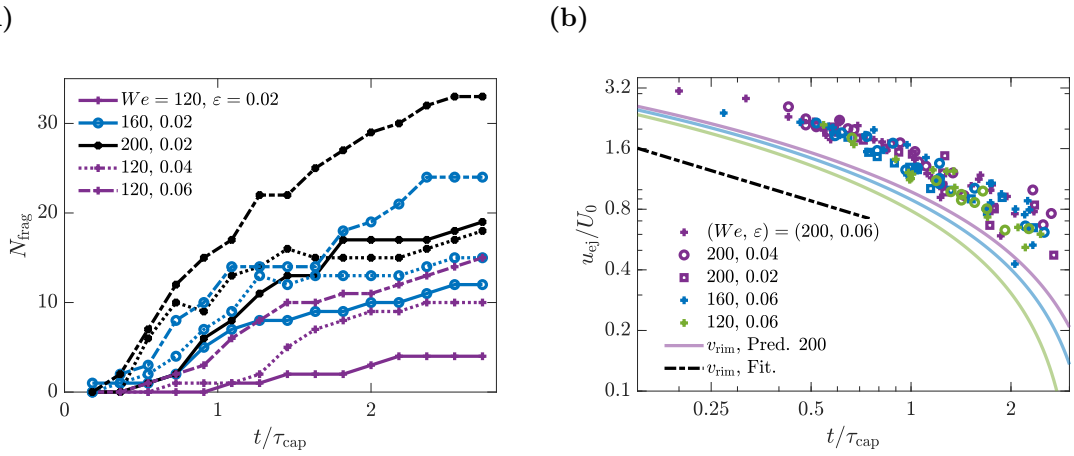

Figure 6.16: The evolution of the total number density N_{frag} (a) and the ejection velocity (b) of primary fragments, compared with the rim velocity u_{rim} derived from solving Eqs. (6.13)-(6.15) (solid transparent lines) and (6.16) (dash-dotted line).

We first analyse the time evolution of various fragment properties during the rim collision process. Figure 6.16a shows the evolution of the total number density of primary fragments N_{frag}, where it is observed to generally increase over time towards saturation, despite infrequent decreases due to coalescence of primary fragments with another fragment or a neighbouring ligament. It is also noted that N_{frag} increases with both We and ε, as larger We and ε encourages the growth and subsequent pinch-off of liquid ligaments.

The decrease of drop production rate $\Delta N_{\mathrm{frag}}/\Delta t$ can be explained as follows. The ongoing ligament merging phenomenon causes the ligament number density to decrease, hence fewer fragments can detach at the same time. In the meanwhile, merged ligaments become more corrugated and thicker, thus end-pinching events occur at larger ligament widths as time elapses. Consequently, the time interval between successive end-pinching events also becomes longer, since the necking timescale

$$t_{\mathrm{neck}} \equiv 1.13\sqrt{\frac{\rho_l w_{\mathrm{lig}}^3}{\sigma}} \tag{6.23}$$

increases with w_i according to the experimental results of Ref. [78].

Figure 6.16b shows the evolution of the fragment ejection speed u_{ej}, the speed of the drop at the moment it detaches from its parent ligament. The fastest drops found in our simulations feature u_{ej} slightly over $3U_0$, which is comparable to the fragment ejection

velocity in the prompt splashing phenomena [220]. Regardless of the detailed geometrical features of the parent ligaments, when scaled with the initial collision speed U_0, the decay of u_{ej} over time does not significantly depend on either We or ε_0. We further compare the measured u_{ej} values with the predictions of both Eqs. (6.13)–(6.15) and Eq. (6.16). Both capture the early-time evolution of u_{ej} up to $t/\tau_{\mathrm{cap}} \approx 0.5$, after which the decrease of u_{ej} slightly steepens and shows a better agreement with the predictions of Eqs. (6.13)–(6.15). This is most likely due to the late-time capillary deceleration not well-represented by Eq. (6.16). We note that while the rim velocity predicted by Eqs. (6.13)–(6.15) is closer to u_{ej}, they tend to over-predict the three-dimensional simulation results, as already observed in fig. 6.7; suggesting the existence of a gap between the actual rim velocity and the fragment ejection velocity. This agrees with the earlier results of Ref. [84], where their fig. 5 also shows fragment speeds remaining higher than the rim velocity. Similar measurements of the fragment ejection velocity have also been reported by Thoroddsen *et al.* [210] for micro-splashing in drop impact problems at much larger values of We, which were well explained by the theory of Ref. [208]. However, in Ref. [208] the lamella rim fragments under Rayleigh-Taylor and capillary instabilities, and therefore the velocity and size of ejected droplets are directly determined by the rim. In Ref. [210], fragmentation also occurs shortly after the emergence of the lamella sheet, based on which Riboux and Gordillo [208] modelled the droplet ejection velocity using flow field information at the lamella foot. These differ from our scenario where the ejection of droplets are governed by the end-pinching of ligaments erupting on the lamella rim [78]. Development of theoretical models capable of predicting fragment ejection speed in our case thus requires detailed knowledge of ligament growth and merging dynamics, which is out of the scope of the current work.

Since rim collision is a transient process where both the total number and the individual size of fragments increase over time, as shown in fig. 6.13, it is of interest to determine how the fragment size and velocity distribution functions evolve with time. We first show the fragment size distributions $n(r/R_0)$ in fig. 6.17a at different times t_c/τ_{cap}, which are computed by sampling over a time window of $t_c - 0.45\tau_{\mathrm{cap}} \leq t \leq t_c + 0.45\tau_{\mathrm{cap}}$. To ensure statistical convergence of the data, three individual realisations are computed

for each initial configuration (We, ε, $N_{\max}$); and all results presented in figs. 6.17 and 6.18 have been averaged across these ensembles. It can be seen that initially fragments with $r \leq 0.2R_0$ are produced at early time. While the number density n within this range remains largely unchanged over time and does not appear to depend strongly on r, this should be treated with caution due to a lack of fully established grid independence of fragment statistics at small sizes, as discussed in Appendix A. As time elapses, the number of larger fragments increases and causes the falling tail of the distribution to move further to the right, indicating that larger drops are fewer and produced later in time. This can be attributed to the ongoing ligament merging process, as it increases the thickness of individual ligaments.

We now seek to compare our numerical results with the experimental data and the theoretical model of Ref. [62] utilising Gamma distributions. Note, however, that other distributions can be used to model fragment sizes, for example, log-normal distributions [38]. The model of Ref. [62] is now briefly reviewed as follows. The variation in the fragment size distribution for the rim collision problem arises from two sources, namely those of the transverse ligament size and of the fragments produced from the breakup of a single ligament. A linear superposition of these two effects yields the following size distribution function,

$$p\left(\zeta = \frac{r}{\bar{r}}\right) = \frac{2(mn)^{\frac{m+n}{2}}}{\Gamma(m)\Gamma(n)}\zeta^{\frac{m+n}{2}-1}K_{m-n}(2\sqrt{mn\zeta}), \tag{6.24}$$

where K_{m-n} is a modified $(m-n)$-th order Bessel function of the second kind, and m and n reflect the roughness of the distribution of ligament widths and corrugation amplitudes on individual ligaments. Neel *et al.* [62] fit their experimental data at $We = 193$ using Eq. (6.24) with $m = 40$ and $n = 5$, which we can reproduce in fig. 6.17b together with our fragment size probability density function (pdf) at $We = 200$. Note that the fragment sizes were originally normalised in Ref. [62] using the average fragment diameter $\bar{d}$ in their fig. 15b, which is shown in their fig. 13b to saturate at large We values and remain proportional to their interstitial sheet thickness h. The sheet thickness is in turn related to the pre-collisional rim radius R_0 via the rim collision Weber number, given in their

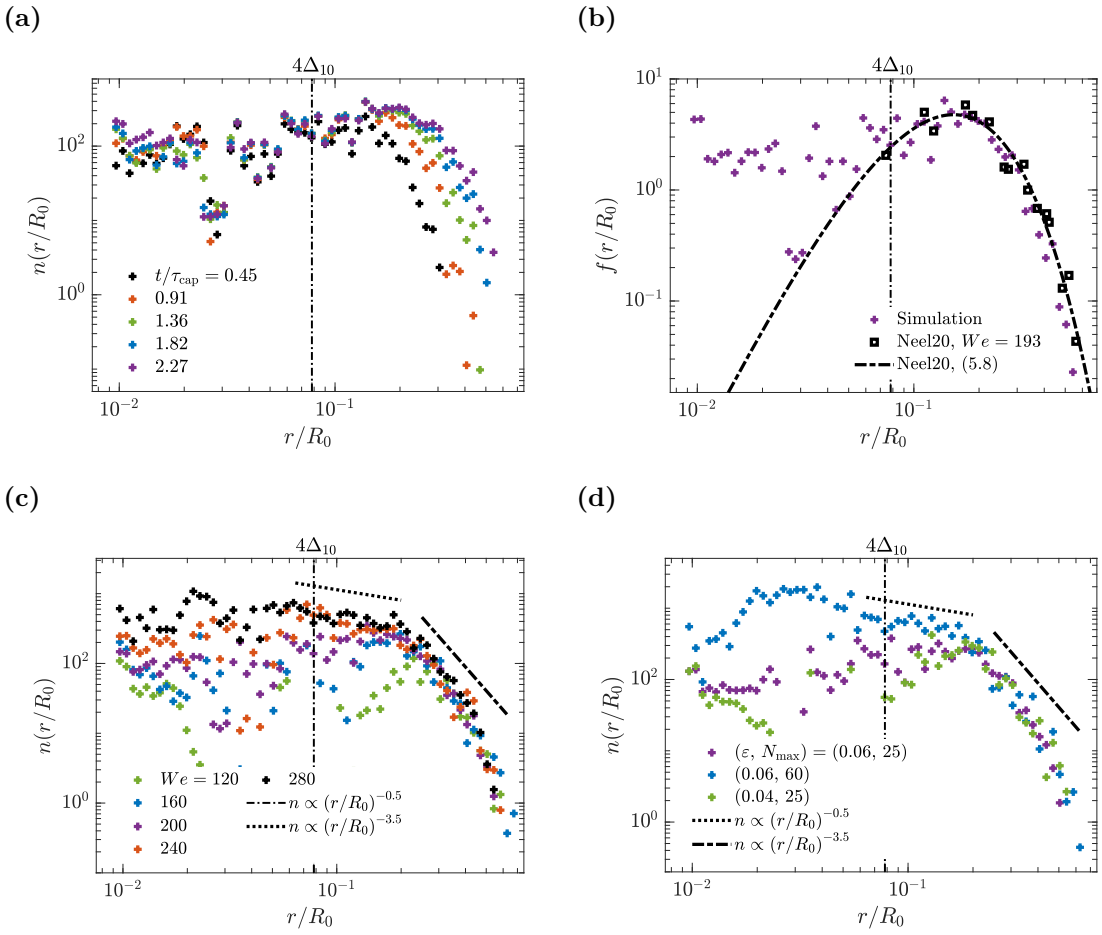

Figure 6.17: (a): The evolution of time- and ensemble-averaged size distribution function $n(r/R_0)$ of all fragments produced by colliding rims at $We = 200$, $\varepsilon = 0.06$, and $N_{max} = 25$. (b): The fragment size probability distribution function $f(r/R_0)$ compared with the experimental data and model of Ref. [62]. (c,d): The influence of We (c) and ε and N_{max} (d) on the fragment size distribution function, where $\varepsilon = 0.06$ and $N_{max} = 25$ for all simulation results presented in (c), and $We = 200$ for those presented in (d).

work as $We = 16R_0/h$. This allows us to estimate their average fragment diameter as

$$\bar{d} = \chi h = \frac{16\chi}{We} R_0. \tag{6.25}$$

We find that setting the coefficient χ to 5 leads to an excellent match between our simulation results with $(We, \varepsilon, N_{max}) = (200, 0.06, 25)$ and the re-normalised data of Ref. [62] for $r \geq 4\Delta_{10}$. Figure 13b of Ref. [62] suggests a χ value of approximately 25 for their controlled rim production setup, which is larger than our fitted value by a factor of 5. This might be because rim fragmentation has completed in the experiments, and the larger fragments produced at later times increases the value of $\bar{d}$. Our numerical results

differ from Ref. [62] for $r \leq 4\Delta_{10}$, where Eq. (6.24) exhibits a fall-off not found in our data. This more uniform portion of fragment size distribution for small r values is also found in fig. 23b of Ref. [54], where they attributed it to the transverse impact between adjacent rim ligaments. The differences between their experimental and our numerical configurations may also play an important role, as their expanding rims feature toroidal shapes and therefore coalesce within a finite period of time. Last but not least, the two liquid rims are connected by an interstitial thin film in the configuration of Ref. [62], whereas in our case the rims come into contact directly.

The dependence of the time-averaged fragment size distribution on the controlling parameters We, ε and $N_{\max}$ is further shown in figs. 6.17c and 6.17d. It can be seen that the number density n of small fragments with $r \leq 4\Delta_{10}$ continues to increase with We, ε and $N_{\max}$, consistent with our observations in fig. 6.16a. More specifically, here the sensitivity of n to ε and $N_{\max}$, as shown in fig. 6.17d, further supports our understanding that the differences between the numerical and experimental initial conditions causes the difference between the corresponding results. The number density of intermediate fragments with $4\Delta_{10} \leq r \leq 0.2R_0$ also increases with We in fig. 6.17c; but different from that of smaller fragments, it appears to asymptote to $(r/R_0)^{-1/2}$ for $We \geq 240$ or $N_{\max} \geq 60$. The tail of the distribution functions consisting of even larger fragments with $r \geq 0.2R_0$ remains approximately independent of the controlling parameters, and its decaying trend agrees well with a power law of $(r/R_0)^{-7/2}$. While this finding differs from that of Ref. [62], where m and n decrease with increasing We and cause the slope of the tail to decrease correspondingly, this may again be due to differences in detail of the initial conditions. Overall, figs. 6.17c and 6.17d suggest that as We increases, the fragment size distribution within $r \geq 4\Delta$ asymptotes to a regime independent of the controlling parameter, and well described by a power-law decay with a break in slope; which may originate from the insensitivity of ligament merging and breakup phenomena to the initial perturbation configurations. It is noted that a similar transition between two power law regimes has been observed in the droplet size distributions associated with wave breaking by Refs. [17] and [74], although their distributions feature steeper slopes, with the power law transitioning from r^{-2} to r^{-6}.

Here we show that the power-law scaling $(r/R_0)^{-1/2}$ we observed in figs. 6.17c and 6.17d at small fragment sizes can be derived from the ligament merging dynamics previously established in this work. The ligament merging timescale is defined as the ratio between the average ligament spacing L_0/N_{lig} and the drift velocity u_{drift}, which can be evaluated based on Eq. (6.18),

$$\Delta t_{\text{merge}} \equiv \frac{L_0}{N_{\text{lig}} u_{\text{drift}}} \propto N_{\text{lig}}^{-2}. \tag{6.26}$$

The rate of droplet shedding is controlled by the ligament necking process, thus $\Delta t_{\text{shed}} = t_{\text{neck}}$ as given in Eq. (6.23) [78]. Consequently, the total number of fragments shed from all ligaments between two consecutive merging events can be estimated as

$$N_{\text{frag}} = N_{\text{lig}} \frac{\Delta t_{\text{merge}}}{\Delta t_{\text{shed}}} \propto N_{\text{lig}}^{-1} w^{-3/2}, \tag{6.27}$$

where w is the average width of ligaments.

As we observed in figs. 6.13a and 6.13b, $w \propto r \propto \sqrt{t/\tau_{\text{cap}}}$, whereas Eq. (6.22) suggests $N_{\text{lig}} \propto (t/\tau_{\text{cap}})^{-1/2}$. Substituting these two scalings into Eq. (6.27) leads to

$$N_{\text{frag}} \propto (t/\tau_{\text{cap}})^{-1/4} \propto (r/R_0)^{-1/2}. \tag{6.28}$$

These derivations suggest that the $(r/R_0)^{-1/2}$ scaling at small fragment sizes can be explained as a competition between ligament merging and end-pinching, whereas the $(r/R_0)^{-7/2}$ scaling found at larger fragment size ranges still awaits further analysis. It is likely that this steeper dependence on r originates from the presence of corrugations on individual ligaments, or the variation of ligament width across the bordering rim [62]; neither of which has been considered in the derivations above.

Lastly, we discuss the fragment velocity statistics. Figs. 6.18a and 6.18b present the ensemble-averaged vertical (fig. 6.18a) and in-plane (fig. 6.18b) components u_y and u_{xz} of the fragment ejection velocity, which are plotted as functions of the fragment radius r. Since most of the initial liquid momentum is deflected in the vertical direction over the collision process, u_y remains a few times to a decade larger than u_{xz}. Figure 6.18a shows that the u_y values for fragments within the size range of $0.1 \leq r/R_0 \leq 0.4$ collapse reasonably well when scaled by the initial rim velocity U_0, and is well predicted by a

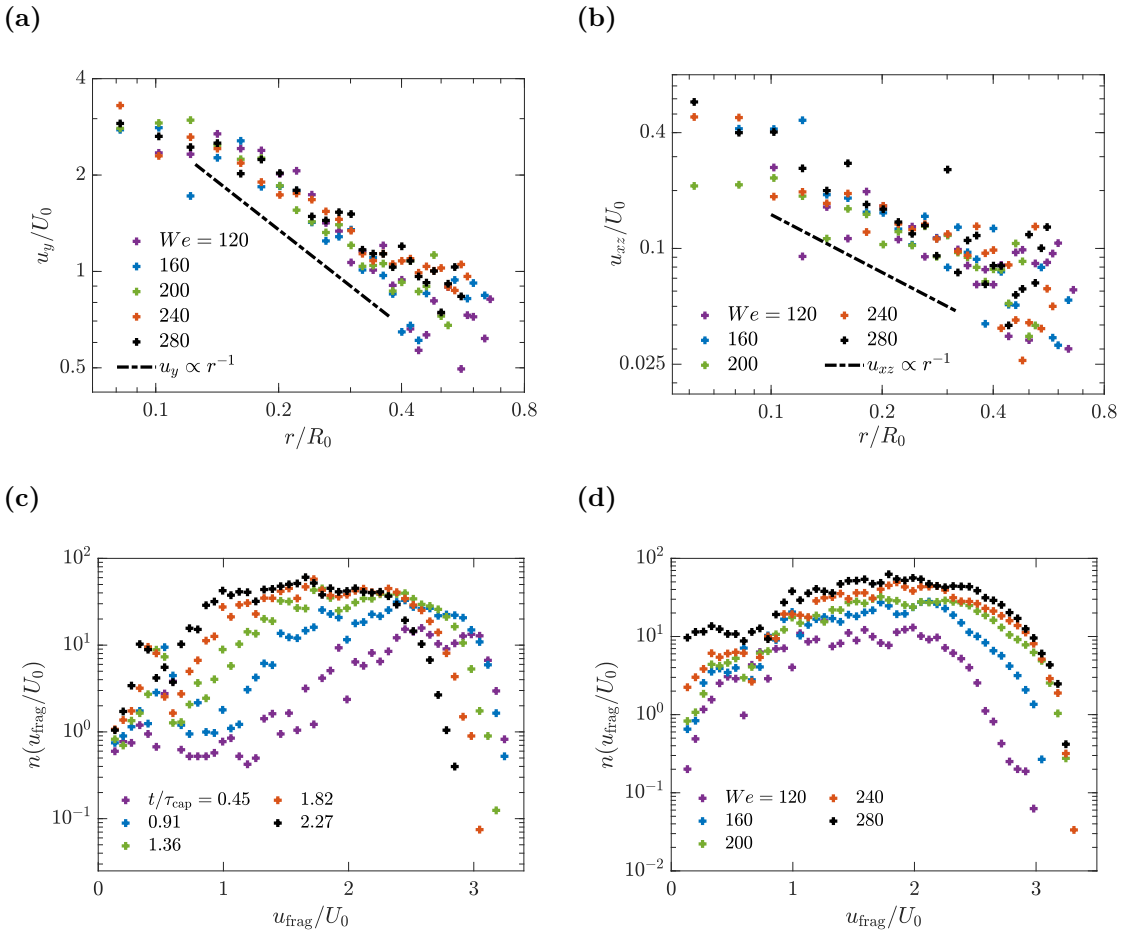

Figure 6.18: (a,b): Ensemble-averaged vertical (a) and in-plane (b) components of fragment ejection velocity u_y and u_{xz} calculated at various We values, with $N_{\max} = 25$. (c): Evolution of the fragment velocity distribution over time, obtained at $We = 200$, $\varepsilon = 0.06$ and $N_{\max} = 25$. (d): The probability distribution functions of fragment velocities at different We values.

power-law decay model $u_y \propto (r/R_0)^{-1}$. The velocity distribution at larger fragment sizes deviate from this power-law scaling, most likely due to a combination of late-time effects including amplified ligament corrugations, rim deceleration and the onset of RP instability on the ligaments. The in-plane velocity component values u_{xz} measured in fig. 6.18b are more scattered compared with fig. 6.18a, but the distribution can still be roughly described by the same power-law decay model $u_{xz} \propto (r/R_0)^{-1}$. These observations further corroborate the fragment size distribution model we proposed in Eq. (6.28), since the power-law exponent of -1 for u_y can be derived based on our observations in figs. 6.16b and Eq. (6.17),

$$u_y \propto (t/\tau_{\mathrm{cap}})^{-1/2} = \left[(t/\tau_{\mathrm{cap}})^{1/2}\right]^{-1} \propto (r/R_0)^{-1}. \tag{6.29}$$

As the only source of the liquid in-plane motion is the transverse drifting of ligaments, the in-plane velocity component u_{xz} can be estimated by the drifting velocity u_{drift}. Combining Eqs. (6.18) and (6.22) similarly leads to

$$u_{xz} \propto u_{\text{drift}} \propto N_{\text{lig}} \propto (t/\tau_{\text{cap}})^{-1/2} \propto (r/R_0)^{-1}. \tag{6.30}$$

The good agreement between the velocity scaling models derived above and our numerical results once again highlights the importance of the rim ligament merging phenomenon in determining the size and velocity statistics of splashing fragments.

Figs. 6.18c and 6.18d show the number density of fragments as a function of their travelling speed u_{frag}. Figure 6.18c suggests that while most of the fragments produced at early time feature a skewed velocity distribution peaking at $u_{\text{frag}} \approx 2.8U_0$, the maximum fragment speed decreases and more fragments travelling at lower speeds are recorded as time elapses, and the distribution function has developed a plateau by $t/\tau_{\text{cap}} = 1.36$. This suggests that as the ligaments continue to grow in length and break up, the droplets produced come to span uniformly across a large range of travelling speeds, with fewer drops featuring very slow or particularly fast speeds. Figure 6.18d shows the velocity distribution at different We values averaged over the entire collision process. It is found that as We increases the velocity distribution becomes broader; and for We beyond 240, the right tail of the velocity distribution appears to reach a We-independent regime, similar to our observation in fig. 6.17c for the size distribution of fragments; and the fastest speeds recorded is around $u_{\text{frag}} \approx 3.2U_0$. While a direct comparison with breaking wave statistics [17, 74] is out of the scope of the current work, it is noted that the shapes of velocity distribution functions obtained here in figs. 6.18c and 6.18d differ from their counterparts in wave breaking phenomena (see, e.g., fig. 16d of Ref. [17] and fig. 12 of Ref. [74]), as the latter are skewed and narrower than our distributions. This may be due to the presence of gravity in wave breaking, which may arrest the ligament fragmentation process and define a short timescale for completing the splashing phenomenon, thereby reducing the total number of fragments. These splash fragments are themselves also decelerated by gravity. In the velocity distribution, this would appear as a narrowing of the distribution, with lower velocities at the peak

and the higher velocities represented by a long tail. Other fragmentation mechanisms in the wave-breaking phenomena may also alter the shape of velocity distribution, for example, the bursting of surface bubbles [54, 98], whose contribution to the production of droplets is known to be significant after the wave splashing phase.

6.7 Conclusions

We have investigated the collision and subsequent fragmentation of perturbed liquid rims, focusing on the range of $120 \leq We \leq 280$ that allows for the growth and merging of transverse ligaments and production of fine drops from such ligaments via the pinch-off mechanism. We look into different parts of the post-collisional liquid bulk as it evolves over time, and our key findings are summarised as below:

Firstly, following the quasi-one-dimensional approach of Ref. [77], we derive analytical solutions of the liquid velocity and free surface profiles for the vertically expanding lamella sheet, which are shown to be in good agreement with the numerical results. Capillary effects have been neglected in this model for sheet evolution, but prove significant for the dynamics of the bordering rim. We then compared the growth of its vertical position and thickness with the theoretical model of Ref. [81], and develop scaling laws collapsing the data.

Secondly, we analyse the behaviour of transverse ligaments on top of the lamella rim. The ligaments produce fragments primarily via the end-pinching mechanism, and when the initial perturbation waveform is polychromatic, they migrate on the rim and merge with each other to form thicker and more corrugated ligaments, thus preventing their absorption into the rim and sustaining the fragmentation process. A novel scaling model is derived for predicting the evolution of ligament number density based on the migration speed model of Ref. [78].

Lastly, we present the size and velocity statistics associated with the rim collision phenomenon. An excellent agreement between our fragment size distribution and the experimental results of Ref. [62] is found within the range of grid convergence ($r \geq 4\Delta_{10}$). The fragment size distribution becomes insensitive to the initial configurations when We or $N_{\max}$ further increases, which can be described using a power law with a break in

slope. A theoretical model is proposed predicting the power-law distribution observed for $r \leq 0.2R_0$. Over time, the fragment speed u_{frag} develops a largely uniform spread over the range of $0 \leq u_{\text{frag}} \leq 3.2U_0$ as their parent ligaments continue to grow vertically and decelerate to form slower drops.

The implications of the present work are manifold. Firstly, it sheds new light on the fluid physics involved in a liquid impact problem that has not received much attention prior to the recent works of Refs. [62] and [63]. Furthermore, the results we obtained are also of reference value for ongoing research works on spherical drop impacts, especially the influence of initial perturbations on the fragmentation process, which may also be present during the early-time prompt splashing phenomena observed in previous experimental studies [185, 220]. Lastly, this work serves as a stepping stone towards understanding the secondary splashing phenomenon observed in wave breaking events and the associated fragment statistics [17, 74], and provides the basis for investigating the influence of other physical mechanisms not covered in the present work, for example, viscosity, gravity and air-phase turbulence effects.

7

Rim Splashing with Gravity

Reproduced entirely from a journal article manuscript in preparation: Tang, K., Adcock, T. A. A., & Mostert, W. (2025). Sea spray generation function for ocean splash drops.

7.1 Introduction

Sea sprays are ejected from the sea surface primarily due to wave breaking, the highly turbulent and transient nature of which greatly facilitates the exchange of mass, momentum and energy between the ocean and the atmosphere. Among other roles of sea sprays in the atmospheric boundary layer (ABL), large spray drops may be crucial for the saturation of the surface drag coefficient leading to the development of large tropical storms [10]. As recent hurricanes show record strengths and growth rates, there is an urgent need for improving the accuracy of air-sea interaction models [23], including the parameterisations of sea spray generation rate and size distributions which are still mostly empirical and feature large variability of several orders of magnitude. This reflects the limited knowledge of the sea spray production mechanisms: while it is known that spray droplets are generated through a few major pathways including surface bubble bursting, wind-driven spume ejection and wave splashing [5, 10], detailed experimental and numerical measurements of spray generation are still limited. Moreover, to the knowledge

of the authors, no existing Sea Spray Generation Function (SSGF) parameterisation has taken into account the contribution of splash drops, as wave splashing is believed to be an inefficient spray generation mechanism [10]. Consequently, a general theoretical model for the associated droplet statistics is not yet available [11, 17].

Facilitated by the development in numerical and experimental techniques which allow for the investigation of highly transient liquid fragmentation processes [60], a few recent studies of wave breaking have reported droplet number densities in the form of power-law scalings $N(r) \propto r^{-\alpha}$ as functions of the droplet radius r [17, 74, 114], which paves the way for the development of physically informed SSGFs [11, 14]. Particularly of interest to the present study is the secondary splashing phase during wave breaking as shown in figs. 7.1a and 7.1b, where the largely intact wave bulk collides with the decelerated splash-up generated from the initial impact [17, 161, 221, 222]. This corresponds to the fragmentation dynamics of Region IA recently investigated by Erinin *et al.* [74], which give rise to one-third of all droplets produced by plunging breakers. The underlying physics of secondary splashing remains poorly understood, although it is observed that a wall of droplets is generated following the closure of the indentation space between the wave bulk and initial splash-up [74].

In our previous work [161], we have modelled secondary wave splashing with the transverse collision of two perturbed liquid rims. We found that the initial surface perturbations on the rims give rise to a number of developing ligaments on the expanding transverse lamella rim. A competition between the merging and end-pinching dynamics of these ligaments leads to a quasi-steady power-law scaling of $N(r) \propto r^{-0.5}$ in the fragment size distributions. In contrast, the steeper tail at larger sizes is not accounted for. Here we further examine rim splashing under the influence of gravity with high-fidelity direct numerical simulations, emphasising the early-time transient effects and proposing a fragment size distribution model covering the entire droplet radius range. This allows us to further elucidate the connection between rim and secondary wave splashing and to develop a physically informed SSGF associated with ocean splash drops for the first time.

7.2 Rim splashing under gravity

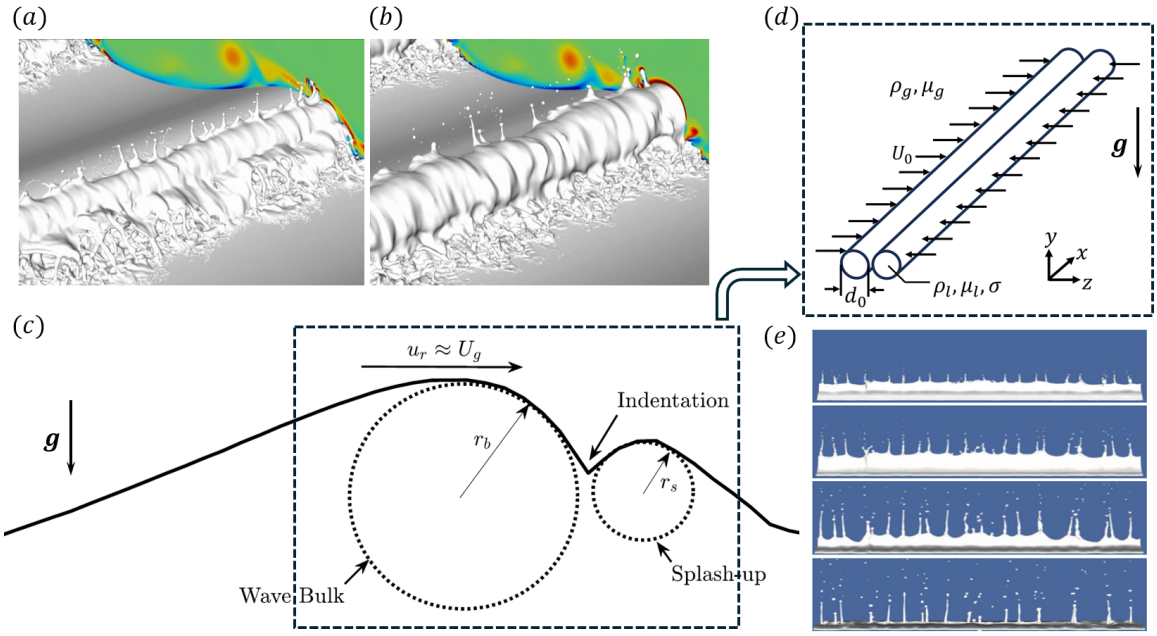

Figure 7.1: (a,b): Visualisation of the secondary wave splashing process of a deep-water plunging breaker, where the wave travels from top left to bottom right. The ambient air-phase is coloured by the strength of local vorticity. The closure of the indentation space between the initial splash-up and wave bulk generates many merging liquid ligaments, whose pinch-off forms secondary splash drops. Reproduced from Ref. [17]. (c,d) Sketches showing the configurations of secondary wave splashing and rim collision, adapted from Refs. [74] and [161]. The collision of the wave bulk and the splash-up is here simplified as the collision of two liquid rims. (e): Visualisation of a typical rim splashing process under gravity taken from the $+z$ direction, with snapshots taken later presented further below. The splash lamella and bordering ligaments are pulled back to the horizontal plane by gravity.

We first introduce the configuration of the present study and establish its link with the secondary wave splashing phenomenon via dimensional analysis. A deep-water surface wave with amplitude a_b, wavenumber k_b, surface tension σ breaking under gravity g as shown in fig. 7.1c can be characterised by the Bond number $Bo_b \equiv \rho_l g/\sigma k_b^2$ and slope $S_b \equiv a_b k_b$. When viewed from a reference frame moving alongside the plunging breaker with speed $\tilde{u} = 0.5c_g = 0.5\sqrt{g/k_b}$, the initial splash-up and the wave bulk collide at relative speed $u_r = c_g$ during secondary wave splashing, where c_g is the phase speed of the breaking wave. This phenomenon is modelled by the collision of two infinitely long cylindrical liquid rims with diameter $d_0 = a_b$ aligned along the transverse direction, as shown in fig. 7.1d. The relative speed between the

two rims is set as u_r. The gravitational field g is perpendicular to the horizontal plane containing the two rims, and the Weber and Bond numbers of rim collision are related to the breaking wave parameters as follows:

$$We \equiv \frac{\rho_l u_r^2 d_0}{\sigma} = Bo_b S_b, \quad Bo \equiv \frac{\rho_l g d_0^2}{\sigma} = Bo_b S_b^2. \tag{7.1}$$

The rim Ohnesorge number $Oh \equiv \mu_l/\sqrt{\rho_l d_0 \sigma}$ is here fixed at 0.01, as fragment statistics are insensitive to Oh in the inviscid limit [17, 161]. Since both the initial splash-up and the wave bulk feature strong surface corrugations under the influence of sub-surface counter-rotating vortices [221], we also impose random transverse perturbations on the rim radii [17, 135, 161] characterised by ε_0, the non-dimensionalised characteristic perturbation amplitude; and $N_{\max}$, the cutoff wavenumber of the perturbation signal spectrum.

Figure 7.1e provides an overview of the rim splashing phenomenon with gravity present. At sufficiently large We values, the two perturbed rims merge along the contact line and generate an expanding liquid lamella bordered by a thickening rim, which is topped by many ligaments ejecting small fragments via the end-pinching mechanism. In the meantime, these ligaments migrate along the corrugated lamella rim and merge to form thicker ligaments, which causes the gradual increase in the diameter of splash droplets [161]. However, gravity causes the lamella base to gradually spread out along the xz-plane, followed by the retraction of the lamella sheet. Ultimately, all ligaments are destroyed and secondary droplets fall back to the xz-plane, a fate shared by spray drops generated through secondary wave splashing [10, 17].

Since the lamella rim sustains the merging cascade of transverse ligaments, the time t_R at which it fully retracts can be considered as the cutoff timescale of the secondary splashing process. Figure 7.2a shows the evolution of the vertical position and average thickness of the lamella rim. When gravity is incorporated, the evolution of its average vertical position y_{rim} can be characterised by a free-fall motion superimposed on the capillary deceleration model where a $t^{1/2}$ power law is observed [161, 223]. This yields,

$$t_R/\tau_{\text{cap}} = 2.31 We^{1/3} Bo^{-2/3}, \tag{7.2}$$

where $\tau_{\text{cap}} \equiv \sqrt{\rho_l d_0^3/8\sigma}$ is the capillary timescale. On the other hand, the bordering rim thickness b_{rim} remains unchanged under gravity. This is because all fluid particles

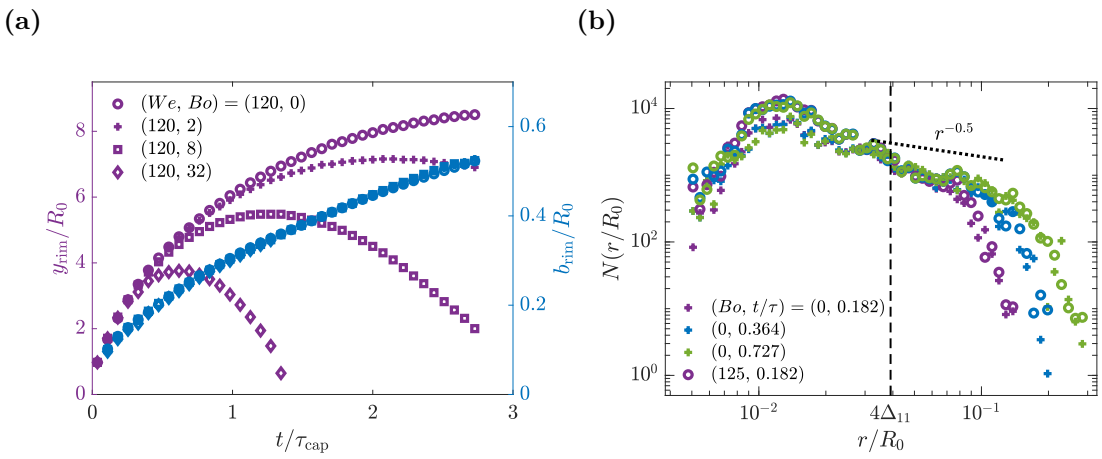

Figure 7.2: The evolution of (a) the vertical position and thickness of the lamella rim at different Bo values, and (b) the fragment size distribution of rim splashing. For (b), coloured crosses and circles indicate rim splashing with $Bo = 125$ and 0, respectively. The threshold for grid convergence $r = 4\Delta_{11}$ has been marked in all following plots presenting fragment size distributions.

within the expanding lamella experience an inviscid free-fall motion [77], which does not affect the mass flux into the bordering rim.

7.3 Modelling splash drop statistics

As the mass influx and thickness of the lamella rim are not affected by gravity, we expect that the ligament dynamics and the resultant fragment size distribution will also remain unchanged. However, the unsteadiness of fragment formation now plays a significant role as gravity suppresses larger splash drops that would have formed at later times [161]. Figure 7.2b shows the fragment number density $N(r)$ for two different Bo values (0 and 125) and three different times ($t/\tau_{\mathrm{cap}} = 0.182$, 0.364 and 0.727), while $We = 280$ and $N_{\mathrm{max}} = 60$. Vertical dashed lines corresponding to the radius threshold $4\Delta_{11}$ are also added, above which the numerical results are considered fully grid-converged. As expected, finite Bo values do not modify the fragment size distribution.

While our previous study has successfully predicted the $r^{-0.5}$ power law based on a quasi-steady scaling analysis, here observed for $4\Delta_{11} \leq r/R_0 \leq 10^{-1}$, the right tail of the droplet size distributions and its evolution cannot be explained based on this model [161]. We now seek to develop a theoretical model describing the evolution of fragment size

distribution $N(r/R_0)$, which is in turn determined by the distribution of ligament width w as the ratio between the radii of secondary droplets r and their parent ligament width w is fixed at 0.7 [78]. The distribution of ligament widths is determined by the initial rim surface perturbation waveform [161] and the subsequent merging dynamics, although predicting this distribution is outside the scope of the current work. Instead, here we model the distribution of ligament widths w with a Gamma distribution of order m [8],

$$p\left[\frac{w}{\bar{w}(t)}\right] = \frac{m^m}{\Gamma(m)}\left[\frac{w}{\bar{w}(t)}\right]^{m-1} e^{-\frac{mw}{\bar{w}(t)}}, \tag{7.3}$$

where $\bar{w}(t) \propto \sqrt{t/\tau_{\text{cap}}}$ is the average ligament width [161]. This model differs from Neel *et* al. [62] as the latter uses the Gamma distribution to describe the maximum volume of each ligament, and therefore does not account for the unsteady ligament growth. We also note that other statistical models aside from the Gamma distribution in Eq. (7.3) may be used to model the distribution of transverse ligament widths and fragment statistics, for example, the log-normal distribution [15]. See Appendix C for detailed analyses.

Now, consider all pinch-off events for ligaments with width w having occurred for $t_0 \leq t \leq T$. The onset time for ligament pinch-off t_0 can be estimated as the duration of rim indentation closure after impact,

$$\frac{t_0}{\tau_{\text{cap}}} \approx \frac{\varepsilon_0 d_0}{U_0\sqrt{\frac{\rho_l d_0^3}{\sigma}}} = \frac{\varepsilon_0}{\sqrt{We}}. \tag{7.4}$$

As ligaments pinch off at a rate of $1/\Delta t_{\text{neck}} \propto w^{-3/2}$ [161], the total number density of fragments with radius r at a given time t is therefore

$$N(r,\, t) \propto \frac{1}{\Delta t_{\text{neck}}}\int_{t_0}^{t} N_{\text{lig}}(t') \cdot p\left[\frac{w}{\bar{w}(t')}\right] dt' \tag{7.5}$$

$$= C\frac{m^3}{\Gamma(m)}\left(\frac{r}{R_0}\right)^{-\alpha}\left(\Gamma_{\text{inc}}\left[m-2,\, m\frac{r}{\bar{r}(t)}\right] - \Gamma_{\text{inc}}\left[m-2,\, m\frac{r}{\bar{r}(t_0)}\right]\right), \tag{7.6}$$

where $\alpha = 0.5$, Γ_{inc} is the incomplete Gamma function, and C is an integral prefactor. Here we use the relation $\bar{r}(t) = 0.7\bar{w}(t)$ as established in Chapter 6. For small fragment sizes $r/R_0 \ll 1$ and pinch-off onset time $t_0/\tau_{\text{cap}} \ll 1$, Eq. (7.6) reduces to the quasi-steady $r^{-0.5}$ power law [161], whereas the right tail at large droplet sizes is now shown to arise from the non-uniform distribution of ligament widths. The functional form of

Eq. (7.6) bears some resemblance to the final fragment size distribution proposed in Refs. [98] and [11], which are based on the analysis of jet and film breakup following the bursting of surface bubbles.

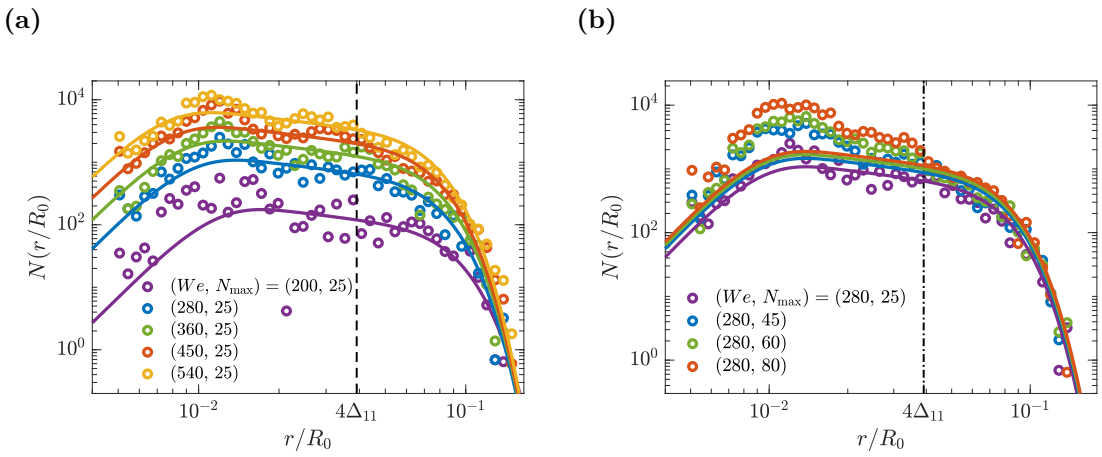

Figure 7.3: Splash drop size distributions at $t/\tau_{\text{cap}} = 0.227$ for different We (a) and $N_{\max}$ (b), in comparison with the prediction of (7.6).

In fig. 7.3 we compare Eq. (7.6) with the fragment size distributions we obtained for simulations with $200 \leq We \leq 540$ and $25 \leq N_{\max} \leq 80$. For fig. 7.3a where $N_{\max} = 25$, increasing We leads to an overall increase in the fragment number density $N(r/R_0)$. Here, Eq. (7.6) matches excellently with the numerical size distributions at different We values, where the integral prefactor in Eq. (7.6) is fitted as $C = 1.29We^{2.6}$ and m is fixed at 12. The power-law decay region where $N(r) \propto r^{-0.5}$ is observed extends to $r/R_0 = 0.01$, below which $N(r)$ starts to decrease. Eq. (7.6) successfully captures this decrease at small fragment sizes, suggesting its possible origin in the initial growth phase of transverse ligaments before the first pinch-off events. The peak at $r/R_0 = 0.01$ becomes more pronounced with increasing $N_{\max}$ in fig. 7.3b for $r \leq 4\Delta_{11}$. Nonetheless, for $r \geq 4\Delta_{11}$ where grid convergence of fragment statistics is established [161], Eq. (7.6) matches excellently with numerical results, and increasing $N_{\max}$ causes only a slight increase in the fragment number density $N(r)$. This is likely because larger $N_{\max}$ yield higher initial ligament merging rates, and as splashing proceeds, the number of thick ligaments becomes less influenced by the initial conditions, which pinch off to produce a relatively stable number of large splash drops.

We further compare our numerical results and Eq. (7.6) for rim splashing with available fragment statistics of secondary wave splashing, utilising the relation between the non-dimensional groups (defined in Eq. (7.1)) of these two scenarios. To our knowledge, the recent experimental study of Erinin *et al.* [74] contains the only report of fragment statistics associated with secondary wave splashing (designated as Region IA therein), which we reproduce in fig. 7.4a. Alternatively, we have included the statistics of all droplets produced by plunging breakers from three recent studies [17, 74, 224] for comparison in fig. 7.4b. A further comparison of fragment speed distributions is included in Appendix D. Here we select $We = 280$ and $Bo = 125$ for the reference rim splashing configuration, which roughly corresponds to the plunging breaker investigated by Mostert *et al.* [17] featuring $Bo_b = 500$ and $S_b = 0.55$. The numerical and theoretical fragment statistics are computed at $t = t_R = 0.6\tau_{\text{cap}}$ according to Eq. (7.2).

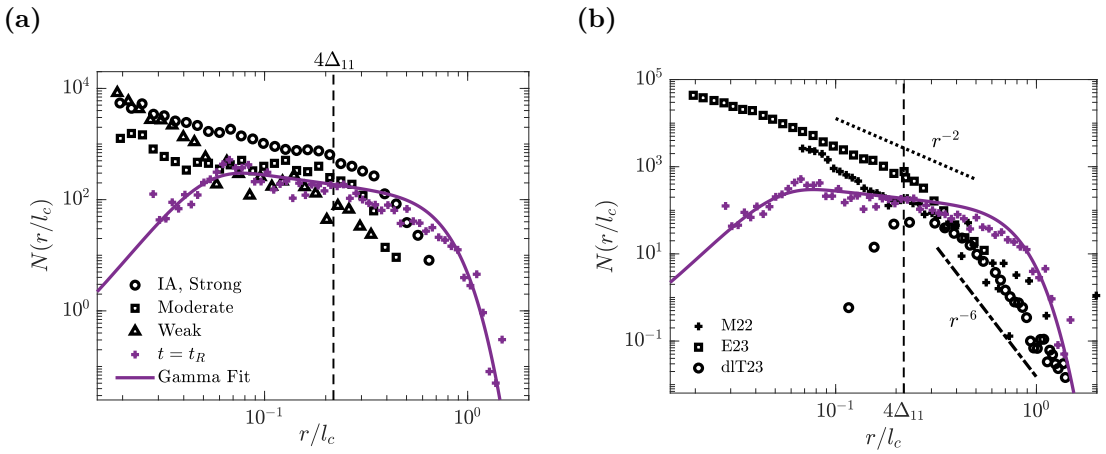

Figure 7.4: Comparison of our splash fragment size distributions with those of Region IA fragments reported by Erinin *et al.* [74] (a) and all droplets produced by wave breaking (b) from Refs. [17, 74] and [224]. The numerical data for rim splashing are obtained for $We = 280$, $Bo = 125$ and $N_{\max} = 25$, with the prediction from Eq. (7.6) shown in solid lines. The results have been non-dimensionalised using the capillary length $l_c \equiv \sqrt{\sigma/\rho_l g}$.

There exists considerable scatter in the experimental splash drop size distributions in fig. 7.4a due to limited measurements and significant variations in the indentation shape between the wave bulk and the initial splash-up [74]. Nonetheless, the total number of splash drops increases with the breaker strength, and the distributions largely follow a power-law decay pattern. When renormalised by the capillary length $l_c \equiv \sqrt{\sigma/\rho_l g}$,

our numerical results fall within the scatter range of the experimental data and match their global decay trends. The $r^{-0.5}$ power law we proposed for small fragment sizes agrees better with the size distributions of the weak and moderate breakers. The tails of our distributions are at slightly larger r/l_c values compared with experiments, which might be because the largest splash drops are short-lived and do not reach the experimental measurement plane. Nonetheless, the shape of our distribution tails still closely resembles experimental data. These observations suggest that perturbed rim collision serves as an excellent model for secondary wave splashing, and Eq. (7.6) successfully predicts the statistics of secondary splash drops.

The available size distributions of all drops produced by wave breaking in fig. 7.4b show two well-defined power-law decay regions with a break in slope around $r/l_c = 0.2$, where the decay rate steepens from $N \propto r^{-2}$ to r^{-6} [17, 74], except for that of Ramirez de la Torre [224] where the measured size distribution falls off at smaller sizes and abides by a Gamma distribution model. Our numerical results and theoretical prediction in Eq. (7.6) are steeper at the right tail than previous results. Furthermore, for $r/l_c \leq 0.3$ the overall size distributions feature more fragments and steeper slopes compared with our theoretical prediction and numerical results, which instead predict $N(r) \propto r^{-0.5}$. This is most likely because the overall fragment size distributions incorporate contributions from film and bubble bursting, which feature fragment size distributions with slopes steeper than -1 [11, 98].

7.4 Sea spray generation function for ocean splash drops

The development of the fragment size distribution in Eq. (7.6) for individual splashing events now prepares us to predict the production of splash drops from realistic sea states where breakers of different length and time scales are present. The sea spray generation function dF/dr measures the production rate of spray drops per unit ocean surface area and drop radius increment, which is indispensable for the calculation of mass, momentum and energy fluxes at the air-sea interface [10]. However, currently available SSGFs feature considerable range of scatter for large spray drops with radii larger than

10μm, and to our knowledge none of these explicitly addresses the production of splash drops [10, 13]. Here we estimate the SSGF of splash drops for the first time.

Assuming that breaking crests at all wavelengths undergo a secondary splashing phase, the SSGF for splash drops can then be computed as follows,

$$\frac{dF}{dr}(r) = \int_{k_{\min}}^{k_{\max}} \frac{\Lambda(k)}{l_0 t_b(k)} N(r,\, t_R) dk. \tag{7.7}$$

Here, $\Lambda(k)$ is the omnidirectional length distribution of breaking crests as a function of the breaking wavelength k. Our calculation of $\Lambda(k)$ is based on the saturated breaking wave field investigated by Wu *et al.* [225], a three-dimensional rendering of which is shown in fig. 7.5a. Detailed information about the calculation process is available in §7.6.2. The scaling factor l_0 accounts for the spanwise length of the rim splashing phenomenon over which the fragment size distribution $N(r)$ is computed. In our simulations l_0 is set as ten times the rim diameter d_0. According to the analogy between rim and wave splashing introduced in §7.1, $d_0 \propto a_b \equiv s_b/k$. $t_b(k) \equiv 1.12\pi/\sqrt{gk}$ is the breaking time for the wave component with wavelength k [225, 227].

The SSGF calculated directly from Eq. (7.7) based on the fragment size distribution model in Eq. (7.6) is shown with the grey solid line in fig. 7.5b. The shape of this SSGF closely resembles that of the fragment size distribution, featuring a plateau where $dF/dr \propto r^{-0.5}$ flanked by two fall-off regions. Notably, the plateau spans over a radius range of $10^2\,\mu\text{m} \leq r \leq 10^4\,\mu\text{m}$, overlapping with the size range for typical ocean spume drops and supporting the speculation of Veron [10] that splash drops may be roughly included in the spume population. Comparison with available SSGFs from literature [10] in fig. 7.5c suggests that this SSGF calculated based on Eq. (7.6) features a small total number of fragments and a large cutoff radius, apparently supporting the speculation that wave splashing is an inefficient ocean spray generation mechanism [10].

However, high-amplitude breaking waves may generate sufficiently large splash drops, which fragment to produce smaller secondary droplets and modify the shape of the fragment size distribution $N(r)$. While such large and long-lived splash drops may be few in total numbers, they can potentially generate considerable amounts of secondary droplets, for example via droplet aerobreakup, where the breakup of bag

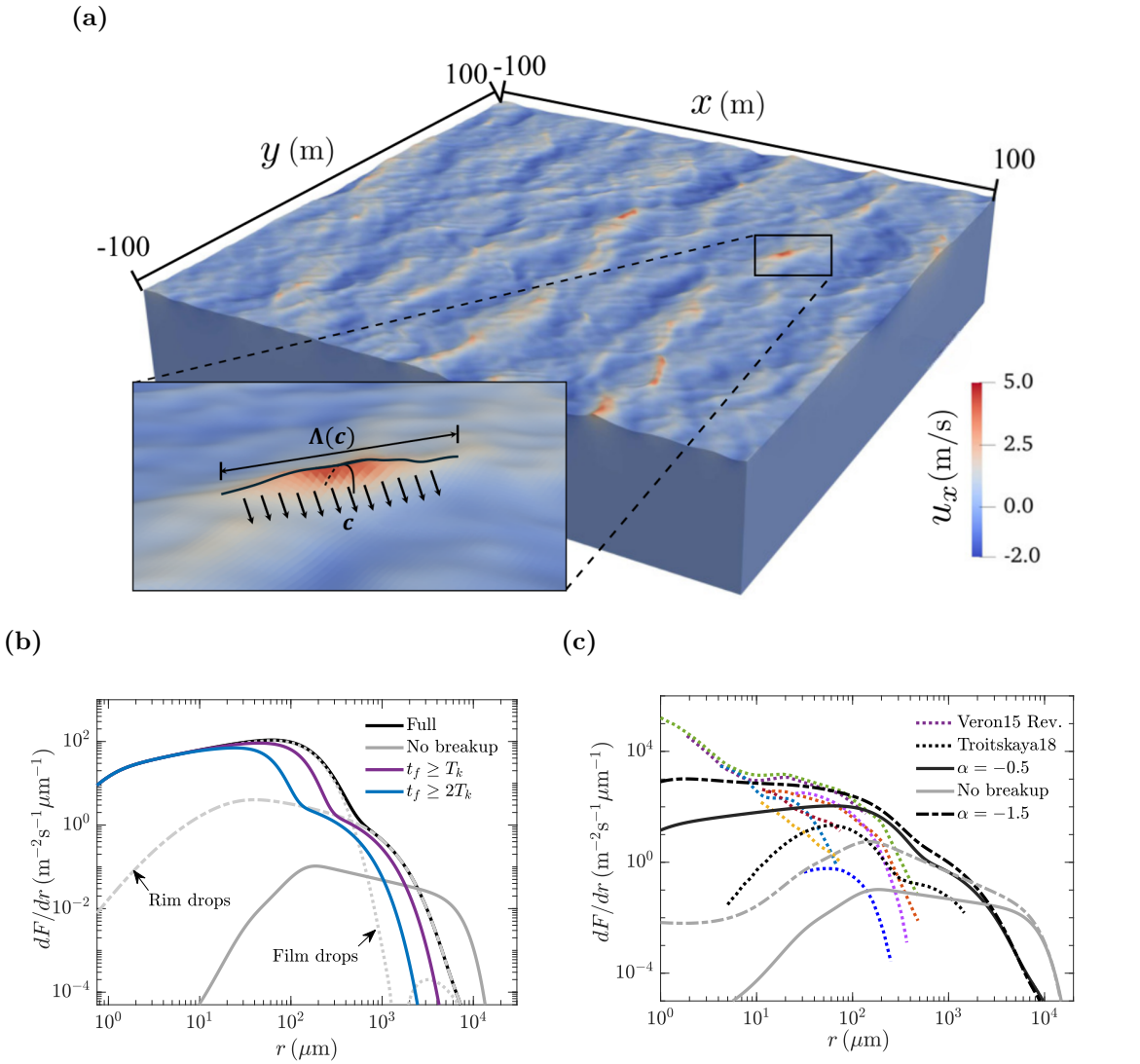

Figure 7.5: (a): Visualisation of a saturated breaking wave field coloured by the local surface flow speed, adapted from Ref. [225]. The inset defines the breaking crest length $\Lambda(c)$. Breaking wave crests are found to feature high local flow speeds. The wave field is calculated with a nonhydrostatic multilayer solver, which is based on a vertically Lagrangian discretisation of the Navier-Stokes Equation and developed specifically to account for breaking surface waves with large local slopes [226]. The wavefield is initialised with a superposition of multi-directional linear waves, and allowed to freely evolve until breakup. (b): Predicted SSGFs without (grey solid line) and with (black solid line) modelling of secondary splash breakup, with contributions from bag film and rim drops indicated by grey dotted and dash-dotted lines. Purple and blue lines indicate SSGFs with fragment life filters $t_f \geq \nu T_k$ applied. (c): Comparison of our SSGFs with those reviewed by Veron [10] (coloured dotted lines) and recently proposed by Troitskaya *et al.* [14] (black dotted lines). Different SSGF versions with power-law exponents $\alpha = -0.5$ (black) and -1.5 (grey) in Eq. 7.6 are presented, both without (solid) and with (dashed) modelling for secondary splash breakup.

films is known to introduce many fragments significantly smaller than the size of the original droplet [14, 15]. Figure 7.5b shows the modified SSGFs incorporating secondary aerobreakup of splash drops in solid black line. This version of the SSGF features two peaks characteristic of film and rim drops produced from bag breakup events [14]. Compared with the previous version of SSGF without secondary aerobreakup, the right tail shifts to smaller fragment sizes as large splash drops break up, while the number of small fragments increases significantly due to bag film eruption. Application of fragment lifetime filters in the form of $t_f \geq \nu T_k$ (where ν is a constant) shifts the SSGFs further towards smaller fragment sizes as large film drops and rim drops are filtered out, but has no significant impact on the shape and magnitude of the SSGFs. The SSGF models incorporating aerobreakup of splash drops compare more favourably with those from literature [10] in fig. 7.5c, as the former approaches the upper envelope of the latter. We note that this match with previous results can be further improved if we modify the prefactor of Eq. (7.6)'s radius dependence to $(r/R_0)^{-1.5}$, which would align the predicted fragment size distribution to more closely with the strong plunging breaker case presented in fig. 7.4a. Overall, our results suggest that once the secondary fragmentation mechanisms of large splash drops are taken into account, wave splashing can in fact be a very efficient spray generation mechanism.

7.5 Discussion

We numerically investigate rim splashing under gravity as a model for the wave splashing phenomenon. Gravity introduces a global cut-off timescale for the ongoing ligament merging and end-pinching competition, which determines the final size distribution of splash drops. To account for the early-time broadening of the fragment size distributions, we propose a theoretical model which compares favourably with both our simulation results and available wave-breaking data. This further enables us to develop an SSGF model accounting for splash drop production for the first time. The prediction of this model suggests that wave splashing can potentially generate much more spray drops than previously expected as large splash drops undergo aerobreaup and produce numerous small film drops. Our results complement the ongoing development of SSGFs centred

around contributions from film and jet drops arising from surface bubble bursting [11, 98], and thus pave the way for the development of more accurate ocean spray parameterisations to be incorporated in future global climate models.

It should be noted, however, that the SSGF models presented in this work are best construed as upper bounds for the production rate of splash drops, as many open questions remain with the wave splashing phenomena. These include the characteristic wavelength and amplitude of the surface perturbations present on the corrugated initial splash-up, and the splashing mechanism in open-ocean conditions as the assumption of two-dimensionality for wave-breaking breaks down [228]. Further experimental and observational studies are therefore required for validation.

7.6 Methods

7.6.1 Numerical setup

We conduct two-phase, three-dimensional direct numerical simulations to model rim splashing within the open-source Basilisk library [102]. The numerical configuration is identical to our previous work [161] apart from the addition of gravity $-g\boldsymbol{e_y}$ in the vertical direction. We have established grid convergence for statistics of fragments with radius $r \geq 4\Delta$ in Appendix A, where Δ is the grid size corresponding to the maximum grid resolution level $L_{\max}$ under the Adaptive Mesh Refinement (AMR) scheme. Due to our focus on the statistics of small fragments generated at early times, in the present work we increase $L_{\max}$ to 11. The two rims are perturbed using filtered white noise signals with a cutoff wavenumber $N_{\max}$ and a characteristic amplitude ε_0.

The parameter space for the present work is set as $200 \leq We \leq 540$, $0 \leq Bo \leq 250$, $25 \leq N_{\max} \leq 80$ and $\varepsilon_0 = 0.06$, corresponding to typical plunging breakers. Since the rim surface perturbations are highly random, we conduct ensemble averaging across 6 individual realisations for each rim splashing configuration (We, Bo, $N_{\max}$) to obtain statistically converged fragment data.

7.6.2 Calculating the sea spray generation function

Phillips [229] introduced the omnidirectional length distribution of breaking crests $\Lambda(c)$, the moments of which have physical interpretations associated with air-sea fluxes [5]. $\Lambda(c)$ is associated with its spectral counterpart $\Lambda(k)$ as follows [227],

$$\Lambda(k) = \Lambda(c)\left|\frac{dc}{dk}\right| = \frac{c^3}{2g}\Lambda(c). \tag{7.8}$$

A purely wind-based scaling $\Lambda(c) \propto u_*^3 g c^{-6}$ (u^* being the wind friction velocity) is also proposed by the same author, although observations do not confirm this scaling [225]. Noting that wave splashing is an inertial process occurring between different parts of a breaking wave and is therefore not directly associated with external wind forcing, here we adopt the scaling for $\Lambda(c)$ recently proposed by Wu *et al.* [225, 230],

$$\Lambda(c)c_p^3 g^{-1} s^{-2} = 800(c/sc_p)^{-6}, \tag{7.9}$$

where c_p is the wave spectrum peak speed, and s is the root-mean-square slope of the spectral wave field $\phi(k)$ defined as follows,

$$s = \sqrt{\int_0^{k_{\max}} k'^2 \phi(k') dk'}. \tag{7.10}$$

We assume $s = 0.16$ for simplicity, at which the breaking wave field has reached nonlinear saturation [225]. The *local* spectral slope for a breaking wave with wavelength k is calculated as $s_b \equiv \sqrt{k^3\phi(k)}$, following Deike *et al.* [231]. The steady-state spectra for breaking waves transit from $\phi \propto k^{-2.5}$ to $\phi \propto k^{-3}$ above the peak wavenumber k_p [225, 227, 231]. The -2.5 slope arises from a dynamical balance among wind input, nonlinear wave interactions and breaking-induced dissipation, whereas the -3 slope corresponds to a state of saturation where wind input and dissipation are balanced [232]. The upper bound of wavelength $k_{\max}$ in Eq. (7.10) is set as 8m, which does not significantly impact the calculations of breaking wave slopes. Additionally, due to the current lack of quantifications for the characteristic perturbation amplitude ε_0 of wave splash-ups, we fix it as 0.02 in our SSGF calculations. We find that changes in ε_0 will only affect the location of the left tail of the SSGFs via the pinch-off onset time t_0.

We also account for mechanisms capable of changing the fragment size distribution $N(r)$ and hence the SSGF dF/dr in realistic open-ocean conditions. Firstly, splash drops carry over a streamwise speed $\tilde{u} = 0.5u_r = 0.5c_g$ from the pre-splashing wave bulk and a vertical ejection speed $u_{y,\,ej} \propto r^{-1}$ [161] upon formation. Consequently, those drops with sufficiently large sizes d_{frag} and lifespans t_f may undergo aerobreakup [15, 42] before they fall back into the ocean. While the absolute number of splash drops experiencing such secondary breakup may be small, they significantly affect the SSGFs as large numbers of small secondary drops are produced from the erupting bag films [14, 51]. We therefore adopt the bag breakup model of Troitskaya *et al.* [14] to account for the potential aerobreakup of splash drops with fragment Weber number $We_{\text{frag}} \equiv \rho_l \tilde{u}^2 d_{\text{frag}}/\sigma \geq 11$. This model uses Gamma functions to model the fragment size distributions of secondary droplets produced from both the bursting of the bag film and the destabilisation of the bag rim. The average diameter of film drops and the bag film thickness are calculated using the model of Lhuissier and Villermaux [54] for bursting surface bubbles.

Secondly, measurements of past SSGFs are conducted at a certain height above sea level and limited in spatial and time resolution, which implies that spray drops with a short lifespan will not be recorded. We therefore compare the lifetimes t_f of individual fragments with the period of the breaking wave $T_k \equiv 2\pi/\sqrt{gk}$ leading to their production. If $t_f \leq \nu T_k$ where ν is a constant of order unity, we consider the droplet too short-lived to be properly measured and remove its contribution to the fragment size distribution function. The lifetime of fragments t_f is determined as follows. For splash droplets not undergoing aerobreakup, we estimate t_f as its flight time $2u_{y,\,ej}/g$ set by gravity, while the lifetime of secondary aerobreakup droplets is estimated as $t_f = 2u_{y,\,ej}/g - T_{aer}$, with the duration of bag breakup T_{aer} estimated using the exponential correlation proposed in our previous work [15].

8 Discussions and Conclusions

Surface waves and physical processes associated with their breaking are crucial participants in the coupled ocean-atmospheric system. While there has been tremendous progress in the understanding and modelling of the generation of small spray droplets with radii $r \leq 1\,\mu$m, our knowledge of the formation mechanisms of larger ocean sprays remains poor, especially at high-wind conditions where the impact of spray fluxes on the development of storms and hurricanes becomes pronounced. The investigation of the formation mechanisms of large spray is therefore urgently needed to develop adequate parameterisations for climate modelling [10]. In this work, we investigated droplet aerobreakup and liquid rim collision as two toy models for the generation of spume and spray drops, respectively, and significant contributions have been made in elucidating various aspects of their fragmentation dynamics. These are summarised separately in the following sections where we also present recommendations for future work.

8.1 Droplet flattening and bag formation

In Chapters 4 and 5 we investigate the early-time flattening stage of the droplet driven by ambient airflows, both laminar (Chapter 4) and turbulent (Chapter 5). Past numerical studies addressing the droplet dynamics in this stage mostly utilise axisymmetric configurations to reduce computational costs, which we also adopt in Chapter 4. There,

we systematically benchmark our axisymmetric results with their three-dimensional and experimental counterparts, and it is found that axisymmetric simulations capture the morphological evolution of the droplet up to the point of bag formation. While this result demonstrates the limits of axisymmetric simulations for aerobreakup studies, we are also able to leverage them to reveal detailed early-time dynamics difficult to retrieve from experimental studies, for example, the interaction between the droplet periphery and the reattached vortices. This allows us to validate various assumptions made in the theoretical model of Jackiw and Ashgriz [42].

Our results in Chapter 5 provide a consistent numerical framework for investigating the influence of air-phase turbulence on the early-time aerobreakup process. Implementing a robust synthetic turbulence generation method, we systematically reproduce and quantify various aspects of droplet deformation observed in previous turbulent aerobreakup studies, including decreased droplet aspect ratio, bag tilting and formation of strong surface corrugations, and link them with possible physical mechanisms associated with turbulence intermittency. This paves the way for the development of scaling models capable of predicting the aforementioned droplet deformation patterns, and sheds light on possible fragmentation mechanisms of distorted bags in turbulence. While resolving all length scales within the air-phase turbulence remains computationally prohibitive, our results suggest that droplet morphology during aerobreakup is only affected by large eddies with sizes comparable to the droplet radius, as observed in turbulent-bubble interactions [233, 234].

As vortices in the vicinity of the droplet surface play a vital role in shaping the early-time droplet morphology, future work on droplet-vortex interactions within the context of aerobreakup can further complement the limitations of the internal flow model in explaining droplet deformation patterns. This will enable the investigation of droplet aerobreakup in ambient flow configurations that more closely resemble the ocean-atmospheric boundary layer, for example, pulsating flows, swirling flows or shear-driven turbulence. Investigations of the influence of surfactants on the bag formation process also remain scarce and largely qualitative [235, 236]. Surfactants are of interest as seawater is abundant in biofilms and contaminants, which affect

its physiochemical properties and can be modeled as surfactants. Surfactants are also known to significantly modify the wave-breaking dynamics [237]. The recent development of a coupled Volume-of-Fluid and Phase-Field method for resolving the transport of surfactants along fluid interfaces [238] also enables numerical investigation of droplet bag breakup with surfactants.

8.2 Fragmentation of bag films

In Chapter 4 we establish grid independence for the bag film breakup process and the associated fragment statistics with the aid of the MD algorithm, which is achieved for the first time in numerical studies of droplet aerobreakup. This grid independence is further demonstrated by excellent agreement with available experimental statistics from Ref. [66]. While noting that the current numerical convergence is realised only for large fragments and bag films much thicker than experimental observations [51], this has enabled us to reproduce and analyse various bag film fragmentation mechanisms observed in previous experimental studies, including hole expansion, rim collision and node detachment. Furthermore, even though the production mechanism of the small film drops remains grid-dependent, the behaviour of these droplets is well resolved, as demonstrated by the excellent agreement between their measured and theoretical oscillation frequencies. Consequently, the lifetimes and child/parent velocity differences of individual fragments measured from numerical simulations serve as excellent indicators of the film fragmentation mechanisms leading to their production.

While these results lay the foundation for a full-scale three-dimensional direct numerical simulation of bag breakup, the latter remains particularly challenging to achieve due to the extremely small thickness of the bag film before its perforation, which requires significantly higher grid resolution levels. Therefore, a specialised adaptive mesh refinement (AMR) scheme is needed to direct available computational resources to refine the grid cells containing the ultra-thin bag film, thus keeping the problem tractable. It is expected that this full-scale bag breakup simulation will be capable of reproducing fragments ejected from destabilised hole rims as they travel along the curved bag surface [51], a film fragmentation mechanism currently absent from our simulations. This will

also lead to significant improvement in our knowledge of the production mechanism of the smallest film fragments and the fidelity of the fragment statistics.

Another prerequisite for conducting high-fidelity simulations of bag breakup is a set of physically informed MD parameters [37], as current numerical results in Chapter 4 show total numbers of holes generated over the bag lifetime $N_H \sim O(10)$, while available experimental results suggest a much lower perforation rate yielding $N_H \sim O(1)$. These improved MD parameters are only attainable with more in-depth knowledge of film perforation and rupture dynamics. While the Navier-Stokes equations do not account for topological changes in thin film structures, some recent works suggest that film rupture is closely linked with attached vertical structures and localised pressure fluctuations [239, 240]. Ongoing numerical investigations also reveal that impurities within liquid films can trigger hole nucleation at thicknesses much greater than molecular scales, challenging previous assumptions that film rupture is driven by van der Waals forces [241]. While these results are intriguing, more advanced experimental studies are needed to fully validate their findings.

8.3 Rim splashing dynamics

In Chapters 6 and 7 we establish a self-consistent theoretical framework capable of predicting the dynamics and fragment statistics of perturbed liquid rim collision. As the two liquid rims merge along the contact line, the expansion of the fused lamella is found to be inviscid and well described by a self-similar model, whereas the bordering lamella rim is subject to capillary deceleration and produces a series of transverse ligaments. The growth, merging and end-pinching behaviour of these ligaments plays a pivotal role in the fragmentation of the liquid lamella, as the competition between the latter two processes leads to the quasi-steady power-law decay of $r^{-0.5}$ observed in the fragment size distributions. The right tail of the fragment size distributions falls off with a steeper slope, which is closely associated with the intrinsic variations in the transverse ligament widths. While gravity does not directly change the underlying fragmentation mechanism of the liquid lamella, it imposes a global cut-off timescale on the lamella fragmentation process. A theoretical model is developed to describe the

evolution of the droplet size distribution, based on which we further construct an SSGF model for the secondary splashing phenomena during wave breaking.

The early-time physics in wave splashing should be addressed in future work, especially those surrounding the formation of the liquid lamella and transverse ligaments following indentation closure. While the current observations suggest that splash drops are produced solely through ligament end-pinching, this might not be the case at higher collision Weber numbers. Droplets will likely be shed directly from the indentation space under these conditions as the nascent lamella becomes subject to the Kelvin-Helmholtz instability. Since the thickness of the nascent liquid lamella may approach grid size, special numerical techniques will also be needed to curb its premature rupture. The flow characteristics at the lamella rim also merit further investigation as this allows one to predict the growth rate and onset of end-pinching of transverse ligaments, together with the formation time, size and velocity of the splash drops [88, 93]. Detailed knowledge of these early-time dynamics will help to reduce the number of fitting parameters in the sea spray generation function we propose for splash drops. The interface perturbation waveforms and the termination time of secondary splashing corresponding to plunging breakers also need to be elucidated to reduce the number of fitting parameters within the current splash drop size distribution model.

Similar to the bag breakup studies, the effects of surfactants on the rim splashing process also merit further investigation, and the recent works of Constante-Amores *et al.* [242, 243] have revealed that while the presence of surfactants does not directly modify the underlying instability governing the formation of corrugations and ligaments upon crown splashes, it facilitates the generation of larger fragments by delaying the end-pinching dynamics and promoting the merging of adjacent rim protrusions. Statistically converged fragment statistics under the influence of surfactants, however, remain difficult to obtain due to high computational costs [243], which will also benefit from the recent numerical development [238] as mentioned above.

Finally, the SSGF model we developed in Chapter 7 is based on a simple dimensional analysis assuming that breaking waves at all wavelengths will undergo a secondary splashing phase as observed in previous studies [17, 74]. While this assumption bridges

the two scenarios of rim and unidirectional wave splashing straightforwardly, it has not accounted for the complexity of wave splashing in the open ocean which remains difficult to capture with current observational techniques, and should be interpreted as the upper bound of ocean splash drop generation. It is expected that under such conditions, assumptions of two-dimensionality and limited breaking wave steepness crucial to the current model will break down [228]. Consequently, more advanced observational and experimental studies are needed to elucidate splashing dynamics in realistic sea states to enable the development of more accurate splash drop production models.

Appendices

A Grid convergence and Oh-dependency of fragment statistics

In this section, we discuss the numerical convergence for the fragment statistics of rim collision reported in this work. For this purpose, we present the time- and ensemble-averaged fragment size and velocity distributions $n(r/R_0)$ and $\bar{v}(r/R_0)$ for $We = 200$, $\varepsilon = 0.06$ and $N_{\max} = 25$ at $t/\tau_{\text{cap}} = 0.23$ in fig. A1, where the upper and lower rows show respectively the results at early ($t/\tau_{\text{cap}} = 0.23$) and late ($t/\tau_{\text{cap}} = 1.82$) times. The recorded fragment data at a given time are first collected across different realisations with the same initial configuration, and then binned according to the fragment radius r. The count in each bin thus produces the fragment size distribution $n(r/R_0)$. We then average the speed of fragments within each bin to obtain the distribution of fragment velocity $\bar{v}(r/R_0)$. Three identical ensemble realisations are obtained at maximum resolution level $L_{\max} = 9$, 10 and 11, whereas in fig. A1a we also include data produced from a single realisation at $L_{\max} = 12$. It has been known from previous numerical studies [15, 17, 72, 185] that grid independence for fragmentation problems can be challenging to obtain, especially for small fragments near the grid size Δ; and a radius threshold of $r \geq 4\Delta$ has been recommended beyond which the fragment size distributions are considered fully converged. We therefore also add vertical dashed lines in each subplot of fig. A1 showing the values of 4Δ corresponding to each resolution level to facilitate comparison with these threshold values.

The early-time fragment size distributions presented in fig. A1a show large ranges of scatter due to relatively small number of fragments produced from each ensemble realisation, with the size of the tiniest fragments becoming increasingly smaller as the resolution level $L_{\max}$ increases. Nevertheless, it is observed that the tail of the distribution functions obtained at $L_{\max} = 10$ and 11 agrees when $r/R_0 \geq 0.1R_0$, which roughly corresponds to the threshold value of $4\Delta_{10}$. We note that the grid convergence behaviour of large fragments at early times are further improved when $N_{\max}$ is increased, although these results are not included in the present work. The distributions of velocity components u_y and u_{xz} in fig. A1b show better agreement across all three resolution levels down to $r = 4\Delta_{10}$. Below this radius threshold, large scatters in the velocity

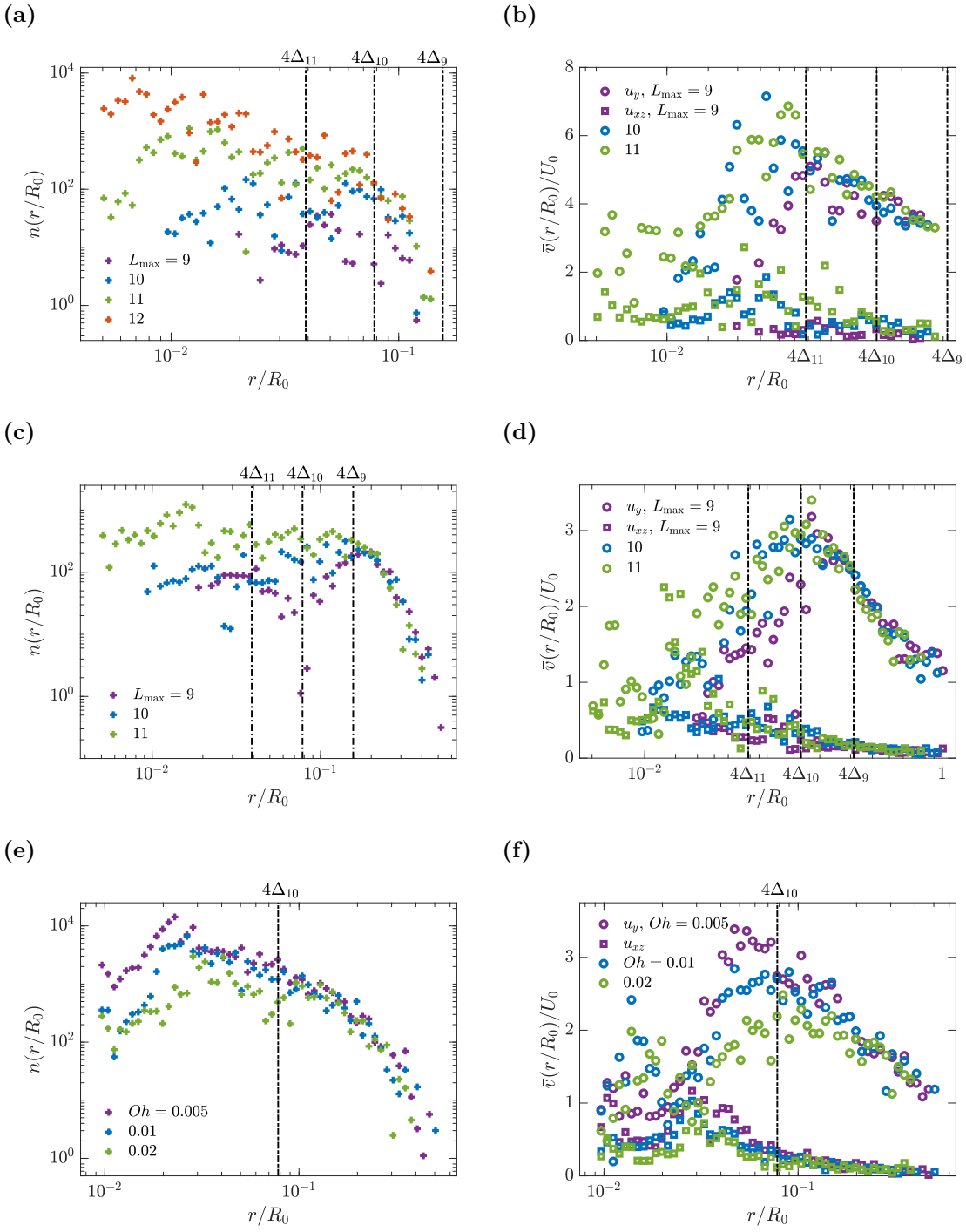

Figure A1: The size (a,c) and velocity (b,d) distributions of fragments $n(r/R_0)$ and $\bar{v}(r/R_0)$ at $We = 200$, $\varepsilon = 0.06$ and $N_{\max} = 25$ at $t/\tau_{\text{cap}} = 0.23$ (a,b) and 1.82 (c,d), binned and averaged across three realisations with the same initial configurations at $L_{\max} = 9$, 10 and 11. Fig. A1a also includes statistics produced from a single realisation at $L_{\max} = 12$. (e,f): The size (e) and velocity (f) distributions of fragments at $We = 280$ and different Oh values at $t/\tau_{\text{cap}} = 1.82$.

data at $L_{\max} = 10$ and 11 are observed, although they appear to agree in trend with each other and differ from the results at $L_{\max} = 9$. When rim collision proceeds to later times, more fragments are produced and the range of scatter in the size and velocity distributions becomes smaller, as shown in figs. A1c and A1d. Nevertheless, the fragment size range where grid convergence of fragment size and velocity distributions is fully established remains largely unchanged from the early time results, namely, the right tail of the fragment size (fig. A1c) and velocity distribution (fig. A1d) are fully converged for $r/R_0 \geq 4\Delta_9$, and the difference between results at $L_{\max} = 10$ and 11 becomes significant for $r/R_0 \leq 4\Delta_{10}$. These results suggest that for a given grid resolution level $L_{\max}$, $4\Delta_{L_{\max}}$ can be regarded as the lower limit of fragment radius above which the fragment size and velocity distributions can be considered fully grid converged, while the statistics of fragments below this threshold are still grid-dependent and should be treated with caution [17].

Figs. A1e and A1f present the fragment size and velocity distributions at a few different Oh values at $t/\tau_{\text{cap}} = 1.82$. Fig. A1e shows that for $r \geq 4\Delta_{10}$ where grid convergence of fragment statistics is fully established, the fragment size distribution is not sensitive to viscous effects. On the other hand, the velocity of fragments with radii near $4\Delta_{10}$ as shown in fig. A1f decreases slightly with increasing Oh values, which might be because of more significant viscous dissipation at the lamella feet and rim necks, as discussed in §6.5.1.

B Theoretical analysis of the lamella foot advancement

Here, we analytically solve for the evolution of the advancement of the lamella foot position y_n after the two cylinders come into contact. This is similar to the axisymmetric analysis due to Ref. [203], having here been adapted for the planar problem; and it is expected that similar to their case, $y_n \propto \sqrt{U_0 t/R_0}$. Taking into account the geometrical symmetry present in the problem, we consider the equivalent configuration where a single liquid rim impacts on a flat plane. Neglecting viscous effects and

air entrainment, the flow field within the liquid phase is prescribed by the Laplace equation within the Cartesian coordinate yOz,

$$\nabla^2\phi = \frac{\partial^2\phi}{\partial y^2} + \frac{\partial^2\phi}{\partial z^2} = 0, \tag{B1}$$

where ϕ is the velocity potential. From now on, we select the rim radius R_0, the collision velocity U_0 and their quotient R_0/U_0 as reference length, velocity and time scales to non-dimensionalise all physical properties within this section.

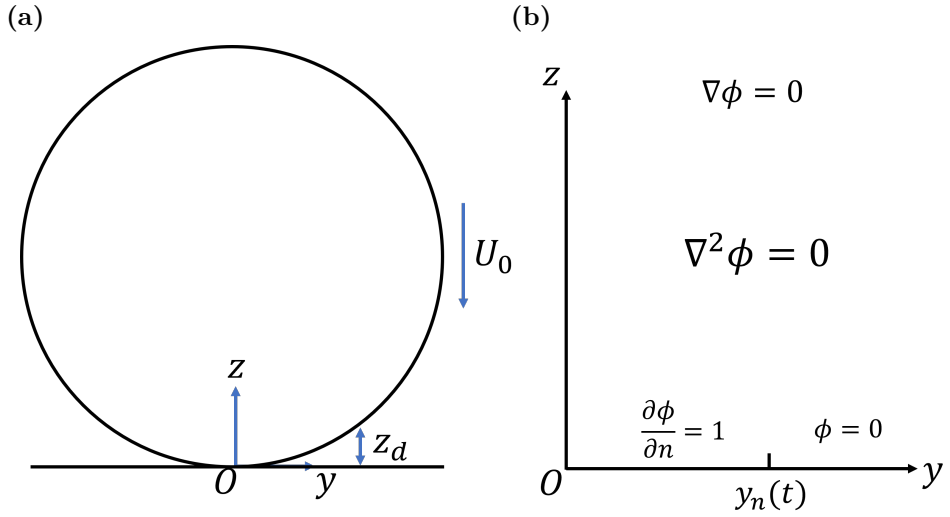

Figure B1: (a): Sketch showing the cross-sectional view of the liquid cylinder collision problem. (b): Sketch showing the boundary conditions defined in Eqs. (B2), (B3) and (B6) under which we solve Eq. (B1).

Now consider the boundary conditions for the domain of interest, namely the contact region $z \ll 1$ within the liquid phase close to the bottom plane. We fix our reference frame on the liquid bulk descending at non-dimensionalised unit velocity -1, thus we impose an opposite normal velocity at the bottom,

$$\frac{\partial\phi}{\partial n} = 1, \quad |y| \leq y_n(t),\ z = 0. \tag{B2}$$

Within the same reference frame, the liquid phase velocity decays to 0 far away from the contact region, thus

$$\nabla\phi = 0, \quad z \gg 1. \tag{B3}$$

The final boundary condition comes from considering the flow condition on the drop surface (but outside the contact area) for $1 \gg y \geq y_n(t)$ and $z = z_d\ (y)$. At very early time immediately after the impact, the rim bulks largely retain their cylindrical shape, as shown in fig. B1a. Thus, the drop shape in the vicinity of the stagnation point can be approximated as

$$z_d = 1 - \sqrt{1 - y^2} \approx \frac{y^2}{2} + o(y^2) \approx 0 \tag{B4}$$

up to first order in y. At high We values capillary effects can be neglected, and the unsteady Bernoulli Equation can be applied along the drop surface,

$$\frac{\partial \phi}{\partial t} + \frac{u^2}{2} = \left[\frac{\partial \phi}{\partial t} + \frac{u^2}{2}\right]_{y=y_n(t)} \approx \frac{1}{2}. \tag{B5}$$

For small values of t, unsteady effects dominate and Eq. (B5) can be further simplified using $\phi(t = 0) = 0$ at the free surface,

$$\phi \approx \phi(t=0) - \frac{1}{2}\left(1 - |\nabla\phi|^2\right) t \approx \phi(t=0) = 0, \quad |y| \geq y_n(t),\ z = 0. \tag{B6}$$

The solution of Eq. (B1) subject to boundary conditions (B2), (B3) and (B6) thus corresponds to the flow field induced by an infinitely long lamina with width $2y_n$ moving perpendicular to its surface. The following solution written in elliptical coordinates is provided in Art. 71, 3° of Ref. [244]:

$$\psi = ae^{-\xi}\cos\eta, \tag{B7}$$

where $y = a\cosh\xi\cos\eta$, $z = a\sinh\xi\sin\eta$. Utilising $\eta = 0$ at $z = 0$, we derive the total vertical velocity u_z for $y > y_n(t)$, $z = 0$ within the laboratory frame,

$$u_z(z=0) = -1 - \frac{\partial \psi}{\partial z} = -1 - \frac{2}{\left[\frac{y}{y_n} + \sqrt{\left(\frac{y}{y_n}\right)^2 - 1}\right]^2 - 1}. \tag{B8}$$

Now apply Wagner's condition [203, 245] to Eq. (B8); namely, the lamella foot position $y_n(t)$ is fixed by the time when a point on the drop interface with initial coordinates $y = y_n(t)$, $z_d = y_n^2/2$ reaches $z = 0$,

$$\frac{y_n^2}{2} - t - \int_0^{y_n} \frac{2}{\left[\frac{y_n}{\kappa} + \sqrt{\left(\frac{y_n}{\kappa}\right)^2 - 1}\right]^2 - 1} \frac{d\tau}{d\kappa} d\kappa = 0. \tag{B9}$$

Where κ is a dummy variable indicating the lamella foot location for $\tau < t$. Taking $\kappa = y_n(t)\sin\lambda$, and since we already know $\kappa \propto \sqrt{t}$, we assume that $d\tau/d\kappa = C\kappa$. Thus one arrives at

$$\frac{y_n^2}{2} - t - Cy_n^2 \int_0^{\pi/2} (\sin\lambda - \sin\lambda\cos\lambda) d\lambda = 0, \tag{B10}$$

which leads to

$$\frac{dt}{dy_n} = y_n(1-C) = Cy_n. \tag{B11}$$

Thus $C = 1/2$, and by integration one finds $y_n = 2\sqrt{t}$, or written dimensionally as

$$y_n/R_0 = 2\sqrt{U_0 t/R_0}. \tag{B12}$$

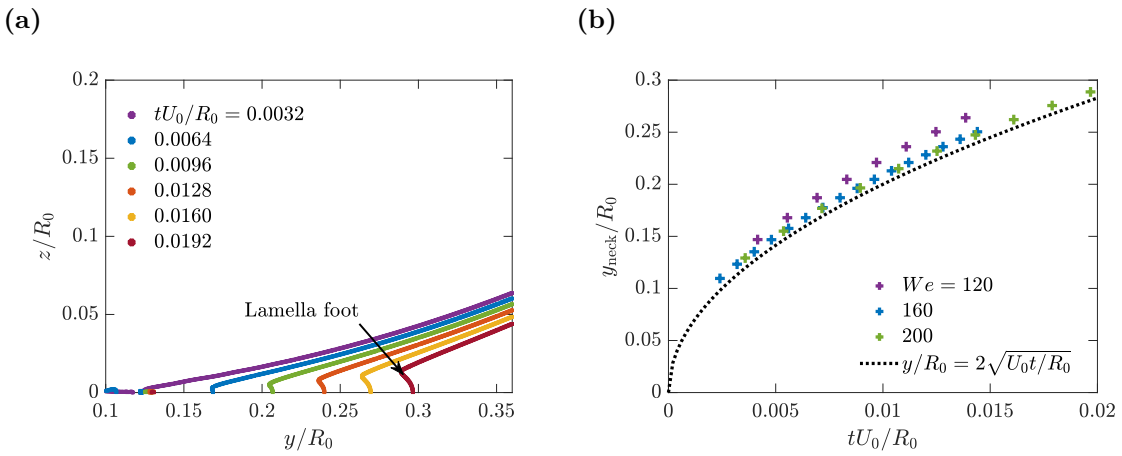

Figure B2: (a): Two-dimensional simulation results at $L_{\max} = 15$ for $We = 160$ showing the evolution of the contact region. (b): Comparison between simulation results at different values of We and Eq. (B12) at very early time.

We conduct two-dimensional numerical simulations at a very high resolution level $L_{\max} = 15$ to investigate the evolution of the interface profile close to the contact region, which we show in fig. B2a. It can be observed that for $tU_0/R_0 \geq 0.0096$, a bulge on the interface profile appears at $z = 0$ representing the nascent lamella, whereas the local minimum in y denotes the lamella foot. Fig. B2b further compares the evolution of the lamella foot location y_n measured from the numerical simulations with the theoretical prediction (B12), where a good agreement is reached for $We \geq 160$,

indicating that the potential flow analysis employed in this section indeed captures the lamella ejection at very early time.

Solving Eqs. (6.13)-(6.15) requires the initial values of ($b_{\rm rim}$, $y_{\rm rim}$, $v_{\rm rim}$) at the moment of lamella foot formation t_e. (B12) suggests that

$$y_{\rm rim}(t_e) = 2\sqrt{t_e}, \quad v_{\rm rim}(t_e) = 1/\sqrt{t_e}. \tag{B13}$$

We also expect that the nascent rim thickness $b_{\rm rim}(t_e)$ can be approximated using the lamella height function $h[y_{\rm rim}(t_e),\, t_e]$. Thus the ejection time t_e remains the only unknown in the initial conditions, although our numerical simulations suggest that it is close to zero. To regularize the initial conditions, we choose a well-resolved and sufficiently small time $t_e' = 4.5 \times 10^{-3}\tau_{\rm cap}$ when solving Eqs. (6.13)-(6.15). We have confirmed that changing values of t_e' does not have significant influences on the solution of Eqs. (6.13)-(6.15).

C Alternative fragment size distribution model

Here we assume that the ligament widths follow a log-normal distribution [15, 98],

$$p\left[\frac{w}{\bar{w}(t)}\right] = \frac{1}{\sqrt{2\pi}\sigma}\left[\frac{w}{\bar{w}(t)}\right]^{-1} e^{-\frac{1}{2\sigma^2}\ln^2[w/\bar{w}(t)]}, \tag{C1}$$

where σ is the scale parameter. An alternative form of $N(r)$ can thus be calculated via time integration as follows,

$$N(r) = C'\left(\frac{r}{R_0}\right)^{-1/2}\left[\mathrm{erf}\left(\frac{\sqrt{2}}{2}\tilde{m}\left(\ln\frac{r}{\bar{r}(t_0)}+2\right)\right) - \mathrm{erf}\left(\frac{\sqrt{2}}{2}\tilde{m}\left(\ln\frac{r}{\bar{r}(t)}+2\right)\right)\right]. \tag{C2}$$

In figs. C1a and C1b we present the comparison between the numerical measurements and the theoretical splash drop size distribution (C2). Excellent agreement is also observed within the parameter space we explore, although model (C2) slightly underpredicts the right tail of the fragment size distribution at $We = 200$ compared with (7.6). These results suggest the robustness of our modelling approach of the fragment size distributions.

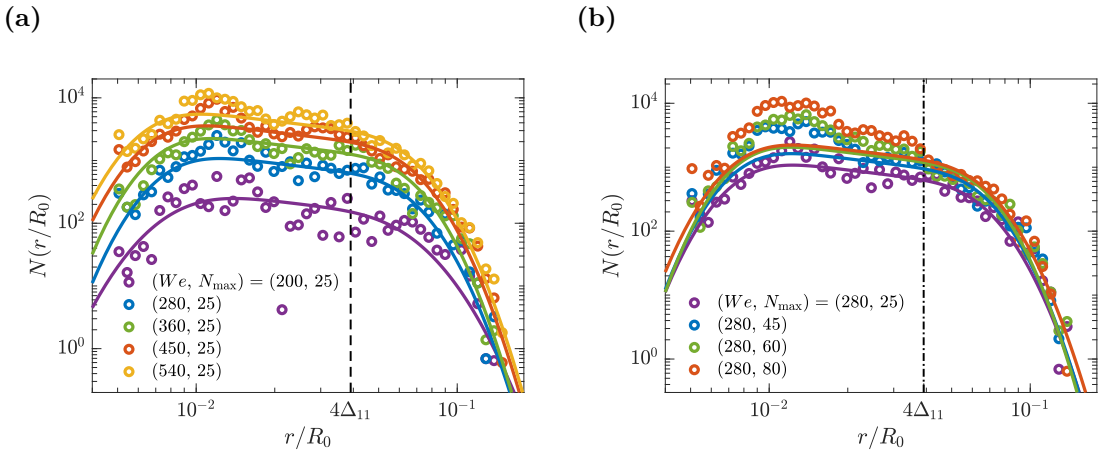

Figure C1: Fragment size distributions at $t/\tau_{\text{cap}} = 0.227$ for different We (a) and $N_{\max}$ (b) values, in comparison with the prediction of Eq. (C2). The solid curves are computed assuming that the ligament widths w abide by the the log-normal distribution in Eq. (C1).

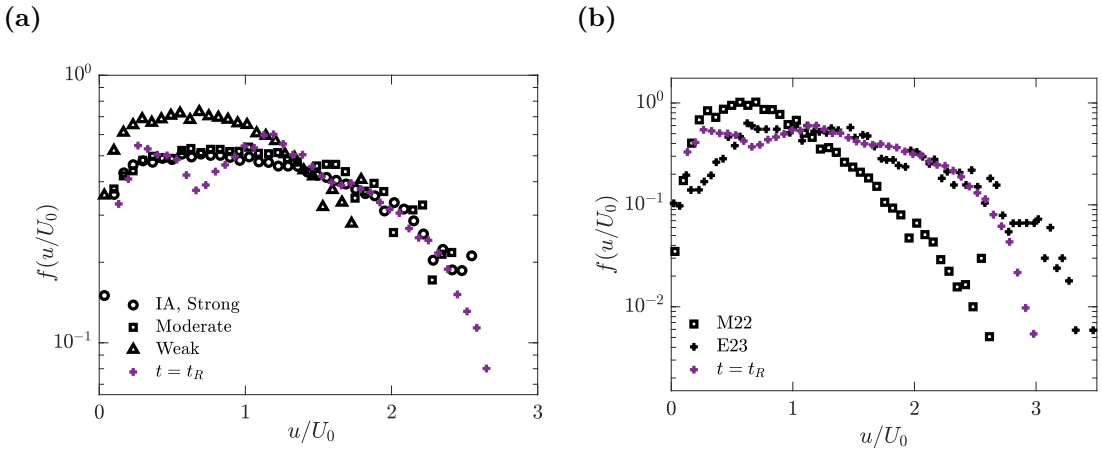

Figure D1: Comparison of our splash fragment speed distributions at various times with available wave-breaking statistics from Refs. [17, 74]. The numerical data are obtained at $We = 280$, $Bo = 125$ and $N_{\max} = 25$.

D Comparison of fragment speed distributions with wave breaking data

In figs. D1a and D1b we compare the fragment speed distributions of rim splashing and wave breaking. The speed distribution of rim splash drops is double-peaked, which is likely because the smallest fragments ejected start to fall back to the bottom of the simulation domain under gravity (corresponding to the peak at $u/U_0 \approx 0.4$), while larger fragments continue to be ejected at higher speeds (hence the peak at $u/U_0 \approx 2.4$).

Records of intermediate fragment speeds ($0.5 \leq u/U_0 \leq 2$) increase as more fragments start to fall back, and the distribution becomes skewed towards large speeds, which matches excellently with those of the Region IA drops for moderate and strong breakers [74] in fig. D1a. Fig. D1b suggests that the speed distribution of rim splash drops more closely resembles the overall speed distribution of Mostert *et al.* [17] within the range of $1 \leq u/U_0 \leq 2.5$, where the results from Erinin *et al.* [74] feature a steeper slope. It is also noted that compared with Mostert *et al.* [17], Erinin *et al.* [74] recorded a higher occurrence of slow fragments within the range of $u/U_0 \leq 1$, which likely corresponds to the smallest fragments produced as it remains particularly challenging to fully resolve these in direct numerical simulations [15, 17, 161]. While the current work focuses on the fragment size distribution of rim splashing, our results on the fragment speed distribution here suggest that the behaviour of these rim splash drops closely resembles those produced from wave splashing and breaking.

References

[1]K. Karnauskas, *Physical oceanography and climate* (Cambridge University Press, 2020).

[2]P. C. Reid, A. C. Fischer, E. Lewis-Brown, M. P. Meredith, M. Sparrow, A. J. Andersson, A. Antia, N. R. Bates, U. Bathmann, G. Beaugrand, et al., "Impacts of the oceans on climate change", in, Vol. 56, Advances in Marine Biology (Academic Press, 2009), pp. 1–150.

[3]L. D. Talley, *Descriptive physical oceanography: an introduction* (Academic Press, 2011).

[4]P. P. Sullivan and J. C. McWilliams, "Dynamics of winds and currents coupled to surface waves", Annual Review of Fluid Mechanics **42**, 19–42 (2010).

[5]L. Deike, "Mass transfer at the ocean–atmosphere interface: the role of wave breaking, droplets, and bubbles", Annual Review of Fluid Mechanics **54**, 191–224 (2022).

[6]M. Perlin, W. Choi, and Z. Tian, "Breaking waves in deep and intermediate waters", Annual Review of Fluid Mechanics **45**, 115–145 (2013).

[7]D. G. Boettger, S. R. Keating, M. L. Banner, R. P. Morison, and X. Barthélémy, "An energetic signature for breaking inception in surface gravity waves", Journal of Fluid Mechanics **959**, A33 (2023).

[8]E. Villermaux, "Fragmentation", Annual Review of Fluid Mechanics **39**, 419–446 (2007).

[9]K. T. Kiger and J. H. Duncan, "Air-entrainment mechanisms in plunging jets and breaking waves", Annual Review of Fluid Mechanics **44**, 563–596 (2012).

[10]F. Veron, "Ocean spray", Annual Review of Fluid Mechanics **47**, 507–538 (2015).

[11]L. Deike, B. Reichl, and F. Paulot, "A mechanistic sea spray generation function based on the sea state and the physics of bubble bursting", AGU Advances **3**, e2022AV000750 (2022).

[12]E. Monahan, D. Spiel, and K. Davidson, "A model of marine aerosol generation via whitecaps and wave disruption", in *Oceanic whitecaps: and their role in air-sea exchange processes* (Springer, 1986), pp. 167–174.

[13]J. A. Mueller and F. Veron, "A sea state–dependent spume generation function", Journal of Physical Oceanography **39**, 2363–2372 (2009).

[14]Y. Troitskaya, A. Kandaurov, O. Ermakova, D. Kozlov, D. Sergeev, and S. Zilitinkevich, "The 'bag breakup' spume droplet generation mechanism at high winds. Part I: Spray generation function", Journal of Physical Oceanography **48**, 2168–2188 (2018).

[15]K. Tang, T. Adcock, and W. Mostert, "Bag film breakup of droplets in uniform airflows", Journal of Fluid Mechanics **970**, A9 (2023).

[16]E. L. Andreas, J. B. Edson, E. C. Monahan, M. P. Rouault, and S. D. Smith, "The spray contribution to net evaporation from the sea: a review of recent progress", Boundary-Layer Meteorology **72**, 3–52 (1995).

[17]W. Mostert, S. Popinet, and L. Deike, "High-resolution direct simulation of deep water breaking waves: transition to turbulence, bubbles and droplets production", Journal of Fluid Mechanics **942** (2022).

[18]V. Young, *Liquid rocket engine combustion instability*, Vol. 169 (AIAA, 1995).

[19]L. Bourouiba, "The fluid dynamics of disease transmission", Annual Review of Fluid Mechanics **53**, 473–508 (2021).

[20]L. Chirco, J. Maarek, S. Popinet, and S. Zaleski, "Manifold death: a volume of fluid implementation of controlled topological changes in thin sheets by the signature method", Journal of Computational Physics **467**, 111468 (2022).

[21]Z.-T. Xie and I. P. Castro, "Efficient generation of inflow conditions for large-eddy simulation of street-scale flows", Flow Turbulence and Combustion **81**, 449–470 (2008).

[22]Y. Troitskaya, A. Kandaurov, A. Zotova, E. V. Korsukova, and D. Sergeev, "Statistical characteristics of droplets formed due to the 'bag breakup' fragmentation event at the interface between water and high-speed air flow", Journal of Physical Oceanography (2023).

[23]Y. Troitskaya, A. Kandaurov, O. Ermakova, D. Kozlov, D. Sergeev, and S. Zilitinkevich, "Bag-breakup fragmentation as the dominant mechanism of sea-spray production in high winds", Scientific Reports **7**, 1–4 (2017).

[24]Y. Troitskaya, A. Kandaurov, O. Ermakova, D. Kozlov, A. Zotova, and D. Sergeev, "The small-scale instability of the air–water interface responsible for the bag-breakup fragmentation", Journal of Physical Oceanography **52**, 493–517 (2022).

[25]D. R. Guildenbecher, C. López-Rivera, and P. E. Sojka, "Secondary atomization", Experiments in Fluids **46**, 371–402 (2009).

[26]M. Jalaal and K. Mehravaran, "Transient growth of droplet instabilities in a stream", Physics of Fluids **26**, 012101 (2014).

[27]W. Yang, M. Jia, Z. Che, K. Sun, and T. Wang, "Transitions of deformation to bag breakup and bag to bag-stamen breakup for droplets subjected to a continuous gas flow", International Journal of Heat and Mass Transfer **111**, 884–894 (2017).

[28]A. N. Zotova, Y. I. Troitskaya, D. A. Sergeev, and A. A. Kandaurov, "Direct numerical simulation of bag-breakup-mechanism of sea spray generation in strong winds", Journal of Physics: Conference Series **1163**, 012028 (2019).

[29]F. Marcotte and S. Zaleski, "Density contrast matters for drop fragmentation thresholds at low Ohnesorge number", Physical Review Fluids **4**, 103604 (2019).

[30]W. Yang, M. Jia, K. Sun, and T. Wang, "Influence of density ratio on the secondary atomization of liquid droplets under highly unstable conditions", Fuel **174**, 25–35 (2016).

[31]S. S. Jain, N. Tyagi, R. S. Prakash, R. V. Ravikrishna, and G. Tomar, "Secondary breakup of drops at moderate Weber numbers: effect of density ratio and Reynolds number", International Journal of Multiphase Flow **117**, 25–41 (2019).

[32]L.-P. Hsiang and G. M. Faeth, "Drop deformation and breakup due to shock wave and steady disturbances", International Journal of Multiphase Flow **21**, 545–560 (1995).

[33]T. Kékesi, G. Amberg, and L. P. Wittberg, "Drop deformation and breakup", International Journal of Multiphase Flow **66**, 1–10 (2014).

[34]T. G. Theofanous, "Aerobreakup of Newtonian and viscoelastic liquids", Annual Review of Fluid Mechanics **43**, 661–690 (2011).

[35]P. K. Kirar, S. K. Soni, P. S. Kolhe, and K. C. Sahu, "An experimental investigation of droplet morphology in swirl flow", Journal of Fluid Mechanics **938** (2022).

[36]C. L. Ng, R. Sankarakrishnan, and K. A. Sallam, "Bag breakup of nonturbulent liquid jets in crossflow", International Journal of Multiphase Flow **34**, 241–259 (2008).

[37]Y. Kulkarni, C. Pairetti, R. Villiers, S. Popinet, and S. Zaleski, "The atomising pulsed jet", Journal of Fluid Mechanics **1009**, A35 (2025).

[38]P. Kant, C. Pairetti, Y. Saade, S. Popinet, S. Zaleski, and D. Lohse, "Bag-mediated film atomization in a cough machine", Physical Review Fluids **8**, 074802 (2023).

[39]V. Kulkarni, "An analytical and experimental study of secondary atomization of vibrational and bag breakup modes", PhD thesis (Purdue University, 2013).

[40]J. A. Nicholls and A. A. Ranger, "Aerodynamic shattering of liquid drops", AIAA Journal **7**, 285–290 (1969).

[41]L. Opfer, I. V. Roisman, J. Venzmer, M. Klostermann, and C. Tropea, "Droplet-air collision dynamics: evolution of the film thickness", Physical Review E **89**, 013023 (2014).

[42]I. M. Jackiw and N. Ashgriz, "On aerodynamic droplet breakup", Journal of Fluid Mechanics **913** (2021).

[43]Y. Zhou, R. J. R. Williams, P. Ramaprabhu, M. Groom, B. Thornber, A. Hillier, W. Mostert, B. Rollin, S. Balachandar, P. D. Powell, et al., "Rayleigh–Taylor and Richtmyer–Meshkov instabilities: A journey through scales", Physica D: Nonlinear Phenomena, 132838 (2021).

[44]H. Zhao, H.-F. Liu, W.-F. Li, and J.-L. Xu, "Morphological classification of low viscosity drop bag breakup in a continuous air jet stream", Physics of Fluids **22**, 114103 (2010).

[45]P. G. Drazin, *Introduction to hydrodynamic stability*, Vol. 32 (Cambridge university press, 2002).

[46]T. Theofanous, G. Li, and T.-N. Dinh, "Aerobreakup in rarefied supersonic gas flows", J. Fluids Eng. **126**, 516–527 (2004).

[47]L.-P. Hsiang and G. M. Faeth, "Near-limit drop deformation and secondary breakup", International Journal of Muhiphase Flow **18**, 635–652 (1992).

[48]A. B. Liu, D. Mather, and R. D. Reitz, "Modeling the effects of drop drag and breakup on fuel sprays", SAE Transactions, 83–95 (1993).

[49]E. Villermaux and B. Bossa, "Single-drop fragmentation determines size distribution of raindrops", Nature Physics **5**, 697–702 (2009).

[50]D. G. Obenauf and P. E. Sojka, "Theoretical deformation modeling and drop size prediction in the multimode breakup regime", Physics of Fluids **33**, 092113 (2021).

[51]I. M. Jackiw and N. Ashgriz, "Prediction of the droplet size distribution in aerodynamic droplet breakup", Journal of Fluid Mechanics **940** (2022).

[52]G. K. Batchelor, *An introduction to fluid dynamics* (Cambridge University Press, 1967).

[53]A. Vledouts, J. Quinard, N. Vandenberghe, and E. Villermaux, "Explosive fragmentation of liquid shells", Journal of Fluid Mechanics **788**, 246–273 (2016).

[54]H. Lhuissier and E. Villermaux, "Bursting bubble aerosols", Journal of Fluid Mechanics **696**, 5–44 (2012).

[55]F. Pigeonneau and A. Sellier, "Low-Reynolds-number gravity-driven migration and deformation of bubbles near a free surface", Physics of Fluids **23**, 092102 (2011).

[56]J. Magnaudet and M. J. Mercier, "Particles, drops, and bubbles moving across sharp interfaces and stratified layers", Annual Review of Fluid Mechanics **52**, 61–91 (2020).

[57]S. Joshi and T. Anand, "Droplet deformation during secondary breakup: role of liquid properties", Experiments in Fluids **63**, 1–19 (2022).

[58]S. Poulain, E. Villermaux, and L. Bourouiba, "Ageing and burst of surface bubbles", Journal of Fluid Mechanics **851**, 636–671 (2018).

[59]N. Savva and J. W. M. Bush, "Viscous sheet retraction", Journal of Fluid Mechanics **626**, 211–240 (2009).

[60]Y. Wang, R. Dandekar, N. Bustos, S. Poulain, and L. Bourouiba, "Universal rim thickness in unsteady sheet fragmentation", Physical Review Letters **120**, 204503 (2018).

[61]H. Lhuissier and E. Villermaux, "'Effervescent'atomization in two dimensions", Journal of Fluid Mechanics **714**, 361–392 (2013).

[62]B. Néel, H. Lhuissier, and E. Villermaux, "'Fines' from the collision of liquid rims", Journal of Fluid Mechanics **893** (2020).

[63]G. G. Agbaglah, "Breakup of thin liquid sheets through hole–hole and hole–rim merging", Journal of Fluid Mechanics **911** (2021).

[64]S. S. Ade, L. D. Chandrala, and K. C. Sahu, "Size distribution of a drop undergoing breakup at moderate Weber numbers", Journal of Fluid Mechanics **959**, A38 (2023).

[65]H. Zhao, H. Liu, J. Xu, and W. Li, "Experimental study of drop size distribution in the bag breakup regime", Industrial and Engineering Chemistry Research **50**, 9767–9773 (2011).

[66]D. R. Guildenbecher, J. Gao, and P. E. Chen J.and Sojka, "Characterization of drop aerodynamic fragmentation in the bag and sheet-thinning regimes by crossed-beam, two-view, digital in-line holography", International Journal of Multiphase Flow **94**, 107–122 (2017).

[67]V. Radhakrishna, W. Shang, L. Yao, J. Chen, and P. E. Sojka, "Experimental characterization of secondary atomization at high Ohnesorge numbers", International Journal of Multiphase Flow **138**, 103591 (2021).

[68]D. Jiao, K. Jiao, F. Zhang, and Q. Du, "Direct numerical simulation of droplet deformation in turbulent flows with different velocity profiles", Fuel **247**, 302–314 (2019).

[69]H. Zhao, D. Nguyen, D. J. Duke, D. Edgington-Mitchell, J. Soria, H.-F. Liu, and D. Honnery, "Effect of turbulence on drop breakup in counter air flow", International Journal of Multiphase Flow **120**, 103108 (2019).

[70]Z. Xu, T. Wang, and Z. Che, "Droplet deformation and breakup in shear flow of air", Physics of Fluids **32**, 052109 (2020).

[71]Z. Xu, T. Wang, and Z. Che, "Droplet breakup in airflow with strong shear effect", Journal of Fluid Mechanics **941** (2022).

[72]A. Rivière, W. Mostert, S. Perrard, and L. Deike, "Sub-Hinze scale bubble production in turbulent bubble break-up", Journal of Fluid Mechanics **917**, A40 (2021).

[73]A. Rivière, D. J. Ruth, W. Mostert, L. Deike, and S. Perrard, "Capillary driven fragmentation of large gas bubbles in turbulence", Physical Review Fluids **7**, 083602 (2022).

[74]M. A. Erinin, C. Liu, S. D. Wang, X. Liu, and J. H. Duncan, "Plunging breakers. Part 2. Droplet generation", Journal of Fluid Mechanics **967**, A36 (2023).

[75]W. Mostert and L. Deike, "Inertial energy dissipation in shallow-water breaking waves", Journal of Fluid Mechanics **890** (2020).

[76]X. Cheng, T.-P. Sun, and L. Gordillo, "Drop impact dynamics: impact force and stress distributions", Annual Review of Fluid Mechanics **54**, 57–81 (2022).

[77]Y. Wang and L. Bourouiba, "Drop impact on small surfaces: thickness and velocity profiles of the expanding sheet in the air", Journal of Fluid Mechanics **814**, 510–534 (2017).

[78]Y. Wang and L. Bourouiba, "Unsteady sheet fragmentation: droplet sizes and speeds", Journal of Fluid Mechanics **848**, 946–967 (2018).

[79]Y. Wang and L. Bourouiba, "Growth and breakup of ligaments in unsteady fragmentation", Journal of Fluid Mechanics **910**, A39 (2021).

[80]Y. Wang and L. Bourouiba, "Mass, momentum and energy partitioning in unsteady fragmentation", Journal of Fluid Mechanics **935**, A29 (2022).

[81]J. M. Gordillo, G. Riboux, and E. S. Quintero, "A theory on the spreading of impacting droplets", Journal of Fluid Mechanics **866**, 298–315 (2019).

[82]S. Wildeman, C. W. Visser, C. Sun, and D. Lohse, "On the spreading of impacting drops", Journal of Fluid Mechanics **805**, 636–655 (2016).

[83]A. L. Yarin, "Drop impact dynamics: splashing, spreading, receding, bouncing...", Annual Review of Fluid Mechanics **38**, 159–192 (2006).

[84]B. Liu, J. Hernandez-Rueda, H. Gelderblom, and O. O. Versolato, "Speed of fragments ejected by an expanding liquid tin sheet", Physical Review Fluids **7**, 083601 (2022).

[85]M. A. Erinin, X. Liu, S. D. Wang, and J. H. Duncan, "Plunging breakers. Part 1. Analysis of an ensemble of wave profiles", Journal of Fluid Mechanics **967**, A35 (2023).

[86]N. Kim, Y. L. Fan, H. Park, and D. van der Meer, "Dynamics of a liquid lamella during vertical impact of a solid plate", Journal of Fluid Mechanics **1007**, A69 (2025).

[87]J. M. Gordillo, H. Lhuissier, and E. Villermaux, "On the cusps bordering liquid sheets", Journal of Fluid Mechanics **754**, R1 (2014).

[88]S. Gekle and J. M. Gordillo, "Generation and breakup of Worthington jets after cavity collapse. Part 1. Jet formation", Journal of Fluid Mechanics **663**, 293–330 (2010).

[89]C.-Y. Lai, J. Eggers, and L. Deike, "Bubble bursting: universal cavity and jet profiles", Physical Review Letters **121**, 144501 (2018).

[90]J. M. Gordillo and F. J. Blanco-Rodríguez, "Theory of the jets ejected after the inertial collapse of cavities with applications to bubble bursting jets", Physical Review Fluids **8**, 073606 (2023).

[91]F. J. Blanco–Rodríguez and J. Gordillo, "On the sea spray aerosol originated from bubble bursting jets", Journal of Fluid Mechanics **886**, R2 (2020).

[92]J. R. Castrejón-Pita, A. A. Castrejón-Pita, S. S. Thete, K. Sambath, I. M. Hutchings, J. Hinch, J. R. Lister, and O. A. Basaran, "Plethora of transitions during breakup of liquid filaments", Proceedings of the National Academy of Sciences **112**, 4582–4587 (2015).

[93]J. M. Gordillo and S. Gekle, "Generation and breakup of Worthington jets after cavity collapse. Part 2. Tip breakup of stretched jets", Journal of Fluid Mechanics **663**, 331–346 (2010).

[94]A. M. Gañán-Calvo, "Revision of bubble bursting: universal scaling laws of top jet drop size and speed", Physical Review Letters **119**, 204502 (2017).

[95]A. Berny, L. Deike, S. Popinet, and T. Séon, "Size and speed of jet drops are robust to initial perturbations", Physical Review Fluids **7**, 013602 (2022).

[96]P. Marmottant and E. Villermaux, "On spray formation", Journal of Fluid Mechanics **498**, 73–111 (2004).

[97]E. Villermaux, "Fragmentation versus cohesion", Journal of Fluid Mechanics **898**, `10.1017/jfm.2020.366` (2020).

[98]A. Berny, S. Popinet, T. Séon, and L. Deike, "Statistics of jet drop production", Geophysical Research Letters **48**, e2021GL092919 (2021).

[99]S. Pal, "Investigation of complex liquid-gas interfacial flows: a numerical study using advanced volume-of-fluid methods", PhD thesis (Sorbonne Université, 2020).

[100]S. Popinet, "Numerical models of surface tension", Annual Review of Fluid Mechanics **50**, 49–75 (2018).

[101]S. Popinet, "An accurate adaptive solver for surface-tension-driven interfacial flows", Journal of Computational Physics **228**, 5838–5866 (2009).

[102]S. Popinet, *Basilisk flow solver and PDE library*, Available at: `http://basilisk.fr`, 2019.

[103]J. B. Bell, P. Colella, and H. M. Glaz, "A second-order projection method for the incompressible Navier-Stokes equations", Journal of Computational Physics **85**, 257–283 (1989).

[104]L. Prouvost, "Mesh adaptation for elliptic equations on quadtree/octree grids", PhD thesis (Sorbonne Université, 2022).

[105]J. Wu, "Ocean wave dynamics with high fidelity numerical simulations", PhD thesis (Princeton University, 2023).

[106]J. A. Van Hooft, S. Popinet, C. C. Van Heerwaarden, S. J. Van der Linden, S. R. De Roode, and B. J. Van de Wiel, "Towards adaptive grids for atmospheric boundary-layer simulations", Boundary-Layer Meteorology **167**, 421–443 (2018).

[107]Y. Ling, D. Fuster, S. Zaleski, and G. Tryggvason, "Spray formation in a quasiplanar gas-liquid mixing layer at moderate density ratios: a numerical closeup", Physical Review Fluids **2**, 014005 (2017).

[108]X. Wu, "Inflow turbulence generation methods", Annual Review of Fluid Mechanics **49**, 23–49 (2017).

[109]Z. A. Rana, B. Thornber, and D. Drikakis, "Transverse jet injection into a supersonic turbulent cross-flow", Physics of fluids **23** (2011).

[110]Y. Chen, K. Djidjeli, and Z.-T. Xie, "Freestream turbulence effects on the aerodynamics of an oscillating square cylinder at the resonant frequency", Fluids **7**, 329 (2022).

[111]Y. Kim, I. P. Castro, and Z.-T. Xie, "Divergence-free turbulence inflow conditions for large-eddy simulations with incompressible flow solvers", Computers & Fluids **84**, 56–68 (2013).

[112]M. Klein, A. Sadiki, and J. Janicka, "A digital filter based generation of inflow data for spatially developing direct numerical or large eddy simulations", Journal of Computational Physics **186**, 652–665 (2003).

[113]C. Pairetti, S. Popinet, S. Damián, N. Nigro, and S. Zaleski, "Bag mode breakup simulations of a single liquid droplet", in 6th european conference on computational mechanics (2018).

[114]M. A. Erinin, S. D. Wang, R. Liu, D. Towle, X. Liu, and J. H. Duncan, "Spray generation by a plunging breaker", Geophysical Research Letters **46**, 8244–8251 (2019).

[115]M. Jalaal and K. Mehravaran, "Fragmentation of falling liquid droplets in bag breakup mode", International Journal of Multiphase Flow **47**, 115–132 (2012).

[116]P. Mehta, R. Haj-Ahmad, M. Rasekh, M. S. Arshad, A. Smith, S. M. van der Merwe, X. Li, M.-W. Chang, and Z. Ahmad, "Pharmaceutical and biomaterial engineering via electrohydrodynamic atomization technologies", Drug Discovery Today **22**, 157–165 (2017).

[117]W.-H. Chou and G. M. Faeth, "Temporal properties of secondary drop breakup in the bag breakup regime", International Journal of Multiphase Flow **24**, 889–912 (1998).

[118]M. Jain, R. S. Prakash, G. Tomar, and R. V. Ravikrishna, "Secondary breakup of a drop at moderate Weber numbers", Proceedings of the Royal Society A: Mathematical, Physical and Engineering Sciences **471**, 20140930 (2015).

[119]T. G. Theofanous, V. V. Mitkin, C. L. Ng, C. H. Chang, X. Deng, and S. Sushchikh, "The physics of aerobreakup. II. Viscous liquids", Physics of Fluids **24**, 022104 (2012).

[120]P. Kundu, I. Cohen, and D. Dowling, *Fluid mechanics* (Elsevier Science, 2012).

[121]M. Gorokhovski and M. Herrmann, "Modeling primary atomization", Annual Review of Fluid Mechanics **40**, 343–366 (2008).

[122]Y. Ling and T. Mahmood, "Detailed numerical investigation of the drop aerobreakup in the bag breakup regime", Journal of Fluid Mechanics **972**, A28 (2023).

[123]Y. Ling, S. Zaleski, and R. Scardovelli, "Multiscale simulation of atomization with small droplets represented by a Lagrangian point-particle model", International Journal of Multiphase Flow **76**, 122–143 (2015).

[124]J. Shinjo, "Recent advances in computational modeling of primary atomization of liquid fuel sprays", Energies **11**, 2971 (2018).

[125]E. Coyajee and B. J. Boersma, "Numerical simulation of drop impact on a liquid–liquid interface with a multiple marker front-capturing method", Journal of Computational Physics **228**, 4444–4467 (2009).

[126]J. Zhang, L. Chen, and M.-J. Ni, "Vortex interactions between a pair of bubbles rising side by side in ordinary viscous liquids", Physical Review Fluids **4**, 043604 (2019).

[127]J. U. Brackbill, D. B. Kothe, and C. Zemach, "A continuum method for modeling surface tension", Journal of Computational Physics **100**, 335–354 (1992).

[128]Y. Li, P. Zhang, and N. Kang, "Theoretical analysis of Rayleigh–Taylor instability on a spherical droplet in a gas stream", Applied Mathematical Modelling **67**, 634–644 (2019).

[129]A. K. Flock, D. R. Guildenbecher, J. Chen, P. E. Sojka, and H.-J. Bauer, "Experimental statistics of droplet trajectory and air flow during aerodynamic fragmentation of liquid drops", International Journal of Multiphase Flow **47**, 37–49 (2012).

[130]V. Kulkarni and P. E. Sojka, "Bag breakup of low viscosity drops in the presence of a continuous air jet", Physics of Fluids **26**, 072103 (2014).

[131]H. Kočárková, F. Rouyer, and F. Pigeonneau, "Film drainage of viscous liquid on top of bare bubble: influence of the bond number", Physics of Fluids **25**, 022105 (2013).

[132]M. Guémas, A. Sellier, and F. Pigeonneau, "Slow viscous gravity-driven interaction between a bubble and a free surface with unequal surface tensions", Physics of Fluids **27**, 043102 (2015).

[133]B. Néel and E. Villermaux, "The spontaneous puncture of thick liquid films", Journal of Fluid Mechanics **838**, 192–221 (2018).

[134]K. Tang, W. Mostert, D. Fuster, and L. Deike, "Effects of surface tension on the Richtmyer-Meshkov instability in fully compressible and inviscid fluids", Physical Review Fluids **6**, 113901 (2021).

[135]S. Pal, C. Pairetti, M. Crialesi-Esposito, D. Fuster, and S. Zaleski, "Statistics of drops generated from ensembles of randomly corrugated ligaments", Physics of Fluids **36** (2024).

[136]L. Hu, L. She, Y. Fang, R. Su, and X. Fu, "Deformation characteristics of droplet generated by rayleigh jet breakup", AIP Advances **11**, 045310 (2021).

[137]A. A. Castrejón-Pita, J. R. Castrejón-Pita, and I. M. Hutchings, "Breakup of liquid filaments", Physical Review Letters **108**, 074506 (2012).

[138]P. Vassallo and N. Ashgriz, "Satellite formation and merging in liquid jet breakup", Proceedings of the Royal Society of London. Series A: Mathematical and Physical Sciences **433**, 269–286 (1991).

[139]W. H. R. Chan, M. S. Dodd, P. L. Johnson, and P. Moin, "Identifying and tracking bubbles and drops in simulations: a toolbox for obtaining sizes, lineages, and breakup and coalescence statistics", Journal of Computational Physics **432**, 110156 (2021).

[140]B. Lalanne, O. Masbernat, and F. Risso, "A model for drop and bubble breakup frequency based on turbulence spectra", AIChE Journal **65**, 347–359 (2019).

[141]B. Néel and L. Deike, "Velocity and size quantification of drops in single and collective bursting bubbles experiments", Physical Review Fluids **7**, 103603 (2022).

[142]W. H. R. Chan, P. L. Johnson, and P. Moin, "The turbulent bubble break-up cascade. part 1. theoretical developments", Journal of Fluid Mechanics **912** (2021).

[143]C. Garrett, M. Li, and D. Farmer, "The connection between bubble size spectra and energy dissipation rates in the upper ocean", Journal of Physical Oceanography **30**, 2163–2171 (2000).

[144]G. B. Deane and M. D. Stokes, "Scale dependence of bubble creation mechanisms in breaking waves", Nature **418**, 839–844 (2002).

[145]L. Deike, W. K. Melville, and S. Popinet, "Air entrainment and bubble statistics in breaking waves", Journal of Fluid Mechanics **801**, 91–129 (2016).

[146]A. Prosperetti, "Free oscillations of drops and bubbles: the initial-value problem", Journal of Fluid Mechanics **100**, 333–347 (1980).

[147]I. Rodriguez, R. Borell, O. Lehmkuhl, C. D. P. Segarra, and A. Oliva, "Direct numerical simulation of the flow over a sphere at Re = 3700", Journal of Fluid Mechanics **679**, 263–287 (2011).

[148]B. Boyd, S. Becker, and Y. Ling, "Simulation and modeling of the vaporization of a freely moving and deforming drop at low to moderate Weber numbers", International Journal of Heat and Mass Transfer **218**, 124735 (2024).

[149]D. Lohse, "Fundamental fluid dynamics challenges in inkjet printing", Annual Review of Fluid Mechanics **54**, 349–382 (2022).

[150]S. Sharma, N. K. Chandra, S. Basu, and A. Kumar, "Advances in droplet aerobreakup", The European Physical Journal Special Topics, 1–15 (2022).

[151]J. Wu, S. Popinet, and L. Deike, "Revisiting wind wave growth with fully coupled direct numerical simulations", Journal of Fluid Mechanics **951**, A18 (2022).

[152]Z. Xu, T. Wang, and Z. Che, "Droplet deformation and breakup in shear flow of air", Physics of Fluids **32** (2020).

[153]A. Vela-Martín and M. Avila, "Memoryless drop breakup in turbulence", Science Advances **8**, eabp9561 (2022).

[154]M. Crialesi-Esposito, S. Chibbaro, and L. Brandt, "The interaction of droplet dynamics and turbulence cascade", Communications Physics **6**, 5 (2023).

[155]C. Rosales and C. Meneveau, "Linear forcing in numerical simulations of isotropic turbulence: physical space implementations and convergence properties", Physics of Fluids **17**, 095106 (2005).

[156]S. Perrard, A. Rivière, W. Mostert, and L. Deike, "Bubble deformation by a turbulent flow", Journal of Fluid Mechanics **920**, A15 (2021).

[157]A. Loisy and A. Naso, "Interaction between a large buoyant bubble and turbulence", Physical Review Fluids **2**, 014606 (2017).

[158]N. Kornev and E. Hassel, "Method of random spots for generation of synthetic inhomogeneous turbulent fields with prescribed autocorrelation functions", Communications in Numerical Methods in Engineering **23**, 35–43 (2007).

[159]M. S. Dodd and A. Ferrante, "On the interaction of Taylor length scale size droplets and isotropic turbulence", Journal of Fluid Mechanics **806**, 356–412 (2016).

[160]S. Elghobashi, "Direct numerical simulation of turbulent flows laden with droplets or bubbles", Annual Review of Fluid Mechanics **51**, 217–244 (2019).

[161]K. Tang, T. A. A. Adcock, and W. Mostert, "Fragmentation of colliding liquid rims", Journal of Fluid Mechanics **987**, A18 (2024).

[162]D. Legendre, A. Merle, and J. Magnaudet, "Wake of a spherical bubble or a solid sphere set fixed in a turbulent environment", Physics of Fluids **18**, 048102 (2006).

[163]S. B. Pope, *Turbulent flows* (Cambridge University Press, 2000).

[164]Y. Zhou, K. Nagata, Y. Sakai, H. Suzuki, Y. Ito, O. Terashima, and T. Hayase, "Relevance of turbulence behind the single square grid to turbulence generated by regular-and multiscale-grids", Physics of Fluids **26** (2014).

[165]I. Cannon, G. Soligo, and M. E. Rosti, "Morphology of clean and surfactant-laden droplets in homogeneous isotropic turbulence", Journal of Fluid Mechanics **987**, A31 (2024).

[166]Y. Wang, A. Sierakowski, and A. Prosperetti, "Rotational dynamics of a particle in a turbulent stream", Physical Review Fluids **4**, 064304 (2019).

[167]X. Xu, Y. Qi, S. Zhong, S. Tan, Q. Wu, and R. Ni, "Intermittency of bubble deformation in turbulence", Physical Review Letters **133**, 214001 (2024).

[168]L. Botto and A. Prosperetti, "A fully resolved numerical simulation of turbulent flow past one or several spherical particles", Physics of Fluids **24** (2012).

[169]C. Peng and L.-P. Wang, "Mechanisms and models of particle drag enhancements in turbulent environments", Journal of Fluid Mechanics **959**, A30 (2023).

[170]E. Rind and I. P. Castro, "On the effects of free-stream turbulence on axisymmetric disc wakes", Experiments in fluids **53**, 301–318 (2012).

[171]F. Jiang, L. Zhao, H. I. Andersson, K. Gustavsson, A. Pumir, and B. Mehlig, "Inertial torque on a small spheroid in a stationary uniform flow", Physical Review Fluids **6**, 024302 (2021).

[172]I. Roa, M.-C. Renoult, C. Dumouchel, and J. C. Brändle de Motta, "Droplet oscillations in a turbulent flow", Frontiers in Physics **11**, 1173521 (2023).

[173]Z. Cui, J. Qiu, X. Jiang, and L. Zhao, "Effect of fluid inertial torque on the rotational and orientational dynamics of tiny spheroidal particles in turbulent channel flow", Journal of Fluid Mechanics **977**, A20 (2023).

[174]A. Vela-Martín and M. Avila, "Deformation of drops by outer eddies in turbulence", Journal of Fluid Mechanics **929**, A38 (2021).

[175]A. U. M. Masuk, A. K. Salibindla, and R. Ni, "Simultaneous measurements of deforming Hinze-scale bubbles with surrounding turbulence", Journal of Fluid Mechanics **910**, A21 (2021).

[176]A. U. M. Masuk, A. K. Salibindla, and R. Ni, "The orientational dynamics of deformable finite-sized bubbles in turbulence", Journal of Fluid Mechanics **915**, A79 (2021).

[177]R. Ouchene, "Numerical simulation and modeling of the hydrodynamic forces and torque acting on individual oblate spheroids", Physics of Fluids **32** (2020).

[178]G. A. Voth and A. Soldati, "Anisotropic particles in turbulence", Annual Review of Fluid Mechanics **49**, 249–276 (2017).

[179]F. Mangani, G. Soligo, A. Roccon, and A. Soldati, "Influence of density and viscosity on deformation, breakage, and coalescence of bubbles in turbulence", Physical Review Fluids **7**, 053601 (2022).

[180]Y. Qi, X. Xu, S. Tan, S. Zhong, Q. Wu, and R. Ni, "Breaking bubbles across multiple time scales in turbulence", Journal of Fluid Mechanics **983**, A24 (2024).

[181]A. A. Castrejón-Pita, E. S. Betton, N. Campbell, N. Jackson, J. Morgan, T. R. Tuladhar, D. C. Vadillo, and J. R. Castrejon-Pita, "Formulation, quality, cleaning, and other advances in inkjet printing", Atomization and Sprays **31** (2021).

[182]A. M. Worthington, "On the forms assumed by drops of liquids falling vertically on a horizontal plate", Proceedings of the Royal Society of London **25**, 261–272 (1877).

[183]M.-J. Thoraval, K. Takehara, T. G. Etoh, and S. T. Thoroddsen, "Drop impact entrapment of bubble rings", Journal of Fluid Mechanics **724**, 234–258 (2013).

[184]G. Agbaglah, M.-J. Thoraval, S. T. Thoroddsen, L. V. Zhang, K. Fezzaa, and R. D. Deegan, "Drop impact into a deep pool: vortex shedding and jet formation", Journal of Fluid Mechanics **764**, R1 (2015).

[185]H. Wang, S. Liu, A.-C. Bayeul-Lainé, D. Murphy, J. Katz, and O. Coutier-Delgosha, "Analysis of high-speed drop impact onto deep liquid pool", Journal of Fluid Mechanics **972**, A31 (2023).

[186]R. Cimpeanu and D. T. Papageorgiou, "Three-dimensional high speed drop impact onto solid surfaces at arbitrary angles", International Journal of Multiphase Flow **107**, 192–207 (2018).

[187]P. García-Geijo, E. S. Quintero, G. Riboux, and J. M. Gordillo, "Spreading and splashing of drops impacting rough substrates", Journal of Fluid Mechanics **917**, A50 (2021).

[188]C. He, X. Xia, and P. Zhang, "Non-monotonic viscous dissipation of bouncing droplets undergoing off-center collision", Physics of Fluids **31**, 052004 (2019).

[189]C. He, L. Yue, and P. Zhang, "Spin-affected reflexive and stretching separation of off-center droplet collision", Physical Review Fluids **7**, 013603 (2022).

[190]Q. Liu, J. H. Y. Lo, Y. Li, Y. Liu, J. Zhao, and L. Xu, "The role of drop shape in impact and splash", Nature Communications **12**, 3068 (2021).

[191]G. I. Taylor, "The dynamics of thin sheets of fluid II. Waves on fluid sheets", Proceedings of the Royal Society of London. Series A. Mathematical and Physical Sciences **253**, 296–312 (1959).

[192]F. E. C. Culick, "Comments on a ruptured soap film", Journal of Applied Physics **31**, 1128–1129 (1960).

[193]R. W. Hopper, "Coalescence of two viscous cylinders by capillarity: Part I. Theory", Journal of the American Ceramic Society **76**, 2947–2952 (1993).

[194]R. W. Hopper, "Coalescence of two viscous cylinders by capillarity: Part II. Shape evolution", Journal of the American Ceramic Society **76**, 2953–2960 (1993).

[195]J. Eggers, J. R. Lister, and H. A. Stone, "Coalescence of liquid drops", Journal of Fluid Mechanics **401**, 293–310 (1999).

[196]Z. Wang, J. Yang, and F. Stern, "High-fidelity simulations of bubble, droplet and spray formation in breaking waves", Journal of Fluid Mechanics **792**, 307–327 (2016).

[197]Q. Gao, G. B. Deane, and L. Shen, "Bubble production by air filament and cavity breakup in plunging breaking wave crests", Journal of Fluid Mechanics **929**, A44 (2021).

[198]M. Liu and D. Bothe, "Numerical study of head-on droplet collisions at high Weber numbers", Journal of Fluid Mechanics **789**, 785–805 (2016).

[199]L. V. Zhang, P. Brunet, J. Eggers, and R. D. Deegan, "Wavelength selection in the crown splash", Physics of Fluids **22** (2010).

[200]C. Josserand, P. Ray, and S. Zaleski, "Droplet impact on a thin liquid film: anatomy of the splash", Journal of Fluid Mechanics **802**, 775–805 (2016).

[201]M. S. Longuet-Higgins, "Vertical jets from standing waves", Proceedings of the Royal Society of London. Series A: Mathematical, Physical and Engineering Sciences **457**, 495–510 (2001).

[202]J. Philippi, P.-Y. Lagrée, and A. Antkowiak, "Drop impact on a solid surface: short-time self-similarity", Journal of Fluid Mechanics **795**, 96–135 (2016).

[203]G. Riboux and J. M. Gordillo, "Experiments of drops impacting a smooth solid surface: a model of the critical impact speed for drop splashing", Physical Review Letters **113**, 024507 (2014).

[204]A. Goswami and Y. Hardalupas, "Simultaneous impact of droplet pairs on solid surfaces", Journal of Fluid Mechanics **961**, A17 (2023).

[205]C. Josserand and S. T. Thoroddsen, "Drop impact on a solid surface", Annual Review of Fluid Mechanics **48**, 365–391 (2016).

[206]A. L. Yarin and D. A. Weiss, "Impact of drops on solid surfaces: self-similar capillary waves, and splashing as a new type of kinematic discontinuity", Journal of Fluid Mechanics **283**, 141–173 (1995).

[207]E. Villermaux and B. Bossa, "Drop fragmentation on impact", Journal of Fluid Mechanics **668**, 412–435 (2011).

[208]G. Riboux and J. M. Gordillo, "The diameters and velocities of the droplets ejected after splashing", Journal of Fluid Mechanics **772**, 630–648 (2015).

[209]A. Mongruel, V. Daru, F. Feuillebois, and S. Tabakova, "Early post-impact time dynamics of viscous drops onto a solid dry surface", Physics of Fluids **21** (2009).

[210]S. T. Thoroddsen, K. Takehara, and T. G. Etoh, "Micro-splashing by drop impacts", Journal of Fluid Mechanics **706**, 560–570 (2012).

[211]C. W. Visser, P. E. Frommhold, S. Wildeman, R. Mettin, D. Lohse, and C. Sun, "Dynamics of high-speed micro-drop impact: numerical simulations and experiments at frame-to-frame times below 100 ns", Soft Matter **11**, 1708–1722 (2015).

[212]J. M. Gordillo, H. Onuki, and Y. Tagawa, "Impulsive generation of jets by flow focusing", Journal of Fluid Mechanics **894**, A3 (2020).

[213]É. Ghabache, T. Séon, and A. Antkowiak, "Liquid jet eruption from hollow relaxation", Journal of Fluid Mechanics **761**, 206–219 (2014).

[214]B. D. Fudge, R. Cimpeanu, A. Antkowiak, J. R. Castrejón-Pita, and A. A. Castrejón-Pita, "Drop splashing after impact onto immiscible pools of different viscosities", Journal of Colloid and Interface Science **641**, 585–594 (2023).

[215]G. K. Batchelor, *An introduction to fluid dynamics* (Cambridge University Press, 2000).

[216]E. Li, M.-J. Thoraval, J. O. Marston, and S. T. Thoroddsen, "Early azimuthal instability during drop impact", Journal of Fluid Mechanics **848**, 821–835 (2018).

[217]L. Ó Náraigh and J. Mairal, "Analysis of the spreading radius in droplet impact: the two-dimensional case", Physics of Fluids **35** (2023).

[218]S. T. Thoroddsen and J. Sakakibara, "Evolution of the fingering pattern of an impacting drop", Physics of Fluids **10**, 1359–1374 (1998).

[219]H. Marmanis and S. T. Thoroddsen, "Scaling of the fingering pattern of an impacting drop", Physics of Fluids **8**, 1344–1346 (1996).

[220]D. A. Burzynski, I. V. Roisman, and S. E. Bansmer, "On the splashing of high-speed drops impacting a dry surface", Journal of Fluid Mechanics **892**, A2 (2020).

[221]A. Saruwatari, Y. Watanabe, and D. M. Ingram, "Scarifying and fingering surfaces of plunging jets", Coastal Engineering **56**, 1109–1122 (2009).

[222]P. Lubin, O. Kimmoun, F. Véron, and S. Glockner, "Discussion on instabilities in breaking waves: vortices, air-entrainment and droplet generation", European Journal of Mechanics-B/Fluids **73**, 144–156 (2019).

[223]I. V. Roisman and C. Tropea, "Impact of a drop onto a wetted wall: description of crown formation and propagation", Journal of Fluid Mechanics **472**, 373–397 (2002).

[224]R. G. Ramirez de La Torre, P. Vollestad, and A. Jensen, "Experimental investigation of droplet generation by post-breaking plunger waves", Water Waves **4**, 1–21 (2022).

[225]J. Wu, S. Popinet, and L. Deike, "Breaking wave field statistics with a multi-layer model", Journal of Fluid Mechanics **968**, A12 (2023).

[226]S. Popinet, "A vertically-lagrangian, non-hydrostatic, multilayer model for multiscale free-surface flows", Journal of Computational Physics **418**, 109609 (2020).

[227]L. Romero, "Distribution of surface wave breaking fronts", Geophysical Research Letters **46**, 10463–10474 (2019).

[228]M. McAllister, S. Draycott, R. Calvert, T. Davey, F. Dias, and T. van den Bremer, "Three-dimensional wave breaking", Nature **633**, 601–607 (2024).

[229]O. Phillips, "Spectral and statistical properties of the equilibrium range in wind-generated gravity waves", Journal of Fluid Mechanics **156**, 505–531 (1985).

[230]L. Deike and W. K. Melville, "Gas transfer by breaking waves", Geophysical Research Letters **45**, 10–482 (2018).

[231]L. Deike, L. Lenain, and W. K. Melville, "Air entrainment by breaking waves", Geophysical Research Letters **44**, 3779–3787 (2017).

[232]W. K. Melville, L. Lenain, D. R. Cayan, M. Kahru, J. P. Kleissl, P. Linden, and N. M. Statom, "The modular aerial sensing system", Journal of Atmospheric and Oceanic Technology **33**, 1169–1184 (2016).

[233]A. Freund and A. Ferrante, "Wavelet-spectral analysis of droplet-laden isotropic turbulence", Journal of Fluid Mechanics **875**, 914–928 (2019).

[234]A. Calado and E. Balaras, "Dynamics of bubble deformation and breakup in decaying isotropic turbulence", Physical Review Fluids **9**, 123604 (2024).

[235]H. Zhao, W.-B. Zhang, J.-L. Xu, W.-F. Li, and H.-F. Liu, "Influence of surfactant on the drop bag breakup in a continuous air jet stream", Physics of Fluids **28** (2016).

[236]H. Zhao, W.-B. Zhang, J.-L. Xu, W.-F. Li, and H.-F. Liu, "Surfactant-laden drop jellyfish-breakup mode induced by the Marangoni effect", Experiments in Fluids **58**, 1–7 (2017).

[237]M. Erinin, C. Liu, X. Liu, W. Mostert, L. Deike, and J. Duncan, "The effects of surfactants on plunging breakers", Journal of Fluid Mechanics **972**, R5 (2023).

[238]P. K. Farsoiya, S. Popinet, H. A. Stone, and L. Deike, "Coupled volume of fluid and phase field method for direct numerical simulation of insoluble surfactant-laden interfacial flows and application to rising bubbles", Physical Review Fluids **9**, 094004 (2024).

[239]G. G. Agbaglah, "Numerical study of hole formation in a thin flapping liquid sheet sheared by a fast gas stream", Physics of Fluids **33** (2021).

[240]Y. Sasar and G. G. Agbaglah, "Bag film rupture mechanisms in droplet fragmentation under uniform airflows", Physics of Fluids **37** (2025).

[241]A. Dixit, C. Zhao, S. Zaleski, D. Lohse, and V. Sanjay, "Holes-driven rupture: unveiling the dynamics of liquid sheet atomization", in Aps division of fluid dynamics meeting abstracts (2024), pp. C07–006.

[242]C. R. Constante-Amores, J. Chergui, S. Shin, D. Juric, J. R. Castrejón-Pita, and A. A. Castrejón-Pita, "Role of surfactant-induced Marangoni stresses in retracting liquid sheets", Journal of Fluid Mechanics **949**, A32 (2022).

[243]C. Constante-Amores, L. Kahouadji, S. Shin, J. Chergui, D. Juric, J. R. Castrejón-Pita, O. Matar, and A. Castrejón-Pita, "Impact of droplets onto surfactant-laden thin liquid films", Journal of Fluid Mechanics **961**, A8 (2023).

[244]H. Lamb, *Hydrodynamics* (Cambridge University Press, 1932).

[245]H. Wagner, "Über stoß- und gleitvorgänge an der oberfläche von flüssigkeiten", Zeitschrift für Angewandte Mathematik und Mechanik **12**, 193–215 (1932).